energies

Special Issue Reprint

Advanced Energy Technologies and Energy Savings

Low Emissions and High Efficiency

Edited by
Shujun Zhu, Shuai Guo, Zhuozhi Wang and Lianfei Xu

mdpi.com/journal/energies

MDPI

Advanced Energy Technologies and Energy Savings: Low Emissions and High Efficiency

Advanced Energy Technologies and Energy Savings: Low Emissions and High Efficiency

Guest Editors

Shujun Zhu
Shuai Guo
Zhuozhi Wang
Lianfei Xu

MDPI

Basel • Beijing • Wuhan • Barcelona • Belgrade • Novi Sad • Cluj • Manchester

Guest Editors

Shujun Zhu
Institute of Engineering Thermophysics
Chinese Academy of Sciences
Beijing
China

Shuai Guo
School of Energy and Power Engineering
Northeast Electric Power University
Jilin
China

Zhuozhi Wang
School of Chemical Engineering and Technology
Hebei University of Technology
Tianjin
China

Lianfei Xu
School of Energy and Environmental Engineering
Hebei University of Technology
Tianjin
China

Editorial Office
MDPI AG
Grosspeteranlage 5
4052 Basel, Switzerland

This is a reprint of the Special Issue, published open access by the journal *Energies* (ISSN 1996-1073), freely accessible at: https://www.mdpi.com/journal/energies/special_issues/5OQ6Y6H0A0.

For citation purposes, cite each article independently as indicated on the article page online and as indicated below:

Lastname, A.A.; Lastname, B.B. Article Title. *Journal Name* **Year**, *Volume Number*, Page Range.

ISBN 978-3-7258-8653-1 (Hbk)
ISBN 978-3-7258-8654-8 (PDF)
https://doi.org/10.3390/books978-3-7258-8654-8

© 2026 by the authors. Articles in this reprint are Open Access and distributed under the Creative Commons Attribution (CC BY) license. The reprint as a whole is distributed by MDPI under the terms and conditions of the Creative Commons Attribution-NonCommercial-NoDerivs (CC BY-NC-ND) license (https://creativecommons.org/licenses/by-nc-nd/4.0/).

Contents

About the Editors . . . . . **vii**

Yinghui Sun, Bohao Bai, Xu Yang, Shujun Zhu, Jilin Tian, Zhuozhi Wang, et al.
Coal Gangue Utilization: Applications, Challenges, and Sustainable Development Strategies
Reprinted from: *Energies* **2025**, *18*, 444, https://doi.org/10.3390/en18020444 . . . . . **1**

Yu-Shan Cheng, Yi-Yan Chen, Cheng-Ta Tsai and Chun-Lung Chen
Optimal Multi-Area Demand–Thermal Coordination Dispatch
Reprinted from: *Energies* **2025**, *18*, 2690, https://doi.org/10.3390/en18112690 . . . . . **38**

Liying Wang, Dan Lin, Dongjing Liu, Xing Xie, Shihong Zhang and Bin Li
Oxidative Pyrolysis of Typical Volatile Model Compounds Under Low Oxygen Equivalence Ratios During Oxidative Pyrolysis of Biomass
Reprinted from: *Energies* **2025**, *18*, 2996, https://doi.org/10.3390/en18112996 . . . . . **67**

Siyuan Wang, Hong Tang, Zuodong Liu, Lingfang Sun and Zhiming Xu
Numerical Investigation of Combustion Characteristics in a 330 MW Coal-Fired Boiler with Preheating Combustion Devices at Half Load Operation
Reprinted from: *Energies* **2025**, *18*, 5042, https://doi.org/10.3390/en18185042 . . . . . **80**

Braulio Cruz, Luis Ricalde, Roberto Quintal-Palomo, Ali Bassam and Roberto I. Rico-Camacho
Hybrid Artificial Neural Network and Perturb & Observe Strategy for Adaptive Maximum Power Point Tracking in Partially Shaded Photovoltaic Systems
Reprinted from: *Energies* **2025**, *18*, 5053, https://doi.org/10.3390/en18195053 . . . . . **99**

Saltanat Bolegenova, Aliya Askarova, Aizhan Nugymanova, Valeriy Maximov, Symbat Bolegenova, Nariman Askarov, et al.
Implementing Overfire Air Technology in Coal-Fired Power Plants to Promote Environmentally Friendly Energy Generation
Reprinted from: *Energies* **2026**, *19*, 347, https://doi.org/10.3390/en19020347 . . . . . **125**

Sayak Pradhan, Jeremy Simmons and James Van de Ven
Design Requirements for a Common-Shaft Switch-Mode Power Transformer for Ocean Wave-Powered Reverse Osmosis
Reprinted from: *Energies* **2026**, *19*, 2692, https://doi.org/10.3390/en19112692 . . . . . **146**

Xiaoyu Wang, Hongtao Chen, Hongbao Liang, Yang Liu, Zhanheng Ma, Haibo Lin, et al.
Fluid-Driven Opposed-Piston Pumps for Dense-Phase CO_2 Injection: Direct Force Coupling and Energy Efficiency Analysis
Reprinted from: *Energies* **2026**, *19*, 2886, https://doi.org/10.3390/en19122886 . . . . . **171**

About the Editors

Shujun Zhu

Shujun Zhu, Associate Professor at the Institute of Engineering Thermophysics, Chinese Academy of Sciences. He received his Ph.D. degree from University of Chinese Academy of Sciences in 2019. He is mainly engaged in research on the efficient combustion of solid fuel and thermal energy storage technology. He serves as an Editorial Board Member of "*Energies*", and has published more than 70 academic papers, with a H-index of 24. In addition, he has completed appraisal of several scientific and technological achievements, including "Fluidized Preheating Combustion Technology for Pulverized Coal Boilers," and these technological achievements were assessed as reaching an internationally leading level overall.

Shuai Guo

Shuai Guo, Ph.D., is a Professor, PhD Supervisor, and faculty member in the Boiler Teaching and Research Office of the Department of Power Engineering, School of Energy and Power Engineering, Northeast Electric Power University. He was a Visiting Scholar at Nanyang Technological University in Singapore and serves as an expert for the Basel Convention Asia-Pacific Regional Centre's Think Tank on Chemicals and Waste Environmental Management. He is also a Distinguished Expert at the Zhongbolian Institute Think Tank, a Class D Provincial Leading Talent in Jilin Province, and a Third-Tier "Dongdian Scholar" at Northeast Electric Power University. Dr. Guo has led over 10 research projects, including the National Natural Science Foundation of China, Jilin Provincial Natural Science Foundation projects, Jilin City Science and Technology Innovation and Entrepreneurship Programs, and industry-academia collaborative projects. He was awarded the National Study Abroad Fund for Young Backbone Teachers and the China Postdoctoral Science Foundation Grant. His accolades include the Third Prize of the Jilin Provincial Natural Science Award (First Completer) and the Outstanding Teaching Quality Award from Northeast Electric Power University. He serves as a reviewer for international journals such as *Energy* and *Bioresource Technology*. He has published over 50 SCI/EI-indexed papers as first or corresponding author.

Zhuozhi Wang

Zhuozhi Wang, male, is a Doctor of Engineering, Associate Professor, and Doctoral Supervisor, and is a member of the School of Chemical Engineering, Hebei University of Technology. He obtained his PhD in Thermal Engineering from Harbin Institute of Technology in 2019. His research focuses on the resource utilization of multi-source organic solid waste, clean and efficient combustion technology for carbon-neutral fuels, application of artificial intelligence technology in the field of combustion. He currently presides over 1 National Natural Science Foundation project, 5 Hebei Provincial Natural Science Foundation projects, and 6 Enterprise technology development/service projects. He has also participated in 5 key research programs, including the Key Program of the National Natural Science Foundation of China and national major science and technology special projects. He is a core member of the Innovation Team for Pollutant Control in Energy Utilization Processes. He has published over 100 high-level academic papers in prestigious journals including *Energy*, *Fuel*, and *Journal of Power Sources*.

Lianfei Xu

Lianfei Xu, male, is a Doctor of Engineering, Associate Professor, and Doctoral Supervisor, and is a member of the School of Energy and Environmental Engineering, Hebei University of Technology. He obtained his PhD in Thermal Engineering from Harbin Institute of Technology in 2018. His research focuses on coal-based/biomass-based carbon material preparation, novel electrochemical energy storage, and air pollutant control. He currently presides over 2 national research projects (including projects supported by the National Natural Science Foundation of China and sub-projects of the National Key R&D Program of China), 2 Hebei Provincial Natural Science Foundation projects, and 2 horizontal projects. He has also participated in 5 key research programs, including the Key Program of the National Natural Science Foundation of China and national major science and technology special projects. He is a core member of the Innovation Team for Pollutant Control in Energy Utilization Processes. He has published over 30 high-level academic papers in prestigious journals including *Energy*, *Fuel*, and *Journal of Power Sources*.

energies

MDPI

Review

Coal Gangue Utilization: Applications, Challenges, and Sustainable Development Strategies

Yinghui Sun [1,†], Bohao Bai [1,†], Xu Yang [1], Shujun Zhu [2], Jilin Tian [2], Zhuozhi Wang [1,*], Li Xu [3,*], Lianfei Xu [1] and Boxiong Shen [1]

[1] School of Chemical Engineering, Hebei University of Technology, Tianjin 300401, China
[2] Shanxi Key Laboratory of Coal Flexible Combustion and Thermal Conversion, Datong 037000, China
[3] Anhui Special Equipment Inspection Institute, 45 Dalian Road, Hefei 230051, China
* Correspondence: 2021115@hebut.edu.cn (Z.W.); dps_1987@163.com (L.X.)
† These authors contributed equally to this work.

Abstract: Coal gangue is a kind of typical by-product emitted during the coal mining and washing process. With the increase in coal resource utilization, a large amount of coal gangue was not reasonably utilized, causing environmental pollution and resource waste. The main purpose of this article is to introduce the surface structural features and compositional characteristics of coal gangue and to summarize the utilization of coal gangue in the fields of building materials, energy production, agricultural utilization, and high-value-added areas such as catalysts and adsorbents. Secondly, this review discussed the environmental challenges and technical difficulties derived from the process of coal gangue utilization and how to solve these problems through innovative methods and technological improvements. Finally, the article proposed the development direction and strategies for the future resource utilization of coal gangue, emphasizing the importance of coal gangue as a sustainable resource and its significant role in achieving a circular economy for reducing environmental pollution. By analyzing the potentiality of coal gangue for resource utilization systematically, this article aims to provide valuable references and insights for researchers and decision-makers in related fields.

Keywords: coal gangue; environmental impact; energy applications; high-value products

1. Introduction

As one of the main energy sources in China, in 2024, the country produced 4.76 billion tons of raw coal, an increase of 1.06% compared to the previous year [1,2]. Coal gangue, as a major by-product associated with coal, accounts for 40% of the total volume of industrial solid waste. Its comprehensive utilization and supply side structural reform have become focal points of concern for both the coal industry and society [3,4]. Figures 1 and 2 show the coal gangue production and percentage across various provinces and cities in China from 2017 to 2023.

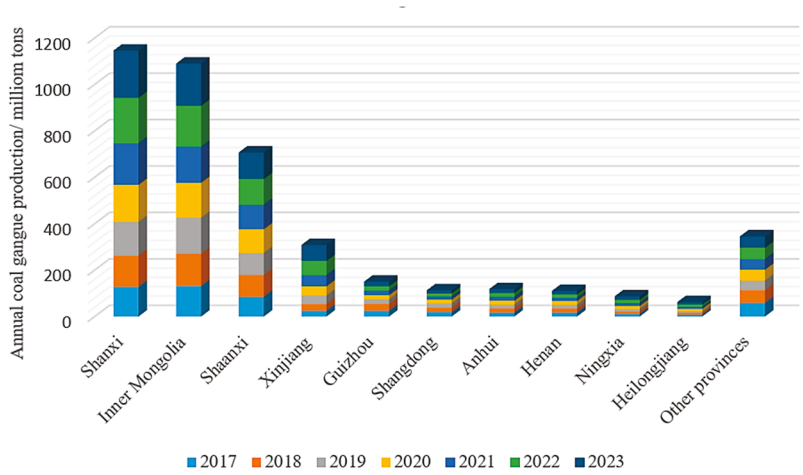


Figure 1. The annual coal gangue production in different provinces of China from 2017 to 2023 [5].

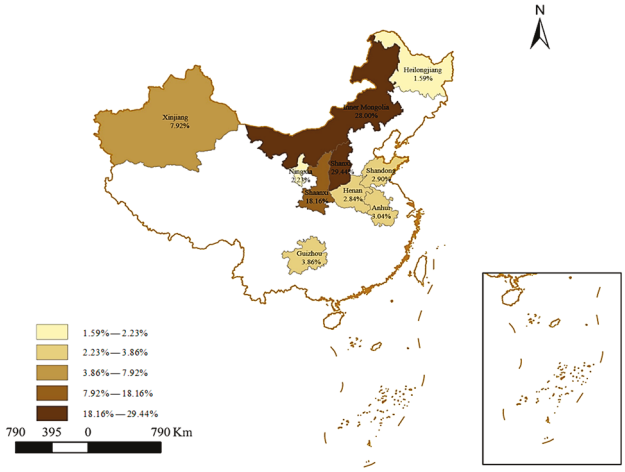


Figure 2. The percentages of coal gangue production in different provinces of China from 2017 to 2023 [5].

Coal gangue is generated during the coal mining and washing process, accounting for 10–15% of the total coal output, making it one of the largest industrial solid wastes in China [6,7]. Additionally, the production of coal gangue mainly comes from several sources: the process of roadway excavation; the roof, floor, and interlayer during the mining process [8,9]. According to the standards of the China Coal Industry Association for gangue classification. It is classified into four categories based on total sulfur content: low, medium, medium-high, and high, as shown in Table 1. This standard specifies the classification categories and naming conventions for coal gangue, applicable to its output and resource utilization. In the traditional coal gangue pre-selection process, the intensity of manual labor is high, efficiency is low, and there are potential safety risks. The improved ResNet18-YOLO algorithm can detect coal gangue at a speed of 45.5 ms per frame, with the model size only about 65.34 MB, and the mAP of coal gangue detection is 96.27%, offering better real-time performance and a smaller model size [10].

Table 1. Classification of coal gangue based on total sulfur content.

Category	Low Sulfur	Medium Sulfur	Medium High Sulfur	Sulfur High Sulfur
W (Std)	W (Std) $\leq$ 1%	1% < W (Std) < 3%	3% < W (Std) < 6%	W (Std) > 6%

Note: Std refers to total sulfur on a dry basis.

Coal gangue, as a commonly encountered industrial solid waste, has a multidimensional and profound environmental impact [11,12]. Firstly, the massive accumulation of coal gangue occupies a significant amount of land resources, especially near mining areas. Extensive stacking can lead to the ineffective use of land resources and may trigger soil erosion and desertification, thereby negatively affecting the local ecosystem [13,14]. Additionally, the toxic elements in coal gangue can penetrate the soil through leaching, altering the soil's chemical composition, and consequently affecting soil fertility and agricultural production [15,16]. The dissolved heavy metals and other harmful substances in coal gangue can also enter groundwater and surface water bodies through leaching, posing potential threats to aquatic life and even human health [17,18]. The organic materials in coal gangue can release harmful gases, such as hydrogen sulfide and nitrogen oxides, under natural conditions or during incineration, further exacerbating air pollution [19]. In terms of social and public health, the harmful substances in coal gangue can enter the human body through the food chain, air, and water sources, increasing the risk of respiratory diseases and skin conditions [20,21]. The spontaneous combustion of coal gangue heaps is a non-negligible issue. According to related research statistics, among approximately 1900 coal gangue heaps in China, more than 600 have experienced or are experiencing spontaneous combustion [22]. This combustion releases harmful gases such as sulfur dioxide (SO_2), carbon monoxide (CO), and nitrogen oxides (NO_X), causing damage to the surrounding environment and vegetation [23,24].

Therefore, the implementation of effective coal gangue management strategies, particularly through resource utilization measures, has become a critical issue in environmental protection and sustainable development strategies. The resource utilization of coal gangue not only effectively reduces its negative environmental impact but also transforms waste into valuable resources, promoting the development of a circular economy. Currently, the main avenues for coal gangue resource utilization include its application in construction materials, soil conditioners, and energy resources. For instance, coal gangue can be used as raw material for cement and bricks after high-temperature sintering. Additionally, with specific treatments, it can serve as a soil conditioner to improve the fertility of degraded lands. Furthermore, the combustion of coal gangue or its co-combustion with biomass can realize its reuse as an energy source. In summary, the resource utilization of coal gangue not only helps mitigate environmental pollution but also creates new development opportunities for related industries, driving the realization of a green and low-carbon economy.

2. Physical and Chemical Features of Coal Gangue

The chemical composition of coal gangue determines its various potential industrial applications. For instance, coal gangue with high silicon and aluminum content can be used as raw materials in the construction materials industry for the production of cement, bricks, and tiles. Additionally, due to the high content of silicon and aluminum in coal gangue, it can also be utilized in the preparation of silicate and aluminate chemical products. Furthermore, some components of coal gangue can be used in the production of adsorption materials, ceramics, and more [25,26].

2.1. Main Chemical Components

Coal gangue contains a large amount of inorganic substances, such as silicates, aluminates, calcium salts, and iron-manganese salts [27]. Specifically, the primary chemical components in coal gangue are silicon dioxide (SiO_2) and aluminum oxide (Al_2O_3) [19], with the mass fractions of SiO_2 and Al_2O_3 in most regions ranging from 37% to 72% and 4.5% to 42%, respectively [28]. In addition, coal gangue may also contain other minerals such as iron oxide (Fe_2O_3), calcium oxide (CaO), magnesium oxide (MgO), and sulfates [29].

The main mineral composition and elemental analysis of coal gangue are shown in Figure 3 and Table 2, respectively. About Figure 3 Gangue samples from the open pit coal mine in Hequ County, Xinzhou City, Shanxi Province, China. The coal gangue samples in Table 2 were obtained from Dazhe Coal Mine, Yulin City, Shaanxi Province, China.

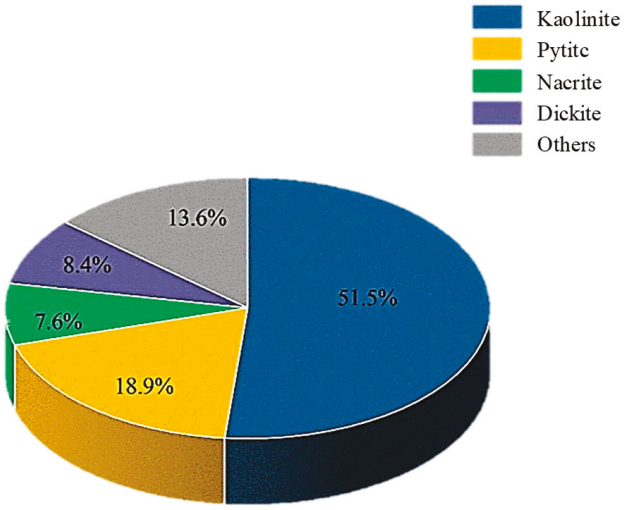


Figure 3. Distribution of main mineral components in coal gangue [30].

Table 2. Elemental analysis of coal gangue [31].

Serial Number	Element	Content (wt%)
1	O	47.549
2	Si	24.686
3	Al	10.601
4	Ca	6.06
5	Fe	3.176
6	S	2.689
7	K	2.134
8	Ti	1.297
9	Na	0.811
10	Mg	0.770
11	Mn	0.075
12	Dy	0.053
13	P	0.037
14	Cr	0.018
15	Sr	0.016
16	Zr	0.08
17	Cu	0.07
18	Rb	0.07
19	Zn	0.06

In recent years, research on the resource utilization of coal gangue has deepened, and the technology has gradually matured. For example, technologies for preparing lightweight aggregates, adsorbents, and ceramic materials from coal gangue have gradually become commercialized [32,33]. In summary, the resource utilization of coal gangue is a complex system engineering project involving environmental science, material science, chemical engineering, and other fields [34]. With the continuous deepening of related research and technological progress, the future pathways for coal gangue resource utilization will become more diversified, and its role in environmental protection and resource conservation will become even more significant.

2.2. Physical Properties

The physical properties of coal gangue include particle size, shape, density, hardness, and porosity, as well as thermal and electrical conductivity [35,36]. Particle size and shape: The particle size of coal gangue varies widely, from dust-like microparticles to large rocks, and the particles are usually irregular in shape, which affects their bulk density and flowability [37,38]. Understanding the particle size and shape helps optimize the processing technology and equipment design when using coal gangue as a raw material. Density and hardness: the density of coal gangue is relatively low, typically between 1.2 and 2.4 g/cm^3, while its hardness varies with its composition. These characteristics affect the load-bearing capacity of coal gangue when it is used as a building material or for roadbeds [39,40]. Porosity: coal gangue has a high porosity, allowing it to absorb and retain moisture [41]. A high porosity also means a higher surface area, which is an important factor when using coal gangue as an adsorbent material or catalyst carrier. The porosity of naturally piled broken gangue is about 47.5%, with micro-pores (less than 0.075 mm) dominating [42]. Thermal and electrical conductivity: the thermal conductivity and electrical conductivity of coal gangue are generally low, making them suitable for use as insulating materials or insulation materials. Understanding these properties facilitates the application of coal gangue in the construction and electric power industries.

As shown in Table 3, the physical properties of coal gangue not only affect their processing and management methods but also determine their potential applications and impact in resource utilization. For instance, small particles of coal gangue can be used as fillers or made into bricks, while large chunks of coal gangue can be utilized in building materials. The low density and high porosity of coal gangue make it an ideal choice for the preparation of lightweight aggregates, adsorbent materials, or filtration materials.

Table 3. Physical properties of coal gangue.

Physical Property	Impact of Resource Utilization
Particle size morphology	Different uses for small and large particles
Density and hardness	Load-bearing capacity when used as a building material
Porosity	Important factors for use as adsorbent materials or catalysts
Thermal and electrical conductivity	Important factors for insulation or insulating materials

3. Coal Gangue Applications

As environmental regulations become increasingly stringent, society has set higher standards for the efficient use of coal gangue. Coal gangue has shown a wide range of uses in emerging fields such as construction, energy, and agriculture, as illustrated in Figure 4. Its recycling and utilization not only solve the disposal problem but also help reduce material costs, promoting the sustainable development of resources. Table 4 shows the source, role, and application of gangue.

Table 4. The source, application, and role of coal gangue.

Source	Application	Functions	References
Coal mining and washing processes	Construction materials (e.g., cement, bricks), soil conditioners, energy recovery	Produces building materials through high-temperature sintering, improves soil quality, provides energy	[43,44]
Coal gangue stockpiles	Soil remediation, environmental pollution control (e.g., heavy metal pollution remediation)	Acts as a soil conditioner, reduces soil pollution, restores ecosystems	[45,46]
Coal gangue stockpiles	Heavy metal pollution control, ecological restoration, solid waste treatment	Adsorbs heavy metals, promotes plant growth, reduces secondary pollution	[47]
Coal mining by-products	Energy recovery (combustion, gasification)	Provides energy, reduces reliance on other energy resources	[48]

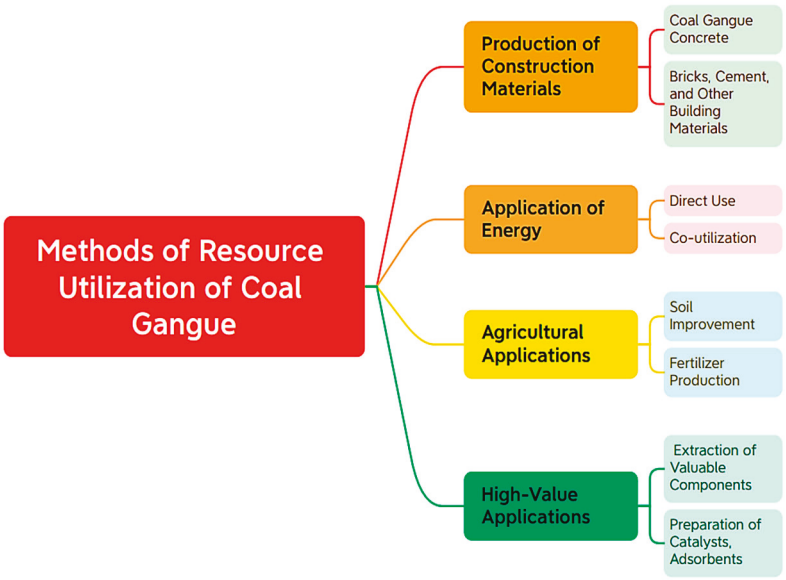


Figure 4. Methods of resource utilization of coal gangue.

3.1. Production of Construction Materials

Using coal gangue as a construction material, especially as coarse aggregate for concrete, aligns with environmental protection concepts and conserves natural resources like sand and gravel [44]. In recent years, significant achievements have been made in the resource utilization of coal gangue in the field of construction materials, mainly in the following aspects: lightweight aggregate: After processes such as crushing and screening, coal gangue can be utilized as lightweight aggregate [11,49]. This type of aggregate can reduce the unit weight of concrete, applicable in the production of lightweight concrete, thereby decreasing the structural weight and enhancing the seismic performance of buildings. Cement material: coal gangue contains silicates and aluminates, essential ingredients for cement production [50,51]. With appropriate processing, coal gangue can partially replace traditional cement production materials, reducing production costs while also decreasing resource consumption [43,52]. Wall material: coal gangue can serve as a raw material for producing sintered bricks, hollow blocks, and other wall materials [53,54]. Sintered bricks made from coal gangue exhibit good thermal insulation properties and adequate mechanical strength, suitable for constructing various building walls. Road Base material: due to its satisfactory compaction properties, coal gangue can also be used as a material for road bases [55,56]. Ceramic material: the silicates and aluminates in coal gangue can form vitreous bodies at high temperatures, thus suitable for manufacturing various ceramic materials [43,57]. These ceramic products can be utilized in areas such as architectural decoration and sanitary ware.

3.1.1. Coal Gangue Concrete

Compared to ordinary concrete, the fluidity of coal gangue concrete decreases by 20% to 53% under different water-cement ratios [58]. The incorporation of coal gangue reduces the early strength of concrete and increases its porosity and water absorption but also enhances its resistance to chloride ion or gas permeability [52,59]. An increase in porosity typically leads to a decrease in the density of concrete, which in turn affects its compressive strength, permeability, and durability. Higher porosity may cause concrete to perform poorly in structures that require long-term load-bearing capacity, especially in fields such as hydraulic engineering and road construction. An increase in water absorption means that concrete is more likely to absorb moisture, leading to internal expansion and

reduced strength, which further impacts its durability, especially under humid conditions or extreme climates. Compressive strength is a key indicator of concrete's load-bearing capacity; higher strength enhances its structural stability and durability, which is crucial for seismic and heavy-load applications. Therefore, in the design of coal gangue concrete, it is necessary to control porosity and water absorption effectively to ensure high compressive strength and durability, meeting the requirements of various engineering applications. The strength of coal gangue concrete, constrained by external layers of Carbon Fiber-Reinforced Polymer (CFRP) or Alkali-resistant Fiber-Reinforced Polymer (BFRP), increases by 16.9% to 145.8%, and its axial ultimate strain is 4.787 to 8.812 times that of ordinary coal gangue concrete [60]. Figure 5 shows the lateral strain-axial strain curve of BFRP/CFRP-constrained coal gangue concrete specimens. For CFRP-constrained coal gangue concrete specimens, the lateral strain-axial strain relationship and the slope of the second stage of volumetric expansion have smaller absolute values. Compared to BFRP-constrained specimens, CFRP-constrained specimens have a lower final expansion rate due to their relatively higher constraining stiffness. The mechanical properties of coal gangue concrete differ from those of ordinary concrete due to the substitution of fine and coarse aggregates with coal gangue [61,62]. Using artificial coal gangue sand in concrete fine aggregates can mitigate the environmental negative effects of coal gangue stockpiling and promote the conservation of natural resources [63]. The utilization of coal gangue sand provides an ecological solution to the shortage of natural sand and landfill of mineral tailings. The use of coal gangue sand yields positive social and environmental benefits when the transportation distance exceeds a certain threshold [63]. With the increase in stress level, the frost resistance of coal gangue concrete deteriorates, and the degradation rates of four macro-performance indicators, namely compressive strength, relative dynamic modulus of elasticity, mass loss, and damage layer thickness, significantly accelerate [64].

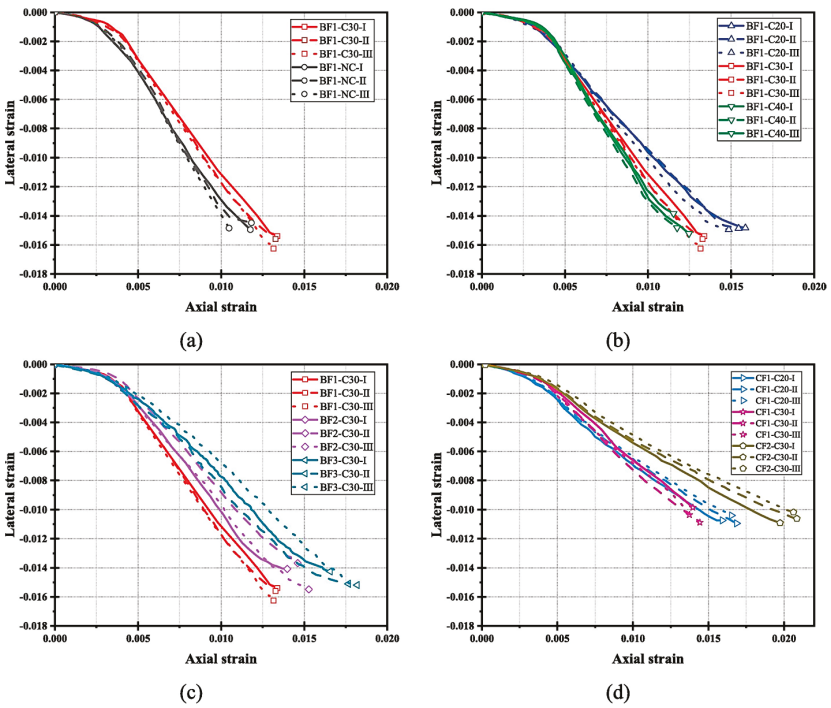


Figure 5. Lateral strain-axial strain curves of BFRP/CFRP-confined coal gangue concrete specimens. (**a**) Comparison between normal concrete and coal gangue concrete; (**b**) Comparison of coal gangue concrete under different pressures; (**c**) Comparison of coal gangue concrete with different number of BF laminations applied; (**d**) Comparison of coal gangue concrete with different number of CF liner applied [60].

Adding nanosilica and coarse coal gangue aggregate to concrete significantly affects a range of concrete properties. Studies have shown that the optimal mix ratio is 25% coarse coal gangue aggregate and 2% nanosilica [65]. This ratio not only improves the mechanical properties of concrete but also realizes the effective utilization of coarse coal gangue aggregate. Municipal solid waste incineration fly ash (MSWI FA) was used as a supplement to compensate for the lack of calcium elements in coal gangue (CG) to synthesize geopolymer materials [27,42]. To further study the impact of replacing coarse aggregate with coal gangue aggregate on its performance, a model was developed to predict the shrinkage behavior of concrete combined with coal gangue coarse and fine aggregates (CGCA and CGFA). Both CGCA and CGFA significantly increased the concrete shrinkage strain, which increased by 145% when both were used at 100%; compared to CGFA, CGCA had a more significant impact on shrinkage; the addition of CGCA led to faster development of concrete shrinkage, while CGFA had no significant effect on the development of shrinkage [66]. By replacing coarse aggregate with coal gangue aggregate (CGA) and using a machine learning model, it was found that the back-propagation neural network (BPNN) exhibited high correlation coefficients in predicting compressive strength and density [67].

3.1.2. Bricks, Cement, and Other Building Materials

Coal gangue, rich in SiO_2, Al_2O_3, Fe_2O_3, and CaO, serves as an appropriate raw material for brick production. The main mineral phases in coal gangue from different mining areas include quartz, kaolinite, and muscovite. The reactivity of the product obtained varies with different temperatures and calcination times [68]. Figure 6 shows the microstructure of sintered bricks at different temperatures. Figure 6a reveals that the cross-section of an unsintered brick is mostly composed of discrete particles of varying sizes and random arrangement. Figure 6b demonstrates the initial formation of small silicate layers and crystalline mineral particles in the brick's cross-section when the sintering temperature reaches 1000 °C, as shown in Figure 6c. The molten glass phase envelops and binds the tiny crystalline mineral particles, filling the gaps and pores between materials, bringing them closer together, leading to an increase in BD (bulk density) and CS (compressive strength), as shown in Figure 6d for the sintered brick at the optimal sintering temperature of 1100 °C, where the brick's melting and solidification degree is very high, resulting in a flat cross-section and a dense structure. The results indicate that the sintered bricks have fine and evenly distributed pores, and the liquid phase bonding action increases the BD and CS of the sintered bricks while decreasing the porosity and WA (water absorption rate) [69]. By adding an appropriate amount of activated coal gangue powder, the performance of coal gangue-based green cement fillers can be significantly enhanced. From an economic perspective, it is recommended that the substitution rate of activated coal gangue powder should be between 50 and 75% [70,71]. Activated calcined coal gangue can produce metakaolin with higher pozzolanic activity, which, when added as a supplementary cementitious material to cement, can not only replace part of the cement but also improve the later performance of cement materials [72,73]. Calcining coal gangue at 600–800 °C can transform the kaolinite phase into metakaolin [74]. Replacing 30% of standard cement with coal gangue reduces the early strength significantly at 3 days but increases the later strength substantially at 28 days, achieving an activity level of over 85%, meeting the basic requirements for the calcination activity of coal gangue [75]. Additionally, coal gangue can be categorized into reactive and non-reactive types, with reactive coal gangue being broadly applicable in various cement productions, while non-reactive coal gangue is limited to specific types of cement production [50]. Appropriate activation methods can significantly

enhance the pozzolanic reactivity and hydration characteristics of coal gangue, thereby improving the mechanical and durability properties of cement-based materials [76,77].

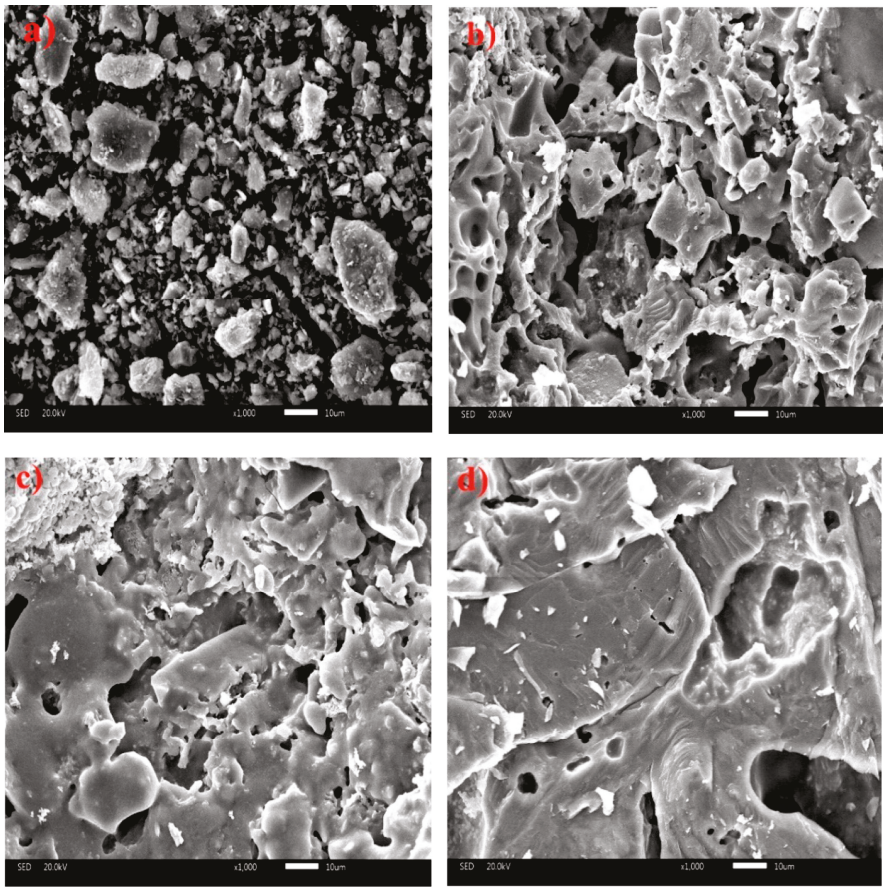


Figure 6. Microstructures of the sections of sintered bricks at different temperatures. (**a**)—raw materials; (**b**)—1000 °C; (**c**)—1050 °C; (**d**)—1100 °C [69].

Thermal activation of coal gangue is key in cement applications, with Figure 7 illustrating the dual benefits achieved by introducing steel slag [78]. The mechanism for achieving can be attributed to the introduction of steel slag, which provides a rich supply of calcium. On one hand, it promotes the fixation of sulfur by forming $CaSO_4$. On the other hand, it aids in the effectiveness of CaO in cement-based materials, accelerating the formation of C-S-H gel. When coal gangue and fly ash replace part of the cement and coarse aggregate, an increase in their proportion significantly improves the permeability coefficient but reduces the mechanical properties [79,80]. Up to 20% of coal gangue can replace portland cement without sacrificing strength [81]. Adding 4–6% of low-sulfur coal gangue with a calorific value of less than 6000 J/g to cement raw meal for producing cement clinker can reduce the unit energy consumption of cement clinker [82]. On the other hand, studies have adjusted the ratio of coal gangue to sludge, adding clay and foaming agents as auxiliary materials, to produce ceramsite with physical properties, including bulk density and cylindrical compressive strength, meet the Chinese standard "Lightweight Aggregates and their Test Methods" [83]. Research on modifying coal gangue powder through chemical intercalation and high-temperature activation treatment improved its microstructural characteristics, applying it to the matrix asphalt, and preparing modified asphalt by the melt blending method. The results showed that the treated coal gangue powder has a larger specific surface area and physical adsorption capacity, which can improve the high-temperature deformation resistance and anti-aging properties of asphalt by enhancing the interaction between coal gangue powder and the asphalt matrix [84].

A proper ratio of coal gangue lime and coal gangue powder can enhance the microwave healing capability of asphalt mixtures [85].

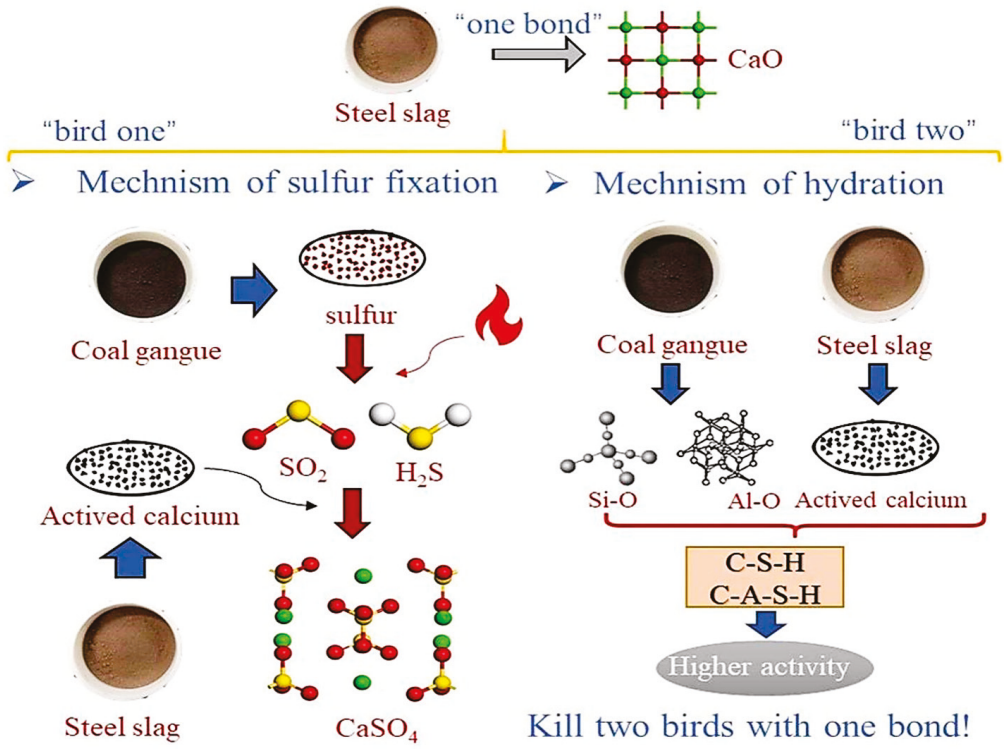


Figure 7. The mechanism of "kill two birds with one stone" [78].

3.1.3. Environmental Impact of Coal Gangue in the Production of Building Materials

When considering the resource utilization of coal gangue, its potential environmental impacts must also be considered. Coal gangue may contain harmful elements such as arsenic, lead, cadmium, and other heavy metals, as well as sulfides. If used directly without proper treatment, it could pose threats to the environment and human health [86]. As shown in Figure 8, this is a schematic diagram of gangue discharge into the environment and its eventual entry into the human body. Therefore, in the process of resource utilization of coal gangue, appropriate treatment measures, such as stabilization and physical and chemical separation, must be taken to ensure its safe use. The economic benefits of different coal gangue utilization methods are ranked as follows: extraction of chemical products > power generation > cement calcination > brick making > mineral admixture and road base material. The environmental effects of various utilization methods, from best to worst, are ranked as follows: brick making and cement calcination > road base and mineral admixture > power generation > extraction of chemical products [87]. Different resource utilization methods have varying impacts on the environment; considering benefits should also account for environmental impacts to avoid secondary pollution. Environmental pollution management strategies need to be developed for each stage of coal gangue utilization, including production, transportation, and comprehensive use, to minimize its impact on the environment [88].

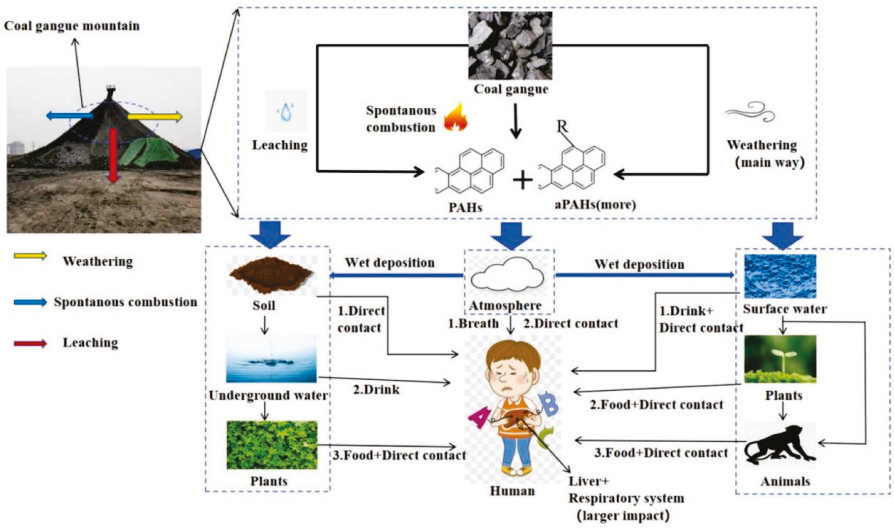


Figure 8. Schematic diagram of the discharge of PACs from coal gangue into the environment and finally entering the human body [89].

When coal gangue is used as a raw material for building materials or other applications, the long-term stability of the products depends on the composition of the coal gangue itself and its interactions with other materials. Coal gangue contains certain amounts of heavy metals and harmful substances, which may leach, weather, or otherwise enter the environment over time, affecting the durability and environmental performance of the products. The measures to ensure long-term stability and safety are as follows: (1) Composition Control and Pretreatment: Pretreating coal gangue to reduce the content of harmful substances. For example, using physical or chemical methods to remove heavy metals, sulfides, and other harmful components, thereby reducing their potential environmental impact. (2) Leaching Tests: Conducting leaching tests (such as the American Standard Leaching Test, European Leaching Test, etc.) to assess the release of heavy metals from coal gangue under specific environmental conditions, ensuring compliance with environmental protection standards. (3) Blending and Stabilization Technologies: Mixing coal gangue with other stabilizing materials (such as cement, lime, etc.) and using solidification or encapsulation techniques to reduce the migration of harmful substances. For example, using cement solidification methods, where coal gangue reacts with cement to form more stable compounds, thereby reducing its leaching potential. (4) Use of Additives: Adding appropriate additives, such as chemical stabilizers, to enhance the chemical stability of coal gangue and reduce its reactivity with the environment. (5) Long-term Monitoring and Assessment: Establishing a long-term environmental monitoring system to regularly test leachates during the product's use, ensuring that they do not cause long-term harm to the environment.

The heavy metal elements abundant in coal gangue, such as lead (Pb), cadmium (Cd), chromium (Cr), and mercury (Hg), may be released into the environment during the production process, causing pollution to soil and water sources. In the preparation of building materials using coal gangue, the high content of some heavy metals is an important consideration for its application and environmental risk management. The production of building materials often requires high-temperature calcination. During the calcination of coal gangue, pollutants such as nitrogen oxides (NOx), sulfur dioxide (SO_2), and heavy metals are released [90]. When firing bricks, dust is generated during raw material crushing; during the baking process, the temperature in the tunnel kiln reaches about 980 °C to 1100 °C. The combustion of coal and spontaneous combustion of coal gangue in tunnel kilns produce gases such as HF, smoke, and SO_2 [91,92]. During the sintering process, trace

elements are released and redistributed in bricks, fly ash, and flue gases. Cadmium, copper, mercury, lead, selenium, and tin have high volatility, mainly emitted in the form of flue gases, potentially impacting the atmosphere and soil of the surrounding areas [93]. To reduce environmental impacts, efficient desulfurization and dust removal equipment and optimized production processes can be used.

Due to its relatively stable chemical structure, the reactivity of coal gangue in cement materials needs to be activated to improve its pozzolanic reactivity. This activation could affect the environmental burden and impact of cement-based materials [94]. Microwave-activated coal gangue powder, used as an auxiliary cement material, changes the mineral composition, potentially impacting the environmental and economic aspects of cement production [75]. Adding coal gangue reduces most environmental impacts of cement clinker, such as potential for human toxicity and potential for depletion of abiotic resources. However, the potential for global warming and acidification slightly increases [95]. Although the use of coal gangue in the production of building materials can bring certain environmental benefits, such as waste reduction and carbon footprint reduction, it also raises concerns about increased global warming potential, acidification, and heavy metal pollution. Balancing these factors to ensure environmental sustainability is crucial.

3.2. In the Energy Sector

In recent years, with the increasing awareness of sustainable energy and environmental protection, the application of coal gangue in the energy sector has received greater attention and development. With the changes in national energy and environmental policies as well as adjustments in the coal industry structure, the comprehensive utilization of coal resources for power generation faces a new development situation [96]. Especially, technological advancements have significantly improved the utilization efficiency of resources such as coal gangue and coal slime, which not only helps in conserving resources but also reduces environmental pollution.

3.2.1. Direct Use

Coal gangue is commonly regarded as a low-calorific-value material. However, for those with a higher carbon content, such as between 20% and 30%, its calorific value significantly increases, making it a potential resource for energy recovery and power generation [97]. The high carbon content of this type of coal gangue provides sufficient thermal energy, making it feasible for use in energy conversion processes such as combined heat and power generation. Compared to conventional coal-fired boilers, circulating fluidized bed technology offers significant environmental advantages, including reduced pollutant emissions and improved waste utilization efficiency [98,99]. Moreover, the application of coal gangue in power generation also helps reduce dependence on traditional fossil fuels, thereby alleviating the issue of fossil fuel scarcity to some extent and providing a viable solution for the environmentally friendly disposal of coal gangue. Although direct combustion of coal gangue for power generation is theoretically feasible, it presents a series of technical complexities in maintaining stability during the power generation process, especially for those with high ash content and low calorific value. These challenges highlight the necessity for in-depth research into coal gangue as a fuel for power generation, particularly in optimizing combustion technology, improving energy efficiency, and reducing environmental pollution [100]. Therefore, research in this field is far from mature and requires continuous exploration and innovation.

For coal gangue with ultra-low calorific value, the Aspen Plus 11.0 software can be used for the design and optimization of coal gangue pyrolysis and carbonization processes, with the optimal pyrolysis temperature being about 600 °C [101]. For spontaneously

combusting waste coal gangue, energy recovery can be achieved by constructing a novel artificial heat reservoir system. The concept diagram of the coal gangue artificial heat reservoir system is shown in Figure 9 [102].

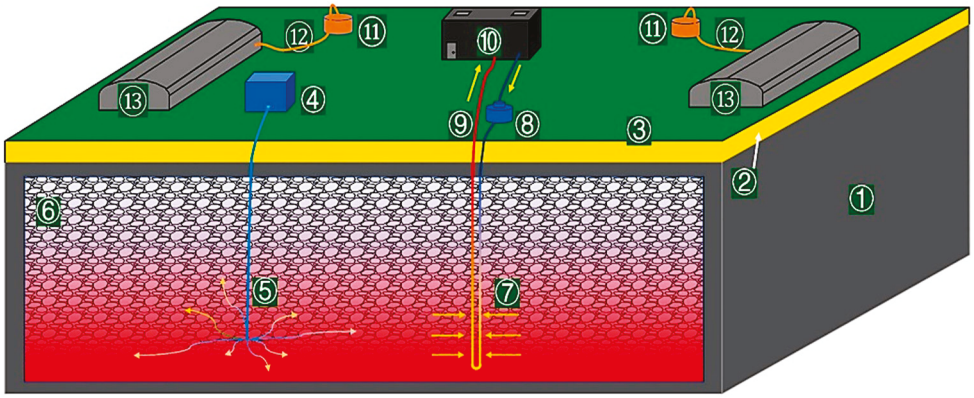


Figure 9. Concept diagram of CGAHR system [102].

Direct calcination of coal gangue is a method of resource utilization. Mainly through high-temperature treatment, coal gangue is transformed into useful products. During the calcination process, usually above 800 degrees Celsius, its organic matter is decomposed and transformed into gas and ash [103]. As the combustion temperature increases, coal gangue minerals decompose at certain temperatures; at 1200 °C, the mineral phases of combustion ash are mullite, quartz, magnetite, hematite, lime, and anhydrite [104]. Figure 10 shows the morphological characteristics during the combustion process of coal gangue; uncalcined fine particles of coal gangue with a diameter of 1.0 micrometer (Figure 10A) form needle-like shapes and cluster together. The coal gangue is in a molten phase, and its surface gradually becomes viscous as the combustion temperature increases (Figure 10B–F). The volatility of trace elements in coal gangue increases with the combustion temperature and can be divided into two categories: the highly volatile first category (Ni, Cu, Zn, Cd, Sn, Pb, and As), and the low volatility second category (Co, Cr, V) [104]. Figure 11 shows the volatility of trace elements at different temperatures. The decomposition of organic matter and pyrite can lead to an increase in the volatility of trace elements at 500 °C. As the combustion temperature increases, carbonate minerals, sulfides, and other minerals decompose, increasing the volatiles [104]. However, combustion of coal gangue can lead to significant emissions of sulfur, arsenic, mercury, and fluorine, which may exceed the emissions from traditional coal combustion [105].

Reducing the emission of pollutants during the combustion process of coal gangue is currently one of the important issues. Moreover, the direct combustion utilization of coal gangue requires specific combustion techniques and equipment. Overall, the direct use of coal gangue is a potential method of energy recovery, which can reduce the environmental impact of waste while providing some energy value. However, to achieve its widespread application, technical, economic, and environmental challenges need to be addressed.

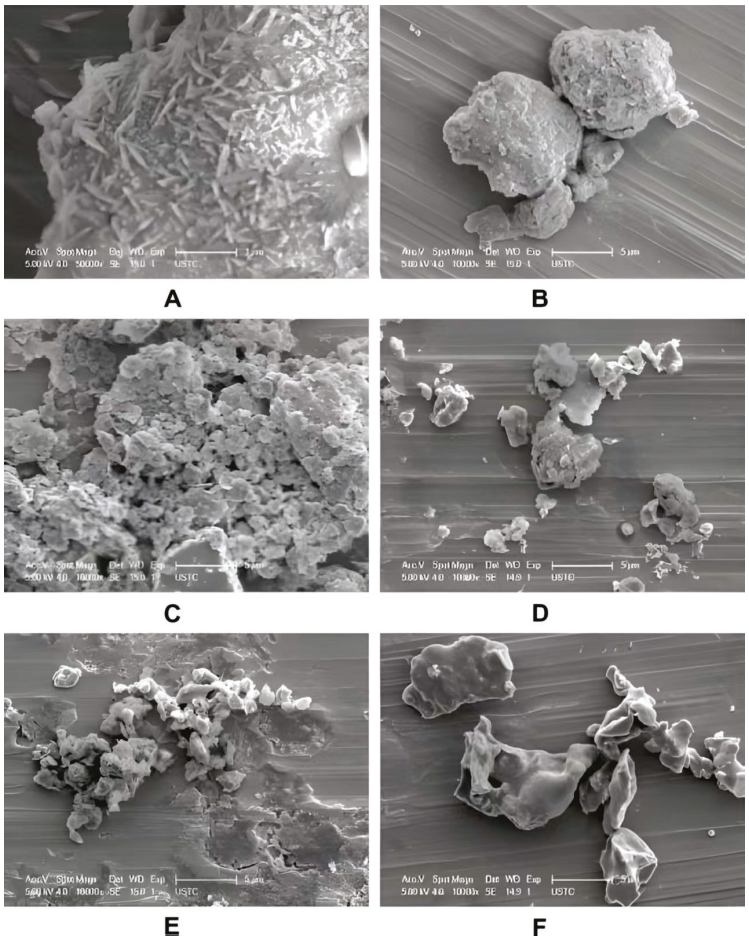


Figure 10. The morphological characterization of coal gangue during combustion. (**A**) uncalcined coal gangue, (**B**) uncalcined coal gangue, (**C**) 500 °C, (**D**) 700 °C, (**E**) 900 °C, and (**F**) 1200 °C [104].

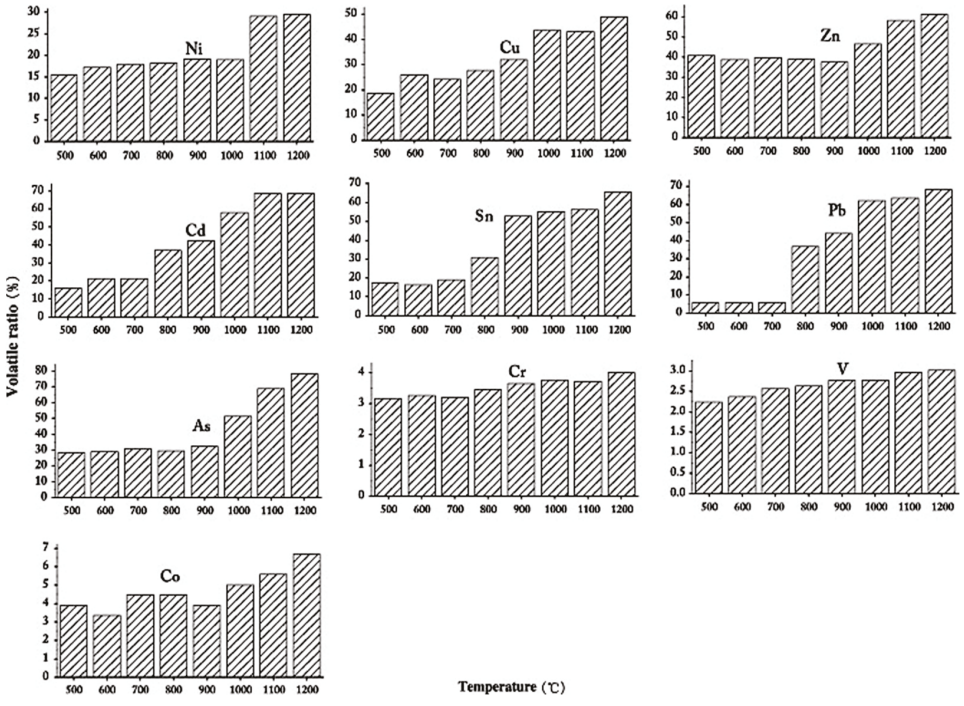


Figure 11. The volatilize of trace elements at various temperatures [104].

3.2.2. Co-Utilization

Adding an appropriate amount of biomass can not only improve the combustion performance of coal gangue but also reduce the emissions of trace elements, thereby contributing to environmental protection. A biomass addition ratio of 20–30% is considered the optimal proportion [48]. In exploring the retention mechanism of trace elements (TEs) during the co-combustion of coal gangue (CG) and soybean straw (SS), it was found that the retention of gaseous TEs increased during co-combustion, which might be due to reactions with active mineral surfaces, chemical adsorption, and interactions with ash components and elements [106]. When sludge (SS) and coal gangue (CG) are co-combusted, it has been found that co-combustion helps improve ignition performance and has a synergistic effect on desulfurization and denitrification. Enhanced retention of trace elements (especially Pb and Zn) was observed during co-combustion [107]. By adding coal gangue as an additive to other biomass fuels (willow branches, wheat straw), not only can the combustion effect of coal gangue be improved, but also the emission of NO can be reduced, with the best proportion being 80% biomass + 20% coal gangue [108]. The real-time NO release curve, as shown in Figure 12, indicates that when 20% coal gangue is added to the composite fuel, the NO emission temperature of the composite fuel increases, and NO emissions decrease. This is because the alkali metals in coal gangue react with the biomass, with the reaction mechanism shown in Figure 13, and possible reactions are as follows [108].

$$Al_2Si_2O_5(OH)_4 \rightarrow Al_2O_3{\cdot}2SiO_2{+}2H_2O\,\# \quad (1)$$

$$Al_2O_3{\cdot}2SiO_2{+}2MCl + H_2O \rightarrow 2MAlSiO_4{+}2HCl \quad (2)$$

$$2MAlSiO_4{+}H_2O \quad (3)$$

$$Al_2O_3{\cdot}2SiO_2{+}2MOH + 2SiO_2 \rightarrow 2MAlSi_2O_6{+}H_2O \quad (4)$$

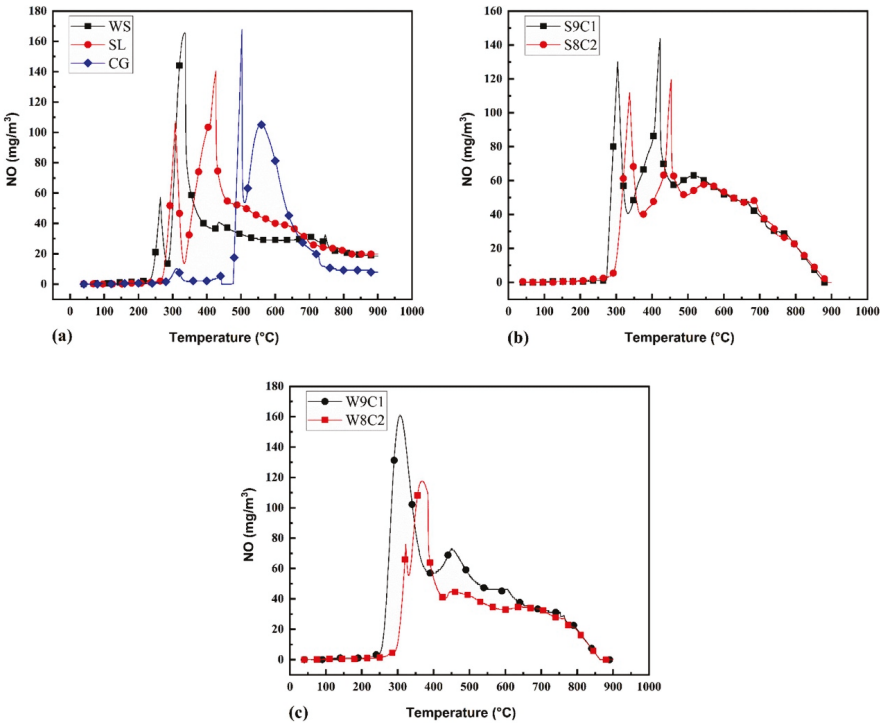


Figure 12. NO real-time emission curve: (**a**) The mono-combustion of WS (Wheat straw), SL (Salix limb) and CG. (**b**) The composite fuel of SL and CG. (**c**) The composite fuel of WS and CG [108].

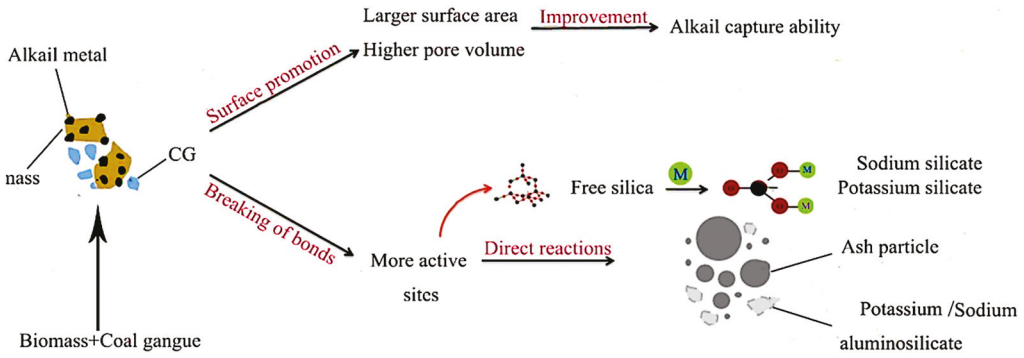


Figure 13. The mechanisms of biomass slagging abatements by coal gangue [108].

During the co-combustion process of straw and coal gangue, when the mixing ratio of coal gangue is 30%, it is expected to reduce sulfur dioxide emissions by 18.19% [109]. In the co-combustion process of low-calorific-value coal mixtures in a fluidized bed, a mixture ratio of raw coal, coal gangue, and coal slime at 20:60:20 may be a suitable choice for co-combustion in a fluidized bed reactor [110].

In the co-firing of coal gangue and peanut shells, an optimal predictive model for the co-combustion of coal gangue and peanut shells was established using the artificial neural network (ANN) method, and ANN20 was determined to be the best model through comparison [111,112]. Figure 14 shows the ANN20 model used to predict the combustion behavior of coal gangue and peanut shells. The ANN20 model is divided into an input layer, hidden layers, and an output layer. The input parameters for the input layer are combustion experimental conditions: heating rate, temperature, and mixing ratio. There are two hidden layers. The number of neurons in the first hidden layer is 5, and in the second hidden layer is 17. The parameters for the output layer are the residual mass percentage from the thermogravimetric experiments. The activation function for the hidden layers is nonlinear, while the activation function for the output layer is linear [111]. Interactions also exist between coal gangue and sawdust, and the addition of sawdust can enhance the oxidative combustion reactivity of coal gangue [113,114]. A study on the synergistic effects of the co-gasification of coal gangue and sawdust was conducted on a homemade two-stage gasification fixed bed experimental setup. The best synergistic effect, with a synergy coefficient of 0.22, was observed under conditions of a gasification temperature of 850 °C, catalytic reforming temperature of 900 °C, steam flow rate of 2 mL/min, and a mixing ratio of coal gangue to sawdust of 1:1. The synergistic effect of coal gangue and sawdust is due to the cracking of -OH functional groups, enhanced by the catalytic action of alkali and alkaline earth metals in the co-gasified char [115]. The effect of different mixing ratios of coal gangue and sawdust on the composition of co-gasification gas is shown in Figure 15. As seen in Figure 15a, with the increase in the sawdust mixing ratio, the volume fraction of H_2 initially increases, then decreases, and finally increases [115]. A significant interaction between coal gangue and weathered coal was observed under oxygen-enriched combustion conditions, likely related to thermal effects [116]. Further research found that a mixture of 70% coal and 30% coal gangue exhibited the strongest synergistic effect, while a mixture of 30% coal and 70% coal gangue showed the strongest inhibitory effect [117]. For coal gangue and polypropylene (PP), when the polypropylene content was 20%, the maximum weight loss rate at the first peak temperature of the mixed fuel increased, and the average thermal coupling degree at 50% and 80% was 1.64 and 2.30 times, respectively [118].

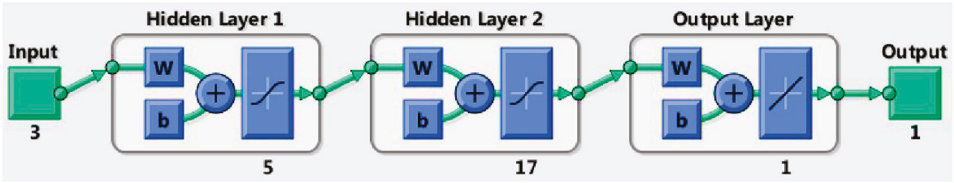


Figure 14. ANN20 structure diagram used for predicting combustion behavior of CG and PS [111].

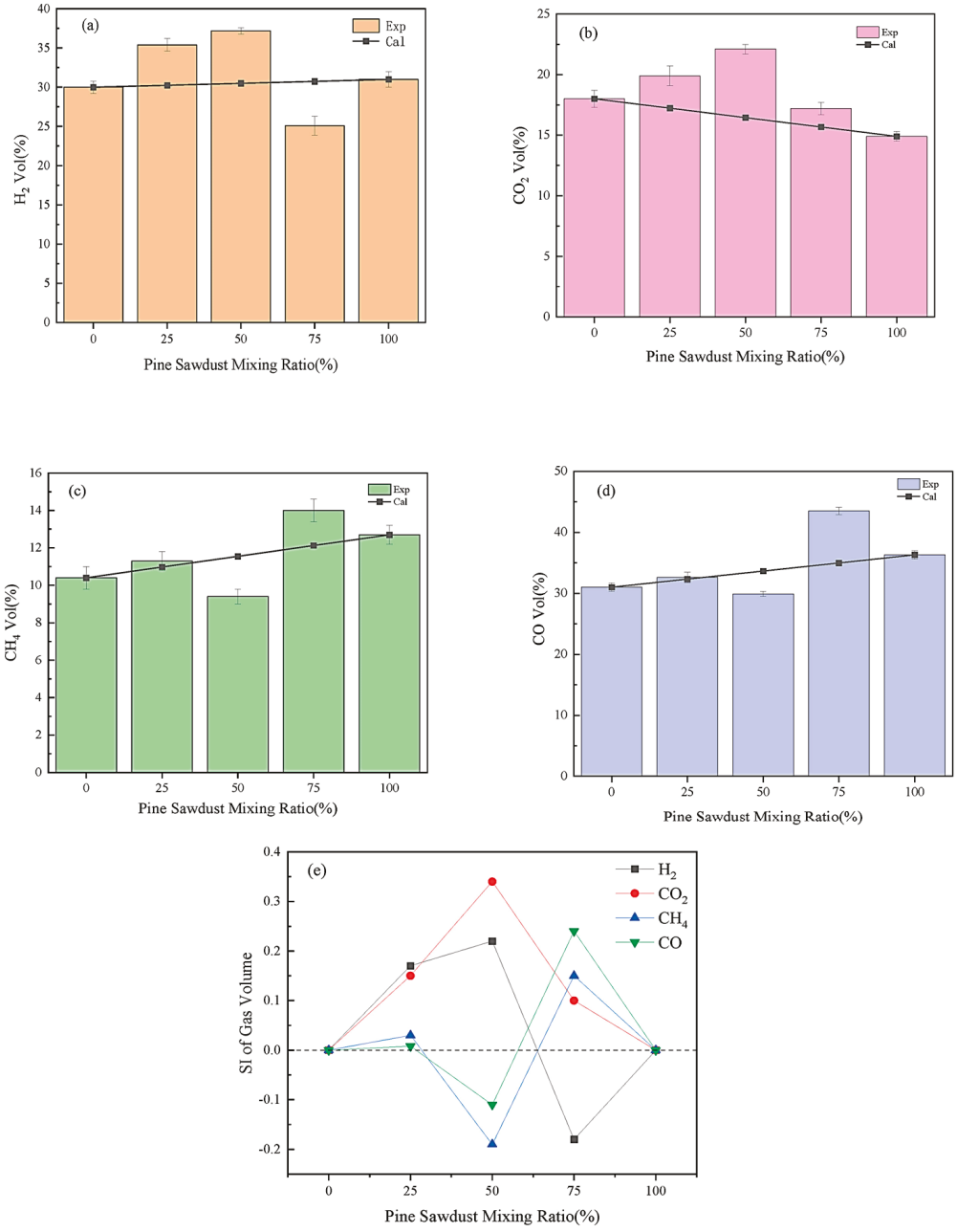


Figure 15. Effect of mixing ratio on gas composition of co-gasification. (**a**) The volume fraction of H_2 as a percentage for different mixing ratios; (**b**) The volume fraction of CO_2 as a percentage for different mixing ratios; (**c**) The volume fraction of CH_4 as a percentage for different mixing ratios; (**d**) The volume fraction of CO as a percentage for different mixing ratios; (**e**) SI values for each gas at different mixing ratios [115].

Pyrolysis is an effective method for transforming coal gangue into high-value materials, offering advantages such as low cost, continuity in the production process, and

product diversity. However, the pyrolysis of coal gangue has drawbacks, including low efficiency, high cost, and the emission of harmful gases [104]. Biomass materials are potential feedstocks to enhance the pyrolysis process of coal gangue, compensating for its shortcomings as the volatile substances within biomass can lower the ignition temperature and shorten the reaction time [119,120]. The addition of cellulosic biomass not only significantly affects the pyrolysis characteristics and gas emission patterns of coal gangue but also increases the release of volatiles during pyrolysis [121]. Adding biomass to coal gangue can promote the release of gaseous organic compounds during pyrolysis and has a suppressing effect on the formation of carbon dioxide, which is significant for reducing greenhouse gas emissions [122]. In the co-pyrolysis experiments of coal gangue and peanut shells, mixing ratios of 3:1 and 1:3 are considered suitable for the co-pyrolysis of coal gangue and peanut shells [123]. Research on the co-pyrolysis of coal gangue and coffee grounds shows that adding 30% coffee grounds can increase the CPI value of the sample by 148.56 times, significantly improving the pyrolysis performance of the sample [124]. There is also an interaction in the co-pyrolysis of coal gangue and lignin, with the optimal mixing ratio being 1:3, where the synergistic effect is most evident [125].

3.2.3. Environmental Impact of Coal Gangue in Energy Applications

With the continuous increase in energy demand, coal gangue has been widely applied as a raw material for energy. For coal gangue with high calorific value, the presence of non-mineral impurities in the coal and gangue mixture may affect the combustion efficiency and emissions of power plants [126]. Fly ash and bottom slag produced by the combustion of coal gangue may be enriched in toxic metal elements such as mercury (Hg), arsenic (As), beryllium (Be), and cadmium (Cd). The volatilization characteristics of these elements during the combustion process can cause secondary pollution to the environment [127]. Additionally, workers in coal gangue power plants are exposed to occupational hazards such as silica dust, coal dust, and noise [128,129]. The addition of semi-coke in an oxygen-rich environment with coal gangue can reduce NO emissions under certain conditions. The increase in O_2 concentration significantly affects CO and NO emissions, but the impact on SO_2 emissions depends on the specific value of O_2 concentration [130]. The calcination of coal gangue leads to the migration and diffusion of heavy metals and other harmful substances, which may cause serious impacts on the surrounding ecological environment [131]. Heavy metals in coal gangue may enter the soil and water bodies through weathering and leaching after calcination, thereby polluting these environmental media [132].

The resource utilization of coal gangue in the energy sector holds significant potential, but several key considerations must be addressed during implementation. First, coal gangue exhibits considerable compositional variability, especially in terms of harmful elements such as heavy metals and sulfides, which could impact the safety and environmental effects of the energy production process. Therefore, before using coal gangue as an energy feedstock, comprehensive compositional analysis must be conducted to identify potential pollutants. Appropriate treatment technologies, such as high-temperature roasting and chemical treatments, should be employed to remove harmful components and prevent secondary pollution of the environment. Second, coal gangue has a relatively low calorific value and complex composition, which may affect its combustion efficiency as a fuel. To improve the combustion performance of coal gangue, it is often mixed with other high-calorific-value materials or pre-treated. For example, methods such as crushing and drying can optimize the particle size and moisture content of coal gangue, enhancing its combustibility and combustion stability. Furthermore, during the combustion process, temperature and atmospheric conditions must be strictly controlled to prevent the harmful

emissions of gases containing sulfur, nitrogen, and other elements present in coal gangue. Additionally, the use of coal gangue as an energy feedstock should consider its impact on equipment and systems. During combustion, coal gangue may produce by-products such as ash and soot, which can cause corrosion, blockages, or wear on equipment such as boilers and flue gas treatment systems. Therefore, the design of combustion systems must account for the unique physicochemical properties of coal gangue, and careful preparation should be made in equipment selection and maintenance to ensure long-term, stable operation.

In summary, the application of coal gangue resource utilization in the energy sector should focus on multiple aspects, including compositional analysis, combustion performance, equipment compatibility, environmental emissions, and economic feasibility, to ensure its safe, efficient, and sustainable conversion into an energy resource.

3.3. Agricultural Applications

Coal gangue contains a high proportion of organic matter, making it an ideal substrate for carrying nitrogen, phosphorus, and potassium. Appropriately adding coal gangue can improve the soil environment [133]. As a soil amendment material, coal gangue not only helps improve problematic soils such as sandy soil and saline soil but can also be used to prepare fertilizers [134]. In terms of land conservation, direct filling technology can significantly reduce land subsidence and also reduce the environmental impact of coal gangue accumulation [135].

3.3.1. Soil Improvement

The long-term use of chemical fertilizers leads to the gradual depletion of organic matter and humus in the soil, which in turn causes soil compaction and salinization, among other land degradation issues [136]. The addition of coal gangue can significantly improve the physicochemical properties of saline-alkali soil, reducing soil PH, salt concentration, and bulk density, while increasing the content of organic matter, total nitrogen, total phosphorus, total potassium, hydrolyzed nitrogen, and available potassium in the soil [137,138]. Moreover, coal gangue has certain porosity and permeability, which, when added to the soil, can improve its aeration and water retention, especially for problematic soils such as sandy soil and saline soil, significantly improving their physical properties [54]. Through activation treatment, coal gangue's ability to fix and release available phosphorus in reclaimed mine soils has been significantly enhanced, with small particle size alkali-modified activated coal gangue showing the best activation effects, its maximum phosphate adsorption capacity being 11.796 mg/g [45]. AS-FCG is a cost-effective, durable, and environmentally friendly material that can be used for phosphorus fixation as well as for the slow release of phosphorus as a fertilizer, with its phosphorus adsorption mechanism and specific reaction equations illustrated in Figure 16 [45].

$$Ca^{2+} + 2H_2PO^- \rightarrow \text{Ca-P} \downarrow \quad (5)$$

$$Al^{3+} + 3H_2PO_4^- \rightarrow \text{Al-P} \downarrow \quad (6)$$

The preparation of coal gangue soil amendments can help increase available land resources and facilitate the reuse of solid waste. However, current issues with coal gangue amendments include high sulfur content, nutrient deficiencies, and heavy metal pollution, necessitating the addition of other substances to optimize their nutrient content [31].

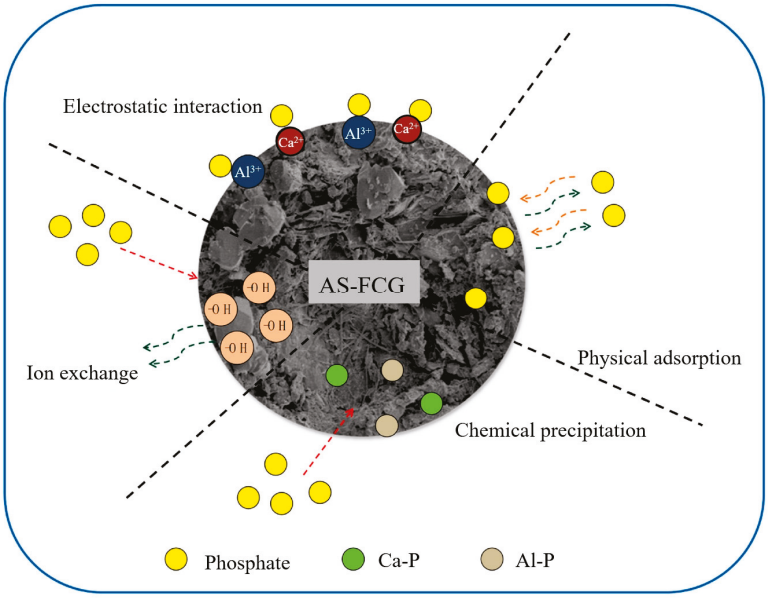


Figure 16. The mechanisms of phosphate adsorption of AS-FCG [45].

Coal gangue has shown significant effects in improving the condition of medium- and low-yield fields [39]. Using coal gangue to construct sand barriers for sand fixation can also increase the content of organic matter, total nitrogen, available phosphorus, and available potassium in the soil by 2.65, 2.66, 1.30, and 1.24 times, respectively [87]. The reactive silicates and aluminates in fly ash and coal gangue undergo hydration in alkaline conditions, lowering the soil's pH value, which is beneficial for the amelioration of saline-alkali soil. A novel compound made from phosphoric acid-modified cauliflower leaf biochar (CLH) and coal gangue-based Na-X zeolite (ZL), mixed together, acts as a soil stabilizer to immobilize heavy metals in polluted alkaline soils [139]. Modified coal gangue (MGE) prepared by a low-temperature alkali fusion method and applied to the immobilization of cadmium (Cd^{2+}) polluted soil resulted in a significant increase in active groups on the surface of the modified coal gangue, aiding the removal of Cd^{2+}. The content of available Cd^{2+} in the treated soil was reduced by 14.2% to 29.8% [46]. Bacterial treatment can significantly improve the availability of nutrients in coal gangue. Research found that using the Stenotrophomonas maltophilia YZ1 bacteria to activate coal gangue, the content of soluble phosphorus, potassium, and silicon significantly increased after treatment with the YZ1 bacterial strain [140].

3.3.2. Fertilizer Production

Research on coal gangue as a fertilizer shows that it can reduce air pollution and nitrogen pollution in groundwater, bringing significant economic, social, and environmental protection benefits. Compared with the background values of soil elements in the Loess Plateau and the national standards for harmful substances control, coal gangue from the Weibei coalfield has tremendous potential as a clay fertilizer [141]. Therefore, coal gangue has significant advantages as a raw material for producing agricultural fertilizers. Coal gangue can be used as a silicon fertilizer, and high-efficiency coal gangue-based silicon fertilizer has been produced through high-temperature activation technology, achieving significant available silicon content and meeting agricultural needs [142]. Studies have found that the maximum phosphate adsorption capacity of rapeseed straw coal gangue-modified biochar (CG-OR700) prepared at 700 °C is 7.9 mg/g at pH4.0, which is 4.6 times that of the original biochar [143]. This can not only be used to remove phosphates from wastewater but also serve as a slow-release fertilizer for agricultural production. After activation and

modification, coal gangue can significantly improve its reactivity and soil improvement capabilities. Activation methods include thermal activation, chemical activation, microwave activation, mechanical activation, and composite activation [144].

3.3.3. Environmental Impact of Coal Gangue in Agricultural Applications

The application of coal gangue in agriculture, especially as a raw material for fertilizers and a soil amendment, poses certain potential risks. Experiments on phytostabilization using coal gangue in copper mine tailings have shown that the application of coal gangue not only increased the pH value, organic matter content, and nutrient components of the amended tailings but also reduced the DTPA-extractable concentrations of Zn, Pb, Cd, and Cu [145]. In soils reclaimed with coal gangue, the concentrations of copper, lead, and zinc were enriched by 1.51 times, 1.48 times, and 2.05 times, respectively, compared to original agricultural soil, indicating that these heavy metals could migrate from the coal gangue into the soil [146]. When coal gangue is directly applied to soil as fertilizer, it may contain harmful elements, which could negatively impact the soil and crops. There are potential risks associated with the agricultural application of coal gangue, especially concerning the presence of harmful elements and the health of soil and crops. Therefore, when considering the use of coal gangue as a raw material for fertilizers or a soil amendment, it is necessary to carefully assess its potential impact on the environment and crops.

When applying coal gangue in agriculture, particular attention must be paid to its compositional analysis and treatment. Coal gangue may contain harmful substances such as heavy metals and sulfides, which, if used untreated, could harm the soil and crops. Therefore, coal gangue must undergo purification and modification processes, such as high-temperature roasting or acid-base washing, to remove these harmful components. As a soil amendment, coal gangue can improve soil aeration and drainage, but due to its alkalinity, excessive use may lead to soil alkalization. Thus, it is essential to control the application rate appropriately. The minerals in coal gangue, such as silicon and calcium, can promote crop growth; however, it should be applied in conjunction with other fertilizers to avoid nutrient imbalances. Long-term use of coal gangue may have adverse effects on the soil, potentially contaminating groundwater or compromising crop safety. Therefore, regular monitoring of soil and crop conditions is necessary to assess its long-term impacts. To improve the utilization efficiency of coal gangue, it can be integrated with other agricultural waste materials to increase soil organic matter content and promote resource recycling. In conclusion, the application of coal gangue in agriculture should be scientifically and rationally managed, with strict control over its usage and treatment methods, ensuring its safe and sustainable improvement of soil quality and promotion of crop growth.

3.4. High-Value Applications

Coal gangue contains rare earth elements such as scandium and gallium, which play a crucial role in advanced technologies [147]. Additionally, coal gangue is rich in kaolinite and other clay minerals, constituting a vast potential resource of aluminum and lithium. Therefore, coal gangue can provide essential raw materials for industries such as solar energy and new energy vehicles.

3.4.1. Extraction of Valuable Components

Currently, extraction methods primarily focus on extracting alumina, which is the most feasible and economically valuable. Using hydrochloric acid to extract alumina from coal gangue is a simple and convenient method. Under optimal conditions of calcination temperature at 700 °C, leaching temperature at 150 °C, reaction time of 2 h, hydrochloric acid concentration of 20%, and a liquid-to-solid ratio of 3:1, the extraction efficiency of alumina can reach 91.56% [148]. In the presence of alkali metals Na_2CO_3 and Na_2SO_4,

the extraction rate of aluminum from coal gangue is enhanced, reaching a peak value of 91.39% at 850 °C [149]. Various methods of extracting Al from gangue are shown in Table 5. The optimal calcination temperature for converting and separating coal gangue components is 1050 °C ± 50 °C. For the leaching process, the optimal temperature is about 85 °C with a leaching time of 60 to 80 min, under which conditions valuable components of coal gangue, alumina, and silica can be efficiently extracted [150]. At pH values of 2.6, 4.2, 6.5, and 8.1, the leaching rates of chloride after 105 h are 57.21%, 35.97%, 26.65%, and 18.98%, respectively [151]. Coal gangue calcination for desilication, with the addition of 6% secondary aluminum slag, can increase the Al/Si ratio of the desilication product from 0.91 to 1.94 and the desilication rate from 42.99% to 56.16% [152]. Figure 17 shows a schematic diagram of the catalytic behavior of $Al(OH)_3$ and secondary aluminum oxide slag. The active alumina produced by the dehydration of $Al(OH)_3$ can combine with metakaolin in coal gangue to form mullite, releasing active silica in the process. Active silica can be dissolved and separated through a caustic desilication process, and regenerated aluminum slag also has this function, with a stronger catalytic effect. Recovering iron from coal gangue can be performed using magnetic separation methods, calcining coal gangue at temperatures ranging from 300 °C to 1000 °C for 30 to 180 min. After calcination, the magnetization rate of coal gangue significantly increases to 17 times that of the original ore [153].

Table 5. Methods for extracting aluminum from coal gangue—efficiency and drawbacks.

Extraction Method	Efficiency	Drawbacks	References
Acid Leaching	Above 90% (high efficiency)	May cause environmental pollution, difficult waste liquid treatment, and the use of corrosive acidic solutions.	[148,154]
Alkaline Leaching	80–90% (relatively high)	Requires large amounts of alkaline solutions, complex treatment process, and the corrosive nature of alkaline solutions.	[155]
High-Temperature Sintering	70–80% (lower efficiency)	High energy consumption during heating, lower aluminum recovery efficiency, and high equipment investment.	[156]
Gasification	60–70% (lower efficiency)	Requires high temperatures, high equipment investment, and relatively low aluminum recovery efficiency.	[157]

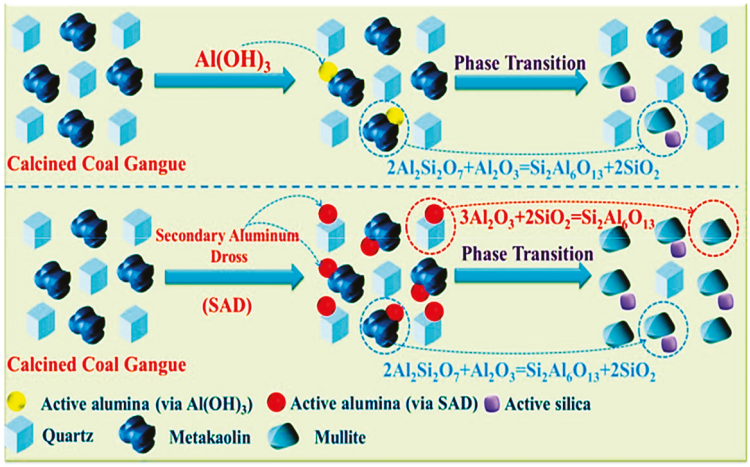


Figure 17. Schematic diagram of the catalytic behavior of $Al(OH)_3$ and secondary alumina dross [152].

Pretreatment and cyclic sintering can effectively promote the green extraction and utilization of key metals in coal gangue. Pretreatment significantly reduces the particle size of coal gangue, effectively strips away the layered silicate structure of the gangue, and improves leaching efficiency [158]. Ga and Li in coal gangue mainly exist in the form of

silicates, so enriching and extracting Ga and Li is an effective method [158]. In the process of calcification and desilication of coal gangue, with the addition of 6% secondary aluminum slag and a calcification temperature of 1000–1050 °C, the desilication rate can be increased to 56.16%. The sodium silicate solution after desilication can be used as a silicon source, and the high-aluminum-content desilication slag can be used to extract and produce sodium aluminate solution as an aluminum source [152]. The stenotrophomonas maltophilia (YZ-1) strain can promote the release of soluble phosphorus in coal gangue; its produced organic acids can accelerate the leaching of phosphorus and lead, forming phosphate precipitates with lead ions; thus coal gangue has a synergistic effect on the stabilization of lead [159]. The stabilization mechanism is illustrated in Figure 18.

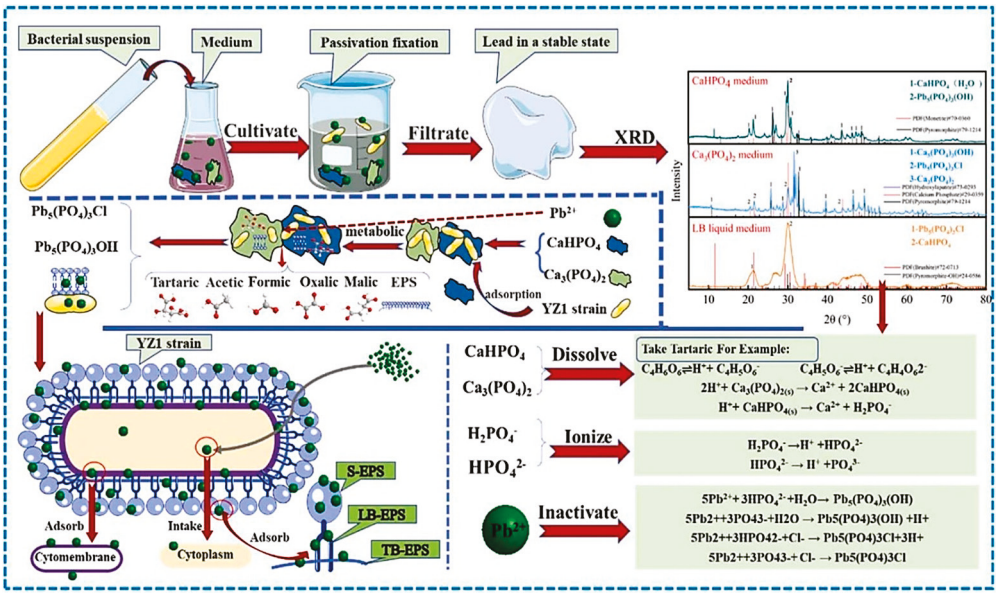


Figure 18. The fixation mechanism of Pb ions with YZ-1 strain [159].

3.4.2. Preparation of Catalysts and Adsorbents

Metal-enriched coal gangue can be directly prepared into carbon-supported catalysts for the in situ catalytic pyrolysis of biomass and the cracking of secondary tar [160]. Through a dual activation method of air calcination and hydrothermal alkali treatment, coal gangue is transformed into a high-performance, low-cost Ni-based catalyst for the hydrogenation of dioctyl phthalate, achieving a conversion rate of 99.9% and can be recycled multiple times without significant loss of activity [161]. The copper-modified ZSM-5 catalyst synthesized from coal gangue (Cu/ZSM-5) effectively decomposes phenol, with 7% Cu/ZSM-5 being able to completely degrade phenol within 30 min, and the total organic carbon (TOC) removal efficiency can reach 92% in 8 h [162]. The copper-silver (Cu-Ag) catalyst system based on coal gangue activates persulfate under visible light radiation to efficiently degrade tetracycline hydrochloride (TC), with the 15% copper and 5% silver ZSM-5 (15%Cu–5%Ag/ZSM-5) catalyst showing a high degradation rate of 75% for TC within 60 min. After five cycles, the degradation rate of TC decreased from 74% to 63%, demonstrating good stability and potential application prospects [163]. Coal gangue activated persulfate degradation of tetracycline hydrochloride follows the mechanism shown in Figure 19, providing three pathways, with the final degradation products being CO_2 and H_2O, in line with the concept of no pollutant release [164]. The catalytic material based on coal gangue (CG-Ca-N) activates peroxymonosulfate (PMS) and can completely degrade Bap within 20 min, and the degradation rate reaches 72.06% in soil slurry medium within 60 min [165]. The main advantages of various catalysts are shown in Table 6.

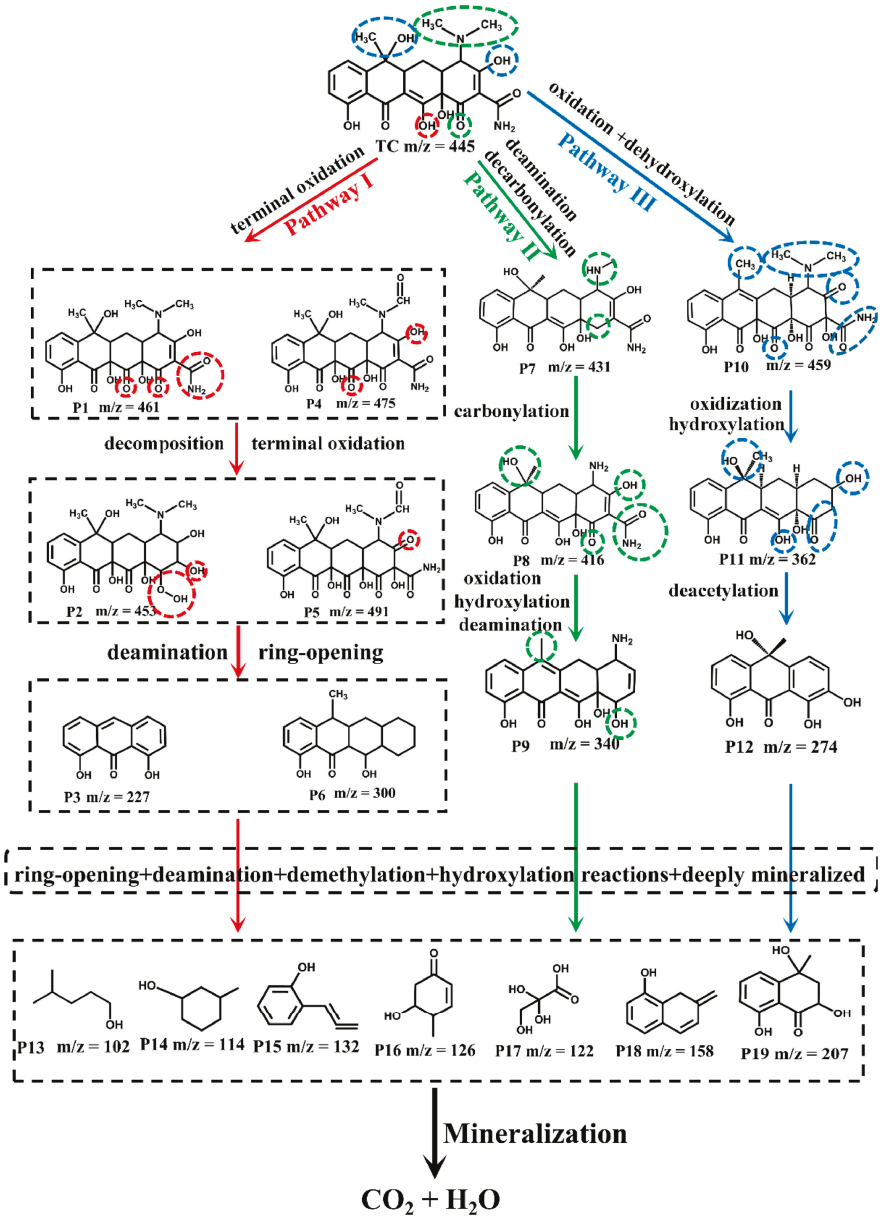


Figure 19. Possible degradation pathways of TC in CG/PMS system [164].

Table 6. Advantages of each catalyst.

Catalysts/Adsorbents	Advantage
Carbon supported catalysts	Low cost, high performance
Ni-based catalysts	Low cost and can be recycled many times
Copper-modified catalysts	Greatly accelerates catalytic speed
Copper and silver catalysts	Good stability

Currently, numerous domestic studies have found that coal gangue has a certain effect on removing some conventional pollutants, heavy metals, and organic substances [166,167]. Coal gangue's liquid permeability can meet regulatory requirements, and it has significant adsorption capacity for heavy metals such as lead and zinc [168]. By loading layered double hydroxides (LDH) on the inner pore walls of coal gangue's "ball window" porous monoliths (CBPM) to construct its framework, this structure displays a large specific surface area and abundant binding sites, making it especially suitable for removing trace emulsified water from contaminated oil, particularly as a flow-through filtration unit [169]. Coal gangue

can be transformed into low-cost ceramic microsphere adsorbents for removing cationic dyes from aqueous solutions [170]. Layered porous carbon prepared from coal gangue exhibits excellent adsorption properties for heavy metals (such as Cr(VI)) and organic pollutants (such as Rhodamine B) [171]. Figure 20 shows the adsorption mechanism of coal gangue-RS600 for Cr(VI). Under acidic conditions, due to the positive charge on the CG-RS surface and the release of a large number of metal cations, Cr(VI) anions are attracted electrostatically to the positively charged biochar surface; adsorbed Cr(VI) ions are reduced to Cr(III) by electron donors composed of surface functional groups of CG-RS 600; the reduced Cr(III) reacts with the surface's C-O, Fe-O, forming stable Cr(III) on the surface of RS 600 and CG-RS 600, with the specific reaction equations as follows [172].

$$HCrO_4^- + 7H^+ + 3e^- \rightarrow Cr^{3+} + 4H_2O \quad (7)$$

$$3C_xOH + Cr_2O_7^{2-} + 4H^+ \rightarrow 3CxO + Cr^{3+} + 3H_2O \quad (8)$$

$$nCr^{3+} + (1 - n)Fe^{3+} + 2H_2O \rightarrow Cr_nFe_{(1-n)}OOH + 3H^+ \quad (9)$$

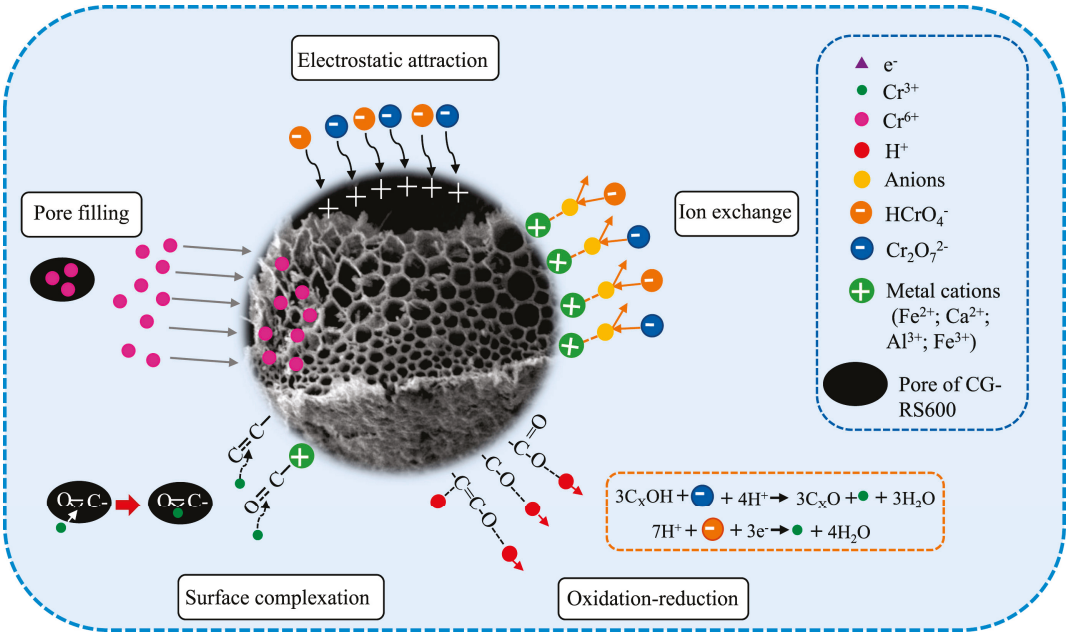


Figure 20. The adsorption mechanisms of Cr(VI) onto CG-RS600 [172].

Coal gangue geopolymers (GP) with a mesoporous structure can effectively interact with and capture Cu [47]. Magnetic zeolites synthesized from red mud and coal gangue through alkali reduction calcination-hydrothermal methods show maximum adsorption capacities for Cu^{2+}, Cd^{2+}, and Pb^{2+} of 76.2, 92.2, and 178.4 mg/g, respectively [173]. By modifying coal gangue through calcination and acid reflux, it can be used to treat fish pond aquaculture wastewater, achieving removal rates of 44.93% for COD (Chemical Oxygen Demand), 25.51% for turbidity, and 97.8% for total nitrogen [174]. Zeolite-activated carbon composite materials synthesized from coal gangue through CO_2 activation and hydrothermal synthesis methods exhibit efficient adsorption performance for Cu^{2+} and Rh-B, at 92.8% and 94.2%, respectively [160]. Figure 21 shows SEM images of zeolite (a-b) ZMC with different carbon contents. In low magnification (Figure 21a), zeolite exhibits good dispersibility, uniform particle size distribution, and regular geometric shapes without large impurities, indicating that carbon elements have been completely combusted. From high magnification (Figure 21b), individual zeolite is a regular hexahedron, with each

side about 1.5–2 μm. For zeolite (ZTC) prepared from coal gangue that retains carbon elements, some zeolites show agglomeration (Figure 21c), suggesting that the introduction of carbon elements can form additional nucleation sites, and zeolites tend to grow on the exposed surfaces of carbon-based materials. From Figure 21d, it can be seen that the length variation in individual zeolites compared to ZMC is negligible. However, more zeolites in the ZTC sample show coplanar and co-facial phenomena. Using coal gangue as raw material mixed with a certain amount of coal, the resulting sample is called carbon-added zeolite (ZAC). In this sample, some irregular bulk materials appear, and more zeolites grow on the surface of these bulk materials to form larger agglomerates as in Figure 21e. The carbon-based material is activated carbon with a porous structure, which can be clearly observed in Figure 21f. The composite material (AICCG) made of iron alginate oxide and calcined coal gangue has an adsorption effect on zinc and manganese, with adsorption capacities of 115.6 mg/g and 101.8 mg/g under optimal conditions, respectively [175]. Using coal gangue-based zeolite particles in a fluidized bed to treat methylene blue in aqueous solutions, under specific conditions, this method can effectively adsorb and remove methylene blue from water, showing good adsorption performance and industrial application potential [176]. The adsorbent (HM-CFB-FA) made by hydrothermal modification can remove Cd^{2+} from wastewater, with a maximum adsorption capacity of 183.7 mg/g at 25 °C and an initial pH value of 6.0 [177]. Modified coal gangue-supported $FeCo_2O_4$ nanoparticles activating persulfate can effectively degrade humic acid, with an efficiency of up to 85% [178].

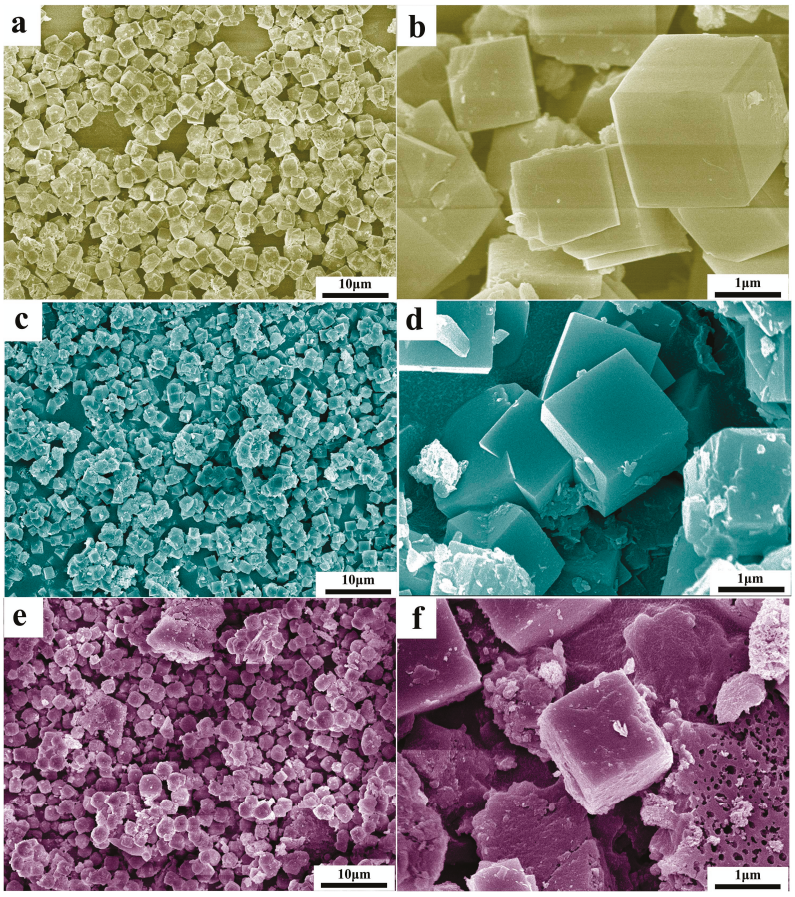


Figure 21. SEM images of zeolites containing different contents of carbon (**a**,**b**) ZMC, (**c**,**d**) ZTC, (**e**,**f**) ZAC [179].

In recent years, with the continuous advancement of materials science and technology, researchers have gradually realized that coal gangue is not merely a waste product but also holds great potential, especially in the development of high-performance materials. By applying advanced materials science technologies, the performance of coal gangue-based products can be significantly improved, thereby expanding their application across various fields. Table 7 presents the advantages of advanced technologies in coal gangue utilization.

Table 7. Advantages of advanced technologies in coal gangue utilization.

Advantages	Description	References
Enhanced Performance	Advanced technologies like nanotechnology and composite materials significantly improve the mechanical properties, durability, and corrosion resistance of coal gangue-based products, broadening their application fields.	[180]
Multifunctionality	Coal gangue can be functionalized with additional properties such as adsorption, antibacterial, and self-healing capabilities, making it useful for water treatment, environmental remediation, etc.	[166,172]
Improved Resource Efficiency	Advanced technologies allow for more diversified uses of coal gangue, increasing resource recovery efficiency and reducing reliance on single-use applications.	[181]
Higher Economic Value	Advanced techniques enable coal gangue to be transformed into high-value products, such as high-performance construction materials and chemical products, increasing economic benefits.	[58,60]
Higher Resource Recovery	Advanced materials technologies enable the extraction of valuable metals and other useful components from coal gangue, improving resource recovery rates.	[148,149]
Automation and Smart Processing	Future automated and smart technologies will optimize the processing and utilization of coal gangue, improving efficiency and reducing costs.	[10]

In addition, there are significant synergies between coal gangue utilization and emerging technologies such as carbon capture and storage (CCS), renewable energy integration, and the circular economy model. Coal gangue can react with carbon dioxide, helping to fix CO_2, reduce carbon emissions, and provide raw materials for products like construction materials, thereby promoting the development of carbon capture and storage technologies. It can also serve as a support material for renewable energy projects, enhancing the flexibility and stability of energy systems, for example, as an energy storage material or biomass fuel. Combined with the circular economy model, valuable resources in coal gangue, such as rare earth metals and aluminum, can be extracted and reused, reducing waste disposal and resource wastage. Furthermore, the application of intelligent technologies has improved the precision of coal gangue management, enhancing resource utilization rates through real-time monitoring and automated sorting. Through these synergies, the resource utilization of coal gangue not only contributes to environmental protection but also brings economic benefits, fostering a win-win situation for regional economies and sustainable development.

3.4.3. Environmental Impact of Coal Gangue in High-Value Applications

When extracting metals such as aluminum and silicon from coal gangue, attention should be paid to the gases emitted to avoid secondary pollution to the environment. Due to the very stable structure of the original minerals in coal gangue, high-temperature calcination activation and the use of strong acids and pressurized leaching are often required to achieve very high leaching rates [182]. If pyrite is present in the coal gangue, this process can produce sulfur dioxide, polluting the atmosphere, and the release rate may even be higher than that of pure pyrite [183]. Coal gangue is a huge reserve of aluminum and silicon resources. However, the acidic leaching process involved in extracting aluminum and silicon from coal gangue can negatively impact the environment. Acidic conditions

can promote the release of heavy metals from coal gangue, potentially polluting groundwater resources [184,185]. When using coal gangue as an adsorbent, the treatment of the adsorbent after use can also impact the environment [170]. The adsorption study on zinc and manganese by the iron alginate oxide-coal gangue composite demonstrated effective adsorption but also raised concerns about the environmental impact of by-products from this process [175].

When extracting metals from coal gangue or using it as a catalyst, several factors must be carefully considered. First, the metal composition and content in coal gangue can vary significantly, so a thorough compositional analysis must be conducted before extraction. Appropriate extraction methods, such as acid leaching or alkaline leaching, should be selected to ensure efficient metal recovery while minimizing secondary pollution. Second, when using coal gangue as a catalyst, its activity and stability must be evaluated. High-temperature roasting or surface modification may be required to enhance its catalytic performance. Additionally, the physicochemical properties of coal gangue, such as specific surface area and pore structure, directly affect its catalytic efficiency, and thus physical or chemical modifications might be necessary. The selectivity and efficiency of catalytic reactions also need to be optimized to ensure high performance in specific reactions. Moreover, coal gangue may contain harmful components that could release toxic substances during the catalytic process. Therefore, environmental monitoring should be strengthened to ensure that harmful gas emissions during the catalytic reactions comply with environmental standards. The recovery and regeneration of the catalyst are also crucial, and effective methods for restoring its activity must be explored to improve resource utilization. Lastly, the economic feasibility of metal extraction and catalytic applications of coal gangue should be taken into account. Optimizing processes and reducing costs are essential to achieving sustainable development in these applications.

4. Future Development Directions and Suggestions

The future development trend of coal gangue resource utilization can be considered in conjunction with some popular research directions, including environmentally friendly technologies, innovative applications in material science, and the concept of a circular economy. Here are some specific views: environmentally friendly technologies: with the increase in environmental awareness and policy promotion, the development and application of coal gangue utilization technologies with low pollution and low emissions will become a trend. For example, researching how to effectively use coal gangue without generating or with minimal production of carbon dioxide. Comprehensive utilization: the composition of coal gangue is diverse, making it a source of various resources. For instance, it can be used as raw material for building materials or as a source for extracting rare metals and minerals. Future research may focus more on how to extract these valuable components from coal gangue efficiently and economically. Innovative applications in material science: transforming coal gangue into high-performance materials, such as lightweight building materials, adsorbents, or catalysts, using advanced material science technologies, could be a research hotspot in the future. Circular economy and sustainable development: integrating the concept of a circular economy, researching how to incorporate the use of coal gangue into a broader industrial ecosystem to maximize resource utilization and minimize environmental impact will be important.

Along with the increase in coal extraction, coal gangue, an inevitable solid waste produced during the coal mining and washing process, also expressed an increasing tendency. Coal gangue is generally regarded as an environmental burden, occupying a vast amount of land and potentially polluting the surrounding land and water bodies through weathering and rainwater erosion. In 2022, China's comprehensive utilization

of coal gangue reached 597 million tons, a year-on-year increase of 9.94%. The utilization of coal gangue in power generation and heating accounted for approximately 6.87%, and other fields accounted for 93.13%. Despite the positive outcomes brought by the utilization of coal gangue resources, the process has also revealed some issues and challenges. Low economic benefits, slow technological updates, and technical complexity are the main problems faced in extracting the valuable components. In terms of energy applications, low thermal efficiency, high pollutant emissions, and related technical and economic challenges remain issues that need priority resolution. In agricultural applications, while the use of coal gangue provides a way of resource recovery, the potential risks of harmful substances and limitations on nutrient supply also need to be fully considered.

Moreover, while many studies focus on the utilization of coal gangue resources, there is relatively less concern for the potential environmental risks during its utilization process. Avoiding secondary pollution to the environment during resource utilization is an important consideration. Therefore, conducting environmental risk assessments, identifying and quantifying the potential impacts on the environment during the coal gangue utilization process are the key steps for ensuring the sustainable use of this resource. In this way, a better balance between economic benefits and environmental protection ought to be taking into account, promoting the resource utilization of coal gangue towards more efficient and eco-friendly directions. In summary, the resource utilization of coal gangue is not only an effective way to achieve the reduction, resource utilization, and harmlessness of solid waste, but also an important means to promote sustainable development and realize a green and low-carbon transition. With the advancement in energy technology and the enhancement of environmental protection awareness, the comprehensive utilization of coal gangue will show even greater potential in the future.

5. Conclusions

To fully utilize coal gangue and promote its resource utilization, the government can implement a series of policies and regulations to support the development of this field. The following are some recommendations: (1) Financial incentives and subsidies: The government can provide financial subsidies or tax incentives to enterprises engaged in the resource utilization of coal gangue, reducing their operational costs and encouraging investment in research and development. This could include tax exemptions on the import of related equipment, funding support for R&D, or offering lower interest rates on loans to such enterprises. (2) Establishing standards and certification systems: Developing quality and environmental standards for coal gangue products to ensure product quality and environmental safety. Additionally, setting up a certification system to certify products that meet the standards, thereby enhancing their market competitiveness. (3) Promoting industry-academia-research collaboration: Encouraging cooperation among enterprises, universities, and research institutions to jointly develop new technologies and products. The government can provide platforms to facilitate resource sharing and information exchange, as well as funding support for collaborative projects. (4) Environmental regulations and guidelines: Formulating clear environmental regulations to ensure that the utilization of coal gangue does not negatively impact the environment. This includes regulations on waste discharge, pollution control, and resource recycling.

In addition, based on the current research and practical status of coal gangue utilization, the main research gaps that need to be addressed are as follows: (1) Technological standardization and normalization: The technical standard system for the comprehensive utilization of coal gangue is still incomplete. There is a lack of specialized technical guidance and operating procedures for different regions and coal types, leading to uncertainties in practical operations. (2) High-value utilization technologies: The development

of high-value-added products from coal gangue is relatively limited. How to transform coal gangue into high-value materials or products, such as high-performance building materials or chemical products, requires further in-depth research. (3) Environmental impact assessment and remediation: Coal gangue may cause secondary pollution, such as soil and water contamination, during its treatment and utilization processes. There is a need to strengthen research on the assessment of its environmental impact and the development of remediation technologies. (4) Regional differentiation studies: Due to the significant differences in coal gangue composition across regions, its comprehensive utilization approaches also vary. Currently, there is insufficient systematic research on regional differentiation.

Future research priorities: (1) Environmentally friendly utilization: Explore the application of coal gangue in soil remediation, heavy metal pollution control, and other fields, developing environmentally friendly utilization technologies to reduce its negative environmental impact. (2) Industry chain integration and optimization: Build a multi-level, comprehensive utilization industry chain for coal gangue, promote its synergistic use across different fields, and improve its overall utilization efficiency and economic benefits. (3) Interdisciplinary research integration: Strengthen the interdisciplinary integration of materials science, environmental science, chemical engineering, and other fields to drive innovation and breakthroughs in coal gangue comprehensive utilization technologies.

Funding: This work was financially supported by Foundation of Shanxi Key Laboratory of Coal Flexible Combustion and Thermal Conversion (Project: No. CFCTC202303); Anhui Province Quality Infrastructure Standardization Special Project (Project: No. 2023MKS19); Natural Science Foundation of Hebei Province (Project: No. E2024202187, E2021202006); Undergraduate Innovation and Entrepreneurship Training Program (202410080020); Joint Funds of the National Natural Science Foundation of China (Project: No. U20A20302).

Conflicts of Interest: The authors declare no conflict of interest.

References

1. Zhao, Z.-Y.; Hao, Y.-X.; Chang, R.-D.; Wang, Q.-C. Assessing the vulnerability of energy supply chains: Influencing factors and countermeasures. *Sustain. Energy Technol. Assess.* **2023**, *56*, 103018. [CrossRef]
2. Zhang, C.; Li, X.; Sun, Y.; Chen, J.; Streimikiene, D. Policy modeling consistency analysis during energy crises: Evidence from China's coal power policy. *Technol. Forecast. Soc. Change* **2023**, *197*, 122931. [CrossRef]
3. Li, D.; Wu, D.; Xu, F.; Lai, J.; Shao, L. Literature overview of Chinese research in the field of better coal utilization. *J. Clean. Prod.* **2018**, *185*, 959–980. [CrossRef]
4. Zhang, Y.; Nie, R.; Shi, R.; Zhang, M. Measuring the capacity utilization of the coal sector and its decoupling with economic growth in China's supply-side reform. *Resour. Conserv. Recycl.* **2018**, *129*, 314–325. [CrossRef]
5. Song, W.; Zhang, J.; Li, M.; Yan, H.; Zhou, N.; Yao, Y.; Guo, Y. Underground Disposal of Coal Gangue Backfill in China. *Appl. Sci.* **2022**, *12*, 12060. [CrossRef]
6. Shao, S.; Ma, B.; Wang, C.; Chen, Y. Extraction of valuable components from coal gangue through thermal activation and HNO3 leaching. *J. Ind. Eng. Chem.* **2022**, *113*, 564–574. [CrossRef]
7. Chen, Y.; Zhou, S.; Zhang, W. Effect of coal gangue with different kaolin content son compressive strength and pore. *J. Wuhan Univ. Technol.-Mat. Sci. Ed.* **2008**, *23*, 12–15. [CrossRef]
8. Wang, G.; Xie, Y.; Qin, Y.; Wang, J.; Shen, J.; Han, B.; Liang, C.; Wang, Q. Element geochemical characteristics and formation environment for the roof, floor and gangue of coal seams in the Gujiao mining area, Xishan coalfield, China. *J. Geochem. Explor.* **2018**, *190*, 336–344. [CrossRef]
9. Ke, G.; Jiang, H.; Li, Z. Study on the calorific value and cementitious properties of coal gangue with 0-1 mm particle size. *Constr. Build. Mater.* **2024**, *414*, 135061. [CrossRef]
10. Xue, G.; Li, S.; Hou, P.; Gao, S.; Tan, R. Research on lightweight Yolo coal gangue detection algorithm based on resnet18 backbone feature network. *Internet Things* **2023**, *22*, 100762. [CrossRef]
11. Moghadam, M.J.; Ajalloeian, R.; Hajiannia, A. Preparation and application of alkali-activated materials based on waste glass and coal gangue: A review. *Constr. Build. Mater.* **2019**, *221*, 84–98. [CrossRef]

12. Han, B.; Zhang, Y.; Zou, Z.; Wang, J.; Zhou, C. Study on controlling factors and developing a quantitative assessment model for spontaneous combustion hazard of coal gangue. *Case Stud. Therm. Eng.* **2024**, *54*, 104039. [CrossRef]
13. Wu, F.; Liu, Y.; Gao, R. Challenges and opportunities of energy storage technology in abandoned coal mines: A systematic review. *J. Energy Storage* **2024**, *83*, 110613. [CrossRef]
14. Zheng, Q.; Zhou, Y.; Liu, X.; Liu, M.; Liao, L.; Lv, G. Environmental hazards and comprehensive utilization of solid waste coal gangue. *Prog. Nat. Sci. Mater. Int.* **2024**, *34*, 223–239. [CrossRef]
15. Ju, Q.; Hu, Y.; Liu, Q.; Chai, H.; Chen, K.; Zhang, H.; Wu, Y. Source apportionment and ecological health risks assessment from major ions, metalloids and trace elements in multi-aquifer groundwater near the Sunan mine area, Eastern China. *Sci. Total Environ.* **2023**, *860*, 160454. [CrossRef] [PubMed]
16. Luo, C.; Li, S.; Ren, P.; Yan, F.; Wang, L.; Guo, B.; Zhao, Y.; Yang, Y.; Sun, J.; Gao, P.; et al. Enhancing the carbon content of coal gangue for composting through sludge amendment: A feasibility study. *Environ. Pollut.* **2024**, *348*, 123439. [CrossRef] [PubMed]
17. Jiang, C.; Zhao, D.; Chen, X.; Zheng, L.; Li, C.; Ren, M. Distribution, source and ecological risk assessment of polycyclic aromatic hydrocarbons in groundwater in a coal mining area, China. *Ecol. Indic.* **2022**, *136*, 108683. [CrossRef]
18. Xu, Z.; Qian, Y.; Hong, X.; Luo, Z.; Gao, X.; Liang, H. Contamination characteristics of polycyclic aromatic compounds from coal sources in typical coal mining areas in Huaibei area, China. *Sci. Total Environ.* **2023**, *873*, 162311. [CrossRef] [PubMed]
19. Qing, Z.; Guijian, L.; Shuchuan, P.; Chuncai, Z.; Arif, M. Immobilization of hexavalent chromium in soil-plant environment using calcium silicate hydrate synthesized from coal gangue. *Chemosphere* **2022**, *305*, 135438. [CrossRef]
20. Gasparotto, J.; Da Boit Martinello, K. Coal as an energy source and its impacts on human health. *Energy Geosci.* **2021**, *2*, 113–120. [CrossRef]
21. Wang, Y.; Bai, D.; Luo, X.; Zhang, Y. Effects of Setaria viridis on heavy metal enrichment tolerance and bacterial community establishment in high-sulfur coal gangue. *Chemosphere* **2024**, *351*, 141265. [CrossRef] [PubMed]
22. Wang, C.; Wang, D.; Xin, H.; Qi, Z.; Zhang, W.; Zhang, K. Study on secondary oxidation characteristics of coal gangue at different pyrolysis rank. *Fuel* **2023**, *345*, 128231. [CrossRef]
23. Liang, Y.; Liang, H.; Zhu, S. Mercury emission from spontaneously ignited coal gangue hill in Wuda coalfield, Inner Mongolia, China. *Fuel* **2016**, *182*, 525–530. [CrossRef]
24. Zhai, X.; Wu, S.; Wang, K.; Drebenstedt, C.; Zhao, J. Environment influences and extinguish technology of spontaneous combustion of coal gangue heap of Baijigou coal mine in China. *Energy Procedia* **2017**, *136*, 66–72. [CrossRef]
25. Li, X.; Qiao, Y.; Shao, J.; Bai, C.; Li, H.; Lu, S.; Zhang, X.; Yang, K.; Colombo, P. Sodium-based alkali-activated foams from self-ignition coal gangue by facile microwave foaming route. *Ceram. Int.* **2022**, *48*, 33914–33925. [CrossRef]
26. Wang, H.; Chen, Z.; Meng, Z.; Liu, L.; Wang, X.; Xing, Y. Integrated utilization of coal gangue for synthesis of β-Sialon multiphase ceramic materials. *Ceram. Int.* **2023**, *49*, 11275–11284. [CrossRef]
27. Feng, D.; Wang, J.; Wang, Y.; Xiao, X.; Hou, W.; Liang, S. Alkali-activated geopolymer materials prepared from coal gangue and municipal solid waste incineration byproducts. *J. Build. Eng.* **2023**, *80*, 108074. [CrossRef]
28. Jin, J.; Li, M.; Liu, T.; Chen, Y.; Qin, Z.; Liu, Q.; Liang, B.; Zhao, J.; Zuo, S. Insights into factors influencing coal gangue-filled backfill cemented by self-consolidating alkali-activated slag grouts. *Constr. Build. Mater.* **2024**, *411*, 134422. [CrossRef]
29. Wang, H.; Xiong, R.; Zong, Y.; Li, L.; Guo, H.; Wang, Z.; Guan, B.; Chang, M. Effect of raw material ratio and sintering temperature on properties of coal gangue-feldspar powder artificial aggregate. *Constr. Build. Mater.* **2023**, *384*, 131400. [CrossRef]
30. Zhang, Y.; Qi, X.; Zou, J.; Rao, Y.; Chen, L.; Zhang, L.; Ji, Y.; Liang, Z. Effects of water immersion on the pore structure and thermodynamic properties of coal gangue. *Fuel* **2023**, *346*, 128273. [CrossRef]
31. Zhang, M.; Qu, Z.; Xie, M.; Chen, X.; Yang, Y.; Bai, Y. Research on the regulatory mechanism of pore structure in soil matrix prepared by fluidized bed calcination of coal gangue. *Arab. J. Chem.* **2024**, *17*, 105814. [CrossRef]
32. Duan, X.; Huang, Y.; Li, Y.; Zhang, W.; Huang, Z. Evolution mechanism of pore structure in sintered coal gangue ceramsites. *Ceram. Int.* **2023**, *49*, 31385–31395. [CrossRef]
33. Li, C.; Zhang, P.; Li, D. Study on low-cost preparation of glass–ceramic from municipal solid waste incineration (MSWI) fly ash and lead–zinc tailings. *Constr. Build. Mater.* **2022**, *356*, 129231. [CrossRef]
34. Yu, L.; Feng, Y.; Yan, W. The Current Situation of Comprehensive Utilization of Coal Gangue in China. *Adv. Mater. Res.* **2012**, *524–527*, 915–918. [CrossRef]
35. Li, Z.; Gao, Y.; Zhang, J.; Zhang, C.; Chen, J.; Liu, C. Effect of particle size and thermal activation on the coal gangue based geopolymer. *Mater. Chem. Phys.* **2021**, *267*, 124657. [CrossRef]
36. Cheng, L.; Qin, Y.; Li, X.; Zhao, X. A Laboratory and Numerical Simulation Study on Compression Characteristics of Coal Gangue Particles with Optimal Size Distribution Based on Shape Statistics. *Math. Probl. Eng.* **2020**, *2020*, 046156. [CrossRef]
37. Akdemir, Ü.; Sönmez, İ. Investigation of coal and ash recovery and entrainment in flotation. *Fuel Process. Technol.* **2003**, *82*, 1–9. [CrossRef]
38. Huang, H.; Dou, D.; Liu, G. Modeling of coal and gangue volume based on shape clustering and image analysis. *Int. J. Coal Prep. Util.* **2023**, *43*, 329–345. [CrossRef]
39. Long, G.; Li, L.; Li, W.; Ma, K.; Dong, W.; Bai, C.; Zhou, J.L. Enhanced mechanical properties and durability of coal gangue reinforced cement-soil mixture for foundation treatments. *J. Clean. Prod.* **2019**, *231*, 468–482. [CrossRef]

40. Ma, Q.Q.; Liu, H. Analysis of Obstacle of Development and Application that Coal Gangue Used in China Road Engineering. *Adv. Mater. Res.* **2014**, *900*, 510–513. [CrossRef]
41. Li, S.; Li, N. Effects of composition and temperature on porosity and pore size distribution of porous ceramics prepared from $Al(OH)_3$ and kaolinite gangue. *Ceram. Int.* **2007**, *33*, 551–556. [CrossRef]
42. Feng, D.; Wang, J.; Chen, D.; Hou, W.; Liang, S. Experimental study on municipal solid waste incineration fly ash as a component of coal gangue geopolymer and the feasibility of making geopolymer mortar. *Constr. Build. Mater.* **2023**, *409*, 133862. [CrossRef]
43. Feng, X.; Liu, N.; Lu, X. Investigation of un-calcined coal gangue together with ground granulated blast furnace slag and fly ash to ambient-curing production high-strength geopolymer. *J. Mater. Res. Technol.* **2023**, *25*, 3985–3997. [CrossRef]
44. Wen, B.; Huang, D.; Zhang, L.; Song, Q.; Gao, G.; Huo, D. Study on mechanical properties and size effect of coal gangue concrete at mesoscale. *Constr. Build. Mater.* **2022**, *360*, 129551. [CrossRef]
45. Ye, T.; Min, X.; Li, X.; Zhang, S.; Gao, Y. Improved holding and releasing capacities of coal gangue toward phosphate through alkali-activation. *Chemosphere* **2022**, *287*, 132382. [CrossRef]
46. Zhao, H.; Li, P.; He, X. Remediation of cadmium contaminated soil by modified gangue material: Characterization, performance and mechanisms. *Chemosphere* **2022**, *290*, 133347. [CrossRef] [PubMed]
47. Mei, Y.; Pang, J.; Wang, X.; Chen, E.; Wu, D.; Ma, J. Coal gangue geopolymers as sustainable and cost-effective adsorbents for efficient removal of Cu (II). *Environ. Technol. Innov.* **2023**, *32*, 103416. [CrossRef]
48. Zhou, C.; Liu, G.; Fang, T.; Lam, P.K.S. Investigation on thermal and trace element characteristics during co-combustion biomass with coal gangue. *Bioresour. Technol.* **2015**, *175*, 454–462. [CrossRef] [PubMed]
49. Jiao, Y.; Qiao, J.; Jia, R.; Wei, P.; Li, Y.; Ke, G. The influence of carbon imperfections on the physicochemical characteristics of coal gangue aggregates. *Constr. Build. Mater.* **2023**, *409*, 133965. [CrossRef]
50. Guo, Z.; Xu, J.; Xu, Z.; Gao, J.; Zhu, X. Performance of cement-based materials containing calcined coal gangue with different calcination regimes. *J. Build. Eng.* **2022**, *56*, 104821. [CrossRef]
51. Zhang, J.; Han, H.; Wang, L. Pozzolanic activity experimental dataset of calcined coal gangue. *Data Brief* **2023**, *51*, 109802. [CrossRef] [PubMed]
52. Zhang, S.; Cao, M.; Zhang, K.; Yuan, J.; Wang, Y. Wrapped coal gangue aggregate enhancement ITZ and mechanical property of concrete suitable for large-scale industrial use. *J. Build. Eng.* **2023**, *72*, 106649. [CrossRef]
53. Wu, J.; Bai, G.; Wang, P.; Liu, Y. Mechanical properties of a new type of block made from shale and coal gangue. *Constr. Build. Mater.* **2018**, *190*, 796–804. [CrossRef]
54. Zhao, G.; Wu, T.; Ren, G.; Zhu, Z.; Gao, Y.; Shi, M.; Ding, S.; Fan, H. Reusing waste coal gangue to improve the dispersivity and mechanical properties of dispersive soil. *J. Clean. Prod.* **2023**, *404*, 136993. [CrossRef]
55. Cao, D.; Ji, J.; Liu, Q.; He, Z.; Wang, H.; You, Z. Coal Gangue Applied to Low-Volume Roads in China. *Transp. Res. Rec.* **2011**, *2204*, 258–266. [CrossRef]
56. Li, Y.; Zhang, J.; Yan, C.; Bold, T.; Wang, J.; Cui, K. Effect of activated coal gangue on the hydration and hardening of Portland cement. *Constr. Build. Mater.* **2024**, *422*, 135740. [CrossRef]
57. Wang, Y.; Wang, Y.; Nian, P.; Wang, W.; Wei, D.; Xu, N.; Wu, Z.; Zhu, T.; Wei, Y. Reaction-bonded robust SiC ceramic membranes sintered at low temperature with coal gangue. *Ceram. Int.* **2023**, *49*, 19798–19805. [CrossRef]
58. Li, Y.; Liu, S.; Guan, X. Multitechnique investigation of concrete with coal gangue. *Constr. Build. Mater.* **2021**, *301*, 124114. [CrossRef]
59. Zhang, J.; Chen, T.; Gao, X. Incorporation of self-ignited coal gangue in steam cured precast concrete. *J. Clean. Prod.* **2021**, *292*, 126004. [CrossRef]
60. Yu, L.; Xia, J.; Xia, Z.; Gu, J.; Xu, H.; Wang, Y. Axial compressive behavior of basalt and carbon FRP-confined coal gangue concrete. *Constr. Build. Mater.* **2023**, *371*, 130803. [CrossRef]
61. Yu, L.; Xia, J.; Xia, Z.; Chen, M.; Wang, J.; Zhang, Y. Study on the mechanical behavior and micro-mechanism of concrete with coal gangue fine and coarse aggregate. *Constr. Build. Mater.* **2022**, *338*, 127626. [CrossRef]
62. Liu, H.; Bai, G.; Gu, Y.; Yan, F. The influence of coal gangue coarse aggregate on the mechanical properties of concrete columns. *Case Stud. Constr. Mater.* **2022**, *17*, e01315. [CrossRef]
63. Zhang, T.; Wen, Q.; Gao, S.; Tang, J. Comparative study on mechanical and environmental properties of coal gangue sand concrete. *Constr. Build. Mater.* **2023**, *400*, 132646. [CrossRef]
64. Xiao, G.; Yang, G.; Jixi, C.; Ruyi, Z. Deterioration mechanism of coal gangue concrete under the coupling action of bending load and freeze–thaw. *Constr. Build. Mater.* **2022**, *338*, 127265. [CrossRef]
65. Al Khazaleh, M.; Kumar, P.K.; Mohamed, M.J.S.; Kandasamy, A. Influence of coarse coal gangue aggregates on properties of structural concrete with nano silica. *Mater. Today Proc.* **2023**, *72*, 2089–2095. [CrossRef]
66. Gao, W.-C.; Zhang, X.-L.; Du, G.-Z.; Ma, Y.-P.; Fan, J.-B.; Geng, Y.; Zhang, H. Shrinkage model for concrete incorporating coal gangue coarse and fine aggregates. *J. Build. Eng.* **2023**, *80*, 107865. [CrossRef]
67. Sun, J.; Liu, S.; Ma, Z.; Qian, H.; Wang, Y.; Al-azzani, H.; Wang, H. Mechanical properties prediction of lightweight coal gangue shotcrete. *J. Build. Eng.* **2023**, *80*, 108088. [CrossRef]

68. Moussadik, A.; Ouzoun, F.; Ez-zaki, H.; Saadi, M.; Diouri, A. Mineralogical study of a binder based on alkali-activated coal gangue. *Mater. Today Proc.* **2023**, 260256556. [CrossRef]
69. Luo, L.; Li, K.; Fu, W.; Liu, C.; Yang, S. Preparation, characteristics and mechanisms of the composite sintered bricks produced from shale, sewage sludge, coal gangue powder and iron ore tailings. *Constr. Build. Mater.* **2020**, *232*, 117250. [CrossRef]
70. Qiu, J.; Cheng, K.; Zhang, R.; Gao, Y.; Guan, X. Study on the influence mechanism of activated coal gangue powder on the properties of filling body. *Constr. Build. Mater.* **2022**, *345*, 128071. [CrossRef]
71. Cheng, Y.; Shen, H.; Zhang, J. Understanding the effect of high-volume fly ash on micro-structure and mechanical properties of cemented coal gangue paste backfill. *Constr. Build. Mater.* **2023**, *378*, 131202. [CrossRef]
72. Jiu, S.; Cheng, S.; Li, H.; Wang, L. Reaction mechanism of metakaolin materials prepared by calcining coal gangue. *Mater. Res. Express* **2021**, *8*, 015508. [CrossRef]
73. Cai, B.; Li, K.; Fu, F. Flexural behavior of steel fiber-reinforced coal gangue aggregate concrete beams. *Structures* **2023**, *52*, 131–145. [CrossRef]
74. Cao, Z.; Cao, Y.; Dong, H.; Zhang, J.; Sun, C. Effect of calcination condition on the microstructure and pozzolanic activity of calcined coal gangue. *Int. J. Miner. Process.* **2016**, *146*, 23–28. [CrossRef]
75. Guan, X.; Chen, J.; Zhu, M.; Gao, J. Performance of microwave-activated coal gangue powder as auxiliary cementitious mate-rial. *J. Mater. Res. Technol.* **2021**, *14*, 2799–2811. [CrossRef]
76. Li, Y.; Yao, Y.; Liu, X.; Sun, H.; Ni, W. Improvement on pozzolanic reactivity of coal gangue by integrated thermal and chemical activation. *Fuel* **2013**, *109*, 527–533. [CrossRef]
77. Zhao, Y.; Yang, C.; Qu, F.; Li, K.; Yang, J.; Wu, Z. Mechanical Properties and Drying Shrinkage of Alkali-Activated Coal Gangue Concrete. *Sustainability* **2022**, *14*, 14736. [CrossRef]
78. Zhang, X.; Xiao, Y.; Wang, T.; Xia, J.; Lu, M.; Xue, Y. Kill two birds with one stone: Contribution of steel slag on enhancing the performance of coal gangue-based cementitious materials and simultaneous sulfur fixation. *J. Environ. Chem. Eng.* **2023**, *11*, 111169. [CrossRef]
79. Wang, J.; Qin, Q.; Hu, S.; Wu, K. A concrete material with waste coal gangue and fly ash used for farmland drainage in high groundwater level areas. *J. Clean. Prod.* **2016**, *112*, 631–638. [CrossRef]
80. Gao, S.; Zhao, G.; Guo, L.; Zhou, L.; Yuan, K. Utilization of coal gangue as coarse aggregates in structural concrete. *Constr. Build. Mater.* **2021**, *268*, 121212. [CrossRef]
81. Qin, L.; Gao, X. Properties of coal gangue-Portland cement mixture with carbonation. *Fuel* **2019**, *245*, 1–12. [CrossRef]
82. Zhang, X.; Pang, S.; Su, L.; Geng, J.; Cai, G.; Liu, J. Triaxial mechanical properties and microscopic characterization of fiber-reinforced cement stabilized aeolian sand–coal gangue blends. *Constr. Build. Mater.* **2022**, *346*, 128481. [CrossRef]
83. Wang, C.; Duan, D.; Huang, D.; Chen, Q.; Tu, M.; Wu, K.; Wang, D. Lightweight ceramsite made of recycled waste coal gangue & municipal sludge: Particular heavy metals, physical performance and human health. *J. Clean. Prod.* **2022**, *376*, 134309. [CrossRef]
84. Liu, S.; Jin, J.; Yu, H.; Gao, Y.; Du, Y.; Sun, X.; Qian, G. Performance enhancement of modified asphalt via coal gangue with microstructure control. *Constr. Build. Mater.* **2023**, *367*, 130287. [CrossRef]
85. Li, J.; Cao, Y.; Sha, A.; Song, R.; Li, C.; Wang, Z. Prospective application of coal gangue as filler in fracture-healing behavior of asphalt mixture. *J. Clean. Prod.* **2022**, *373*, 133738. [CrossRef]
86. Dong, J.; Li, J.; Huang, Y.; Zhong, J.; Dun, K.; Wu, M.; Zhang, L.; Chen, Q.; Pan, B. Understanding the release, migration, and risk of heavy metals in coal gangue: An approach by combining experimental and computational investigations. *J. Hazard. Mater.* **2024**, *461*, 132707. [CrossRef]
87. Li, J.; Wang, J. Comprehensive utilization and environmental risks of coal gangue: A review. *J. Clean. Prod.* **2019**, *239*, 117946. [CrossRef]
88. Wang, J.L.; Hu, S.R.; Peng, J.C.; Zhang, Y.X.; Tong, W.B.; Chen, M.; Ji, C. Research Environmental Pollution and Management of Coal Gangue in Pingdingshan. *Adv. Mater. Res.* **2013**, *807–809*, 750–755. [CrossRef]
89. Du, Z.; Hong, X.; Yang, K.; Wang, Z.; Zhang, Y.; Wang, X.; Zhang, L.; Zhu, Y. Enrichment characteristics of polycyclic aromatic hydrocarbons in coal gangue of the Huaibei Coalfield, China. *Environ. Technol. Innov.* **2024**, *36*, 103769. [CrossRef]
90. Paoli, L.; Guttová, A.; Grassi, A.; Lackovičová, A.; Senko, D.; Loppi, S. Biological effects of airborne pollutants released during cement production assessed with lichens (SW Slovakia). *Ecol. Indic.* **2014**, *40*, 127–135. [CrossRef]
91. Li, J.; Feng, H.; Liu, Y.; Zhang, J.; Ma, Y.; Ma, T. Determining the optimal gradation of mixed recycled aggregate containing coal gangue brick aggregate. *Case Stud. Constr. Mater.* **2024**, *20*, e02968. [CrossRef]
92. Zhu, M.; Wang, H.; Liu, L.; Ji, R.; Wang, X. Preparation and characterization of permeable bricks from gangue and tailings. *Constr. Build. Mater.* **2017**, *148*, 484–491. [CrossRef]
93. Zhou, C.; Liu, G.; Cheng, S.; Fang, T.; Lam, P.K.S. The Environmental Geochemistry of Trace Elements and Naturally Radionuclides in a Coal Gangue Brick-Making Plant. *Sci. Rep.* **2014**, *4*, 6221. [CrossRef] [PubMed]
94. Zhang, Y.; Ling, T.-C. Reactivity activation of waste coal gangue and its impact on the properties of cement-based materials—A review. *Constr. Build. Mater.* **2020**, *234*, 117424. [CrossRef]
95. Cui, J.P.; Liu, Y.; Wang, Z.H.; Gong, X.Z.; Gao, F.; Zhao, L.L.; Hao, L. Life Cycle Assessment of Cement Clinker Production Using Coal Gangue as Alternative Raw Material and Fuel. *Mater. Sci. Forum* **2015**, *814*, 435–440. [CrossRef]

96. Zhao, J.; Liu, Q.; Long, B.; Cheng, Z.; Wang, H.; Wang, D. Utilization of coal gangue power generation industry by-product CFA in cement: Workability, rheological behavior and microstructure of blended cement paste. *Fuel* **2023**, *345*, 128185. [CrossRef]
97. Huang, X.; Jin, X.; Dong, L.; Li, R.; Yang, K.; Li, Y.; Deng, L.; Che, D. CPFD numerical study on tri-combustion characteristics of coal, biomass and oil sludge in a circulating fluidized bed boiler. *J. Energy Inst.* **2024**, *113*, 101550. [CrossRef]
98. Yuansheng, H.; Mengshu, S. What are the environmental advantages of circulating fluidized bed technology?—A case study in China. *Energy* **2021**, *220*, 119711. [CrossRef]
99. Yan, Y. Analysis and Discussion on Burning Low Calorific Value Fuel of Circulating Fluidized Bed Boiler. *E3S Web Conf.* **2021**, *329*, 01074. [CrossRef]
100. Peng, H.; Li, Y.; Jia, X. Experimental study on thermoelectric generation Device based on accumulated temperature waste heat of coal gangue. *Energy Rep.* **2022**, *8*, 210–219. [CrossRef]
101. Zhang, H.; Shu, Y.; Yue, S.; Yu, W.; Zhang, Y.; Wang, X. Process design and optimization on self-sustaining pyrolysis and carbonization of ultra-low calorific value coal gangue. *Sustain. Energy Technol. Assess.* **2023**, *60*, 103491. [CrossRef]
102. Zhou, X.; Guo, L.; Zhang, Y.; Wang, Z.; Ma, Y.; Li, X. Feasibility investigation of utilizing spontaneous combustion energy of abandoned coal gangue by constructing a novel artificial heat reservoir. *J. Clean. Prod.* **2022**, *373*, 133948. [CrossRef]
103. Liu, L.; Liu, Q.; Zhang, S.; Li, Y.; Yang, L. The thermal transformation behavior and products of pyrite during coal gangue combustion. *Fuel* **2022**, *324*, 124803. [CrossRef]
104. Zhou, C.; Liu, G.; Yan, Z.; Fang, T.; Wang, R. Transformation behavior of mineral composition and trace elements during coal gangue combustion. *Fuel* **2012**, *97*, 644–650. [CrossRef]
105. Wang, S.; Luo, K.; Wang, X.; Sun, Y. Estimate of sulfur, arsenic, mercury, fluorine emissions due to spontaneous combustion of coal gangue: An important part of Chinese emission inventories. *Environ. Pollut.* **2016**, *209*, 107–113. [CrossRef]
106. Zhou, C.; Liu, G.; Xu, Z.; Sun, H.; Lam, P.K.S. The retention mechanism, transformation behavior and environmental implication of trace element during co-combustion coal gangue with soybean stalk. *Fuel* **2017**, *189*, 32–38. [CrossRef]
107. Yang, Z.; Zhang, Y.; Liu, L.; Wang, X.; Zhang, Z. Environmental investigation on co-combustion of sewage sludge and coal gangue: SO2, NOx and trace elements emissions. *Waste Manag.* **2016**, *50*, 213–221. [CrossRef] [PubMed]
108. Huo, X.; Jia, X.; Song, C.; Yun, F.; Hao, S.; Ding, Y.; Liu, S.; Lei, M. Investigation of mitigation of nitric oxide emission characteristics and slagging properties from biomass combustion by the additive of coal gangue. *J. Environ. Chem. Eng.* **2022**, *10*, 107573. [CrossRef]
109. Liu, L.; Ren, S.; Yang, J.; Jiang, D.; Guo, J.; Pu, Y.; Meng, X. Experimental study on K migration, ash fouling/slagging behaviors and CO2 emission during co-combustion of rice straw and coal gangue. *Energy* **2022**, *251*, 123950. [CrossRef]
110. Ma, Z.; Cheng, L.; Li, L.; Luo, G.; Zhang, W.; Wu, Y. Pollutant emission and attrition performance of low calorific blended coals during co-combustion in fluidized bed. *Fuel* **2023**, *331*, 125782. [CrossRef]
111. Bi, H.; Wang, C.; Lin, Q.; Jiang, X.; Jiang, C.; Bao, L. Combustion behavior, kinetics, gas emission characteristics and artificial neural network modeling of coal gangue and biomass via TG-FTIR. *Energy* **2020**, *213*, 118790. [CrossRef]
112. Shafizadeh, A.; Shahbeik, H.; Rafiee, S.; Fardi, Z.; Karimi, K.; Peng, W.; Chen, X.; Tabatabaei, M.; Aghbashlo, M. Machine learning-enabled analysis of product distribution and composition in biomass-coal co-pyrolysis. *Fuel* **2024**, *355*, 129464. [CrossRef]
113. Zhang, Y.; Zhao, J.; Ma, Z.; Yang, F.; Cheng, F. Effect of oxygen concentration on oxy-fuel combustion characteristic and interactions of coal gangue and pine sawdust. *Waste Manag.* **2019**, *87*, 288–294. [CrossRef]
114. Zhang, Y.; Zhang, Z.; Zhu, M.; Cheng, F.; Zhang, D. Interactions of coal gangue and pine sawdust during combustion of their blends studied using differential thermogravimetric analysis. *Bioresour. Technol.* **2016**, *214*, 396–403. [CrossRef] [PubMed]
115. Niu, Y.; Hu, Y.; Wang, W. Co-gasification of coal gangue and pine sawdust on a self-made two-stage fixed bed: Effect of mixing ratio. *Int. J. Hydrogen Energy* **2022**, *47*, 21713–21724. [CrossRef]
116. Zhang, Y.; Li, W.; Cheng, X.; Yan, K.; Zhao, W.; Yang, F. Air and oxy-fuel combustion characteristics of coal gangue and weathered coal blends. *Energy* **2023**, *284*, 128660. [CrossRef]
117. Wu, M.; Li, H.; Wang, L.; Feng, S.; Wang, Y.; Yang, N.; Wang, K.; Yu, M. Investigation on coal/coal gangue mixtures co-combustion via TG-DSC tests, multicomponent reaction model, and artificial neural network. *Fuel* **2024**, *359*, 130443. [CrossRef]
118. Li, J.; Hu, X.; Qiao, X. Thermogravimetric experimental study on the co-combustion of coal gangue and polypropylene. *Thermochim. Acta* **2023**, *732*, 179660. [CrossRef]
119. Bi, H.; Ni, Z.; Tian, J.; Wang, C.; Jiang, C.; Zhou, W.; Bao, L.; Sun, H.; Lin, Q. Influence of biomass on multi-component reaction model and combustion products of coal gangue. *Combust. Flame* **2022**, *240*, 111999. [CrossRef]
120. Zhu, B.; Dong, X.; Fan, Y.; Ma, X.; Fu, Y.; Chang, M.; Xue, H. Investigation on pyrolysis mechanism and emission characteristics of CO_2, NOx and SO_2 during co-pyrolysis of coal gangue and sodium alginate/sodium carboxymethylcellulose/chitosan/guar gum. *Fuel* **2024**, *356*, 129600. [CrossRef]
121. Bi, H.; Ni, Z.; Jiang, C.; Zhou, W.; Sun, H.; Lin, Q.; He, L. Thermal degradation of cellulose and coal gangue based on lumped reaction model and principal component analysis. *Combust. Flame* **2022**, *245*, 112290. [CrossRef]

122. Bi, H.; Ni, Z.; Tian, J.; Wang, C.; Jiang, C.; Zhou, W.; Bao, L.; Sun, H.; Lin, Q. The effect of biomass addition on pyrolysis characteristics and gas emission of coal gangue by multi-component reaction model and TG-FTIR-MS. *Sci. Total Environ.* **2021**, *798*, 149290. [CrossRef] [PubMed]
123. Bi, H.; Wang, C.; Lin, Q.; Jiang, X.; Jiang, C.; Bao, L. Pyrolysis characteristics, artificial neural network modeling and environmental impact of coal gangue and biomass by TG-FTIR. *Sci. Total Environ.* **2021**, *751*, 142293. [CrossRef]
124. Ni, Z.; Bi, H.; Jiang, C.; Tian, J.; Sun, H.; Zhou, W.; Lin, Q. Research on the co-pyrolysis of coal gangue and coffee industry residue based on machine language: Interaction, kinetics, and thermodynamics. *Sci. Total Environ.* **2022**, *804*, 150217. [CrossRef] [PubMed]
125. Bi, H.; Ni, Z.; Tian, J.; Jiang, C.; Sun, H.; Lin, Q. Influence of lignin on coal gangue pyrolysis and gas emission based on multi-lump parallel reaction model and principal component analysis. *Sci. Total Environ.* **2022**, *820*, 153083. [CrossRef] [PubMed]
126. Hobson, D.M.; Carter, R.; Yan, Y.; Lv, Z. Differentiation between Coal and Stone through Image Analysis of Texture Features. In Proceedings of the 2007 IEEE International Workshop on Imaging Systems and Techniques, Krakow, Poland, 5 May 2007; pp. 1–4. [CrossRef]
127. Zhang, Y.; Nakano, J.; Liu, L.; Wang, X.; Zhang, Z. Trace element partitioning behavior of coal gangue-fired CFB plant: Experimental and equilibrium calculation. *Environ. Sci. Pollut. Res.* **2015**, *22*, 15469–15478. [CrossRef] [PubMed]
128. Su, R.J. Study and Analysis on Pollution of Expanding Project of Coal Gangue Power Plant. *Adv. Mater. Res.* **2012**, *485*, 518–521. [CrossRef]
129. Kumari, M.; Bhattacharya, T. A review on bioaccessibility and the associated health risks due to heavy metal pollution in coal mines: Content and trend analysis. *Environ. Dev.* **2023**, *46*, 100859. [CrossRef]
130. Dai, R.; Zhao, R.; Wang, Z.; Qin, J.; Chen, T.; Wu, J. Study on the oxy-fuel co-combustion of coal gangue and semicoke and the pollutants emission characteristics. *J. Fuel Chem. Technol.* **2022**, *50*, 152–159. [CrossRef]
131. Chuncai, Z.; Guijian, L.; Dun, W.; Ting, F.; Ruwei, W.; Xiang, F. Mobility behavior and environmental implications of trace elements associated with coal gangue: A case study at the Huainan Coalfield in China. *Chemosphere* **2014**, *95*, 193–199. [CrossRef]
132. Hua, C.; Zhou, G.; Yin, X.; Wang, C.; Chi, B.; Cao, Y.; Wang, Y.; Zheng, Y.; Cheng, Z.; Li, R. Assessment of heavy metal in coal gangue: Distribution, leaching characteristic and potential ecological risk. *Environ. Sci. Pollut. Res.* **2018**, *25*, 32321–32331. [CrossRef]
133. Halecki, W.; Klatka, S. Long term growth of crop plants on experimental plots created among slag heaps. *Ecotoxicol. Environ. Saf.* **2018**, *147*, 86–92. [CrossRef]
134. Song, W.; Xu, R.; Li, X.; Min, X.; Zhang, J.; Zhang, H.; Hu, X.; Li, J. Soil reconstruction and heavy metal pollution risk in reclaimed cultivated land with coal gangue filling in mining areas. *CATENA* **2023**, *228*, 107147. [CrossRef]
135. Guo, G.; Li, H.; Zha, J. An approach to protect cultivated land from subsidence and mitigate contamination from colliery gangue heaps. *Process Saf. Environ. Prot.* **2019**, *124*, 336–344. [CrossRef]
136. Marchuk, S.; Marchuk, A. Effect of applied potassium concentration on clay dispersion, hydraulic conductivity, pore structure and mineralogy of two contrasting Australian soils. *Soil. Tillage Res.* **2018**, *182*, 35–44. [CrossRef]
137. Li, X.; Zheng, J.; Zheng, K.; Su, F.; Zhao, Z.; Bai, C.; Zheng, T.; Wang, X.; Qiao, Y.; Colombo, P. Rapid fabrication of coal gangue-based alkali activated foams and application as pH regulators. *Mater. Lett.* **2023**, *338*, 134020. [CrossRef]
138. Haghighizadeh, A.; Rajabi, O.; Nezarat, A.; Hajyani, Z.; Haghmohammadi, M.; Hedayatikhah, S.; Delnabi Asl, S.; Aghababai Beni, A. Comprehensive analysis of heavy metal soil contamination in mining Environments: Impacts, monitoring Techniques, and remediation strategies. *Arab. J. Chem.* **2024**, *17*, 105777. [CrossRef]
139. Ge, Q.; Tian, Q.; Wang, S.; Zhu, F. Synergistic effects of phosphoric acid modified hydrochar and coal gangue-based zeolite on bioavailability and accumulation of cadmium and lead in contaminated soil. *Chin. J. Chem. Eng.* **2022**, *46*, 150–160. [CrossRef]
140. Zhu, X.; Gong, W.; Li, W.; Bai, X.; Zhang, C. Reclamation of waste coal gangue activated by Stenotrophomonas maltophilia for mine soil improvement: Solubilizing behavior of bacteria on nutrient elements. *J. Environ. Manag.* **2022**, *320*, 115865. [CrossRef] [PubMed]
141. Tong, W.; Ying, W.; Jun, W. Research on Potential Fertilization of Coal Gangue in the Weibei Coalfield, China. *Acta Geol. Sin.-Engl. Ed.* **2008**, *82*, 717–721. [CrossRef]
142. Lv, B.; Zhao, Z.; Deng, X.; Fang, C.; Dong, B.; Zhang, B. Sustainable and clean utilization of coal gangue: Activation and preparation of silicon fertilizer. *J. Mater. Cycles Waste Manag.* **2022**, *24*, 1579–1590. [CrossRef]
143. Wang, B.; Ma, Y.; Lee, X.; Wu, P.; Liu, F.; Zhang, X.; Li, L.; Chen, M. Environmental-friendly coal gangue-biochar composites reclaiming phosphate from water as a slow-release fertilizer. *Sci. Total Environ.* **2021**, *758*, 143664. [CrossRef]
144. Wu, H.; Kang, S.; Zhang, H.; Sun, Q.; Shen, R.; Shu, Z. Research of the workability, mechanical and hydration mechanism of coal gangue-construction solid waste backfilling materials. *Constr. Build. Mater.* **2023**, *408*, 133833. [CrossRef]
145. Chu, Z.; Wang, X.; Wang, Y.; Zha, F.; Dong, Z.; Fan, T.; Xu, X. Influence of coal gangue aided phytostabilization on metal availability and mobility in copper mine tailings. *Environ. Earth Sci.* **2020**, *79*, 68. [CrossRef]
146. Tang, Q.; Li, L.; Zhang, S.; Zheng, L.; Miao, C. Characterization of heavy metals in coal gangue-reclaimed soils from a coal mining area. *J. Geochem. Explor.* **2018**, *186*, 1–11. [CrossRef]
147. Zhang, P.; Han, Z.; Jia, J.; Wei, C.; Liu, Q.; Wang, X.; Zhou, J.; Li, F.; Miao, S. Occurrence and Distribution of Gallium, Scandium, and Rare Earth Elements in Coal Gangue Collected from Junggar Basin, China. *Int. J. Coal Prep. Util.* **2019**, *39*, 389–402. [CrossRef]
148. Zhang, Y.; Sun, J.; Lü, G.; Zhang, T.; Gong, Y. Kinetics of alumina extraction from coal gangue by hydrochloric acid leaching. *Trans. Nonferrous Met. Soc. China* **2023**, *33*, 1932–1942. [CrossRef]

149. Miao, H.; Wang, Z.; Wang, Z.; Sun, H.; Li, X.; Liu, Z.; Dong, L.; Zhao, J.; Huang, J.; Fang, Y. Effects of Na_2CO_3/Na_2SO_4 on catalytic gasification reactivity and mineral structure of coal gangue. *Energy* **2022**, *255*, 124498. [CrossRef]
150. Xie, M.; Liu, F.; Zhao, H.; Ke, C.; Xu, Z. Mineral phase transformation in coal gangue by high temperature calcination and high-efficiency separation of alumina and silica minerals. *J. Mater. Res. Technol.* **2021**, *14*, 2281–2288. [CrossRef]
151. Peng, B.; Li, X.; Zhao, W.; Yang, L. Study on the release characteristics of chlorine in coal gangue under leaching conditions of different pH values. *Fuel* **2018**, *217*, 427–433. [CrossRef]
152. Liu, F.; Xie, M.; Yu, G.; Ke, C.; Zhao, H. Study on Calcination Catalysis and the Desilication Mechanism for Coal Gangue. *ACS Sustain. Chem. Eng.* **2021**, *9*, 10318–10325. [CrossRef]
153. Zhang, K.; Liu, L.; Liu, L.; Yang, Y.; Liu, Q. Iron removal from kaolinitic coal gangue via magnetic separation after oxidizing calcination with the crystal structure of kaolinite protected. *Mater. Today Commun.* **2023**, *37*, 107175. [CrossRef]
154. Qin, Q.; Geng, H.; Deng, J.; Xu, H.; Ye, Y.; Li, B.; Gui, X.; Park, C. Waste-free technologies of coal gangue processing: Extraction of metals and improvement of soil. *Sep. Purif. Technol.* **2025**, *361*, 131203. [CrossRef]
155. Wang, H.; Cao, Z.; Wang, J.; Wang, Z.; Chen, J.; Shen, L. Alkali Methods for Alumina Extraction from the By-products of High Alumina Coal: A Review. *Min. Metall. Explor.* **2023**, *40*, 1681–1694. [CrossRef]
156. Xiao, J.; Li, F.; Zhong, Q.; Bao, H.; Wang, B.; Huang, J.; Zhang, Y. Separation of aluminum and silica from coal gangue by elevated temperature acid leaching for the preparation of alumina and SiC. *Hydrometallurgy* **2015**, *155*, 118–124. [CrossRef]
157. Miao, H.; Wang, Z.; Sun, H.; Li, X.; Mei, Y.; Liu, Z.; Dong, L.; Huang, J.; Bai, J.; Fang, Y. Gasification and activation behaviors of coal gangue with Na2CO3 in CO2 atmosphere. *Fuel Process. Technol.* **2022**, *228*, 107163. [CrossRef]
158. Dai, S.; Sun, F.; Wang, L.; Wang, L.; Zhang, R.; Guo, H.; Xing, Y.; Gui, X. A new method for pre-enrichment of gallium and lithium based on mode of occurrence in coal gangue from Antaibao surface mine, Shanxi Province, China. *J. Clean. Prod.* **2023**, *425*, 138968. [CrossRef]
159. Zhu, X.; Gong, W.; Li, W.; Zhang, C. Fixating lead in coal gangue with phosphate using phosphate-dissolving bacteria: Phosphorus dissolving characteristics of bacteria and adsorption mechanism of extracellular polymer. *J. Hazard. Mater.* **2023**, *458*, 131923. [CrossRef]
160. Du, S.; Mao, S.; Guo, F.; Dong, K.; Shu, R.; Bai, J.; Xu, L.; Li, D. Investigation of the catalytic performance of coal gangue char on biomass pyrolysis in a thermogravimetric analyzer and a fixed bed reactor. *Fuel* **2022**, *328*, 125216. [CrossRef]
161. Sun, Y.; Yan, Y.; Zheng, X.; Han, J.; Wang, B.; Wu, Q.; Bai, G. Fabrication of dual-activated coal gangue-loaded nickel-based catalyst for dioctyl phthalate hydrogenation. *Mol. Catal.* **2024**, *553*, 113732. [CrossRef]
162. Li, H.; Cheng, R.; Liu, Z.; Du, C. Waste control by waste: Fenton–like oxidation of phenol over Cu modified ZSM–5 from coal gangue. *Sci. Total Environ.* **2019**, *683*, 638–647. [CrossRef] [PubMed]
163. Li, H.; Wang, L.; Liu, Z.; Du, C. Cu, Ag–containing systems based on coal gangue as catalysts for highly efficient antibiotics removal via persulfate activation under visible light irradiation. *J. Environ. Chem. Eng.* **2021**, *9*, 105016. [CrossRef]
164. Zhang, P.; Zhang, H.; Liu, Z.; Du, C. Natural coal gangue activated persulfate for tetracycline hydrochloride degradation: Mechanisms, theoretical calculations, and comparative study. *J. Mol. Struct.* **2023**, *1291*, 136097. [CrossRef]
165. Li, C.; Yin, S.; Yan, Y.; Liang, C.; Ma, Q.; Guo, R.; Zhang, Y.; Deng, J.; Sun, Z. Efficient benzo(a)pyrene degradation by coal gangue-based catalytic material for peroxymonosulfate activation. *J. Environ. Manag.* **2024**, *351*, 119645. [CrossRef] [PubMed]
166. Wang, C.; Yang, Z.; Song, W.; Zhong, Y.; Sun, M.; Gan, T.; Bao, B. Quantifying gel properties of industrial waste-based geopolymers and their application in Pb2+ and Cu2+ removal. *J. Clean. Prod.* **2021**, *315*, 128203. [CrossRef]
167. Duan, D.; Wang, C.; Bai, D.; Huang, D. Representative coal gangue in China: Physical and chemical properties, heavy metal coupling mechanism and risk assessment. *Sustain. Chem. Pharm.* **2024**, *37*, 101402. [CrossRef]
168. Wu, H.; Wen, Q.; Hu, L.; Gong, M.; Tang, Z. Feasibility study on the application of coal gangue as landfill liner material. *Waste Manag.* **2017**, *63*, 161–171. [CrossRef] [PubMed]
169. Sun, G.; Zhang, J.; Li, X.; Hao, B.; Xu, F.; Liu, K. Reuse of coal gangue to prepare adsorbent with multiscale pore structure for emulsified water removal. *Inorg. Chem. Commun.* **2023**, *151*, 110632. [CrossRef]
170. Zhou, L.; Zhou, H.; Hu, Y.; Yan, S.; Yang, J. Adsorption removal of cationic dyes from aqueous solutions using ceramic adsorbents prepared from industrial waste coal gangue. *J. Environ. Manag.* **2019**, *234*, 245–252. [CrossRef] [PubMed]
171. Wu, J.; Yan, X.; Li, L.; Gu, J.; Zhang, T.; Tian, L.; Su, X.; Lin, Z. High-efficiency adsorption of Cr(VI) and RhB by hierarchical porous carbon prepared from coal gangue. *Chemosphere* **2021**, *275*, 130008. [CrossRef] [PubMed]
172. Zhao, R.; Wang, B.; Zhang, X.; Lee, X.; Chen, M.; Feng, Q.; Chen, S. Insights into Cr(VI) removal mechanism in water by facile one-step pyrolysis prepared coal gangue-biochar composite. *Chemosphere* **2022**, *299*, 134334. [CrossRef] [PubMed]
173. Yan, K.; Zhang, J.; Liu, D.; Meng, X.; Guo, Y.; Cheng, F. Feasible synthesis of magnetic zeolite from red mud and coal gangue: Preparation, transformation and application. *Powder Technol.* **2023**, *423*, 118495. [CrossRef]
174. Abdelwahab, O.; Thabet, W.M. Natural zeolites and zeolite composites for heavy metal removal from contaminated water and their applications in aquaculture Systems: A review. *Egypt. J. Aquat. Res.* **2023**, *49*, 431–443. [CrossRef]
175. Mohammadi, R.; Azadmehr, A.; Maghsoudi, A. Enhanced competitive adsorption of zinc and manganese by alginate-iron oxide-combusted coal gangue composite: Synthesizing, characterization and investigation. *J. Environ. Chem. Eng.* **2021**, *9*, 105003. [CrossRef]

176. Lv, B.; Dong, B.; Zhang, C.; Chen, Z.; Zhao, Z.; Deng, X.; Fang, C. Effective adsorption of methylene blue from aqueous solution by coal gangue-based zeolite granules in a fluidized bed: Fluidization characteristics and continuous adsorption. *Powder Technol.* **2022**, *408*, 117764. [CrossRef]
177. Qiu, R.; Cheng, F.; Huang, H. Removal of Cd2+ from aqueous solution using hydrothermally modified circulating fluidized bed fly ash resulting from coal gangue power plant. *J. Clean. Prod.* **2018**, *172*, 1918–1927. [CrossRef]
178. Zhao, B.-H.; Zhu, Y.-H.; Wang, C. Degradation of humic acid via peroxymonosulfate activation by $FeCo_2O_4$ nanoparticles supported on modified coal gangue. *Inorg. Chem. Commun.* **2023**, *152*, 110736. [CrossRef]
179. Li, H.; Zheng, F.; Wang, J.; Zhou, J.; Huang, X.; Chen, L.; Hu, P.; Gao, J.; Zhen, Q.; Bashir, S.; et al. Facile preparation of zeolite-activated carbon composite from coal gangue with enhanced adsorption performance. *Chem. Eng. J.* **2020**, *390*, 124513. [CrossRef]
180. Yang, F.; Lv, J.; Zheng, Y.; Cui, J.; Huang, Y.; Cao, X.; Liu, H.; Zhao, L. Enhancement of coal gangue performance by surface micro-crystalline glaze derived from mineral powder. *Sci. Total Environ.* **2023**, *858*, 159986. [CrossRef]
181. Zhao, G.; Chang, F.; Chen, J.; Si, G. Research and prospect of underground intelligent coal gangue sorting technology: A review. *Miner. Eng.* **2024**, *215*, 108818. [CrossRef]
182. Li, X.; Wang, H.; Zhou, Q.; Qi, T.; Liu, G.; Peng, Z. Efficient separation of silica and alumina in simulated CFB slag by reduction roasting-alkaline leaching process. *Waste Manag.* **2019**, *87*, 798–804. [CrossRef] [PubMed]
183. Qin, Q.; Geng, H.; Deng, J.; Su, X.; Chen, M.; Park, C.B. Al and other critical metals co-extraction from coal gangue through delamination pretreatment and recycling strategies. *Chem. Eng. J.* **2023**, *477*, 147036. [CrossRef]
184. Li, C.; Zheng, L.; Jiang, C.; Chen, X.; Ding, S. Characteristics of leaching of heavy metals from low-sulfur coal gangue under different conditions. *Int. J. Coal Sci. Technol.* **2021**, *8*, 780–789. [CrossRef]
185. Dong, L.; Li, Y.; Yan, J.; Shu, X.Q. Efficient Extraction of SiO_2 and Al_2O_3 from Coal Gangue by Means of Acidic Leaching. *Adv. Mater. Res.* **2014**, *878*, 149–156. [CrossRef]

Disclaimer/Publisher's Note: The statements, opinions and data contained in all publications are solely those of the individual author(s) and contributor(s) and not of MDPI and/or the editor(s). MDPI and/or the editor(s) disclaim responsibility for any injury to people or property resulting from any ideas, methods, instructions or products referred to in the content.

energies

MDPI

Article

Optimal Multi-Area Demand–Thermal Coordination Dispatch

Yu-Shan Cheng [1], Yi-Yan Chen [1], Cheng-Ta Tsai [2] and Chun-Lung Chen [3,*]

[1] Department of Electrical Engineering, National Taiwan Ocean University, Keelung 202301, Taiwan; yscheng@mail.ntou.edu.tw (Y.-S.C.); 11053015@mail.ntou.edu.tw (Y.-Y.C.)
[2] Maritime Development and Training Center, National Taiwan Ocean University, Keelung 202301, Taiwan; cttsai@mail.ntou.edu.tw
[3] Department Marine of Engineering, National Taiwan Ocean University, Keelung 202301, Taiwan
* Correspondence: cclung@mail.ntou.edu.tw

Abstract: With the soaring demand for electric power and the limited spinning reserve in the power system in Taiwan, the comprehensive management of both thermal power generation and load demand turns out to be a key to achieving the robustness and sustainability of the power system. This paper aims to design a demand bidding (DB) mechanism to collaborate between customers and suppliers on demand response (DR) to prevent the risks of energy shortage and realize energy conservation. The concurrent integration of the energy, transmission, and reserve capacity markets necessitates a new formulation for determining schedules and marginal prices, which is expected to enhance economic efficiency and reduce transaction costs. To dispatch energy and reserve markets concurrently, a hybrid approach of combining dynamic queuing dispatch (DQD) with direct search method (DSM) is developed to solve the extended economic dispatch (ED) problem. The effectiveness of the proposed approach is validated through three case studies of varying system scales. The impacts of tie-line congestion and area spinning reserve are fully reflected in the area marginal price, thereby facilitating the determination of optimal load reduction and spinning reserve allocation for demand-side management units. The results demonstrated that the multi-area bidding platform proposed in this paper can be used to address issues of congestion between areas, thus improving the economic efficiency and reliability of the day-ahead market system operation. Consequently, this research can serve as a valuable reference for the design of the demand bidding mechanism.

Keywords: demand bidding mechanism; demand response; economic dispatch; spinning reserve; direct search method

1. Introduction

With the soaring demand for electric power and the rising environmental awareness, governments from many countries have actively developed renewable energy generation systems (REGS), implemented energy-saving actions, and performed user-side load management measures to realize the energy transition more smoothly. At present, Taiwan's government puts focus on increasing the proportion of renewable energies in the energy supply system in response to the net zero emissions. The goal is to increase the ratio of power generation from renewable energy resources to 20% by 2025 [1]. As the penetration of renewable energy keeps increasing, the impact of REGS on the stability and robustness of the power system is attracting a lot of attention. Due to the characteristics of uncertainty and intermittency of the output from renewable energy resources, power dispatching becomes a challenge for system operators [2–4]. Moreover, the electricity demand during peak hours has increased sharply in recent years in Taiwan. With limited generators to

compensate and a sudden rise in load demand, many problems have occurred, including high variations in load demand during peak hours and off-peak hours, inefficient usage of energy, regional imbalances between supply and demand, and even the insufficiency of backup capacity. The question of how to ensure the safety and reliability of the operation of Taiwan power system becomes an important and challenging one.

As many distributed energy resources (DERs) are introduced into the power system, the development of a virtual power plant (VPP) plays a key role to integrate the resources from both supply and demand sides. VPP is regarded as a novel power supply service that consists of DERs, controllable load, and battery energy storage system (BESS), etc., giving VPP flexible adjustability and rapid response ability. In this way, it can effectively handle the unstable issues in the power system, such as a sudden increase in load, failure of thermal generator, or uncertainty in the output of renewable energy generation [5–7]. In addition, many papers have investigated the strategies applied for demand response (DR) [8–12]. In Ref. [8], a large number of end-users, namely DR sources, are formed as DR aggregators in the electricity market, and an approach based on game theory is developed for the bidding strategy. In Ref. [9], the load aggregator (LA) takes the risk of the uncertainty of the wholesale market prices and bids in the wholesale market to purchase electricity to satisfy the demand of the customers in the electricity market. To relieve the risks of financial loss caused by price volatility, an optimal bidding strategy model is designed for the LA to perform DR program. Furthermore, to ensure the aggregator fully grasps the information of available DR capacity, Ref. [10] has proposed an optimal bidding strategy for the aggregator, considering the bottom-up responsiveness of residential customers. In Ref. [11], a novel hybrid stochastic–robust optimal trading strategy for a DR aggregator in the wholesale electricity market has been proposed, aiming to improve scheduling and manage risk by considering both stochastic market prices and non-stochastic consumer participation, while also incorporating energy storage and multiple demand response programs. In contrast, Ref. [12] focuses on the self-scheduling problem of a generation company and a DR aggregator in a competitive market. It models temporal load characteristics and employs a Fuzzy Inference System (FIS) to represent DR aggregator participation based on load behavior and customer willingness. The circumstances of multi-grid and the inclusion of distributed energy resources or renewable energy resources are also considered in Refs. [13–17]. Ref. [13] introduces a low-carbon economic dispatch (ED) model tailored for multi-energy microgrids, aiming to reduce daily operating costs through the integration of DR and a multi-stage carbon trading scheme. Ref. [14] presents a decentralized optimization approach for managing the operation strategy of hierarchical systems, taking into account the competitive interactions among individual agents. Ref. [15] provides a comprehensive review of ED problems, examining their mathematical formulation; evolution from conventional to modern power systems, including VPPs and multi-energy systems; and the various conventional, uncertainty-based, AI-based, and hybrid optimization techniques used to solve them. In contrast, Ref. [16] focuses on a specific control strategy, namely Model Predictive Control (MPC), for microgrids to participate in real-time ancillary service markets. This paper addresses the integration of DERs and the potential for microgrids to enhance power system stability and reliability. Finally, a comprehensive review of demand response programs within multi-energy systems (MESs) can be found in Ref. [17], which highlights the increasing research and the potential of MESs, often incorporating energy hubs and storage, to enhance flexibility and consumer comfort during DR operation.

Apart from the supply–demand balance for electricity, the ancillary services, including frequency regulation, voltage control, and reserve capacity, also play a crucial role in the power market for a robust and stable power system operation. Ref. [18] analyzes the current development and historical evolution of the unified power market in Europe and

regional power markets in the US and further highlights the critical factors influencing the design of ancillary service trading mechanisms in regional electricity markets. Therefore, some studies focus on the bidding strategies that consider the spinning reserve [19–26]. In Ref. [19], an optimal bidding strategy is presented considering flexible ramping products; thus, a microgrid is able to optimally allocate the capacities for energy, spinning reserve, and ramping. In Ref. [20], the reserve cost and penalty cost of over and under estimation of outputs of renewable energy resources were considered, respectively, for more robust optimal bidding. Ref. [21] developed an optimal bidding strategy in energy and reserve markets considering environmental restrictions for a grid-connected combined-heat-and-power-based multi-microgrid system. Ref. [22] and Ref. [23] specifically focus on optimal bidding strategies for microgrids considering uncertainties of renewable energy resources and market prices, which employ stochastic modeling and risk management techniques for participation in energy and ancillary service markets such as regulation and reserves. Ref. [24] broadens this to the distribution system level and proposes a framework for optimizing profits by local resources such as wind, PV, EVs, and BESS in the joint energy, regulation, and ramp markets. Ref. [25] investigates a more advanced paradigm of transactive energy management in distribution systems, enabling bidirectional exchange of both energy and ancillary services between the distribution system operator and microgrids through a stochastic bilevel programming model to manage interactions under uncertainty. To prevent the shortage of power supply during the peak hours, Taiwan Power Company, namely Taipower, has implemented the DB mechanism since 2015 [26]. It is noted that a DB mechanism is one of the load management measures used by Taipower to perform demand response. Within the energy bidding platform, DR participants can specify both the amount of load reduction for peak shaving and the corresponding bid price during their available time slots. All participants will join the bidding process, together with thermal generators of Taipower. Therefore, a collaboration between the customers and suppliers can be achieved. Through the load management strategy, the significant load consumption during peak hours can be reduced. In addition, DR users in the ancillary service bidding platform are able to provide reserve capability to enhance the stability of Taipower's system.

The day-ahead market enables participants to submit bids for the purchase or sale of electricity for each hour of the following day through a closed auction mechanism. In order to further strengthen Taipower's DB mechanism, operated at the day-ahead market, this paper intends to integrate the energy bidding platform and the ancillary service bidding platform to comprehensively investigate the optimum dispatch problem of multi-area economic generation and reserve under DB mechanism. Meanwhile, the coordination between thermal generators and substantial industrial users under DB mechanism is also discussed to further improve the power system operation efficiency and stability. Due to the complex constraints and many coupling conditions, it is very difficult to achieve optimal power dispatch for both generation and reserve in power system. Many studies have applied analytical methods and optimization techniques to investigate power dispatch problems, such as direct search method (DSM) [27], Simulated Annealing (SA) [28], Genetic Algorithm (GA) [29], Particle Swarm Optimization (PSO) [30], and Grey Wolf Optimizer (GWO) [31], etc. This paper aims to expand the application of the DSM and develop a software analysis tool to assist the day-ahead market bidding platform. To dispatch energy and reserve markets concurrently, a hybrid approach of combining dynamic queuing dispatch (DQD) with DSM is developed to solve the multi-area ED problem. The proposed method is designed to simultaneously optimize the power dispatch of DR users and thermal power generation systems to enhance the fairness of DR user competition in the generation scheduling of the system and further optimize the bidding results of actual DR users. The

results show that allocation of generation and reserve capacity cooperated by thermal units and equivalent DR units is able to relieve congested areas and supply bottlenecks. It should be noted that although the increasing share of renewable energy is a key driver behind the need for demand-side flexibility, this paper focuses solely on the design and evaluation of a multi-area demand bidding mechanism.

The main technical innovations and contributions of this paper are summarized as follows:

1. A multi-area DB mechanism is developed to enhance customer–supplier collaboration in DR, aiming to alleviate regional congestion and address supply bottlenecks.
2. This paper integrates the multi-area DB platform of energy market and ancillary services market with the actual bidding prices and information from the DR users to enhance the transparency and the efficiency of the day-ahead market.
3. An improved technique based on a DSM is proposed to address the multi-area generation and reserve dispatch problem under the DB mechanism of Taipower.
4. Simulation results are presented to evaluate the effectiveness and economic benefits of implementing the DB program. The proposed DSM approach demonstrates both practical applicability and operational efficiency.

This paper is organized as follows. In Section 2, the DB mechanism of Taipower will be introduced. In Section 3, the problem description will be given. In Section 4, the DSM including DQD will be explained in detail. Eventually, in Section 5, the simulation results and three case studies will be discussed.

2. A Brief Introduction of the Demand Bidding Mechanism of Taipower

The DB mechanism was initially implemented in 2015. Until now, it has been revised and changed to meet the up to date supply–demand conditions. Depending on the system requirement, the day-ahead market for the bidding mechanism can be divided into the energy market and ancillary services market. In the day-ahead market, the key factors, such as the bidding prices given by DR users, output power from thermal generators, and the requirements from the power system, etc., are all taken into account in the optimum dispatch algorithm to determine the bid winners in the energy market and ancillary services market, individually. A brief description of Taipower's current DB mechanism is provided in the following section.

2.1. Regulations of Load Reduction by DR Users

The DB mechanism for participants, i.e., DR users, can be divided into three types: economical type, reliable type, and aggregated type. Among them, the economical type is of interest for most of the participants, due to the incentives. According to Taipower, participants must follow the rules to join the DB mechanism. That is, the minimum load reduction in participants is 20 kW and the maximum bidding price is 10 TWD/kWh. Participants can choose to perform load reduction for 2 h or 4 h for each time, and the total load reduction in a month is limited to 36 h. The actual amount of load reduction is determined by the difference between customer baseline load (CBL) and the average load demand in the period of DR implementation shown in Figure 1. Herein, the CBL is calculated by averaging the demand power during the same DR period, except for the load-reduction day, off-peak days, weekends, and holidays [32].

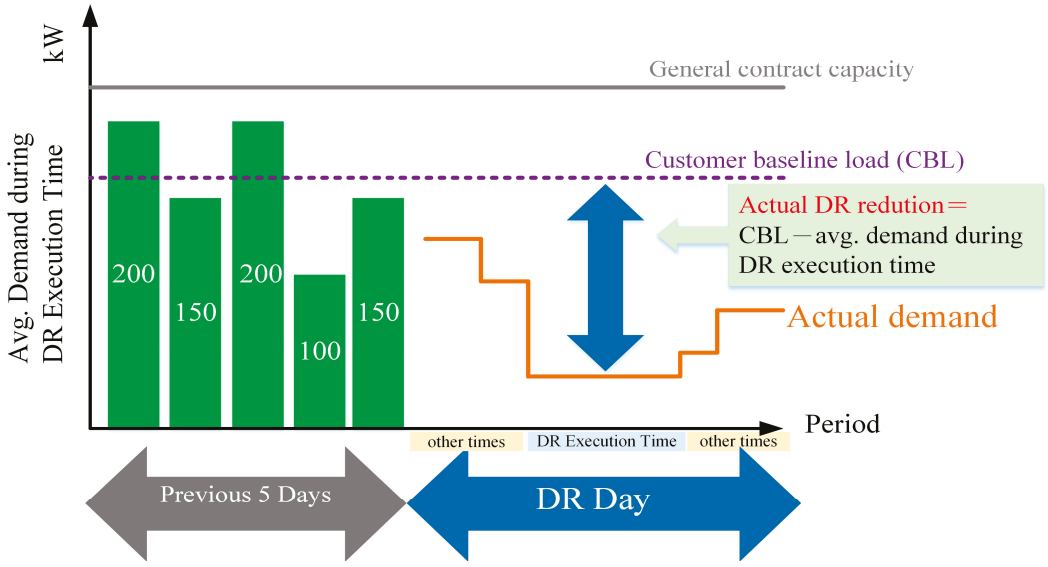


Figure 1. Conceptual illustration to calculate load reduction by DR users.

2.2. Equivalent Groups of Multiple DR Users

In the DB mechanism, customers with larger load reduction capability can participate directly in the bidding market, while customers with less load reduction capability need to be integrated through an aggregator. Because most of the DB participants have relatively limited capability to perform load reduction, it is difficult for them to participate in the bidding process with thermal generator units of Taipower. A DR user formed via the integration of participants through an aggregator, which not only enhances the competitivity of individuals but also benefits the systematic allocation. Therefore, the formation of DR users enables the equal demonstration of the bidding procedure for participants with various levels of load reduction capabilities. As illustrated in Figure 2, there are *LP* levels of prices corresponding to the equivalent DR segments bidding with the same prices. The quotes of DR users in the day-ahead market are ranked from low to high. Taipower groups DR users with similar bidding prices into equivalent segments, each representing a defined amount of load reduction from a DR unit [32]. As a result, the DR bidding structure is organized into six price levels, with each level corresponding to a specific DR segment bidding at the same price. This process enables the unit to possess competitive DR capability compared with the existing thermal generator units in the bidding procedure.

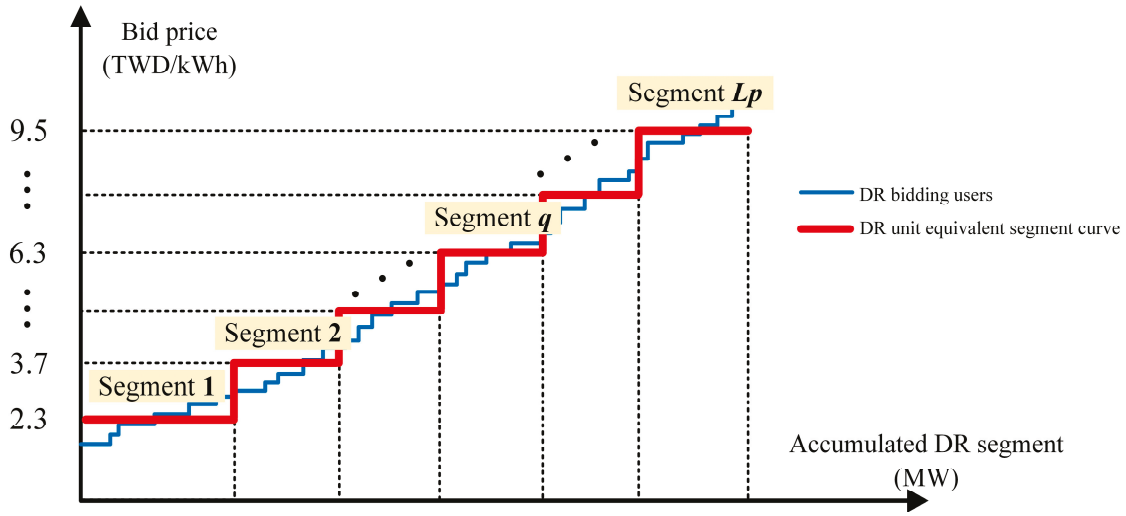


Figure 2. The segmented bidding prices and reduction capacity for an equivalent DR unit.

2.3. Determination of the Bid Winner

Taipower has built the DB mechanism to allow the substantial small and medium-scale DB participants to form a DR unit in the design of power dispatch strategy. The DR user groups will win the bid when their prices are lower than the marginal price of the thermal generator unit. As presented in Figure 3, DR user group #1 and #2 win the bid and perform load reduction in place of starting up thermal generator D. Similarly to the energy market, there is an ancillary service market open for DR users to participate in the bidding mechanism [32]. Figure 4 represents an illustration of the determination of the dealing prices for the bid winners. In the ancillary service bidding framework, Taipower will decide the total required amount for ancillary service in advance. Next, the ancillary service demand will be satisfied by the DR users, matched from low bidding prices to high ones. Unlike DB for generation, the price of the last bidding winner (DR user x) in ancillary service is applied for all the bidding winners, regardless of the initial bidding prices [33]. As a result, unit commitment and economic dispatch play the crucial roles in the DB mechanism. It is necessary to develop a software tool to determine whether the equivalent DR unit wins the bid and tell the corresponding users to perform load reduction. Importantly, this tool can help Taipower to implement the DB mechanism and provide a better understanding for system operators of interactions between the players.

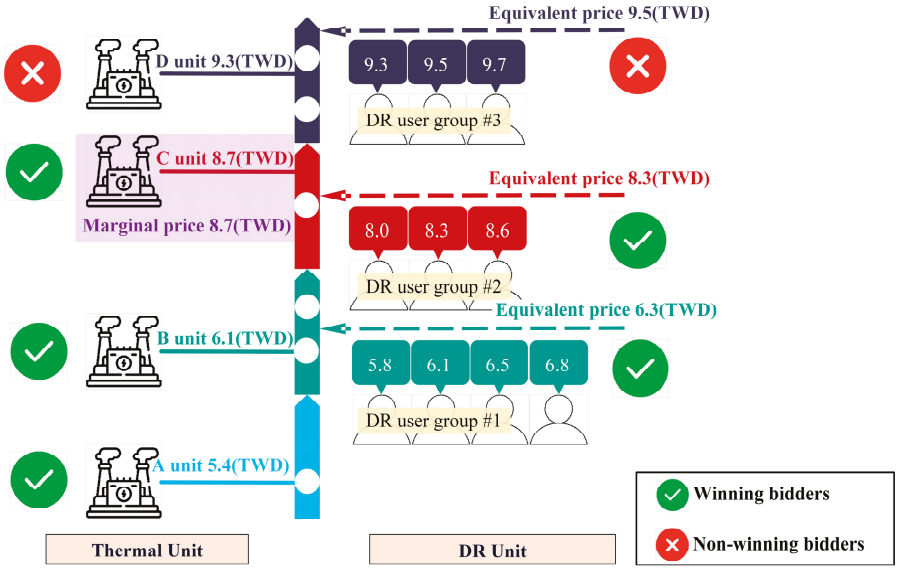


Figure 3. Conceptual illustration for the DB mechanism.

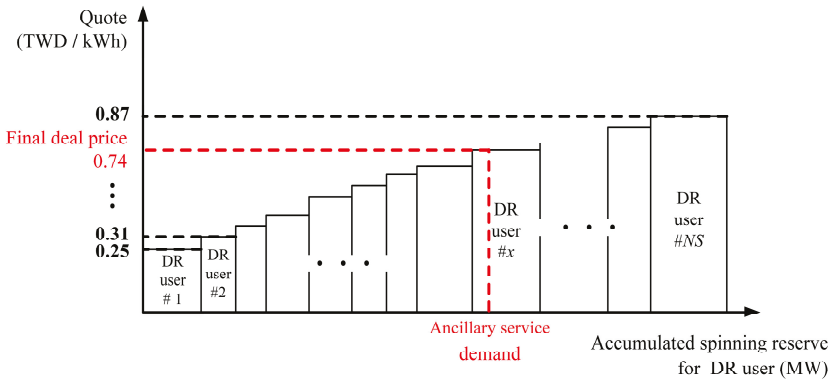


Figure 4. Conceptual illustration of DB mechanism for the ancillary services market.

3. Problem Description Considering Multi-Area Scenario

Taiwan's power system can be modeled as a simplified network including northern, central, and southern areas, as shown in Figure 5. It is noted that the northern thermal units take 30% of power generation, but the northern load demand consumes almost 50% of the total load [34]. Since the severe unbalance occurs in the northern area, the transmission of power flow among areas becomes significant and even results in congestion of power lines. The allocation of spinning reserve will also be affected, which brings the issues of instability and lack of robustness for the power system. To strengthen system security and reliability, ensuring adequate emergency reserves distributed among multiple thermal units in each area significantly improves the ability of system to respond to frequency deviations and load pick-up following a contingency, particularly in isolated systems like the Taiwan power system. Each thermal unit is subject to generation limits (both upper and lower) and can provide only a restricted amount of spinning reserve, based on its ramping capacity. The spinning reserve requirements for each area can be met by the combined sum of local and imported reserves during forced outages of thermal generators. The local reserve in each area is determined to ensure an adequate amount of reserve capacity. As a result, tie-lines are responsible for transmitting both generation and reserve simultaneously. To enhance the transparency and the efficiency of the day-ahead market for DB mechanism, this paper integrates the DB platform of energy and ancillary service market with the actual bidding prices and information from the DR users, which enables the associated DR users to compete with the thermal units. Through the proposed optimum dispatch algorithm, the resulting day-ahead procurement quantity and the price can be obtained.

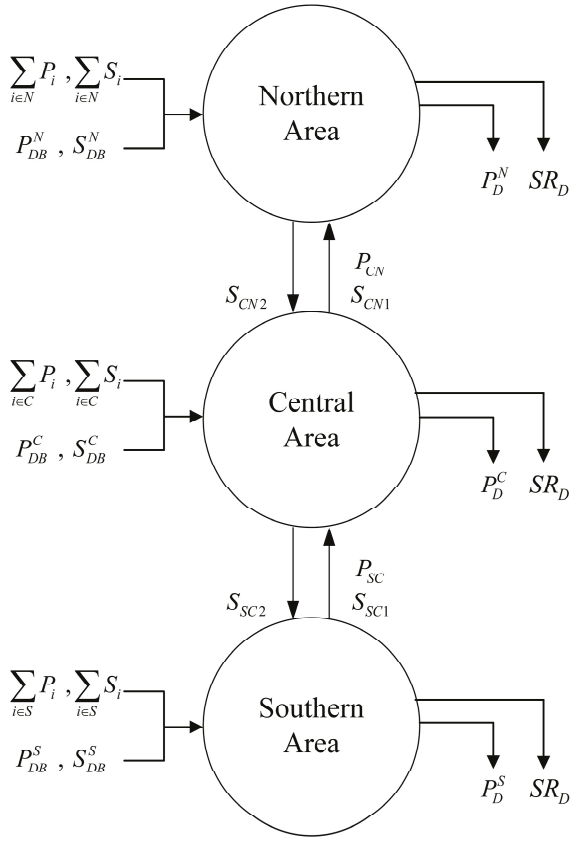


Figure 5. A simplified model of the investigated power system.

Under the DB framework of the day-ahead market, the purpose of optimal multi-area demand–thermal coordination dispatch is to allocate the required generation and reserve capacity to thermal units and equivalent DR units. Namely, the goal is to minimize the total

dispatch cost, subject to the satisfaction of regional load and reserve capacity requirements, the upper and lower output limits of the thermal unit, the coupling restrictions of reserve capacity for the thermal unit, and the operational limitations of the DR units. The objective function (1) includes two terms: the operation cost of thermal units and the summation of energy and spinning reserve cost of DR unit. The mathematical model is represented as follows:

Objective function

$$Minimize\ TC = \sum_{i=1}^{NT} F_i(P_i) + \sum_{a \in N,C,S} F_{DB}^a(P_{DB}^a) + G_{DB}^a(S_{DB}^a) \tag{1}$$

3.1. Calculation of the Cost for Thermal Unit and DR Unit

Generally, the fuel cost of thermal units can be represented by a second-order, strictly increasing function, shown in (2) [35]. The spinning reserve cost of thermal units from the public utility is almost negligible.

$$F_i(P_i) = \alpha_i + \beta_i P_i + \gamma_i P_i^2 \tag{2}$$

The quotes of DR users in the day-ahead market are ranked from low to high. The participants with low capacity are aggregated into a DR user. Then, the DR users are aggregated into an equivalent DR unit with multiple segments to simplify the calculation. In this way, substantial small and medium-scale DB users are grouped based on bidding prices to form a multi-segment equivalent DR unit for energy generation. Figure 6 represents a conceptual illustration to calculate the cost of DR unit. Since the price of the bid winner in the DR unit for energy generation is based on the user's bidding price, the cost of the DR unit for energy generation with P_{DB}^a load reduction is calculated as

$$F_{DB}^a(P_{DB}^a) = F_{DB1}^a + F_{DB2}^a \ \ a \in N, C, S \tag{3}$$

where

$$F_{DB1}^a = \sum_{q=1}^{\ell-1} \sum_{j=1}^{NP_q^a} BP_{q,j}^a \times CP_{q,j}^a \tag{4}$$

$$F_{DB2}^a = \sum_{j=1}^{m-1} BP_{\ell,j}^a \times CP_{\ell,j}^a + (P_{DB}^a - P_{DB,\ell,m-1}^a) \times CP_{\ell,m}^a \tag{5}$$

$$P_{DB,\ell,m-1}^a \le P_{DB}^a \le P_{DB,\ell,m}^a \tag{6}$$

$$P_{DB,\ell,m-1}^a = \sum_{q=1}^{\ell-1} \sum_{j=1}^{NP_q^a} BP_{q,j}^a + \sum_{j=1}^{m-1} BP_{\ell,j}^a \tag{7}$$

Since the price of bid winner in DR unit for spinning reserve is based on the last user's bidding price, the cost of DR unit for spinning reserve with S_{DB}^a reserve capacity for the user of bid winner is calculated as

$$G_{DB}^a(S_{DB}^a) = S_{DB}^a \times CS_k^a \ \ a \in N, C, S \tag{8}$$

where

$$S_{DB,k-1}^a \le S_{DB}^a \le S_{DB,k}^a \,, k \in 1, 2, \ ..., \ NS^a \tag{9}$$

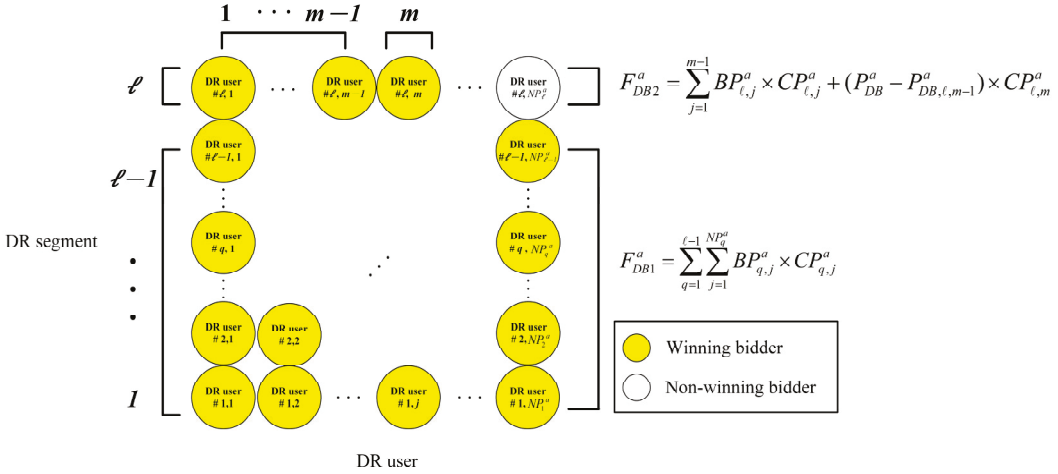


Figure 6. Conceptual illustration to calculate the cost of DR unit.

3.2. Constrains for System Power Dispatch

- Requirement of power balance for each area:

$$\sum_{i \in N} P_i + P^N_{DB} + P_{CN} = P^N_D \tag{10}$$

$$\sum_{i \in C} P_i + P^C_{DB} + P_{SC} - P_{CN} = P^C_D \tag{11}$$

$$\sum_{i \in S} P_i + P^S_{DB} - P_{SC} = P^S_D \tag{12}$$

- Requirement of spinning reserve for each area:

$$\sum_{i \in N} S_i + S^N_{DB} + S_{CN1} \geq SR_D \tag{13}$$

$$\sum_{i \in C} S_i + S^C_{DB} + S_{CN2} + S_{SC1} \geq SR_D \tag{14}$$

$$\sum_{i \in S} S_i + S^S_{DB} + U_{SC2} \geq SR_D \tag{15}$$

- Transmission capacity constraints for power flow among the areas:

$$P_{CN} + S_{CN1} \leq P^{\max}_{CN} \quad if\ P_{CN} > 0 \tag{16}$$

$$|P_{CN}| + S_{CN2} \leq P^{max}_{CN} \quad if\ P_{CN} < 0 \tag{17}$$

$$P_{SC} + S_{SC1} \leq P^{max}_{SC} \quad if\ P_{SC} > 0 \tag{18}$$

$$|P_{SC}| + S_{SC2} \leq P^{max}_{SC} \quad if\ P_{SC} < 0 \tag{19}$$

3.3. Constraints for Thermal Units

- Upper limit of spinning reserve for the thermal unit:

$$S^{\max}_i = d\% \times P^{\max}_i \tag{20}$$

- Spinning reserve contribution of thermal unit:

$$S_i = \min\{S_i^{\max}, P_i^{\max} - P_i\} \tag{21}$$

- Output generation constraint of thermal unit:

$$P_i^{\min} \le P_i \le P_i^{\max} \tag{22}$$

- Constraints of the energy and reserve capacity:

$$P_i + S_i \le P_i^{\max} \tag{23}$$

3.4. Constraints for DR Unit and DR Users

- Constraint of DR unit for energy generation:

$$0 \le P_{DB}^{a} \le P_{DB}^{a,\max} \quad a \in N, C, S \tag{24}$$

- Constraint of a DR user for energy generation:

$$BP_{q,j}^{a,\min} \le BP_{q,j}^{a} \le BP_{q,j}^{a,\max}, \text{ when winning the bid} \tag{25}$$

$$BP_{q,j}^{a} = 0, \text{ others} \tag{26}$$

- Constraint of bidding price of a DR user for energy generation:

$$0 \le CP_{q,j}^{a} \le CP_{DB}^{\max}, \quad q = 1, 2, ..., Lp, \quad j = 1, 2, ..., NP_q^a \tag{27}$$

- Constraint of a DR unit for spinning reserve:

$$0 \le S_{DB}^{a} \le S_{DB}^{a,\max} \quad a \in N, C, S \tag{28}$$

- Constraint of a DR user for spinning reserve:

$$BS_k^{a,\min} \le BS_k^{a} \le BS_k^{a,\max}, \text{ when winning the bid} \tag{29}$$

$$BS_k^{a} = 0 \text{ , others} \tag{30}$$

- Constraint of the bidding price of a DR user for spinning reserve:

$$0 \le CS_k^{a} \le CS_{DB}^{\max}, \text{ k} = 1, 2, ..., NS^a \tag{31}$$

4. The Modified Direct Search Method

DSM is a type of deterministic search algorithm characterized by its simple structure, easy implementation, fast convergence speed, and good convergence quality compared to other general heuristic algorithms. In addition, it is capable of handling various types of cost functions of thermal units to deal with ED problems. However, it has the disadvantage of being prone to falling into local optima. To overcome the shortage of conventional DSM, an improved DSM has been developed with a direct search procedure for multiple points to enhance the exploration and exploitation at the same time, which leads to a higher probability of obtaining the global optimal solution [36]. In consideration of the multi-area DB platform, system operators must simultaneously manage the generation capacity, reserve capacity, and inter-regional transmission capacity constraints for a large number of DB users. The complexity of these constraints makes it challenging to apply traditional DSM or SDSM approaches. To address the optimization problem of combining

generation capacity and reserve capacity scheduling on a multi-area bidding platform, this paper introduces a Hybrid Direct Search Method (HDSM). The complex scheduling problem then can be decomposed into two parts: namely, the traditional DSM is used to coordinate the scheduling of system thermal power units and DR units for each area, serving as the primary problem, meanwhile, the DQD method optimizes spinning reserve allocation for each area and inter-regional sharing of the spinning reserve, serving as the secondary problem. By coordinating between these two problems, the overall dispatch cost can be minimized.

Notably, inequality constraints in this study are handled differently. Equations (10)–(12) and (20)–(31) can be controlled using a direct search procedure. On the other hand, inter-regional flow constraints (16)–(19) and inter-regional reserve capacity supply–demand constraints (13)–(15) can be appropriately controlled through penalty function techniques. To account for transmission capacity limit violations (16)–(19) and area spinning reserve requirement violations (13)–(15), the total operating cost is increased by non-negative penalty terms, PC_1 and PC_2, which penalize any violations of constraints. These penalty terms are directly proportional to the extent of the violations and are zero when no violations occur. The values of PC_1 and PC_2 are selected to be sufficiently large to make any constraint violations undesirable in the final solution. Consequently, the dispatch cost and penalty cost can be combined to form a new objective function called TC_A. Further details are explained as follows:

$$TC_A = TC + PC_1 + PC_2 \tag{32}$$

where

$$PC_1 = \sum_{a \in N,C,S} PF \times \frac{(SR_D - SR^a_{act})}{SR_D} \times H(SR_D - SR^a_{act}) \tag{33}$$

$$PC_2 = \sum_{l \in CN,SC} PF \times \frac{(P^{act}_l - P^{\max}_l)}{P^{\max}_l} \times H(P^{act}_l - P^{\max}_l) \tag{34}$$

$$P^{act}_l = P_l + S_{l1} \quad if\ P_l > 0 \quad l \in CN, SC \tag{35}$$

$$P^{act}_l = |P_l| + S_{l2} \quad if\ P_l < 0 \quad l \in CN, SC \tag{36}$$

Here,

$H(x)$	unit step function
PF	penalty coefficient
PC_1	penalty for the violation of the requirement of area spinning reserve
PC_2	penalty for the violation of the limits of the transmission line
SR_D	spinning reserve requirement at each area
SR^a_{act}	actual supply of spinning reserve at each area
$P^{\max}_l$	maximum power flow between area l where $l \in CN, SC$
P^{act}_l	actual power flow between area $l$where $l \in CN, SC$

The flowchart of the proposed HDSM is shown in Figure 7. In the searching process, the DSM enables the coordination of multi-area demand–thermal generation dispatch and handles constraints properly. At each possible step, the DQD is used to minimize the total reserve cost when the preliminary solution of energy dispatch is frozen. Through the iterations of the proposed method, the minimum dispatch cost can be obtained. Unlike metaheuristics with a stochastic nature and multiple parameters to be determined in the algorithm, the proposed method is characterized by its simplicity and merely two parameters need to be set, namely initial step size (SP_1) and the reduced factor (RF). Particularly, it is able to cope with many coupling conditions and equality or inequality constraints. Below is a detailed explanation of the computational steps in HDSM.

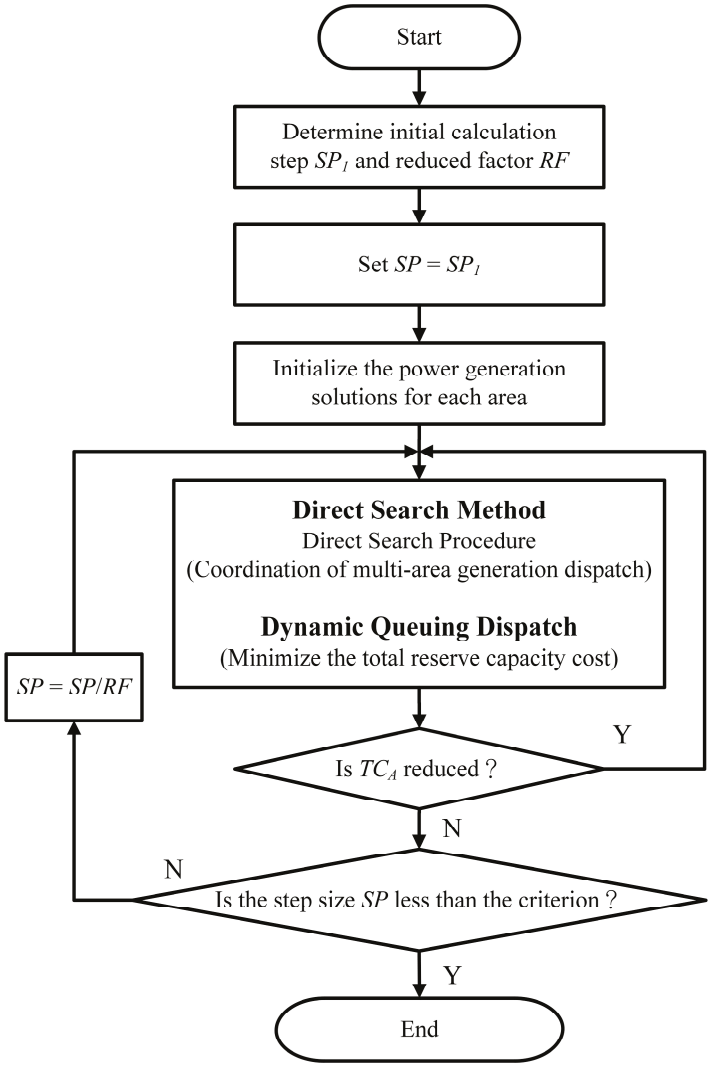


Figure 7. HDSM flowchart.

Step 1: Obtain the data from thermal units and DB users.
Step 2: Group the equivalent DR units in each area based on DB participant's data.
Step 3: Set initial calculation step SP_1 and reduced factor RF.
Step 4: Set $SP = SP_1$.
Step 5: Initialize the power generation solutions for each area.
Step 6: Perform the DSM with step SP to optimize the scheduling of generation and handle additional constraints properly for multiple areas.
Step 7: At each possible step SP, the DQD is applied to optimize the scheduling of reserve capacity for multiple areas.
Step 8: Is the step size SP less than the criterion? Yes, proceed to the next step. Otherwise, $SP = SP/RF$, and return to Step 6.
Step 9: Output the scheduling results and the bid winner in each area. The winning customers in each area are then determined by the area's marginal prices.

4.1. Establishing the Equivalent DR Unit in Individual Area

As mentioned in Section 2.2, to make DR users competitive with the existing thermal generator units in the bidding procedure, DR users are required to form into the equivalent groups as a DR unit. The quoted prices of DR users are arranged in order and divided into LP segments. However, instead of using the equivalent quote introduced in the Taipower

DR bidding mechanism, this paper employs the actual prices of DR users to carry out the simulation to reflect the actual cost. Table 1 provides further explanation on the establishment of an equivalent DR unit for a specific area. The DR users are grouped to simplify the computation. Assuming that there are 12 DR users participating in bidding, and the difference between the highest (TWD 9.80/kWh) and lowest (TWD 6.60/kWh) quoted prices of the DR user is evenly distributed into four segments, namely [6.6, 7.4, 8.2, 9.0]. In this way, the DR users with similar quoted prices are allocated to the same segment, for example, Segment 4 has three customers (#10 to #12) with close quoted prices. Finally, the equivalent bid quantity and bidding cost for each segment can be calculated based on the actual bidding information of DR users within each segment. In fact, the calculation can be simplified by using the equivalent segment. The number of total segments has no effect on the computation results.

Table 1. Accumulated information of an equivalent DR unit.

Index of DR User	Load Reduction Capability (kW)	Accumulated Load Reduction (kW)	Price Quote (TWD/kWh)	Equivalent Segment Number	Accumulated Cost (TWD)	Load Reduction in Segment (kW)
12	3.6	75.2	9.80	4	607.5	16.2
11	4.4	71.6	9.60			
10	8.2	67.2	9.20			
9	3.2	59	8.88	3	454.5	12.2
8	2.8	55.8	8.30			
7	6.2	53	8.25			
6	9.0	46.8	8.12	2	351.7	25.8
5	8.0	37.8	8.06			
4	5.6	29.8	7.82			
3	3.2	24.2	7.60			
2	12.4	21	7.20	1	146.0	21.0
1	8.6	8.6	6.60			

4.2. Initial Solution Estimate

In order to solve the problem of minimizing the objective function TC_A, HDSM must generate an initial solution and perform a series of variable steps in solutions to search in the direction that yields the maximum cost reduction. Since an appropriate initial solution can improve the convergence properties of the subsequent search procedure, this paper designs the procedure to obtain the initial solutions as follows:

Step 1: Allocate a portion of the load to the minimum generation level of units in each area.
Step 2: Dispatch load demand in sequence according to the average cost of generation for all units. The units with lower average costs have priority to supply until the system load demand is met.
Step 3: While maintaining the generation level of the units, optimize the dispatch of multi-area spinning reserve using the DQD method introduced in Section 4.3. If the system violates constraint conditions, evaluate the penalty costs PC_1 and PC_2.
Step 4: Calculate the initial dispatch cost, which includes the generation cost of thermal power units, bidding costs of DR units for power reduction and ancillary service, as well as the penalties.

In this way, the initial solutions for each area can be obtained based on the average bidding costs of each unit (including thermal units and DR units of energy generation).

4.3. Direct Search Procedure to Solve Multi-Area Power Generation Dispatch

Once an initial solution is determined, the technique of DSM can explore the optimal solutions that minimize the total dispatch cost (TC_A). The primary feature of the direct search procedure is that, at each step during the searching process, only a pair of units are selected for modification, effectively controlling additional constraint conditions. These constraints include regional power supply–demand balance, generation limits for units, and coupling relationships between the generation level of thermal units and their reserve capacity, all of which can be handled through the direct search procedure. The calculation steps are further explained as follows:

Step 1: Without violating the power generation limits of the units, the incremental costs (IC_i and IC_a) and the decremental costs (DC_i and DC_a) for each unit can be calculated when there is an increment or decrement for the adjustment of SP power generation, as shown in Equations (37) to (40).

Incremental cost of thermal units: $$IC_i = \frac{F_i(P_i + SP) - F_i(P_i)}{SP} \qquad i = 1, 2, \ldots, NT \qquad (37)$$

Incremental cost of DR units: $$IC_a = \frac{F^a_{DB}(P^a_{DB} + SP) - F^a_{DB}(P^a_{DB})}{SP} \qquad a \in N, C, S \qquad (38)$$

Decremental cost of thermal units: $$DC_i = \frac{F_i(P_i) - F_i(P_i - SP)}{SP} \qquad i = 1, 2, \ldots, NT \qquad (39)$$

Decremental cost of DR units: $$DC_a = \frac{F^a_{DB}(P^a_{DB}) - F^a_{DB}(P^a_{DB} - SP)}{SP} \qquad a \in N, C, S \qquad (40)$$

Subject to $$P_i + SP \le P_i^{\max}, \; P_i - SP \ge P_i^{\min} \qquad i = 1, 2, \ldots, NT \qquad (41)$$

$$P^a_{DB} + SP \le P^{a,\max}_{DB}, \; P^a_{DB} - SP \ge 0 \qquad a \in N, C, S \qquad (42)$$

Step 2: All the pairs of units are examined to check if there is any improvement. If there is no improvement, then stop; otherwise, go to step 3.

Step 3: A pair of units are chosen to perform adjustments to reach the maximum cost reduction. That is, a unit x with the minimum incremental cost ICx is chosen to increase its output by the specific SP adjustment. Simultaneously, a unit y (where $x \neq y$) with the maximum decremental cost DCy is chosen to reduce its output by the specific SP adjustment. In this way, the net power balance is satisfied and the dispatch cost can be reduced. It should be noted that all units stay unchanged except x and y units. Subsequently, the DQD procedure is then proceeded to determine the optimal allocation of spinning reserve and satisfy the spinning reserve in each area.

Step 4: The chosen x, y pair will adjust their output by the predefined step size SP, if it does not violate power generation limits. In this process, only the incremental cost for unit x and the decremental cost for unit y will be recalculated.

Step 5: Go to step 2.

4.4. DQD to Solve Multi-Area Spinning Reserve Dispatch

In this study, the dispatch of spinning reserve in areas is determined by DQD, which is proceeded after a preliminary power generation dispatch is obtained by DSM. When thermal units have sufficient capability to provide spinning reserve, thermal units, which are owned by the Taipower company, will be utilized first because the cost of the reserve

capacity of the thermal units can be almost negligible. However, when the reserve capacity requirement cannot be satisfied, the system may either change the dispatch pattern of the thermal units, or purchase from the ancillary service bidding platform to meet the demand for spinning reserve in the areas. In other words, once the power generation dispatch is determined, the insufficient reserve capacity can be optimized through the DQD method to minimize the purchasing cost of the spinning reserve. As a result, when it comes to purchasing the ancillary services of the system, it is not only about selecting a DR user for spinning reserve with lower quote in each area, but also considering the capacity of transmission between areas. The detailed calculation steps of DQD are given as follows:

Step 1: Obtain the available capacity of spinning reserve that thermal units are able to provide.
Step 2: Initialize the purchase of spinning reserve from ancillary services market.
Step 3: The spinning reserve demand in each area can be satisfied by adding up the spinning reserve of that area itself and the spinning reserve that other areas can provide without violating inter-regional flow constraints.
Step 4: If the requirement for spinning reserve is satisfied in each area?
- Yes, go to step 7.
- Otherwise, continue to Step 5.

Step 5: If there is a congested area?
- If there is no congestion, the system selects the DR user of ancillary service with the lowest bid for fulfilling the system reserve capacity. In addition, it takes the essential factors into consideration, including the bidding quantity of the DR user, the availability of inter-regional transmission capacity, and the demands for reserve capacity in that area to determine the actual purchase quantity of the DR user for ancillary service as given in (43)–(45).

$$A = \min\left\{BS_k^{a,\max},\ P_l^{\max} - P_l^{act},\ SR_D - SR_{act}^a\right\},\ l \in CN, SC\ ,\ \ a \in N, C, S \tag{43}$$

$$BS_k^a\ =\ A,\ if\ BS_k^{a,\min}\ \leq\ A\ \leq\ BS_k^{a,\max} \tag{44}$$

$$BS_k^a\ =\ 0\ ,\ if\ 0\ <\ A\ <\ BS_k^{a,\min} \tag{45}$$

- If congestion occurs, the congested area allocates the required spinning reserve capacity to the DR user of ancillary service based on their bidding prices from low to high until the reserve capacity demand is satisfied.

Step 6: Back to Step 3.
Step 7: Calculate the purchase cost of reserve capacity and check the reserve capacity requirements in each area as well as the inter-regional flow constraints. If any violation of the constraints occurs, impose a penalty cost of PC_1 and PC_2.

An example of the dispatch result by DQD is explained in Figure 8. The maximum power flow capacity of the transmission line is 3000 MW. Firstly, the DR user with the lowest quote for spinning reserve is selected from the three areas. Assume that this user is from the central area, denoted as x, and its bid quantity is 12 MW, i.e., $BS_x^{C,\max} = 12$ MW. Next, consider the supply and demand situation for spinning reserve capacity in the central area, where the demand is $SR_D = 900$ MW and the supply is $SR_{act}^C = 850$ MW. Therefore, there is a shortage of 50 MW in the central area. Subsequently, the available capacity for power flow between areas is assessed. Although there is a surplus of 2350 MW (3000 MW–650 MW) from the central area to the southern area, there is only 8 MW available from the central area to the northern area due to congestion between areas. Finally, the DQD would determine only 8 MW purchased from the DR user x in the central area, as the lower price reserve capacity in the central area cannot be shared with the northern area.

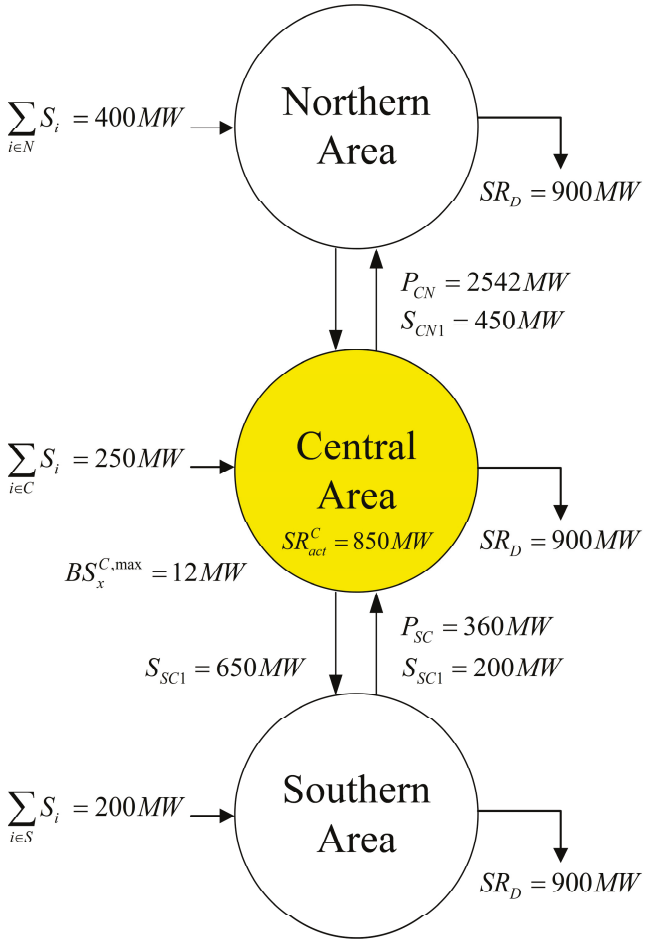


Figure 8. An example of the dispatch result by DQD.

4.5. Determination of Optimal Load Reduction and Optimal Spinning Reserve

Since DR users in the energy market (or in the ancillary services market) are numerous and have limited capability for load reduction, they are typically grouped by aggregators for the bidding. The power company then ranks the equivalent DR users in each area based on the bidding prices, establishing the equivalent DR units for that area. To ensure fair competition among participants, these equivalent DR units must participate in the day-ahead market and compete with the thermal units for scheduling and ED. The impacts of tie-line congestion and area spinning reserve requirements must be consistently reflected in the marginal cost in each area. When transmission capacity and area spinning reserves are not constrained, all generation units, except those operating at their upper or lower generation limits, will operate at the same incremental cost. However, in areas connected by congested tie-lines, differing area marginal costs may arise, but units within each area will maintain the same incremental cost unless constrained by their generation limits. The determination of whether a DR user can win the bid is derived from the ED. When the bidding price of a DR user is lower than the marginal price of the existing thermal power units in the group, it can be considered as the winner of the bid. The proposed HDSM for the multi-area bidding platform can determine the optimal bidding results for equivalent DR units in each area. Furthermore, based on the marginal prices in each area, it can further decide the actual quantities of load reduction for DR users. Simultaneously, considering the supply and demand situation for spinning reserve capacity in each area, it can also determine the optimal bidding results of the DR unit for ancillary service. The proposed algorithm is able to assist the current DB framework in both the energy market and ancillary services market to obtain the optimal load reduction ($P^{*,a}_{DB}$) and optimal spinning reserve ($S^{*,a}_{DB}$) for the demand-side management units. The objective of

area marginal cost is to adjust energy costs to reflect their network properties of Taiwan power system and give correct signals or provide incentives for DR users to avoid undesirable heavy flows among the three areas.

5. Simulation Results and Case Study

In order to demonstrate the feasibility of the multi-area DB platform and the dispatch strategy proposed in this paper, simulations have been carried out with different numbers of thermal units in comparisons. For simplicity, the fuel cost function for each thermal unit in the study has been approximately represented by a quadratic function. The parameter selection in HDSM will not affect the optimal solution when the generator incremental cost curves are monotonically increasing. However, the HDSM with large SP_1 and small RF is usually commended to make the search effective. The parameters of HDSM are selected as SP_1 = 80 MW, RF = 2, $PF = 10^5$, and the convergence criteria is 0.1 MW. The dispatch strategy developed for this study is written in FORTRAN and simulations were carried out on a personal computer (ASUS X512F) with an Intel(R) Core(TM) i5-10210 CPU @ 1.6~4.2 GHz environment. The analysis of case study results is now explained as follows.

5.1. Case Study 1: A System with Four Thermal Units

To validate the feasibility and the effectiveness of the proposed simulation platform and HDSM dispatch algorithm, a scenario of four thermal units is first discussed. Meanwhile, the ancillary service bidding platform is neglected to focus on analyzing the effect of load reductions by DR users on the results of power dispatch. In Case Study 1, the system load demand and requirement for spinning reserve are 1200 MW and 150 MW, respectively. The thermal unit data are presented in Table 2 [37]. It is assumed that the maximum reserve capacity that the thermal unit can provide is 10% of its rated output. On the other hand, it is assumed that there are 15 DR users participating in the bidding platform, with their quotes and availability of load reduction presented in Table 3. They are grouped into six equivalent sections based on their bidding price and formed as a DR unit to compete with the thermal units in the energy market.

The purpose of Case Study 1 is to investigate the impacts of the participation of DR users on the power dispatch. Table 4 illustrates a comparison of the dispatch results with and without the participation of DR users. In Example 1.1, when the system does not include DR users, the dispatch cost is approximately USD 11,310.29, with a system marginal price as high as USD 9.20 per MW. On the contrary, Example 1.2 shows that the participation of DR users is able to reduce the system's dispatch cost to USD 11,142.47. The system can save approximately USD 167.82 (USD 11,310.29–USD 11,142.47) in generation costs due to the participation of DR users in bidding in the energy market. Additionally, the system marginal price decreases to USD 8.99 per MW, which means that all DR users bidding below USD 8.99 are bid winners who will perform corresponding load reduction. Namely, the optimal capacity for the DR unit is 146 MW, with users numbered from #1 to #11 winning the bids. The actual load reduction by DR users can be referred to in Figure 9. The detailed allocation of power dispatch and spinning reserve capacity for thermal units are given in Table 5. Table 6 presents a convergence history of the proposed HDSM, including iteration counts, variation steps, and the dispatch costs for Example 1.2. This table demonstrates that the proposed method exhibits good convergence properties, and the optimum result can be obtained in short execution times below 0.1 s.

Table 2. Data of thermal units.

Index of Thermal Unit	P_i^{max}(MW)	P_i^{min}(MW)	α (USD)	β (USD/MW)	γ (USD/MW^2)
1	600	150	561	7.92	0.001560
2	200	50	78	7.97	0.004820
3	400	100	310	7.85	0.001942
4	340	70	250	7.50	0.001810

Table 3. Information about the DR users and their quotes and capabilities in the segments.

Index of DR User	Availability of Load Reduction (MW)	Accumulated Load Reduction (MW)	Price Quote (USD/MWh)	Equivalent Segment Number	Accumulated Cost (USD)	Load Reduction in Segment (MW)
15	7	180	9.86	6	1477.6	13
14	6	173	9.47			
13	9	167	9.15	5	1351.8	21
12	12	158	9.06			
11	15	146	8.85	4	1160.7	28
10	13	131	8.64			
9	17	118	8.41	3	915.7	29
8	12	101	8.13			
7	11	89	7.82	2	675.1	36
6	15	78	7.79			
5	10	63	7.71			
4	13	53	7.65	1	395.2	53
3	14	40	7.57			
2	12	26	7.34			
1	14	14	7.26			

Table 4. Comparison of the dispatch results with and without DR users.

Example	DR Users	Marginal Price (USD/MWh)	DR Unit (MW)	Cost (USD/h)	Bid Winner	Total Cost (USD/h)
1.1	Without DR users	9.20	---	---	---	11,310.29
1.2	with DR users	8.99	146.00	1161	1~11	11,142.47

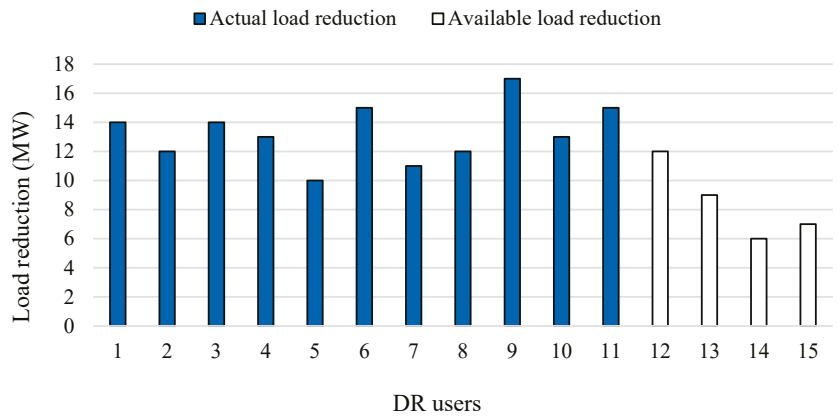


Figure 9. Actual load reduction by DR users.

Table 5. Actual supply by thermal units.

Example	DR Users	Thermal Unit (MW)							
		P_1	S_1	P_2	S_2	P_3	S_3	P_4	S_4
1.1	Without DR users	412.40	60	128.29	20	349.29	40	310.00	30
1.2	With DR users	343.75	60	106.07	20	294.10	40	310.00	30

Table 6. Convergence history of Example 1.2.

Variation Step	Iteration	DR Unit		Total Cost (USD/h)
		Load Reduction (MW)	Cost (USD/h)	
Initial soluiton	---	180	1477.63	11,257.95
SP_1 = 80 MW	2	180	1477.63	11,175.99
SP_2 = 40 MW	2	140	1107.62	11,157.15
SP_3 = 20 MW	2	140	1107.62	11,146.44
SP_4 = 10 MW	2	150	1196.96	11,145.66
SP_5 = 5 MW	2	145	1151.87	11,143.94
SP_6 = 2.5 MW	2	147.5	1174.31	11,143.23
SP_7 = 1.25 MW	2	146.25	1162.98	11,142.81
SP_8 = 0.625 MW	1	146.25	1162.98	11,142.65
SP_9 = 0.3125 MW	3	145.93	1160.16	11,142.56
SP_{10} = 0.15625 MW	2	146.09	1161.56	11,142.52
SP_{11} = 0.078125 MW	1	146.00	1160.86	11,142.45

5.2. Case Study 2: A System of Two Areas with Four Thermal Units

Followed by Section 5.1, Case Study 2 considers two areas with four identical thermal units. The overview of the Case Study 2 is given in Table 7, where thermal unit 1 and 2 are located at Area A and thermal unit 3 and 4 are located at Area B. The maximum capacity of the transmission line for power flow is 300 MW. The system load demand and requirement for spinning reserve are 1600 MW and 150 MW, respectively. Area A accounts for 70% of the total load demand while Area B accounts for 30% of the total load demand, revealing an unbalanced situation of demand and supply in the areas. To solve the issues, multi-area demand–thermal coordination dispatch is investigated, with the energy bidding platform and the ancillary service bidding platform taken into account. The quotes and availability of DR users participating in the energy bidding platform are given in Table 3. The quotes and availability of DR users participating in the ancillary service bidding platform are presented in Table 8. It is assumed that Area A and Area B share the same bidding data of DR users, as given in Tables 3 and 8.

The purpose of Case Study 2 is to investigate the impacts of a transmission constraint on the power dispatch. Table 9 illustrates a comparison of the dispatch results with and without the consideration of the power transmission constraint. The minimum power reduction and the minimum spinning reserve capability for DR users are both assumed to be 1 MW. In Example 2.1, when the system neglects power transmission constraint, each area will have the same marginal cost (USD 9.31/MWh). The optimal load reduction for the DR unit in each area is also the same (i.e., 167 MW), and the bid winners are numbered #1 to #13 DR users. However, when the system considers a 300 MW power transmission

constraint, as demonstrated in Example 2.2, congestion will occur between areas, leading to a higher marginal cost in Area A (USD 9.55/MWh) and a 173 MW load reduction from DR unit. In contrast, Area B requires only 142.53 MW of load reduction with a lower marginal cost of USD 8.85/MWh. Hence, Area A and Area B show different load reduction results for DR users, as shown in Figures 10 and 11.

Table 7. Overview of the Case Study 2.

Area	A	B
Thermal units	#1 and #2	#3 and #4
Load demand (MW)	1120	480
Required spinning reserve (MW)	150	150
DR users for energy generation (Load reduction)	Refer to Table 3	Refer to Table 3
DR users for ancillary service (Spinning reserve)	Refer to Table 8	Refer to Table 8
Load demand (MW)	1600	
Inter-regional power flow constraints (MW)	300	

Table 8. The quotes and availability of DR users in the ancillary service bidding platform.

Index for DR User	**1**	**2**	**3**	**4**	**5**
Price quote (USD/MWh)	0.62	0.68	0.72	0.76	0.79
Available capacity for spinning reserve (MW)	16	10	15	12	13
Index for DR User	**6**	**7**	**8**	**9**	**10**
Price quote (USD /MWh)	0.81	0.83	0.84	0.86	0.89
Available capacity for spinning reserve (MW)	12	11	12	14	15

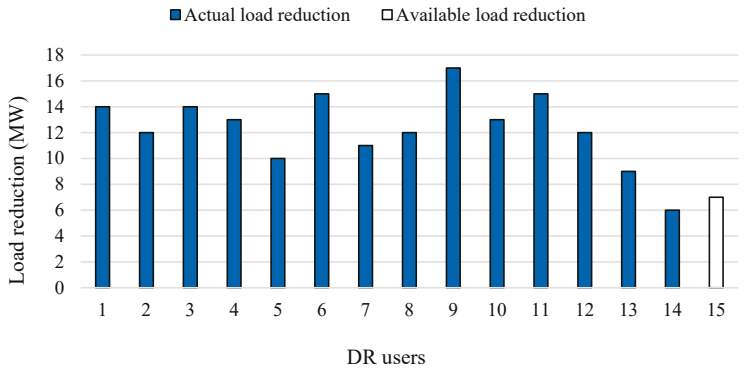


Figure 10. Actual load reduction in DR users in Area A in Example 2.2.

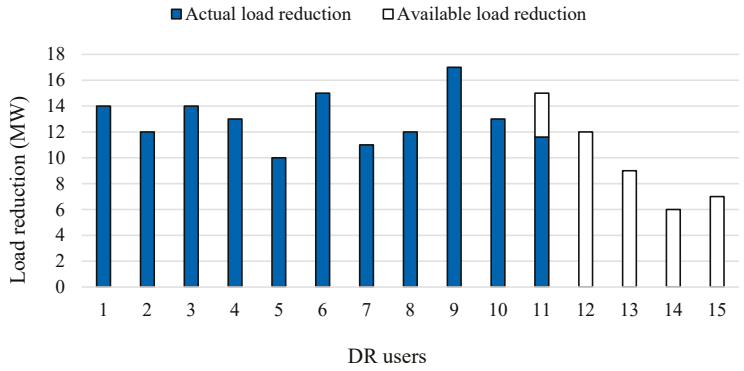


Figure 11. Actual load reduction in DR users in Area B for Example 2.2.

Table 9. Technical and economical results of the Case Study 2.

Example		2.1	2.2
Load demand (Area A/B) (MW)		1120/480	1120/480
Required spinning reserve (Area A/B) (MW)		150/150	150/150
Thermal units	Actual supply of energy generation: Area A (P_1/P_2) (MW) Area B (P_3/P_4) (MW)	446/139 360/320.8	522.93/164.06 257.47/340
	Actual supply of spinning reserve: Area A (S_1/S_2) (MW) Area B (S_3/S_4) (MW)	60/20 40/19.2	60/20 40/0
DR units for energy generation	Availability for load reduction: Area A/B (MW)	180/180	180/180
	Actual supply of load reduction: Area A/B (MW)	167/167	173/142.53
DR units for ancillary service	Availability for spinning reserve Area A/B (MW)	130/130	130/130
	Actual supply of spinning reserve: Area A/B (MW)	10.8/0	30/0
Power transmission line	Maximum limit (MW)	---	300
	Actual flow (MW)	368	260
Economical results			
Marginal prices for energy generation: Area A/B (USD/MWh)		9.31/9.31	9.55/8.85
Bid winner of DR users for energy generation (Area A/Area B)		1~13/1~13	1~14/1~11
Marginal prices for spinning reserve: Area A/B (USD/MWh)		0.62/---	0.72/---
Bid winner of DR users for ancillary service (Area A/B)		1/---	1~3/---
Total cost (USD/h)		14,625.0	14,672.1

Table 9 provides further insights into the dispatch of spinning reserve in each area. When the system ignores power transmission constraints in Example 2.1, thermal units at Area A provide 80 MW of spinning reserve capacity, while thermal units at Area B provide 59.2 MW. The utility company must purchase additional 10.8 MW (from congested Area A) from the ancillary service bidding platform to meet the reserve capacity requirements (150 MW) for each area. However, when the system considers power transmission constraints, as demonstrated in Example 2.2, in order to meet the reserve capacity requirements in Area A (150 MW), the power flow from Area B to Area A is reduced to 260 MW to allow for the transmission of 40 MW of spinning reserve capacity. Simultaneously, thermal units in Area A must adjust their generation to adapt to the decrease in power transmitted from Area B. The utility must also purchase 30 MW (from Area A) from the ancillary service bidding platform. As a result, in Example 2.2, congestion between areas results in an increase in generation costs of approximately USD 47.1/h. Table 10 presents a convergence history of the proposed HDSM, including iteration counts, variation steps, and the dispatch costs for Example 2.2. A penalty calculated by Equation (34), due to violation of power transmission constraint, can be observed at the beginning of the searching process. The time consumption of the search process is approximately 0.1 s. Moreover, since the cost of the thermal units in this study is modeled by a strictly increasing quadratic function, different selections of parameters, namely

SP_1 and RF, do not affect the dispatch results for the proposed HDSM. As shown in Table 11, the simulation results demonstrate the robustness.

Table 10. Convergence history for Example 2.2.

Variation Step	Iteration	Penalty (USD/h)	Total Cost (USD/h)
Initial solution	---	46,666.7	61,370.701
SP_1 = 80 MW	2	0	14,696.362
SP_2 = 40 MW	2	0	14,676.938
SP_3 = 20 MW	1	0	14,673.564
SP_4 = 10 MW	2	0	14,672.511
SP_5 = 5 MW	2	0	14,672.364
SP_6 = 2.5 MW	2	0	14,672.142
SP_7 = 1.25 MW	1	0	14,672.139
SP_8 = 0.625 MW	1	0	14,672.136
SP_9 = 0.3125 MW	1	0	14,672.112
SP_{10} = 0.15625 MW	1	0	14,672.103
SP_{11} = 0.0078125 MW	2	0	14,672.098

Table 11. Comparison of dispatch results under different HDSM parameters for Example 2.2.

SP_1 (MW)	RF	Total Cost (USD/h)
80	8	14,672.1
	4	14,672.1
	2	14,672.1
60	8	14,672.1
	4	14,672.1
	2	14,672.1
40	8	14,672.1
	4	14,672.1
	2	14,672.1

5.3. Case Study 3: A System of Three Areas with 52 Thermal Units

This section considers an actual power system of 52 thermal units in three areas of Taiwan [38]. For each area, the requirement for a spinning reserve is 900 MW in each area. The maximum capacity of the power transmission between areas is 3000 MW. To ensure the stability and robustness of the power system, the DB mechanism is utilized in the day-ahead market integrated with the energy bidding platform and the ancillary service bidding platform for DR users. In this case study, DR users for energy generation are grouped into 10 equivalent segments with similar bidding prices. There are 300 DR users participating in the energy bidding platform, with their capabilities and quotes visualized in Figures 12 and 13. Additionally, there are 100 DR users participating in the ancillary service bidding platform, with corresponding capabilities and quotes presented in Figures 14 and 15. For each individual area, it is assumed the number of DB users, the reduction capability, and the quoted prices are all the same for simplicity. Notably, the minimum power reduction and the minimum spinning reserve capability for DR users are both assumed to be 1 MW. The simulation results are explained as follows.

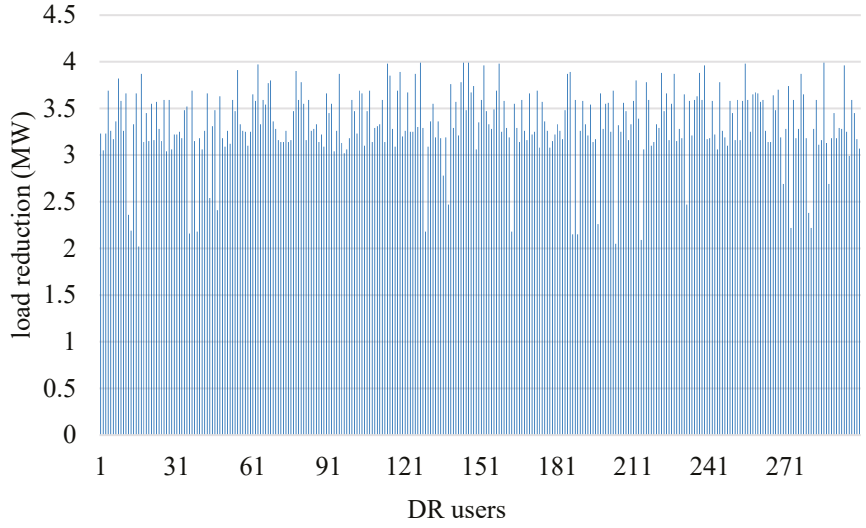


Figure 12. Load reduction availability of DR users for energy generation.

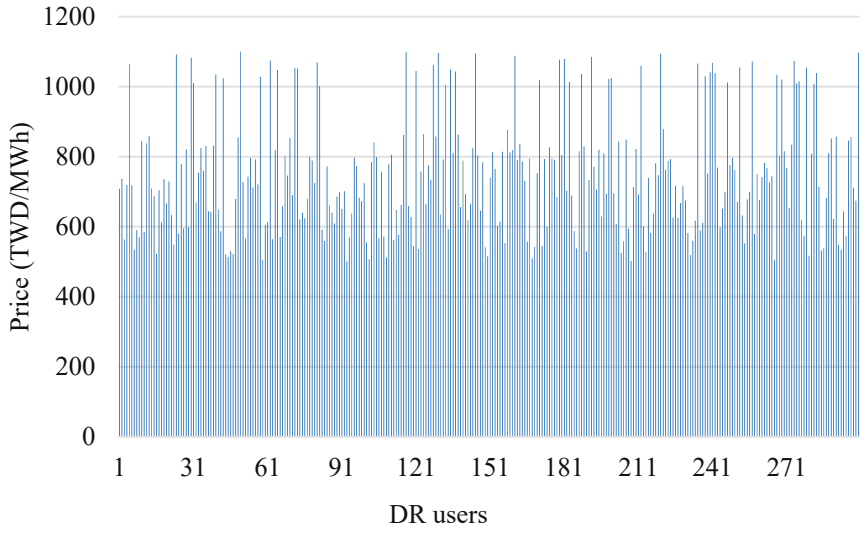


Figure 13. Bidding prices of DR users for energy generation.

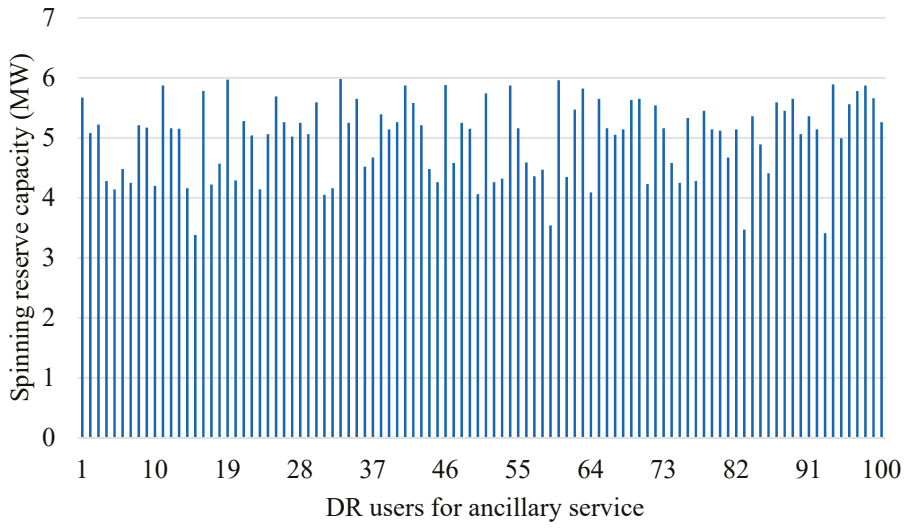


Figure 14. Availability of DR users for ancillary service.

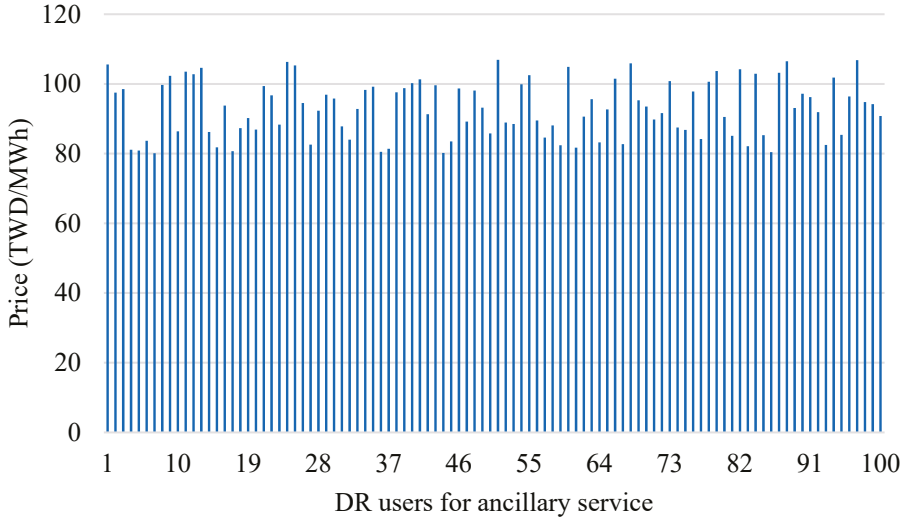


Figure 15. Bidding prices of DR users for ancillary service.

Table 12 presents the dispatch results when the system is in different scenarios for the load demand of 18,000 MW. Through Examples 3.1 and 3.2.1, the effects of DR units to the dispatch results can be examined. As shown in Example 3.1, when the system disregards DR units, the northern area experiences a significantly high marginal price of 1436 TWD/MWh. This high price reflects the congestion between areas and the demand for reserve capacity. The inclusion of DR units in Example 3.2.1 solves the congestion and the high power demand at northern area with the load reduction from the DR units of 828 MW, 609 MW, and 609 MW from the north, center, and south, respectively. In this way, the marginal price can be reduced significantly and save the dispatch cost of 798,850 TWD/h (TWD 12,360,076–TWD 11,561,226). Through Examples 3.2.1 and 3.2.2, the effects of the spinning reserve provided by DR units can be examined. It can be observed that both examples have the capability to supply the required spinning reserve capacity 900 MW for each area. However, the HDSM developed in this paper determines that purchasing reserve capacity for the northern area is more cost-effective, resulting in savings of approximately 44,026 TWD/h (TWD 11,605,232–TWD 11,561,226) in generation costs. This result may be attributed to the increased transmission capacity, allowing more cost-effective generation to be transmitted from the central area to the north. Consequently, the expensive generation from thermal units in the northern area can be reduced from 5663 MW in Example 3.2.2 to 5509 MW in Example 3.2.1. Example 3.3 explains that when the system ignores transmission capacity constraints, each area will have the same marginal cost (791 TWD/MWh) and load reduction amount (647 MW). In this example, congestion between areas would result in an increase in generation costs of approximately 21,085 TWD/h (TWD 11,561,226–TWD 11,540,141). This can be considered as the congestion cost of the transmission lines, and such information can provide a reference for planning the power system. Table 13 presents a convergence history for Example 3.2.1, including iteration counts, variation steps, and dispatch costs. The time consumption of the search process is approximately 2.59 s.

Table 12. Technical and economical results of the Case Study 3.

Example		3.1	3.2.1	3.2.2	3.3
Load demand (N/C/S) (MW)		9000/3600/5400	9000/3600/5400	9000/3600/5400	9000/3600/5400
Required spinning reserve (N/C/S) (MW)		900/900/900	900/900/900	900/900/900	900/900/900
Thermal units	Actual supply of energy generation: (N/C/S) (MW)	6498/5714/5788	5509/5596/4849	5663/5555/4783	5502/5633/4924
	Actual supply of spinning reserve: (N/C/S) (MW)	402/180/318	283/170/286	402/180/318	283/170/297
DR units for energy generation	Availability for load reduction: (N/C/S) (MW)	---	1000/1000/1000	1000/1000/1000	1000/1000/1000
	Actual supply of load reduction: (N/C/S) (MW)	---	828/609/609	834/582/582	647/647/647
DR units for ancillary service	Availability for spinning reserve: (N/C/S) (MW)	---	300/300/300	---	300/300/300
	Actual supply of spinning reserve: (N/C/S) (MW)	---	279/0/0	---	49.71/49.71/49.42
Power transmission line	Maximum limit (P_{CN}^{max}/P_{SC}^{max}) (MW)	3000/3000	3000/3000	3000/3000	---
	Actual flow (P_{CN}/P_{SC}) (MW)	2502/388	2662/58	2502/-35	2851/171
Economical results					
Marginal prices for energy generation: (N/C/S) (TWD/MWh)		1436/944/944	877/774/774	879/762/762	791/791/791
Marginal prices for spinning reserve: (N/C/S) (TWD/MWh)		---	96/---/---	---	82.4/82.4/82.4
Total cost (TWD/h)		12,360,076	11,561,226	11,605,252	11,540,141

Table 13. Convergence history of DR units for Example 3.2.1.

Variation Step	Iteration	Load Reduction (MW) (North/Center/South)	Spinning Reserve (MW) (North/Center/South)	Total Cost (TWD/h)
Initial solution	---	1000/812/0	123/92/89	11,713,046
SP_1 = 80 MW	7	840/572/560	283/0/0	11,567,852
SP_2 = 40 MW	3	840/612/600	283/0/0	11,563,906
SP_3 = 20 MW	2	820/612/620	303/0/0	11,563,247
SP_4 = 10 MW	5	830/602/610	273/0/0	11,562,003
SP_5 = 5 MW	5	830/610/610	278/0/0	11,561,322
SP_6 = 2.5 MW	4	828/609/608	278/0/0	11,561,277
SP_7 = 1.25 MW	5	829/609/609	278/0/0	11,561,243
SP_8 = 0.625 MW	4	828/609/609	279/0/0	11,561,231
SP_9 = 0.3125 MW	3	828/609/609	279/0/0	11,561,228
SP_{10} = 0.15625 MW	5	828/609/609	279/0/0	11,561,226.6
SP_{11} = 0.078125 MW	2	828/609/609	279/0/0	11,561,226.1

Table 14 discusses the impact of changes in different loads on dispatch results. In this example, due to the imbalance between electricity supply and demand in the northern area, a large amount of power flow is transferred from the central area to the northern area. From the simulation results, it is further observed that as the load increases, the congestion on inter-regional transmission lines also increases. The price differences between areas become more significant, leading to a greater chance of winning the bidding for DR users in the congested northern area. For example, when the load increases from 16,000 MW to 18,000 MW, under the same pricing conditions, the generation volume won by DR users in the northern area can increase from 260 MW to 828 MW, while the central and

southern areas only see an increase from 260 MW to 609 MW. It is worth noting that when the load is at 16,000 MW, the system's thermal units have sufficient capacity to meet the reserve capacity requirements of all areas, so there is no need to purchase from the ancillary service bidding platform. However, as the load increases (to 17,000 MW), the power transmitted from the central area to the north also increases, leading to a relative increase in the marginal price in the northern area (724 TWD/MW). The dispatch results indicate that it becomes more economical for the power company to purchase reserve capacity from the ancillary service bidding platform. However, during heavy load conditions (18,000 MW), constrained by the inter-regional transmission limit, the system's thermal units change their allocations and purchase 279 MW of ancillary service reserve capacity from the northern area to meet its reserve capacity requirement (900 MW). Therefore, the multi-area bidding platform proposed in this paper can be used to address issues of congestion between areas and the distribution of reserve capacity in various areas, thus improving the economic efficiency and reliability of the day-ahead market system operation.

Table 14. The impact of changes in different loads on dispatch results for Example 3.2.1.

Load (MW)	Marginal Price for Energy Generation (TWD/MWh)			DR Unit for Energy Generation (MW)			Marginal Prices for Spinning Reserve (TWD/MWh)			DR Unit for Spinning Reserve (MW)			Total Cost (TWD/h)
	N	C	S	N	C	S	N	C	S	N	C	S	
16,000	622	622	622	260	260	260	---	---	---	---	---	---	10,128,682
16,500	661	661	661	345	345	345	81	81	81	30	30	30	10,449,880
17,000	724	699	699	496	440	440	87	80	80	124	4.3	1.3	10,791,601
17,500	808	728	728	715	507	507	88.5	---	---	149	---	---	11,161,920
18,000	877	773	773	828	609	609	95.8	---	---	279	---	---	11,561,226

N—northern area; C—central area; S—southern area.

6. Conclusions

This paper focuses on enhancing the DB mechanism for the day-ahead energy market and ancillary services market. To comprehensively solve the ED problem, this paper integrates thermal units and DR units to satisfy the load demand and the requirement of reserve capacity simultaneously. The imbalance that occurs in multi-area systems is particularly considered, with the maximum power flow constraints being the same as the practical situation. Additionally, this paper introduces the HDSM technique coupled with DQD to optimize the multi-area demand–thermal coordination dispatch problem. The proposed method is able to minimize the overall costs, subject to the satisfaction of regional load and reserve capacity requirements, the upper and lower output limits of the thermal unit, the coupling restrictions of reserve capacity for the thermal unit, and the operational limitations of the DR units. The resulting allocation of generation and reserve capacity generated by the cooperation of thermal units and equivalent DR units is able to relieve congested areas or supply bottlenecks. This study could serve as a guide for system operators to design regulations for a DB mechanism and access the economic benefits.

Author Contributions: Conceptualization, Y.-S.C. and C.-L.C.; Methodology, Y.-S.C., Y.-Y.C., C.-T.T. and C.-L.C.; Software, Y.-Y.C.; Validation, Y.-S.C. and Y.-Y.C.; Formal analysis, C.-T.T. and C.-L.C.; Writing—original draft, Y.-S.C. and Y.-Y.C.; Writing—review & editing, C.-T.T. and C.-L.C.; Visualization, C.-T.T.; Supervision, Y.-S.C., Y.-Y.C. and C.-L.C. All authors have read and agreed to the published version of the manuscript.

Funding: This research was funded by the Ministry of Science and Technology, Taiwan, under grants MOST 109-2221-E-019-014-MY2.

Data Availability Statement: The original contributions presented in this study are included in the article. Further inquiries can be directed to the corresponding authors.

Conflicts of Interest: The authors declare no conflict of interest.

Abbreviations

TC	total operating cost
NT	number of thermal units in system
$F_i(\bullet)$	operation cost function of thermal unit i
i	index for thermal units
P_i	energy generation of thermal unit i
$\alpha_i, \beta_i, \gamma_i$	coefficients to calculate the fuel costs for the thermal unit i
$F^a_{DB}(\bullet)$	energy bidding price function of DR unit for energy generation in area a
P^a_{DB}	energy generation of DR unit in area a
$BP^a_{q,j}$	load reduction in the jth user in segment qth of DR unit for energy generation in area a
$CP^a_{q,j}$	bidding price of the jth user in segment qth of DR unit for energy generation in area a
NP^a_q	the number of users in segment qth of DR unit for energy generation in area a
$G^a_{DB}(\bullet)$	reserve bidding price function of DR unit for spinning reserve in area a
S^a_{DB}	spinning reserve of DR unit in area a
BS^a_k	reserve capacity of the kth user DR unit for spinning reserve in area a
CS^a_k	bidding price of the kth user of DR unit for spinning reserve in area a
NS^a	total number users of DR unit for spinning reserve in area a
P^a_D	load demand in area a
SR_D	spinning reserve requirements at each area
S_i	spinning reserve of thermal unit i
$P_i^{\max}$	upper generation limit of thermal unit i
$P_i^{\min}$	lower generation limit of thermal unit i
$d\%$	percentage of maximum unit capacity
$S_i^{\max}$	maximum spinning reserve contribution of thermal unit i
$P^{a,\max}_{DB}$	the maximum energy reduction in DR unit in area a
$BP^{a,\max}_{q,j}$	maximum of DR user for energy generation in area a
$BP^{a,\min}_{q,j}$	minimum of DR user for energy generation in area a
$CP^{\max}_{DB}$	the highest bidding price of DR users for energy generation
Lp	the number of the equivalent segment of DR unit for energy generation
$S^{a,\max}_{DB}$	the maximum reserve capacity of DR unit for spinning reserve in area a
$BS^{a,\max}_k$	maximum of DR user for spinning reserve in area a
$BS^{a,\min}_k$	minimum of DR user for spinning reserve in area a
$CS^{a,\max}_{DB}$	the highest bidding price of DR users for spinning reserve in area a
$P_{CN}, P^{\max}_{CN}$	transfer power and flow limits from central area to northern area respectively
$P_{SC}, P^{\max}_{SC}$	transfer power and flow limits from southern area to central area respectively
S_{CN1}	transfer spinning reserve from central area to northern area
S_{CN2}	transfer spinning reserve from northern area to central are
S_{SC1}	transfer spinning reserve from southern area to central area
S_{SC2}	transfer spinning reserve from central area to southern area
DB	demand bidding
DQD	dynamic queuing dispatch
DSM	direct search method
REGS	renewable energy generation system
DERs	distributed energy resources
VPP	virtual power plant
DR	demand response
LA	load aggregator
FIS	Fuzzy Inference System

ED	economic dispatch
MPC	Model Predictive Control
MESs	multi-energy systems
CBL	customer baseline load
HDSM	Hybrid Direct Search Method
SP	step size
RF	reduced factor

References

1. Chuang, Y.S.; Cheng, C.C.; Cheng, H.P. The current development of the energy storage industry in Taiwan: A snapshot. *J. Energy Storage* **2022**, *53*, 105117. [CrossRef]
2. Zakaria, A.; Ismail, F.B.; Lipu, M.H.; Hannan, M.A. Uncertainty models for stochastic optimization in renewable energy applications. *Renew. Energy* **2020**, *145*, 1543–1571. [CrossRef]
3. Tan, Z.; Ju, L.; Reed, B.; Rao, R.; Peng, D.; Li, H.; Pan, G. The optimization model for multi-type customers assisting wind power consumptive considering uncertainty and demand response based on robust stochastic theory. *Energy Convers. Manag.* **2015**, *105*, 1070–1081. [CrossRef]
4. Li, Y.; Wang, C.; Li, G.; Chen, C. Optimal scheduling of integrated demand response-enabled integrated energy systems with uncertain renewable generations: A Stackelberg game approach. *Energy Convers. Manag.* **2021**, *235*, 113996. [CrossRef]
5. Yu, S.; Fang, F.; Liu, Y.; Liu, J. Uncertainties of virtual power plant: Problems and countermeasures. *Appl. Energy* **2019**, *239*, 454–470. [CrossRef]
6. Nosratabadi, S.M.; Hooshmand, R.A.; Gholipour, E. A comprehensive review on microgrid and virtual power plant concepts employed for distributed energy resources scheduling in power systems. *Renew. Sustain. Energy Rev.* **2017**, *67*, 341–363. [CrossRef]
7. Riveros, J.Z.; Bruninx, K.; Poncelet, K.; D'haeseleer, W. Bidding strategies for virtual power plants considering CHPs and intermittent renewables. *Energy Convers. Manag.* **2015**, *103*, 408–418. [CrossRef]
8. Abapour, S.; Mohammadi-Ivatloo, B.; Hagh, M.T. Robust bidding strategy for demand response aggregators in electricity market based on game theory. *J. Clean. Prod.* **2020**, *243*, 118393. [CrossRef]
9. Wang, F.; Ge, X.; Li, K.; Mi, Z. Day-ahead market optimal bidding strategy and quantitative compensation mechanism design for load aggregator engaging demand response. *IEEE Trans. Ind. Appl.* **2019**, *55*, 5564–5573. [CrossRef]
10. Lu, X.; Ge, X.; Li, K.; Wang, F.; Shen, H.; Tao, P.; Hu, J.; Lai, J.; Zhen, Z.; Shafie-khah, M.; et al. Optimal bidding strategy of demand response aggregator based on customers' responsiveness behaviors modeling under different incentives. *IEEE Trans. Ind. Appl.* **2021**, *57*, 3329–3340. [CrossRef]
11. Vahid-Ghavidel, M.; Javadi, M.S.; Santos, S.F.; Gough, M.; Mohammadi-Ivatloo, B.; Shafie-Khah, M.; Catalão, J.P. Novel hybrid stochastic-robust optimal trading strategy for a demand response aggregator in the wholesale electricity market. *IEEE Trans. Ind. Appl.* **2021**, *57*, 5488–5498. [CrossRef]
12. Sumaiti, A.; Konda, S.R.; Panwar, L.; Gupta, V.; Kumar, R.; Panigrahi, B.K. Aggregated demand response scheduling in competitive market considering load behavior through fuzzy intelligence. *IEEE Trans. Ind. Appl.* **2020**, *56*, 4236–4247. [CrossRef]
13. Long, Y.; Li, Y.; Wang, Y.; Cao, Y.; Jiang, L.; Zhou, Y.; Deng, Y.; Nakanishi, Y. Low-carbon economic dispatch considering integrated demand response and multistep carbon trading for multi-energy microgrid. *Sci. Rep.* **2022**, *12*, 6218. [CrossRef]
14. Wang, L.; Jing, Z.X.; Zheng, J.H.; Wu, Q.H.; Wei, F. Decentralized optimization of coordinated electrical and thermal generations in hierarchical integrated energy systems considering competitive individuals. *Energy* **2018**, *158*, 607–622. [CrossRef]
15. Marzbani, F.; Abdelfatah, A. Economic Dispatch Optimization Strategies and Problem Formulation: A Comprehensive Review. *Energies* **2024**, *17*, 550. [CrossRef]
16. Nelson, J.R.; Johnson, N.G. Model predictive control of microgrids for real-time ancillary service market participation. *Appl. Energy* **2020**, *269*, 114963. [CrossRef]
17. Vahid-Ghavidel, M.; Javadi, M.S.; Gough, M.; Santos, S.F.; Shafie-khah, M.; Catalão, J.P.S. Demand Response Programs in Multi-Energy Systems: A Review. *Energies* **2020**, *13*, 4332. [CrossRef]
18. Liu, L.; Chen, X.; Li, D.; Liu, C.; Liu, D.; Li, G. Evaluation method for assessing the auxiliary service transaction mechanism in regional power markets. *Glob. Energy Interconnect.* **2023**, *6*, 238–252. [CrossRef]
19. Wang, J.; Zhong, H.; Tang, W.; Rajagopal, R.; Xia, Q.; Kang, C.; Wang, Y. Optimal bidding strategy for microgrids in joint energy and ancillary service markets considering flexible ramping products. *Appl. Energy* **2017**, *205*, 294–303. [CrossRef]
20. Das, S.; Basu, M. Day-ahead optimal bidding strategy of microgrid with demand response program considering uncertainties and outages of renewable energy resources. *Energy* **2020**, *190*, 116441. [CrossRef]
21. Rezaei, N.; Pezhmani, Y.; Khazali, A. Economic-environmental risk-averse optimal heat and power energy management of a grid-connected multi microgrid system considering demand response and bidding strategy. *Energy* **2022**, *240*, 122844. [CrossRef]

22. Nikpour, A.; Nateghi, A.; Shafie-Khah, M. Stochastic-risk based approach for microgrid participation in joint active, reactive, and ancillary services markets considering demand response. *IEEE Open Access J. Power Energy* **2022**, *10*, 2–13. [CrossRef]
23. Nikpour, A.; Nateghi, A.; Shafie-khah, M.; Catalão, J.P. Day-ahead optimal bidding of microgrids considering uncertainties of price and renewable energy resources. *Energy* **2021**, *227*, 120476. [CrossRef]
24. Naseri, A.; Fattaheian-Dehkordi, S.; Abbaspour, A.; Lehtonen, M. Day-Ahead Optimal Scheduling of Resources in a Distribution System in Joint Energy, Regulation and Ramp Markets. *Int. Rev. Electr. Eng.* **2023**, *18*, 1–14. [CrossRef]
25. Wu, Y.; Shi, J.; Lim, G.J.; Fan, L.; Molavi, A. Optimal management of transactive distribution electricity markets with co-optimized bidirectional energy and ancillary service exchanges. *IEEE Trans. Smart Grid* **2020**, *11*, 4650–4661. [CrossRef]
26. Taiwan Power Company. Demand Response Bidding Platform. Available online: https://dbp.taipower.com.tw/TaiPowerDBP/Portal/Login (accessed on 18 May 2025).
27. Chen, C.L.; Chen, N. Direct search method for solving economic dispatch problem considering transmission capacity constraints. *IEEE Trans. Power Syst.* **2001**, *16*, 764–769. [CrossRef]
28. Wong, K.P.; Fung, C.C. Simulated annealing based economic dispatch algorithm. In *IEE Proceedings C Generation, Transmission and Distribution*; IET Digital Library: Hertfordshire, UK, 1993; Volume 140, pp. 509–515.
29. Walters, D.C.; Sheble, G.B. Genetic algorithm solution of economic dispatch with valve point loading. *IEEE Trans. Power Syst.* **1993**, *8*, 1325–1332. [CrossRef]
30. Chaturvedi, K.T.; Pandit, M.; Srivastava, L. Self-organizing hierarchical particle swarm optimization for nonconvex economic dispatch. *IEEE Trans. Power Syst.* **2008**, *23*, 1079–1087. [CrossRef]
31. Pradhan, M.; Roy, P.K.; Pal, T. Grey wolf optimization applied to economic load dispatch problems. *Int. J. Electr. Power Energy Syst.* **2016**, *83*, 325–334. [CrossRef]
32. Taiwan Power Company. Demand Response Bidding Measures. Available online: https://dbp.taipower.com.tw/TaiPowerDBP/Portal/proj_data/%E9%9C%80%E9%87%8F%E7%AB%B6%E5%83%B9%E6%8E%AA%E6%96%BDDM.pdf (accessed on 1 November 2024).
33. Taiwan Power Company. Ancillary Services Market. Available online: https://etp.taipower.com.tw (accessed on 18 May 2025).
34. Chen, C.L.; Chen, Z.Y.; Lee, T.Y. Multi-area economic generation and reserve dispatch considering large-scale integration of wind power. *Int. J. Electr. Power Energy Syst.* **2014**, *55*, 171–178. [CrossRef]
35. Wood, A.J.; Wollenberg, B.F.; Sheblé, G.B. *Power Generation, Operation, and Control*; John Wiley & Sons: Hoboken, NJ, USA, 2013.
36. Chen, C.L. Non-convex economic dispatch: A direct search approach. *Energy Convers. Manag.* **2007**, *48*, 219–225. [CrossRef]
37. Yalcinoz, T.; Short, M.J. Neural networks approach for solving economic dispatch problem with transmission capacity constraints. *IEEE Trans. Power Syst.* **1998**, *13*, 307–313. [CrossRef]
38. Chen, C.L. Key issues of wind capacity integration in congested areas of the Taiwan power system. *IET Renew. Power Gener.* **2014**, *8*, 10–21. [CrossRef]

Disclaimer/Publisher's Note: The statements, opinions and data contained in all publications are solely those of the individual author(s) and contributor(s) and not of MDPI and/or the editor(s). MDPI and/or the editor(s) disclaim responsibility for any injury to people or property resulting from any ideas, methods, instructions or products referred to in the content.

energies

MDPI

Article

Oxidative Pyrolysis of Typical Volatile Model Compounds Under Low Oxygen Equivalence Ratios During Oxidative Pyrolysis of Biomass

Liying Wang [1,2], Dan Lin [1], Dongjing Liu [1], Xing Xie [1], Shihong Zhang [3,*] and Bin Li [1,2,*]

[1] School of Energy and Power Engineering, Jiangsu University, Zhenjiang 212013, China
[2] School of Engineering, Anhui Agricultural University, Hefei 230036, China
[3] State Key Laboratory of Coal Combustion, School of Energy and Power Engineering, Huazhong University of Science and Technology, Wuhan 430074, China
* Correspondence: shzhang@hust.edu.cn (S.Z.); libin198520@126.com (B.L.)

Abstract: This study aims to investigate the oxidative pyrolysis of biomass volatiles with a particular focus on the formation of liquid products. Furfural, hydroxyacetone, and 3,4-dimethoxybenzaldehyde were chosen as volatile model compounds. The impacts of the oxygen equivalence ratio (ER, 0–15%) and temperature (400–500 °C) on the product composition and distribution were examined using a two-stage quartz-tube reactor. The results showed that volatile pyrolysis was limited at the lower temperature of 400 °C even with oxygen introduction, while it could be significantly promoted at 500 °C as illustrated by the observed great decrease in the GC-MS peak areas of the volatile compounds especially under an oxidative atmosphere. For instance, the peak area of 3,4-dimethoxybenzaldehyde at 500 °C under an ER of 4% was only ~9% of that at 400 °C. Oxygen introduction enhanced the volatile decomposition with the formation of mainly permanent gases (although not given in the study) rather than liquid products, but distinct impacts were obtained for varied volatile compounds possibly due to their different chemical structures and autoignition temperatures. From the perspective of liquid product formation, furfural would undergo the cleavage of C-C/C-O bonds to form linear intermediates and subsequent aromatization to generate aromatics (benzene and benzofuran). The presence of oxygen could enhance the oxidative destruction of the C-C/C-O bonds and the removal of O from the molecules to form simple aromatics such as benzene, phenol, and toluene. Hydroxyacetone mainly underwent C-C/C-O cleavage that was further enhanced in the presence of oxygen; the resultant intermediates would recombine to generate acetoin and 2,3-pentanedione. A higher ER would directly oxidize the alcoholic hydroxyl group (-OH) into an aldehyde group (-CHO) to form methyl glyoxal, while 3,4-dimethoxybenzaldehyde mainly underwent cleavage and recombination of bonds connected with the benzene ring including aldehyde group (-CHO), C_{Ar}-O, $C_{Methoxy}$-O bonds, thus forming 1,2-dimethoxybenzene, toluene, and 3-hydroxybenzadehyde. This study provides more fundamental insights into the homogeneous oxidation of volatiles during the oxidative fast pyrolysis of biomass, facilitating the deployment of this technology.

Keywords: oxidative pyrolysis; volatiles; oxygen equivalence ratio; pyrolysis temperature

1. Introduction

Fast pyrolysis of biomass is an efficient thermochemical conversion technology, which enables the direct transformation of the green and net-zero-carbon biomass into more

value-added products such as bio-oil and biochar [1–3]. Bio-oil, also called bio-crude, contains hundreds of chemicals, such as phenols, aromatics, anhydrosugars, furans, linear acids/carbonyls/aldehydes, etc. [4]. It can be used as the feedstock for a centralized biorefinery to produce all kinds of green chemicals and materials to partially substitute fossils [5,6], which is of great importance for the decarbonized future.

At present, the research on the fast pyrolysis of biomass mainly focuses on the chemical reaction aspect; how to selectively generate value-added fuels, chemicals, or materials is of the first priority [7], including optimization of the pyrolysis conditions, in situ catalytic pyrolysis, ex situ catalytic pyrolysis, and other upgrading techniques [8–12]. Some novel pyrolysis technologies as well as catalysts have been successfully developed and demonstrated in the laboratory [3,13,14]. However, the practical/scaled application of the fast pyrolysis of biomass still faces engineering issues, one of which is the rapid heat supply and transfer during the process. Conventional fast pyrolysis of biomass is normally undertaken in an oxygen-free atmosphere at medium temperatures (e.g., 400–600 °C); this inherently endothermic process requires an external heat source to sustain the thermal decomposition reactions [15,16]. Particularly at the commercial scale, supplying external heat typically through gas/solid heat carriers or conduction from reactor walls to the biomass particles would be increasingly difficult due to the complexity and instability of heat exchange systems and the inefficiency of heat transfer [17]. It becomes a challenging issue during the scaling up and commercialization of fast pyrolysis technology.

The oxidative fast pyrolysis of biomass has been recently developed to address the heat supply/transfer bottleneck issue associated with conventional pyrolysis processes [18]. A small amount of oxygen or air is introduced into the pyrolysis process, facilitating the in situ oxidation of certain pyrolysis intermediates to generate the heat demanded for the endothermic reactions; a self-sustained/autothermal pyrolysis process is thus achieved [19–21]. Polin et al. [22] reported that the oxygen equivalence ratios (ERs) for the autothermal pyrolysis of corn stover and red oak in a fluidized-bed reactor at 500 °C were only 0.06 and 0.10, respectively. It should be pointed out that the oxidative fast pyrolysis of biomass is very different from combustion and gasification; it is normally carried out at a medium temperature of 400–600 °C, which is much lower than that of gasification and combustion. The ER used in the oxidative fast pyrolysis process (0–0.15 or 15%) is also much lower than that in gasification (0.2–0.35) [23,24] and combustion (more than 1) [25,26], and the main products from the oxidative fast pyrolysis of biomass are still bio-oil, biochar, and non-condensable gas. Compared with conventional non-oxidative/inert fast pyrolysis of biomass, the oxidative fast pyrolysis of biomass shows a lot of advantages not only in terms of the heat supply and transfer toward scaling up but also in terms of the elimination of the complicated external heating, the ease of scaling up by volume (not surface area) due to the realization of bulk heating instead of surface heating, and the significant process intensification due to the in situ oxidation heating [17]. Moreover, no significant reduction in bio-oil yield is observed for fluidized-bed oxidative fast pyrolysis of biomass at 500 °C under low ERs (0.033–0.104), as found by Kim et al. [27]. The heat demand for pyrolysis is mainly satisfied by the oxidation of biochar with only a very low fraction of light bio-oil being oxidatively consumed [28]. It further confirms the advantage of oxidative fast pyrolysis of biomass in terms of bio-oil production.

As discussed previously, the introduction of oxygen in the oxidative fast pyrolysis of biomass would inevitably induce oxidation reactions of pyrolysis intermediates or products, including the heterogeneous oxidation of biochar and the homogeneous oxidation of volatiles [17,28]. The manner of oxidization of the biochar and volatiles/bio-oil during the process mainly depends on the contact between oxygen and biochar or volatile vapors, as well as on their oxidation reactivities. However, Brown [19] regarded that the autoignition

temperatures of biochar and volatile/bio-oil components determined their oxidation characteristics, and the biochar with the lowest autoignition temperature was more oxidized in the fluidized-bed reactor to provide the largest contribution to the heat demanded for biomass pyrolysis. Li et al. [28] also made a similar observation, while the bio-oil composition was also found to be altered with the introduction of oxygen. Considering that the oxidation of the biochar and the volatiles occurs concurrently, although the tendency of the biochar and volatiles toward being oxidized is known, it would be still challenging to quantitatively distinguish their individual contributions during the process. The role of oxygen in oxidative fast pyrolysis and its influence on the formation and consumption of pyrolysis products remain poorly understood. Jiang et al. [29] proposed a method to decouple the oxidation reactions in oxidative fast pyrolysis by varying the oxygen injection location. A purely "homogeneous" oxidation and the combined "homogeneous + heterogeneous" oxidations for product formation in a fluidized-bed pyrolysis system were obtained and compared in detail. However, not only would the biochar and volatiles compete for oxygen for hetero-/homogeneous oxidation [30], but the different components in the volatiles would also compete for oxygen due to their different reactivities with oxygen; changes in the operating conditions can substantially influence the oxidation process as well. Despite the importance of this topic, research specifically addressing the homogeneous oxidation of volatile components in the oxidative fast pyrolysis process remains limited.

Therefore, in this study, the oxidative pyrolysis of three representative biomass volatiles from the pyrolysis of holocellulose and lignin was carried out under varying temperatures (400–500 °C) and ERs (0–15%) in a two-stage quartz-tube reactor. The characteristic products were analyzed, and the possible conversion pathways during the oxidative pyrolysis process were proposed. Through this study, we expect to gain a more fundamental understanding of the homogeneous oxidation of volatiles/bio-oil and of the selective formation of valuable products from the oxidative fast pyrolysis of biomass.

2. Experimental Section

2.1. Volatile Model Compounds

Furfural (AR, ≥99.5%, Xilong Scientific Co. Ltd., Shantou, China) and hydroxyacetone (AR, 97%, Bidepharm Co. Ltd., Shanghai, China), as the representative furans and linear carbonyls from holocellulose (cellulose and hemicellulose) pyrolysis volatiles, and 3,4-dimethoxybenzaldehyde (AR, ≥98%, Xiya Reagent Co. Ltd., Zaozhuang, China), as the representative aromatic from lignin pyrolysis volatiles, were chosen as the volatile model compounds from the fast pyrolysis of biomass [31]. They were all subjected to homogeneous oxidative pyrolysis experiments.

2.2. Oxidative Pyrolysis of Volatiles

The oxidative pyrolysis of biomass volatile model compounds was conducted in a two-stage quartz-tube reaction system, as shown in Figure 1. It consisted of a gas supply system, a two-stage quartz-tube reactor heated by an electric furnace, a condensation system, and a gas collection bag. The gas supply system mainly provided two gas streams into the reactor, including the carrier gas N_2 and the oxygen-containing oxidation gas. The carrier gas N_2 was injected into the reactor from the top with a flow rate of 250 mL/min. The oxidation gas was a mixture of N_2 and air with a total flow rate of 50 mL/min; it was injected into the reactor from the middle (between the upper and lower sections). The amount of oxygen introduced was controlled by the mass flow controller (MFC). It should be noted that the gas flows did not require preheating due to their low flow rate compared with the large power of the two electric furnaces (both 1.5 kW); insignificant temperature fluctuations were observed during the experiments as the gases were easily heated to the

reaction temperature. The quartz-tube reactor featured an inner diameter of 38 mm, with the lengths of the upper and lower sections being 330 mm and 122 mm, respectively. These two sections were heated separately by two independent electric furnaces (both 1.5 kW) and maintained at different temperatures. The upper section was used to evaporate the volatile model compounds; the temperature was set at 200 °C for furfural and hydroxyacetone and 250 °C for 3,4-dimethoxybenzaldehyde, according to their volatilization temperatures. The lower section was used to oxidize the volatilized model compounds at a lower oxygen ER, and its temperature was set at 400 or 500 °C, which was identical to the oxidative pyrolysis temperature. To ensure the precise control of the temperatures in each section and minimize the mutual influence of both sections due to the large temperature gradient, Kaowool was used to isolate the furnace/reactor from the environment (reducing heat loss) and the upper section from the lower section of the reactor (minimizing mutual influence). The top, middle, and bottom of the furnace/reactor were all well insulated. A K-type thermocouple penetrating through the top rubber plug of the reactor was used to measure the temperatures of both the sections. It should be pointed out that the temperatures given above were the actual measured temperatures, which were normally 8 °C lower than the set temperatures of the electric furnaces. Pre-experiments proved that the temperatures of the two sections could be controlled independently and kept steady over the experimental timescale. The condensation system was made of an acetone (AR) washing bottle immersed in an ice bath to capture the condensable products.

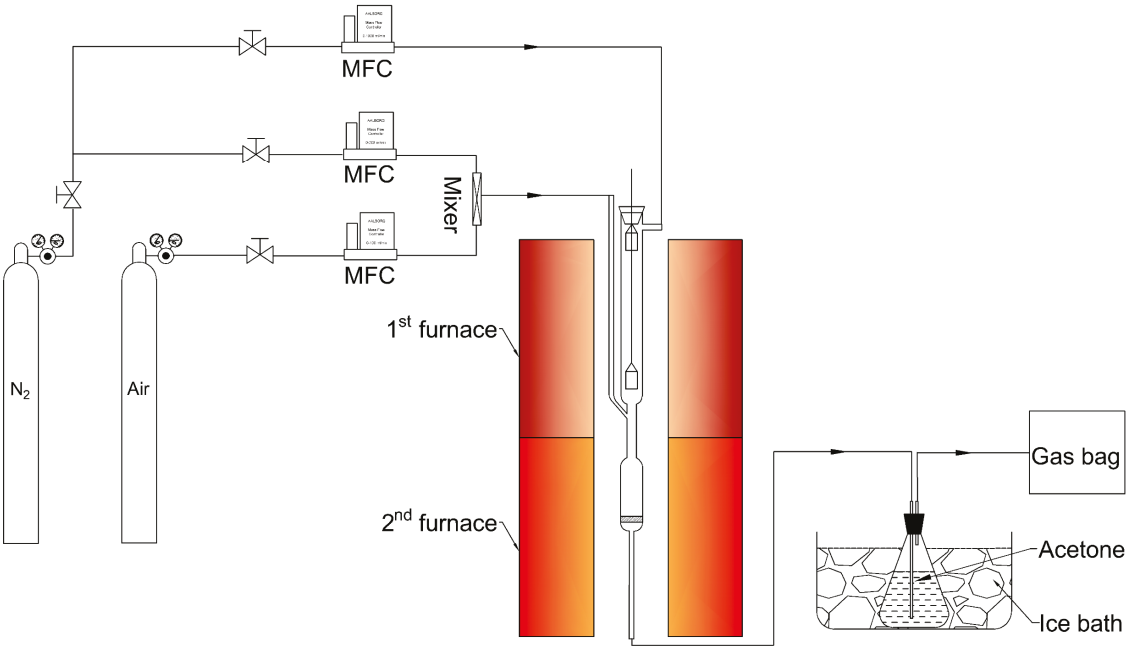


Figure 1. A two-stage reaction system for homogeneous oxidation of volatile model compounds.

For a typical experiment, 0.5 g of the abovementioned volatile model compound was accurately weighed and loaded into a quartz basket; it was put into the upper section of the reactor and initially hung out of the heating zone prior to the experiment. The reactor was heated to the desired temperatures and kept isothermally with the continuous flowing of the carrier gas N_2 and the oxidation gas. The quartz basket was then quickly inserted into the center of the upper heating zone; the volatile model compound was heated and evaporated; it was carried by the N_2 gas, mixed with the oxygen-containing gas, and went into the lower section for homogenous oxidation. The resultant gas vapors coming out of the reactor were condensed and captured inside the acetone washing bottle, and the non-condensable gas was collected in the gas bag. Each experiment lasted for 15 min according

to the volatilization rates of the model compounds. Different ERs were tested during the oxidation process, with 0–6% for 400 °C and 0–15% for 500 °C. It should be noted that the ER was calculated based on the amount of the volatilized model compound (not the initial weight used) during the process. The volatilization rates of furfural, hydroxyacetone, and 3,4-dimethoxybenzaldehyde were determined by pre-experiments, with average results of 100.00 wt.%, 97.83 wt.%, and 22.33 wt.%, respectively. The ER was defined as the ratio of real oxygen input to the theoretical oxygen demand for compete combustion (full oxidation to form CO_2 and H_2O). The real oxygen concentration in the total gas ranged around 0–2 vol.% as it was largely diluted by N_2 gas at an ER of 0–15%. No significant temperature changes induced by the oxidation reactions were observed during the experiments due to the small experiment scale (0.5 g model compound, 15 min evaporation under a low ER). After the experiment finished, the gas bag was switched off and disconnected from the system. The air supply was stopped with N_2 continuously flowing; the quartz basket was lifted out of the heating zone for rapid quenching. The condensation system was also disconnected from the reactor; the liquid captured in the acetone solvent and the condensates in the pipeline were also collected for further analysis.

2.3. Product Characterization

The solid residue remaining in the quartz basket was weighed to determine the volatilization rate of the model compound during the process, as mentioned in the above section.

The gas composition in the gas bag was analyzed using a gas chromatograph equipped with TCD and FID detectors (GC-9790II, Zhejiang Fuli Analytical Instrument Co., Ltd., Taizhou, China). Unfortunately, no feasible results were obtained due to the low oxidation rate of volatile model compounds and the corresponding excessive dilution by N_2. As a result, the gas composition is not reported in this study.

The composition of the liquid products was analyzed using an Agilent gas chromatography–mass spectrometry (GC-MS) system (6890 series GC coupled with a 5975 MS). An HP-5MS capillary column (30 m × 0.25 mm × 0.25 μm) was used. The detailed operating conditions can be found elsewhere [32]. Compound identification was performed using the NIST11 spectral library, with peak areas representing the relative abundance of specific compounds. Considering that the bio-oil is diluted by acetone in different extents due to the varied mass of acetone used for capture, the different acetone volatilization rate, and the different mass of acetone used for washing and collecting after experiment, the peak area of an individual compound detected by GC-MS cannot represent the yield of that compound in the bio-oil but only represents the relative content of the compound in the bio-oil solution. To compare the relative yield of a specific compound generated, the peak area should be generalized by multiplying the peak area and the mass of the liquid product mixed solution (including both bio-oil and acetone). It can thus mitigate the impact of differences in acetone volatilization and acetone solvent dilution and be used for semi-quantitative analysis.

3. Results and Discussion

3.1. Oxidative Pyrolysis of Furfural Under Low ERs at 400 and 500 °C

Figure 2 shows the composition of products detected by GC-MS from the oxidative pyrolysis of furfural under oxygen ERs of 0–15% at 400 and 500 °C. From Figure 2a, it can be seen that, at 400 °C, only furfural (the reactant) was found in the product, with its peak area slightly decreasing with increasing ER. It indicated that a small amount of furfural might be consumed by oxygen under low oxygen ERs at 400 °C, possibly only generating

small-molecular permanent gases (e.g., CO, CO_2, or H_2O) rather than condensable liquid products.

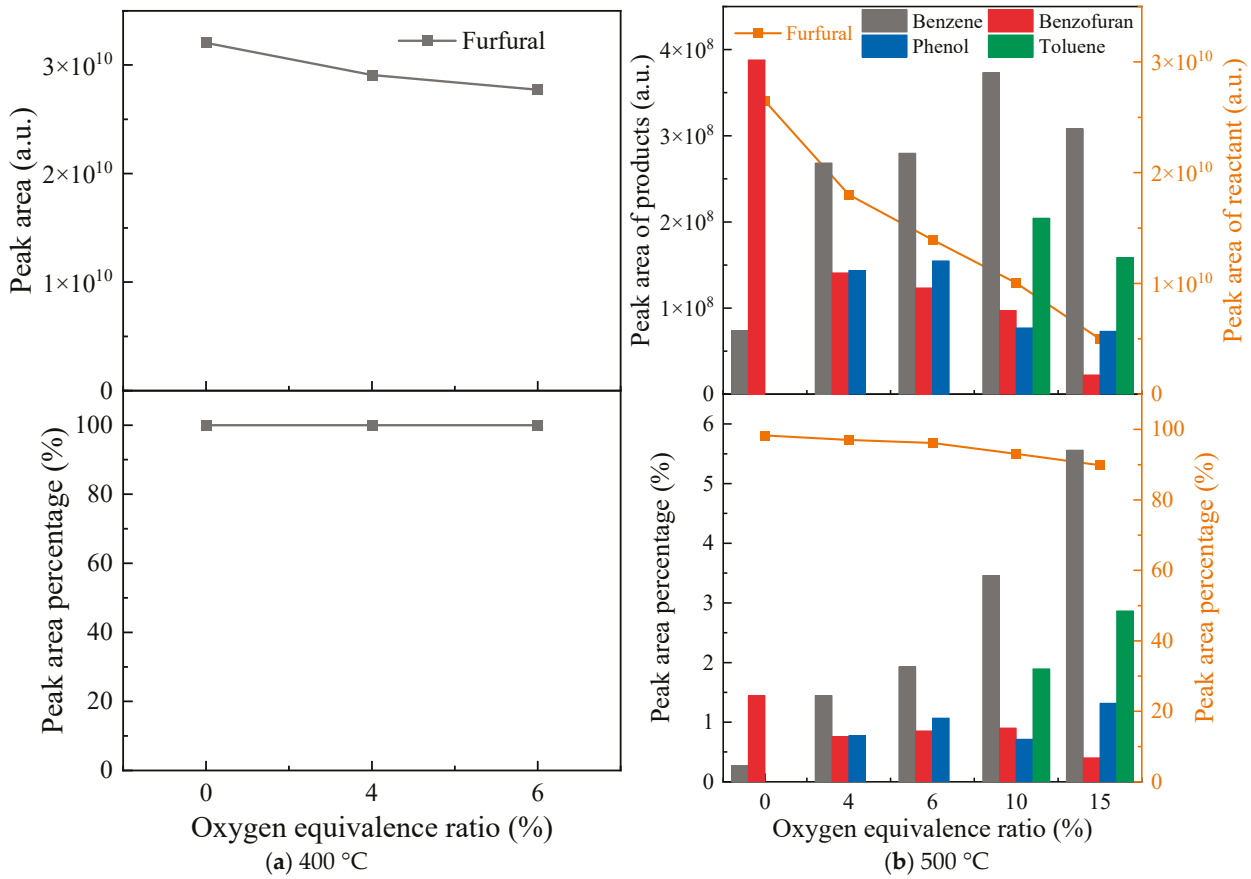


Figure 2. Composition of products detected by GC-MS from oxidative pyrolysis of furfural under low oxygen ERs at (**a**) 400 and (**b**) 500 °C.

When the temperature increased to 500 °C, as shown in Figure 2b, more products were observed both without and with oxygen addition, suggesting that the pyrolysis temperature was an important parameter to improve the reactivity of furfural during the pyrolysis process. The peak area of furfural decreased significantly with increasing ER; even without oxygen (ER of 0), its peak area was much lower than that at 400 °C (Figure 2a), indicating the large thermal decomposition and oxidation consumption of furfural at a higher temperature and under an oxidative atmosphere. But, even under an ER of 15% at 500 °C, the content of furfural (in terms of peak area percentage, same thereafter) in the product still accounted for ~90%, demonstrating that the formation of new condensable liquid products was quite low; most of the furfural was converted into permanent gases.

From the perspective of liquid product formation, under an ER of 0 and at 500 °C, benzene and benzofuran (dominant) were formed from furfural. As we know, furfural could undergo thermal decomposition to form furan and CO ($C_5H_4O_2 \rightarrow C_4H_4O+CO$) [33], while benzofuran could be directly formed from two furan molecules' recombination with subsequent dehydration ($2C_4H_4O \rightarrow C_8H_6O+H_2O$). In addition, furan would further decompose through C-C/C-O cleavage to form linear molecules or free radicals, such as $HC{\equiv}CH$, CH_2CO, $CH_3C{\equiv}CH$, $HCCCH_2$, $CH_2CHCHCO$, CO, and H radical [33], which might be re-aromatized to form benzene or benzofuran. Under an oxidative atmosphere, with the increasing ER, the yield of benzofuran (in terms of peak area) decreased with that of benzene increasing, and other simpler aromatics such as phenol and toluene also appeared in the products. The total detected peak areas (except that for furfural) also

increased. It indicated that the introduction of oxygen promoted the decomposition of furfural and the formation of more aromatic products; the presence of oxygen would lead to the oxidative destruction of C-C/C-O bonds and the O removal of the furan ring (possibly forming CO and CO_2). More linear fractions or radicals apart from the abovementioned ones like CH_3, C≡CH, H_2C=CH, etc., might be generated under an oxidative atmosphere, thus resulting in a decrease in benzofuran and an increase in benzene, phenol, and toluene due to re-aromatization, especially at higher ERs. In addition, the furan might directly react with linear intermediates such as H_2C=CH and H_2C=$CHCH_3$ to form benzene and toluene through Diels–Alder condensation and dehydration reactions [34]. But, under too high an ER of 15%, the formation of these aromatics would also be inhibited.

3.2. Oxidative Pyrolysis of Hydroxyacetone Under Low ERs at 400 and 500 °C

Figure 3 shows the composition of products detected by GC-MS from the oxidative pyrolysis of hydroxyacetone under oxygen ERs of 0–15% at 400 and 500 °C. From Figure 3a, it can be seen that, at 400 °C, with the increasing ER, the peak area of hydroxyacetone decreased, indicating the promoted thermal decomposition/oxidation of hydroxyacetone in the presence of oxygen. But the peak areas of acetoin and acetylacetone also decreased, demonstrating that the decomposition of hydroxyacetone mainly generated permanent gases rather than condensable liquid products. The hydroxyacetone in the liquid product still accounted for ~96%, which was largely higher than the other products, showing the limited decomposition rate at 400 °C. From the perspective of liquid product composition, acetoin and acetylacetone were the major products from both non-oxidative and oxidative pyrolysis of hydroxyacetone. It might be inferred that hydroxyacetone (CH_3COCH_2OH) might undergo C-C and C-O cleavages to form CH_3CO, CH_3COCH_2, and CH_2OH intermediates, while (1) two CH_3CO would be coupled to form $CH_3COCOCH_3$, with one of the C=O bonds hydrogenated (with H radical) to form acetoin ($CH_3COCHOHCH_3$), and (2) CH_3CO and CH_3COCH_2 might also be coupled to form acetylacetone ($CH_3COCH_2COCH_3$). Although the presence of oxygen enhanced the cleavages of C-C and C-O bonds (illustrated by the decreased hydroxyacetone peak area), the coupling of the intermediates was inhibited with the decreased acetoin and acetylacetone under the oxidative atmosphere. It means that the further decomposition of these intermediates under an oxidative atmosphere might be strengthened with CO, CO_2, and hydrocarbon gases such as CH_4 releasing.

When the pyrolysis temperature increased to 500 °C (Figure 3b), the peak area of hydroxyacetone was further decreased compared to that at 400 °C, indicating that a higher temperature promoted the thermal decomposition of hydroxyacetone. But the presence of oxygen did not decrease the peak of hydroxyacetone, instead increasing the peak areas of other products, which means more condensable products formed under an oxidative atmosphere, especially acetoin. The presence of oxygen might promote the cleavage of the C-C bond connected with C=O in the hydroxyacetone molecule and the subsequent coupling of two CH_3CO, with more acetoin formation. While acetylacetone was not found in the product at 500 °C, instead, 2,3-pentanedione ($CH_3COCOCH_2CH_3$) and methyl glyoxal (CH_3COCHO) were observed with the ER at 6–15%. The formation of methyl glyoxal at a higher ER of 10% and 15% might be due to the oxidation of alcoholic hydroxyl in hydroxyacetone ($CH_3COCH_2OH+0.5O_2 \rightarrow CH_3COCHO+H_2O$), which was enhanced with more oxygen. Meanwhile, the formation of 2,3-pentanedione might be due to the intermolecular dehydration of $CH_3COCOCH_3$ and CH_2OH (aforementioned intermediates, $CH_3COCOCH_3+CH_3OH \rightarrow CH_3COCOCH_2CH_2+H_2O$), subsequently stabilized by the H radical ($CH_3COCOCH_2CH_2+H \rightarrow CH_3COCOCH_2CH_3$).

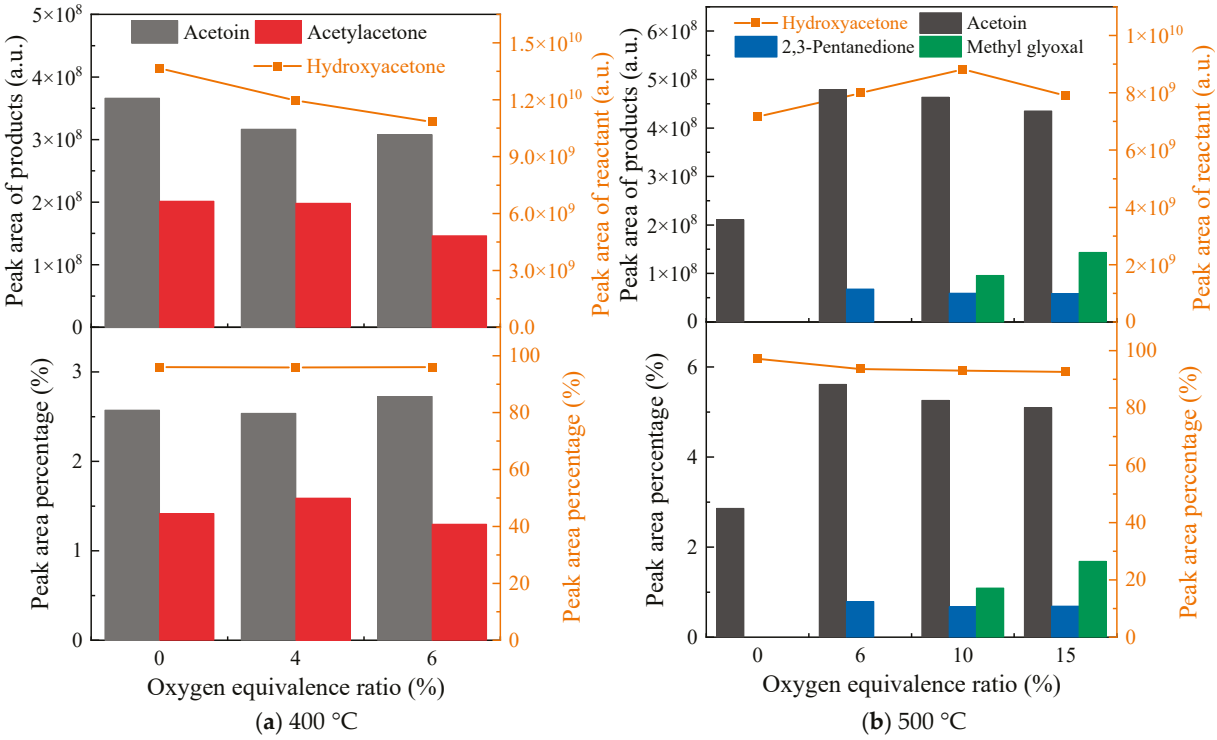


Figure 3. Composition of products detected by GC-MS from oxidative pyrolysis of hydroxyacetone under low oxygen ERs at (**a**) 400 and (**b**) 500 °C.

These findings confirm that pyrolysis temperature and oxygen introduction both significantly affect the thermal decomposition of hydroxyacetone. The presence of oxygen at a lower temperature (400 °C) promoted the decomposition and oxidation of hydroxyacetone to form more permanent gases, while the presence of oxygen at a higher temperature (500 °C) enhanced condensable liquid product formation, with their yields even higher than those at 400 °C, such as acetoin at an ER of 6%, although the yield of acetoin under a non-oxidative atmosphere was lower. The decomposition pathway of hydroxyacetone also changed at a higher temperature, with different products formed.

3.3. Oxidative Pyrolysis of 3,4-Dimethoxybenzaldehyde Under Low ERs at 400 and 500 °C

Figure 4 shows the composition of products detected by GC-MS from the oxidative pyrolysis of 3,4-dimethoxybenzaldehyde under oxygen ERs of 0–15% at 400 and 500 °C. From Figure 4a, it can be observed that the oxidative pyrolysis of 3,4-dimethoxybenzaldehyde only detected one product, i.e., 1,2-dimethoxybenzene, with the majority of the compound still being 3,4-dimethoxybenzaldehyde (~99.8%) at 400 °C. Although the presence of oxygen promoted the decomposition of 3,4-dimethoxybenzaldehyde with the observed decrease in the GC-MS peak area, the decomposition rate was not high, with a very low amount of 1,2-dimethoxybenzene formation. The content of 1,2-dimethoxybenzene even decreased at an ER of 6%, indicating that a higher ER might enhance the oxidation of these compounds to form permanent gases. The formation of 1,2-dimethoxybenzene ($C_6H_4(OCH_3)_2$) might be mainly due to the decarbonylation of the aldehyde (-CHO) group connected to the benzene ring ($CHOC_6H_3(OCH_3)_2 \rightarrow C_6H_4(OCH_3)_2+CO$), which might be enhanced in the presence of oxygen at a lower ER of 4%. But a higher ER might further oxidize it into permanent gases.

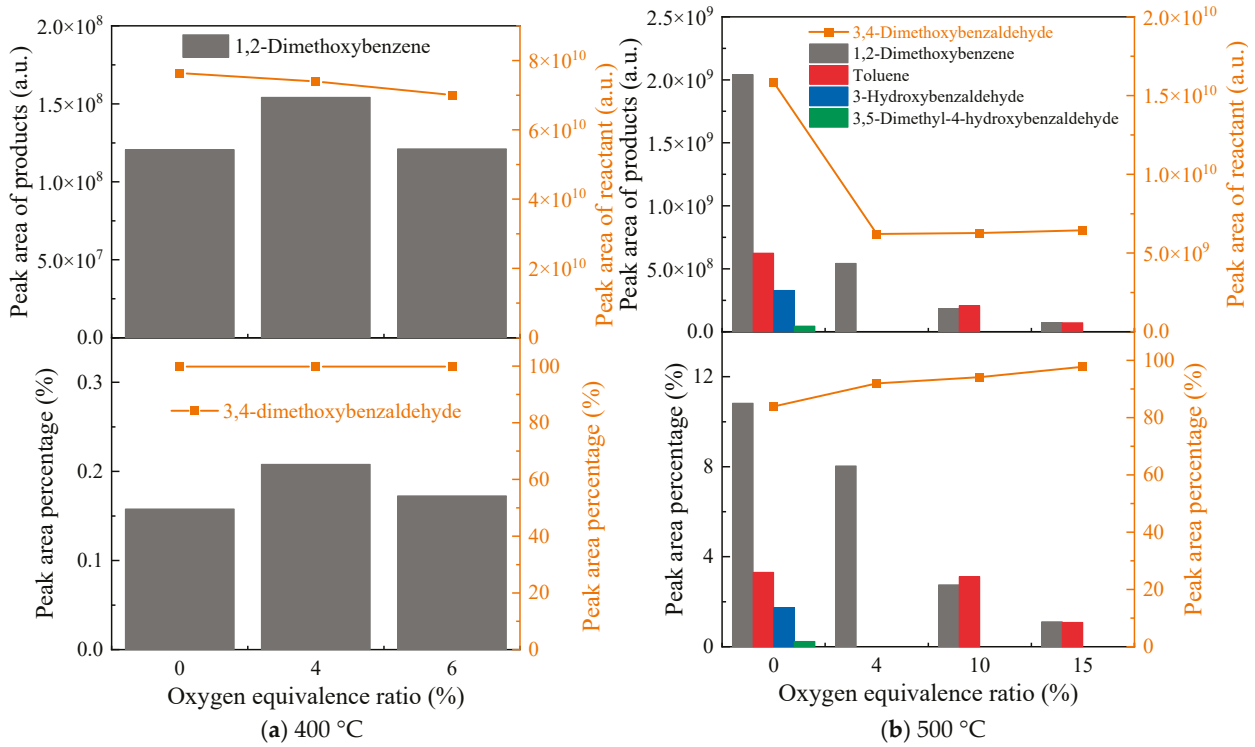


Figure 4. Composition of products detected by GC-MS from oxidative pyrolysis of 3,4-dimethoxybenzaldehyde under low oxygen ERs at (**a**) 400 and (**b**) 500 °C.

When the pyrolysis temperature increased to 500 °C (Figure 4b), under a non-oxidative atmosphere (ER of 0), it can be clearly seen that the peak area of 3,4-dimethoxybenzaldehyde was largely lower than that at 400 °C, indicating the significantly promoted thermal decomposition of 3,4-dimethoxybenzaldehyde at a higher temperature. The peak area of 1,2-dimethoxybenzene was nearly 16 times bigger than that at 400 °C, with more products such as toluene, 3-hydroxybenzadehyde, and 3,5-dimethyl-4-hydroxybenzaldehyde formed at a higher temperature. 1,2-Dimethoxybenzene was the major product followed by toluene and 3-hydroxybenzadehyde. The significantly enhanced direct decarbonylation of 3,4-dimethoxybenzaldehyde (forming 1,2-dimethoxybenzene) was the major reason. Furthermore, the 1,2-dimethoxybenzene ($C_6H_4(OCH_3)_2$) molecule could further remove the methoxy (OCH_3) group and combine with a methyl radical to form toluene (C_7H_8). The formation of 3-hydroxybenzadehyde ($CHOC_6H_4OH$) might be mainly due to the cleavage of the C_{Ar}-O and $C_{Methoxy}$-O bonds of 3,4-dimethoxybenzaldehyde ($CHOC_6H_3(OCH_3)_2$) to form $CHOC_6H_3O$, CH_3, and CH_3O intermediates, then stabilized by the H radical ($CHOC_6H_3(OCH_3)_2 \rightarrow CHOC_6H_3O+CH_3+CH_3O$, $CHOC_6H_3O+2H \rightarrow CHOC_6H_4OH$). Despite its low content in the product, 3,5-dimethyl-4-hydroxybenzaldehyde might be also formed through similar bond (connected to aromatic ring) cleavage and recombination with radicals (H and CH_3). However, an oxidative atmosphere would inhibit the formation of these compounds; not only was the peak area of 3,4-dimethoxybenzaldehyde largely decreased due to enhanced oxidative decomposition but also fewer compounds were detected in the products. Only 1,2-dimethoxybenzene and toluene were observed at 500 °C under an oxidative atmosphere. A higher temperature and an oxidative atmosphere were beneficial for the removal of the aldehyde group, possibly due to the enhanced decarbonylation reaction (forming CO) or the oxidation of the aldehyde group (CHO) to the carboxyl group (COOH) with a subsequent decarboxylation reaction (forming CO_2). A higher ER (e.g., 15%) would significantly enhance these reactions.

3.4. Further Discussion on Oxidative Pyrolysis of Typical Volatile Model Compounds

Figure 5 shows the peak areas of the three volatile model compounds in the products after oxidative pyrolysis under low oxygen ERs of 0–15% at 400–500 °C. The data were gathered from the above sections, with a focus on the comparison of the conversion rate of different compounds during oxidative pyrolysis under different operation conditions. It should be pointed out that the peak areas of different compounds do not represent the amount of such compounds, as the response factors (peak area to weight percentage) for different compounds vary largely. For instance, the volatilization of 3,4-dimethoxybenzaldehyde (22.33 wt.%) was largely lower than that of furfural (100 wt.%), but the peak area of 3,4-dimethoxybenzaldehyde in the product was greatly higher than that of furfural with less of both being decomposed under a non-oxidative atmosphere at 400 °C. But, for the same compound, the peak area can be used to compare the amounts of the compound obtained under different conditions.

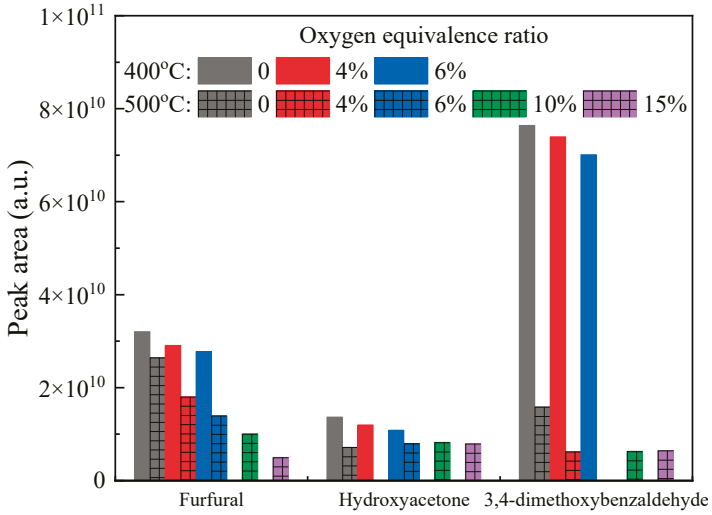


Figure 5. Comparison of oxidative pyrolysis of different volatile model compounds under low oxygen ERs and at 400–500 °C.

Temperature indeed plays an important role during both non-oxidative and oxidative pyrolysis of volatile compounds. For instance, the peak area of 3,4-dimethoxybenzaldehyde at 500 °C under an inert atmosphere (ER of 0) was only ~25% of that at 400 °C, and it further decreased to ~9% at an ER of 4% compared with that at 500 and 400 °C. At 400 °C, with the increasing ER, the peak areas of all three compounds decreased slightly, indicating that the oxidative decomposition of the volatile compounds at a lower temperature is limited. At 500 °C, with the increasing ER, the peak area of furfural showed a clear decreasing trend, and the peak area of hydroxyacetone just changed slightly, while the peak area of 3,4-dimethoxybenzaldehyde first decreased greatly and then was relatively stable. These results demonstrate that the oxidative pyrolysis characteristics of different volatile compounds vary greatly. One possible reason would be the chemical structure differences between different compounds, resulting in distinct reactivities. For instance, hydroxyacetone, as a linear compound with unsaturated bonds, is quite reactive. It can be decomposed quite sufficiently at a higher temperature, thus reducing the impact of oxygen introduction. Another possible reason would be their differences in autoignition temperatures. For instance, 3,4-dimethoxybenzaldehyde with a lower autoignition temperature (192 °C) would be more likely to be oxidatively decomposed [19], as illustrated by the larger decrease ratio in peak area with and without oxygen introduction (500 °C). Meanwhile, furfural with a higher autoignition temperature (392 °C) showed a lower decrease ratio but a continuous

decrease in peak area. For real volatiles, competitive oxidative pyrolysis is expected among different compounds, which necessitates further investigation.

4. Conclusions

Oxidative pyrolysis of three typical volatile model compounds under low ERs at 400 and 500 °C was conducted in a two-stage quartz-tube reactor. It was found that, at a lower temperature of 400 °C, the oxidative pyrolysis of volatiles was limited even with oxygen introduction, while a higher temperature of 500 °C significantly promoted the decomposition of volatile compounds with the observed great decrease in their peak areas. The presence of oxygen could enhance the decomposition of volatile compounds but showed very distinct impacts at different temperatures on varied volatile compounds possibly due to their different chemical structures and autoignition temperatures. During the pyrolysis process, the decomposition of volatile compounds mainly generated permanent gases rather than condensable liquid products. In terms of liquid product formation, furfural would undergo the cleavage of C-C/C-O bonds to form linear intermediates and subsequent aromatization to generate aromatics (benzene and benzofuran). The presence of oxygen could enhance the oxidative destruction of the C-C/C-O bonds and the removal of O from the molecules to form simple aromatics such as benzene, phenol, and toluene. Hydroxyacetone mainly underwent C-C/C-O cleavage that was further enhanced in the presence of oxygen; the resultant intermediates would recombine to generate acetoin and 2,3-pentanedione. A higher ER would directly oxidize the alcoholic hydroxyl group (-OH) into the aldehyde group (-CHO) to form methyl glyoxal, while 3,4-dimethoxybenzaldehyde mainly underwent cleavage and recombination of bonds connected with the benzene ring including aldehyde group (-CHO), C_{Ar}-O, $C_{Methoxy}$-O bonds, thus forming 1,2-dimethoxybenzene, toluene, and 3-hydroxybenzadehyde. This study further deepens the fundamental understanding of the homogeneous oxidation of volatiles during oxidative fast pyrolysis of biomass, offering possibility to selectively producing value-added products through biomass autothermal pyrolysis in the future.

Author Contributions: Conceptualization, B.L.; Methodology, X.X. and B.L.; Formal analysis, L.W.; Investigation, L.W.; Resources, X.X. and B.L.; Data curation, L.W.; Writing—original draft, L.W.; Writing—review & editing, D.L. (Dan Lin), D.L. (Dongjing Liu), S.Z. and B.L.; Supervision, X.X. and B.L.; Project administration, S.Z.; Funding acquisition, B.L. All authors have read and agreed to the published version of the manuscript.

Funding: This research was funded by the National Natural Science Foundation of China (52276196), the Foundation of State Key Laboratory of Coal Combustion (FSKLCCA2508), and the High-level Talent Foundation of Anhui Agricultural University (rc412307).

Data Availability Statement: The raw data supporting the conclusions of this article will be made available by the authors on request.

Conflicts of Interest: The authors declare no conflict of interest.

References

1. Uddin, M.N.; Techato, K.; Taweekun, J.; Rahman, M.M.; Rasul, M.G.; Mahlia, T.M.I.; Ashrafur, S.M. An Overview of Recent Developments in Biomass Pyrolysis Technologies. *Energies* **2018**, *11*, 3115. [CrossRef]
2. Liu, J.; Chen, X.; Chen, W.; Xia, M.; Chen, Y.; Chen, H.; Zeng, K.; Yang, H. Biomass pyrolysis mechanism for carbon-based high-value products. *Proc. Combust. Inst.* **2023**, *39*, 3157–3181. [CrossRef]
3. Qiu, B.; Tao, X.; Wang, J.; Liu, Y.; Li, S.; Chu, H. Research progress in the preparation of high-quality liquid fuels and chemicals by catalytic pyrolysis of biomass: A review. *Energy Convers. Manag.* **2022**, *261*, 115647. [CrossRef]
4. Pires, A.P.P.; Arauzo, J.; Fonts, I.; Domine, M.E.; Fernandez Arroyo, A.; Estrella Garcia-Perez, M.; Montoya, J.; Chejne, F.; Pfromm, P.; Garcia-Perez, M. Challenges and Opportunities for Bio-oil Refining: A Review. *Energy Fuels* **2019**, *33*, 4683–4720. [CrossRef]

5. Dodds, D.R.; Gross, R.A. Chemicals from Biomass. *Science* **2007**, *318*, 1250–1251. [CrossRef] [PubMed]
6. Li, C.; Zhao, X.; Wang, A.; Huber, G.W.; Zhang, T. Catalytic Transformation of Lignin for the Production of Chemicals and Fuels. *Chem. Rev.* **2015**, *115*, 11559–11624. [CrossRef]
7. Dai, L.; Wang, Y.; Liu, Y.; He, C.; Ruan, R.; Yu, Z.; Jiang, L.; Zeng, Z.; Wu, Q. A review on selective production of value-added chemicals via catalytic pyrolysis of lignocellulosic biomass. *Sci. Total Environ.* **2020**, *749*, 142386. [CrossRef]
8. Hu, B.; Zhang, Z.-x.; Xie, W.-l.; Liu, J.; Li, Y.; Zhang, W.-m.; Fu, H.; Lu, Q. Advances on the fast pyrolysis of biomass for the selective preparation of phenolic compounds. *Fuel Process. Technol.* **2022**, *237*, 107465. [CrossRef]
9. Zheng, A.; Chen, T.; Sun, J.; Jiang, L.; Wu, J.; Zhao, Z.; Huang, Z.; Zhao, K.; Wei, G.; He, F.; et al. Toward Fast Pyrolysis-Based Biorefinery: Selective Production of Platform Chemicals from Biomass by Organosolv Fractionation Coupled with Fast Pyrolysis. *ACS Sustain. Chem. Eng.* **2017**, *5*, 6507–6516. [CrossRef]
10. Mahmood, F.; Ali, M.; Khan, M.; Mbeugang, C.F.M.; Isa, Y.M.; Kozlov, A.; Penzik, M.; Xie, X.; Yang, H.; Zhang, S.; et al. A review of biochar production and its employment in synthesizing carbon-based materials for supercapacitors. *Ind. Crops Prod.* **2025**, *227*, 120830. [CrossRef]
11. Reza, M.S.; Iskakova, Z.B.; Afroze, S.; Kuterbekov, K.; Kabyshev, A.; Bekmyrza, K.Z.; Kubenova, M.M.; Abu Bakar, M.S.; Azad, A.K.; Roy, H.; et al. Influence of Catalyst on the Yield and Quality of Bio-Oil for the Catalytic Pyrolysis of Biomass: A Comprehensive Review. *Energies* **2023**, *16*, 5547. [CrossRef]
12. Lahijani, P.; Mohammadi, M.; Mohamed, A.R.; Ismail, F.; Lee, K.T.; Amini, G. Upgrading biomass-derived pyrolysis bio-oil to bio-jet fuel through catalytic cracking and hydrodeoxygenation: A review of recent progress. *Energy Convers. Manag.* **2022**, *268*, 115956. [CrossRef]
13. Wang, Y.; Akbarzadeh, A.; Chong, L.; Du, J.; Tahir, N.; Awasthi, M.K. Catalytic pyrolysis of lignocellulosic biomass for bio-oil production: A review. *Chemosphere* **2022**, *297*, 134181. [CrossRef]
14. Ren, X.; Ghazani, M.S.; Zhu, H.; Ao, W.; Zhang, H.; Moreside, E.; Zhu, J.; Yang, P.; Zhong, N.; Bi, X. Challenges and opportunities in microwave-assisted catalytic pyrolysis of biomass: A review. *Appl. Energy* **2022**, *315*, 118970. [CrossRef]
15. Ferreira, R.A.d.R.; Meireles, C.d.S.; Assunção, R.M.N.; Barrozo, M.A.S.; Soares, R.R. Optimization of the oxidative fast pyrolysis process of sugarcane straw by TGA and DSC analyses. *Biomass Bioenergy* **2020**, *134*, 105456. [CrossRef]
16. Van de Velden, M.; Baeyens, J.; Brems, A.; Janssens, B.; Dewil, R. Fundamentals, kinetics and endothermicity of the biomass pyrolysis reaction. *Renew. Energy* **2010**, *35*, 232–242. [CrossRef]
17. Huang, Y.; Li, B.; Liu, D.; Xie, X.; Zhang, H.; Sun, H.; Hu, X.; Zhang, S. Fundamental Advances in Biomass Autothermal/Oxidative Pyrolysis: A Review. *ACS Sustain. Chem. Eng.* **2020**, *8*, 11888–11905. [CrossRef]
18. Lu, T.; Lin, D.; Isa, Y.M.; Kozlov, A.; Penzik, M.; Xie, X.; Zhang, S.; Yang, H.; Li, B. Influence of oxygen equivalence ratio on biochar oxidation characteristics under biomass oxidative pyrolysis conditions in a fluidized-bed reactor. *J. Energy Inst.* **2025**, *119*, 101995. [CrossRef]
19. Brown, R.C. Heterodoxy in Fast Pyrolysis of Biomass. *Energy Fuels* **2020**, *35*, 987–1010. [CrossRef]
20. Karmee, S.K.; Kumari, G.; Soni, B. Pilot scale oxidative fast pyrolysis of sawdust in a fluidized bed reactor: A biorefinery approach. *Bioresour. Technol.* **2020**, *318*, 124071. [CrossRef]
21. Zhao, S.; Xu, W.; Chen, L. The modeling and products prediction for biomass oxidative pyrolysis based on PSO-ANN method: An artificial intelligence algorithm approach. *Fuel* **2022**, *312*, 122966. [CrossRef]
22. Polin, J.P.; Peterson, C.A.; Whitmer, L.E.; Smith, R.G.; Brown, R.C. Process intensification of biomass fast pyrolysis through autothermal operation of a fluidized bed reactor. *Appl. Energy* **2019**, *249*, 276–285. [CrossRef]
23. Siwal, S.S.; Zhang, Q.; Sun, C.; Thakur, S.; Gupta, V.K.; Thakur, V.K. Energy production from steam gasification processes and parameters that contemplate in biomass gasifier—A review. *Bioresour. Technol.* **2020**, *297*, 122481. [CrossRef]
24. Tezer, O.; Karabag, N.; Ongen, A.; Colpan, C.O.; Ayol, A. Biomass gasification for sustainable energy production: A review. *Int. J. Hydrogen Energy* **2022**, *47*, 15419–15433. [CrossRef]
25. Elwardany, M. Enhancing steam boiler efficiency through comprehensive energy and exergy analysis: A review. *Process Saf. Environ. Prot.* **2024**, *184*, 1222–1250. [CrossRef]
26. Zhu, S.; Lee, S.W. Co-combustion performance of poultry wastes and natural gas in the advanced Swirling Fluidized Bed Combustor (SFBC). *Waste Manag.* **2005**, *25*, 511–518. [CrossRef]
27. Kim, K.H.; Bai, X.; Rover, M.; Brown, R.C. The effect of low-concentration oxygen in sweep gas during pyrolysis of red oak using a fluidized bed reactor. *Fuel* **2014**, *124*, 49–56. [CrossRef]
28. Li, B.; Song, M.; Xie, X.; Wei, J.; Xu, D.; Ding, K.; Huang, Y.; Zhang, S.; Hu, X.; Zhang, S.; et al. Oxidative fast pyrolysis of biomass in a quartz tube fluidized bed reactor: Effect of oxygen equivalence ratio. *Energy* **2023**, *270*, 126987. [CrossRef]
29. Jiang, S.; Hu, X.; Wu, L.; Zhang, L.; Wang, S.; Li, T.; Xia, D.; Li, C.-Z. Oxidative pyrolysis of mallee wood biomass, cellulose and lignin. *Fuel* **2018**, *217*, 382–388. [CrossRef]

30. Zhao, S.; Luo, Y.; Zhang, Y.; Long, Y. Experimental Investigation of Rice Straw and Model Compound Oxidative Pyrolysis by in Situ Diffuse Reflectance Infrared Fourier Transform and Coupled Thermogravimetry–Differential Scanning Calorimetry/Mass Spectrometry Method. *Energy Fuels* **2015**, *29*, 4361–4372. [CrossRef]
31. Wang, S.R.; Dai, G.X.; Yang, H.P.; Luo, Z.Y. Lignocellulosic biomass pyrolysis mechanism: A state-of-the-art review. *Prog. Energy Combust. Sci.* **2017**, *62*, 33–86. [CrossRef]
32. Li, B.; Zhao, L.; Xie, X.; Lin, D.; Xu, H.; Wang, S.; Xu, Z.; Wang, J.; Huang, Y.; Zhang, S.; et al. Volatile-char interactions during biomass pyrolysis: Effect of char preparation temperature. *Energy* **2021**, *215*, 119189. [CrossRef]
33. Vasiliou, A.K.; Kim, J.H.; Ormond, T.K.; Piech, K.M.; Urness, K.N.; Scheer, A.M.; Robichaud, D.J.; Mukarakate, C.; Nimlos, M.R.; Daily, J.W.; et al. Biomass pyrolysis: Thermal decomposition mechanisms of furfural and benzaldehyde. *J. Chem. Phys.* **2013**, *139*, 142386. [CrossRef]
34. Cheng, Y.-T.; Huber, G.W. Production of targeted aromatics by using Diels–Alder classes of reactions with furans and olefins over ZSM-5. *Green Chem.* **2012**, *14*, 3114–3125. [CrossRef]

Disclaimer/Publisher's Note: The statements, opinions and data contained in all publications are solely those of the individual author(s) and contributor(s) and not of MDPI and/or the editor(s). MDPI and/or the editor(s) disclaim responsibility for any injury to people or property resulting from any ideas, methods, instructions or products referred to in the content.

energies

MDPI

Article

Numerical Investigation of Combustion Characteristics in a 330 MW Coal-Fired Boiler with Preheating Combustion Devices at Half Load Operation

Siyuan Wang *, Hong Tang, Zuodong Liu, Lingfang Sun and Zhiming Xu

School of Energy and Power Engineering, Northeast Electric Power University, Jilin 132012, China
* Correspondence: wsyneepu@163.com

Abstract

To reduce the impact of renewable energy generation on power grid stability, preheating combustion technology is introduced to maintain coal-fired boiler efficiency at low loads. A 330 MW coal-fired boiler is retrofitted with preheating combustion devices to improve combustion performance and lower NO_x emissions. The device is installed in the reduction zone between the furnace burnout zone and the burner zone. The combustion characteristics of the boiler with and without these devices are examined at 50% rated load. Numerical simulations are conducted to analyze the effects of preheating coal input and burner arrangement on temperature and species distribution within the boiler. Results show that increasing preheating coal input from 0 to 30 t/h enhances NO_x reduction due to a higher flow rate of preheated products. At a preheating coal input of 20 t/h, the combustion efficiency reaches 96.9%. The NO_x concentration at the furnace exit rises from 122.4 to 171.3 mg/Nm^3 as the height of the burner arrangement increases. The middle three-layer burner arrangement achieves a uniform temperature distribution and a peak combustion efficiency of 97.6%. The bottom and middle three-layer burner arrangements are recommended for efficient and clean combustion. Compared to the original boiler, the retrofitted boiler's combustion efficiency increases from 96.3% to a maximum of 97.6%, while the NO_x concentration at the furnace outlet drops from 168.1 to 93.2 mg/Nm^3, showing that installing preheating combustion devices promotes efficient and clean combustion.

Keywords: preheating combustion; low load; burner arrangement; NO_x emission

1. Introduction

China possesses the world's most extensive power generation and transmission system, where stable grid operation is essential. Renewable energy development has rapidly grown in China to achieve low-carbon emissions from power generation [1]. However, the intermittence and instability of the renewable energy generation present serious challenges to the stable operation of the grid [2]. Based on the context, the role of coal-fired power plants has transitioned from a fundamental power source to a regulating power source [3]. Due to the absence of flexible power sources, such as gas/oil-fired power, pumped storage power, and electrochemical energy storage, utility boilers need advanced peak shaving capabilities to accommodate large-scale renewable energy generation. Consequently, low-load operation (below 50% rated load) of coal-fired boilers has become inevitable [4]. These boilers are designed to operate optimally at more than 70% rated load. The boiler load regulation departs from its designed operating conditions, introducing many issues to the

safe and stable operation. Low-load operation reduces the combustion temperature in the furnace, resulting in unstable combustion or even flameout. Moreover, the reduced flue gas temperature can deactivate catalysts in the selective catalytic reduction (SCR) reactor, resulting in higher nitrogen oxide emissions [5].

To achieve peak load regulation in coal-fired boilers, researchers have proposed flexibility retrofit strategies for stable combustion at low loads, such as ignition enhancement, burner arrangement optimization, and operating oxygen control [6]. Liu [7] investigated the effects of burner arrangement, horizontal swing angle, and methane co-burning on the temperature distribution and pollutant emissions in a 350 MW coal-fired boiler at 20% rated load. The results revealed that increasing the proportion of methane co-burning was conducive to the pulverized coal ignition and raised the average temperature in the furnace. The boiler operating with the AB-layer burners achieved the optimal and lowest NO emissions. The average temperature of the burner area with a swing angle of 15° reached 1559 K. Additionally, Chen [6] investigated the combustion behavior of a 300 MW subcritical boiler at full load and 25% rated load. The results showed that the average temperature in the furnace at ultra-low load was 225.98 K lower than at full load. The two-layer burner operation resulted in more intense combustion and higher NO_x formation during the combustion process. The arrangement of middle burners improved heat transfer in the furnace and reduced NO_x emissions. Jiang [8] performed numerical simulations on optimizing burner configuration, air distribution, and stoichiometric ratio (SR) to improve combustion performance at half load of a 550 MW coal-fired boiler. The results demonstrated that the BCDE-layer burner configuration created an optimal aerodynamic field and lowered NO_x emissions. The combustion process in the furnace was governed by the ratio of close-coupled overfire air (CCOFA) to separated overfire air (SOFA), with optimal combustion efficiency and pollutant emission levels achieved at a CCOFA-to-SOFA ratio of 1:3. Furthermore, a higher SR decreased the average temperature in the furnace and increased pollutant emissions. Wang [9] conducted numerical studies on the combustion process and pollutant emissions at various loads for a 600 MW wall-fired boiler with an SR of 0.95 in the main combustion zone. At low loads, a high oxygen concentration area at the bottom of the furnace indicated incomplete combustion. Changes in boiler load and burner arrangement significantly affected the residence time of pulverized coal in the furnace. During load regulation, maintaining a reasonable combustion temperature and SR was essential for efficient boiler operation. Ma [10] simulated the effects of different loads and excess air ratios on combustion characteristics in tangentially fired, wall-fired, and down-fired boilers. The findings revealed that when the load was below 50%, the temperature in the burner zone dropped sharply, leading to ignition delay and increased NO formation in all three boilers. The down-fired boiler had the smallest temperature drop but the highest NO_x emissions. Moreover, reducing the excess air ratio improved combustion efficiency and decreased pollutant emissions.

Preheating combustion technology is a practical approach to achieving efficient and clean combustion for coal-fired boilers during low-load operation [11,12]. The principle of preheating combustion is to preheat part of the fuel at an SR far less than 1. The fuel nitrogen is converted into nitrogen during this process, and the preheated fuel produces reducing gases. The reducing gases subsequently reduce the nitrogen oxides produced by the combustion in the furnace chamber, leading to a decrease in NO_x emissions [13]. Recently, research on preheating combustion has made significant progress. Lv [14] experimentally investigated the co-firing characteristics of bituminous coal and sewage sludge using a two-stage preheating and combustion test device. The impacts of parameters in the preheating region and the SR in the combustion region on combustion efficiency and NO formation were studied. The experimental results showed that preheating temperature

higher than 1000 °C significantly promoted the generation of reductive gas (H_2/CO/CH_4), with the maximum NO reduction rate of 48.3%. Increasing temperature inhibited NO formation in the combustion region when SR was less than 0.8. Wang [15] conducted both conventional and preheating combustion experiments on semi-coke produced at three different temperatures. The study examined how preheating temperature and combustion patterns affected nitrogen oxides and particulate matter formation. The results showed that preheating combustion with a stronger reducing atmosphere simultaneously lowered NO and particulate matter sources. Additionally, increasing the preheating temperature reduced NO and particulate matter emissions under conventional combustion conditions. In CFD studies on preheating combustion technology, Yao [16,17] numerically investigated the flow field, fuel–nitrogen conversion, and temperature distribution in a pulverized coal preheating burner. The findings indicated that decreasing the excess air ratio increased particle residence time, inhibited char conversion, and reduced flame rigidity. The syngas fraction decreased with rising excess-air coefficient, while the fuel–nitrogen conversion rate followed the opposite trend. Tang [18] performed a numerical assessment of the effects of self-sustaining burners on the performance of a 600 MW utility boiler. The findings revealed that after the burner retrofit, the enhanced rigidity of the coal stream improved furnace combustion stability. The reducing gases and char produced by preheating combustion helped enhance combustion efficiency and lower NO emissions. Zhang [19] conducted numerical simulations to compare the combustion performance of a preheating burner with a swirl burner. The results showed that the preheating burner had better combustion stability at low load compared to the swirl burner, which maintained stable combustion at a minimum load of 15%. At 15% load, optimizing primary and secondary air ratios enabled the preheating burner to sustain stable combustion with an efficiency of 98.6%. Existing numerical simulation studies on preheating combustion have primarily focused on its application in burners, with limited research conducted on its implementation in utility boilers.

Current experimental research on preheating combustion mainly focuses on the combustion and emission characteristics during the preheating stage, with few applications reported in coal-fired boilers. This study comprehensively analyzes the effects of the preheating combustion on the combustion performance of a coal-fired boiler operating at 50% rated load. The boiler was retrofitted by installing preheating combustion devices around the furnace. Numerical simulations compare the combustion characteristics and pollutant emissions between the original and the retrofitted boiler at half load. The effects of preheating coal input on the boiler's temperature field and species distribution are examined. Additionally, a detailed analysis of the combustion characteristics of the retrofitted boiler under various burner arrangements is performed. The simulation results for the boiler equipped with preheating combustion devices show higher combustion efficiency and lower NO_x emissions, providing references for the efficient operation of coal-fired boilers under low loads.

2. Methodology

2.1. Retrofit Scheme and Boiler Description

Our previous work established a full-scale preheating combustion device and conducted experimental investigations. The details of the device, including the configuration, experimental procedures, and results, are provided in the literature [20]. Preheating combustion is a technology that enhances combustion performance by preheating the fuel in advance at a SR of less than 1. Figure 1 illustrates the operational principle of the preheating combustion technology. The char particle size decreases through pulverized coal's devolatilization and gasification reactions, and part of the fuel shifts from solid to

gaseous states. Compared to the original pulverized coal stream, the activation energy of the preheated product is significantly lower, and the jet intensity is greatly increased, thus improving the combustion reaction. During the preheating stage, most fuel nitrogen is converted into nitrogen due to the reducing atmosphere, which helps reduce nitrogen oxide formation in subsequent combustion reactions. Therefore, preheating combustion achieves efficient and clean combustion in coal-fired boilers. A tangentially fired boiler was retrofitted with preheating combustion devices to address issues such as combustion instability, low efficiency, and high pollutant emissions during low-load boiler operation. After the retrofit, the furnace is divided into three functional sections: the burner zone, reduction zone, and burnout zone. The NO produced in the burner zone is reduced by the injection of preheated products in the reduction zone. Subsequently, the air injection in the burnout zone ensures complete combustion by oxidizing residual combustibles.

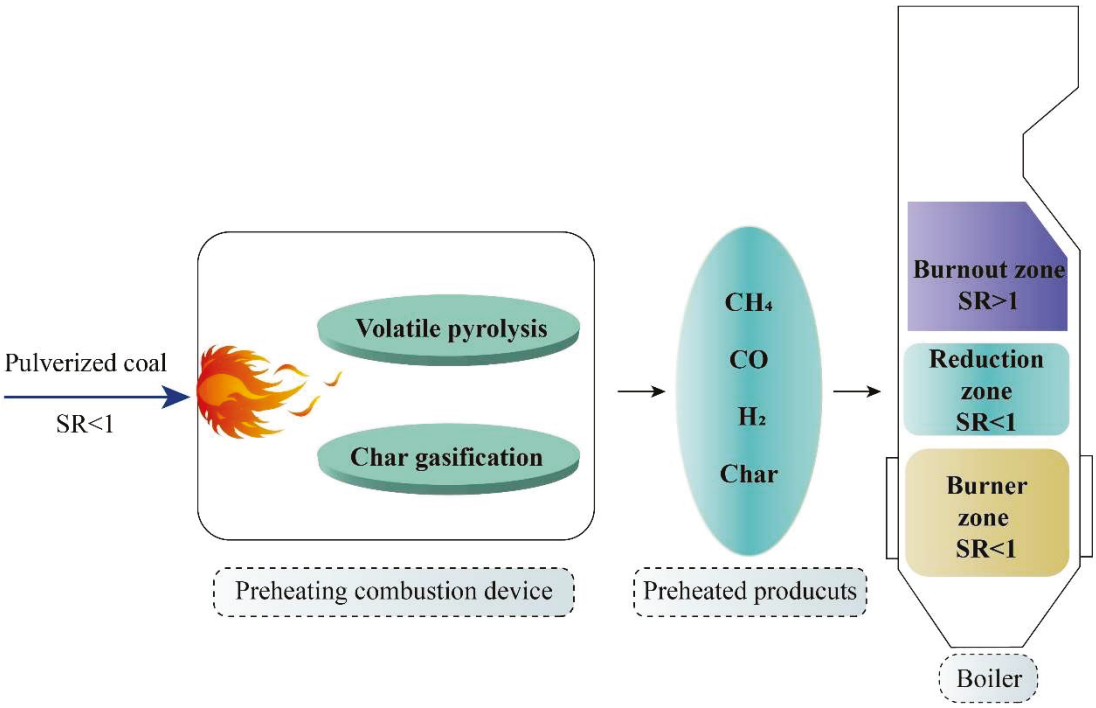


Figure 1. Schematic diagram of preheating combustion technology.

The original boiler is a tangentially coal-fired boiler with a rated electric power of 330 MWe. The boiler's pulverizing system consists of five medium-speed coal mills with four in full-load operation. Figure 2a shows the location of the oblique section plane P1. P1 is the longitudinal oblique section of the boiler used for data analysis. Figure 2b shows the burner arrangement and construction of the retrofitted boiler. The burners are arranged in a corner-tangential configuration, with five layers (A to E) vertically positioned along the furnace height. A group of preheated-product nozzles is installed at a boiler height of 23.5 m to establish the reduction zone. The burnout zone in the upper furnace consists of 16 separated overfire air (SOFA) nozzles located between 27.3 m and 29.6 m in furnace height. The pulverized coal nozzles and secondary air nozzles are arranged in an alternating pattern, with the centerlines of the nozzles forming a co-rotating imaginary circle in the furnace center. One of the advantages of preheating combustion technology is that it uses the same pulverizing system as the original boiler, thus eliminating the need for additional pulverized coal preparation, storage, and conveying equipment. A bypass is installed on the pulverized coal pipe from the E-layer mill to supply coal to the preheating combustion device.

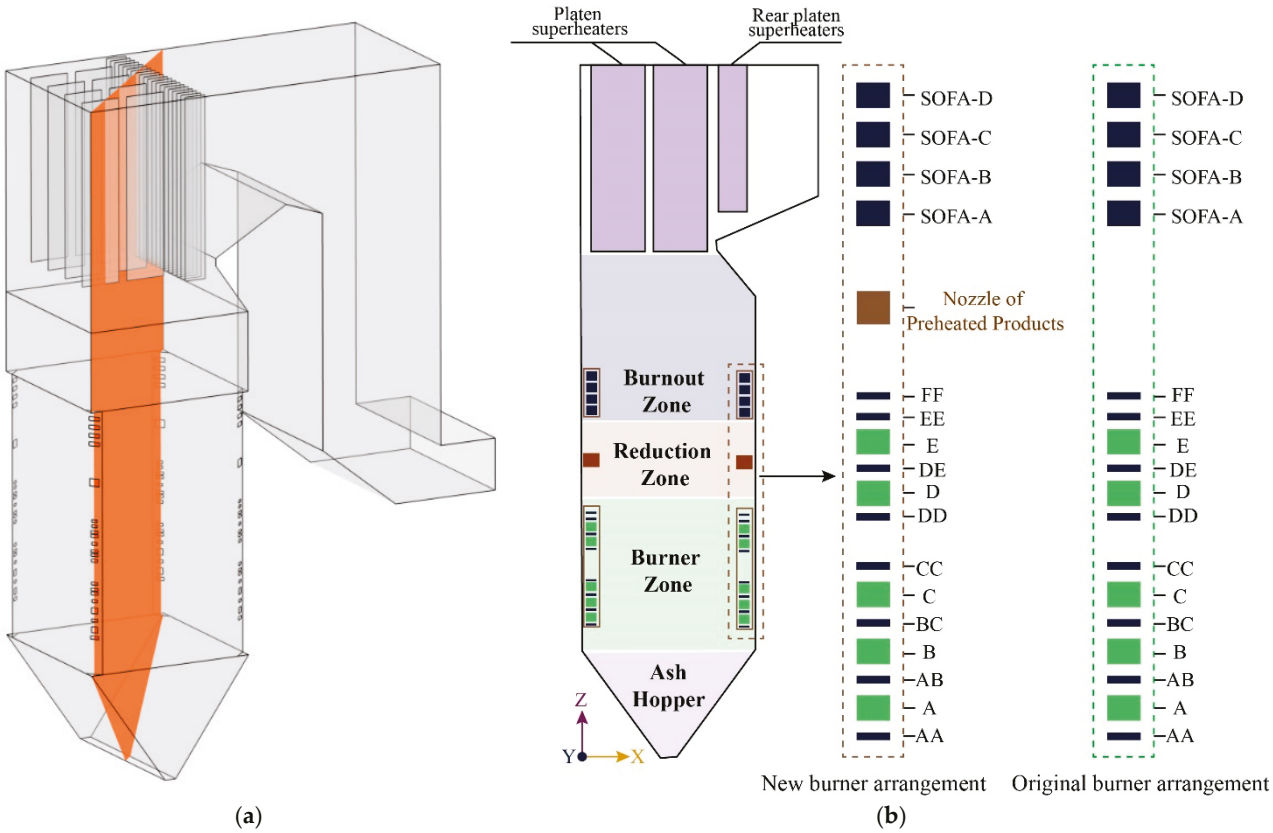


Figure 2. (**a**) Location of the plane P1; (**b**) Schematic of boiler construction and burner arrangement before and after retrofit.

2.2. Cases Setup

The combustion characteristics of the boiler before and after retrofit were numerically simulated at 50% rated load. Table 1 details the key parameters for the boiler operating at 50% rated load. A three-lay burner configuration is typically employed at 50% load during actual boiler operation. The case setup of different preheating coal inputs and burner arrangements is shown in Table 2. Case 1 is the baseline for the original boiler, used to compare its combustion performance with that of the retrofitted boiler. Cases 2–4 examine the effects of preheating coal input of 10 t/h, 20 t/h, and 30 t/h on the combustion characteristics of the retrofitted boiler. The parameters of the products at the outlet of the preheating combustion device are listed in Table 3. Field tests on the preheating combustion device measured the gas–solid flow rate, gas composition, and product temperature at the outlet in detail. The parameters of the preheating product serve as boundary conditions for the reduction zone nozzle. The simulation results show that a preheated fuel flow rate of 20 t/h exhibits the highest combustion efficiency and the low NO_x emissions. Consequently, the study on the effect of burner arrangement on boiler combustion characteristics was performed with a preheated fuel flow rate of 20 t/h. For cases 3 and 5–7, with a preheated fuel input of 20 t/h, the influence of different burner arrangements on the retrofit boiler's combustion properties is analyzed.

Table 1. Operating parameters of the boiler at 50% rated load.

Item	Value
Electrical load (MW)	165
Excess air ratio	1.2
Total coal flow rate (t/h)	95.2

Table 1. *Cont.*

Item	Value
Total air flow rate (t/h)	805.1
Primary air (PA) temperature (K)	343
Secondary air (SA) temperature (K)	567

Table 2. Simulation setup and operating parameters for different cases.

Case Number	Case 1 (Original Boiler)	Case 2	Case 3	Case 4	Case 5	Case 6	Case 7
Burners in operation	ABC	ABC	ABC	ABC	ABD	BCD	CDE
Preheating coal input (t/h)	0	10	20	30	20	20	20
Preheating air mass-flow rate (t/h)	0	25	50	75	50	50	50
Mass flow rate of PA (t/h)	240.3	236.3	232.4	228.4	232.4	232.4	232.4
Mass flow rate of SA (t/h)	364.5	358.5	352.4	346.4	352.4	352.4	352.4
Mass flow rate of SOFA (t/h)	200.3	200.3	200.3	200.3	200.3	200.3	200.3

Table 3. Experimental data at the outlet of the preheating combustion device.

Preheating Coal Input (t/h)	SR	CO (%)	CO_2 (%)	CH_4 (%)	H_2 (%)	N_2 (%)	Flow Rate of Char (t/h)	Flow Rate of Gas (t/h)	Temperature of Gas (K)
10	0.42	11.21	8.06	1.14	8.78	70.81	3.44	31.56	926
20	0.42	11.76	7.73	1.33	9.12	70.06	6.81	63.19	1006
30	0.42	12.03	7.48	1.59	9.60	69.30	10.10	94.90	1121

The simulation uses bituminous coal with particle size following the Rosin–Rammler distribution. Table 4 presents the relevant parameters that describe the pulverized coal. Based on actual boiler operation data, the inlet boundary conditions for the pulverized coal and air nozzles are set as mass flow inlets. The boiler outlet is defined as a pressure outlet with a pressure of −50 Pa. All heating surfaces of the boiler are modeled as no-slip wall boundary conditions. To balance calculating accuracy and efficiency, it is acceptable to model the platen and rear platen superheaters as walls without thickness [21]. The wall temperatures of the platen and rear platen superheaters are 693 K and 759 K, respectively.

Table 4. Coal properties.

Ultimate Analysis (Dry Ash Free, wt%)					Proximate Analysis (As Received, wt%)				R-R Distribution			
C	H	O	N	S	Fixed Carbon	Volatile	Moisture	Ash	d_{min}	d_{mean}	d_{max}	Spread parameter
75.7	4.3	18.1	1.2	0.7	38.7	24.4	25.2	11.7	6 μm	69 μm	230 μm	1.1

2.3. Numerical Models

The turbulent flow, heat transfer, and chemical reactions during pulverized coal combustion are modeled using Ansys Fluent 2020 R2. The conservation equations of species transport, mass, momentum, and energy for the gas phase are expressed as below:

$$\nabla \cdot (\rho u Y_j) = -\nabla \cdot J_j + R_j + S_j \quad (1)$$

$$\nabla \cdot (\rho u) = S_{ma} \quad (2)$$

$$\nabla \cdot (\rho u u) = -\nabla p + \nabla \cdot \tau + \rho g + S_{\mathrm{mo}} \tag{3}$$

$$\nabla \cdot (\rho u h) = \tau : \nabla \cdot u - \nabla \cdot q - \nabla \cdot \left[\sum_j h_j J_j \right] + S_{\mathrm{h}} \tag{4}$$

The velocity-pressure coupling is solved using the SIMPLE method. The turbulent flow of the gas phase within the boiler is simulated using the Realizable k-epsilon model [22]. By introducing modifications to the turbulent dissipation rate (ε) equation, this model significantly improves the prediction accuracy for complex turbulent flows. It performs well when simulating flow with rotation, vortices, and jet diffusion [23]. The turbulence kinetic energy (k) and the dissipation rate (ε) in the model are defined as:

$$\frac{\partial(\rho k u_i)}{\partial x_j} = \frac{\partial}{\partial x_j}\left[\left(\mu + \frac{\mu_t}{\sigma_k} \right) \frac{\partial k}{\partial x_j} \right] + G_k + G_b - \rho\varepsilon \tag{5}$$

$$\frac{\partial(\rho \varepsilon u_i)}{\partial x_j} = \frac{\partial}{\partial x_j}\left[\left(\mu + \frac{\mu_t}{\sigma_\varepsilon} \right) \frac{\partial \varepsilon}{\partial x_j} \right] + \rho C_1 S \varepsilon - \rho C_2 \frac{\varepsilon^2}{k + \sqrt{\nu\varepsilon}} + C_{1\varepsilon} \frac{\varepsilon}{k} C_{3\varepsilon} G_b \tag{6}$$

In Equation (6), $C_1 = \max\left[0.43, \frac{\eta}{\eta+5}\right]$ with $\eta = S\frac{k}{\varepsilon}$, $S = \sqrt{2S_{ij}S_{ij}}$ and $S_{ij} = \frac{1}{2}(\frac{\partial u_j}{\partial x_i} + \frac{\partial u_i}{\partial x_j})$; $C_2 = 1.9$, $C_{1\varepsilon} = 1.44$ and $C_{3\varepsilon} = 0$.

The discrete phase model (DPM) simulates particle behaviors in the continuous phase. The motion of particles is described by the flow field of the continuous phase; in turn, changes in the energy, momentum, and mass of the particles influence the flow field of the continuous phase [24]. DPM achieves two-way coupling between the discrete and continuous phases by calculating flow field parameters and particle source terms. The simulation employs the DO model [25] to compute radiation heat transfer in the furnace because of its high computational accuracy and wide applicability in radiative heat transfer scenarios. The absorption coefficient of the gas phase is obtained through the weighted-sum-of-gray-gas model (WSGGM) [26]. The scattering factor and emissivity of particles are set to 0.6 and 0.9, respectively [27]. The finite rate/eddy dissipation model [28] calculates the turbulent chemical reactions of the gas phase. The model generates a hypothetical volatile compound with the molecular formula ($C_{3.08}H_{10.4}O_{2.95}N_{0.184}S_{0.0818}$) based on coal composition when modeling volatile combustion [29]. Volatile combustion is described by a two-step reaction mechanism, with CO as the intermediate species. The two-competing-rate model proposed by Kobayashi [30] calculates the kinetic devolatilization rate across different temperature ranges, with the expressions of the kinetic devolatilization rate given as:

$$R_1 = A_1 \exp^{(-E_1/RT_p)} \tag{7}$$

$$R_2 = A_2 \exp^{(-E_2/RT_p)} \tag{8}$$

R_1 and R_2 are competing rates that may govern the devolatilization at low and high temperatures, respectively. The kinetic parameters are derived from similar coal properties in the literature [31], and the activation energies E_1 and E_2 are set at 1.046×10^8 J/kmol and 1.674×10^8 J/kmol, respectively, while the pre-exponential factors A_1 and A_2 are set at 2×10^5 s^{-1} and 1.3×10^7 s^{-1}. By weighting the two kinetic rates, the expression of the devolatilization rate is presented as:

$$\frac{m_v(t)}{(1 - f_{w,0})m_{p,0} - m_a} = \int_0^t (\alpha_1 R_1 + \alpha_2 R_2) \exp\left(- \int_0^t (R_1 + R_2) dt \right) dt \tag{9}$$

The kinetic/diffusion-limited model [32] simulates the char combustion reaction. In the model, gas–solid reactions are typically controlled by both combustion kinetics and oxidant diffusion, and the expression of char combustion rate is:

$$\frac{dm_p}{dt} = -\pi d_p^2 p_{ox} \frac{D_0 R_p}{D_0 + R_p} \tag{10}$$

In this simulation, NO_x formation is modeled using a post-processing method within ANSYS Fluent, considering two primary pathways: fuel-NO_x and thermal-NO_x. The thermal-NO_x calculation follows the extended Zeldvich mechanism [33]. The formation of thermal-NO_x depends on the temperature and oxygen concentration. The atomic oxygen concentration is derived from the partial equilibrium assumption in the model. The reaction expressions dominating thermal-NO_x generation are:

$$O + N_2 \underset{k_{r1}}{\overset{k_{f1}}{\rightleftharpoons}} N + NO \tag{11}$$

$$N + O_2 \underset{k_{r2}}{\overset{k_{f2}}{\rightleftharpoons}} NO + O \tag{12}$$

$$N + OH \underset{k_{r3}}{\overset{k_{f3}}{\rightleftharpoons}} H + NO \tag{13}$$

Additionally, the net generation rate of thermal-NO_x is given as:

$$\frac{d[NO]}{dt} = 2\, k_{f1}[O][N_2] \frac{\left(1 - \frac{k_{r1}k_{r2}[NO]^2}{k_{f1}[N_2]\, k_{f2}[O_2]}\right)}{1 + \frac{k_{r1}[NO]}{k_{f2}[O_2] + k_{f3}[OH]}} \tag{14}$$

The De Soete model [34] predicts the formation of fuel-NO_x. Figure 3 illustrates the reaction pathways involved in the generation of fuel-NO_x. Fuel-bound nitrogen is mainly found in both the char and volatile matter. During volatile-N conversion, it is initially transformed into intermediate species such as HCN and NH_3, with about 90% released as HCN [35]. The char-N is assumed to be oxidized into NO. The NO_x reduction sub-model activates to simulate the reducing effects of CH_4 and H_2 in preheating products on the NO produced during pulverized coal combustion.

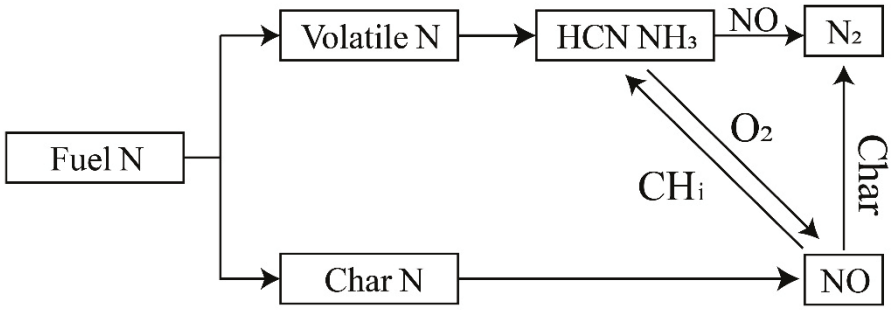
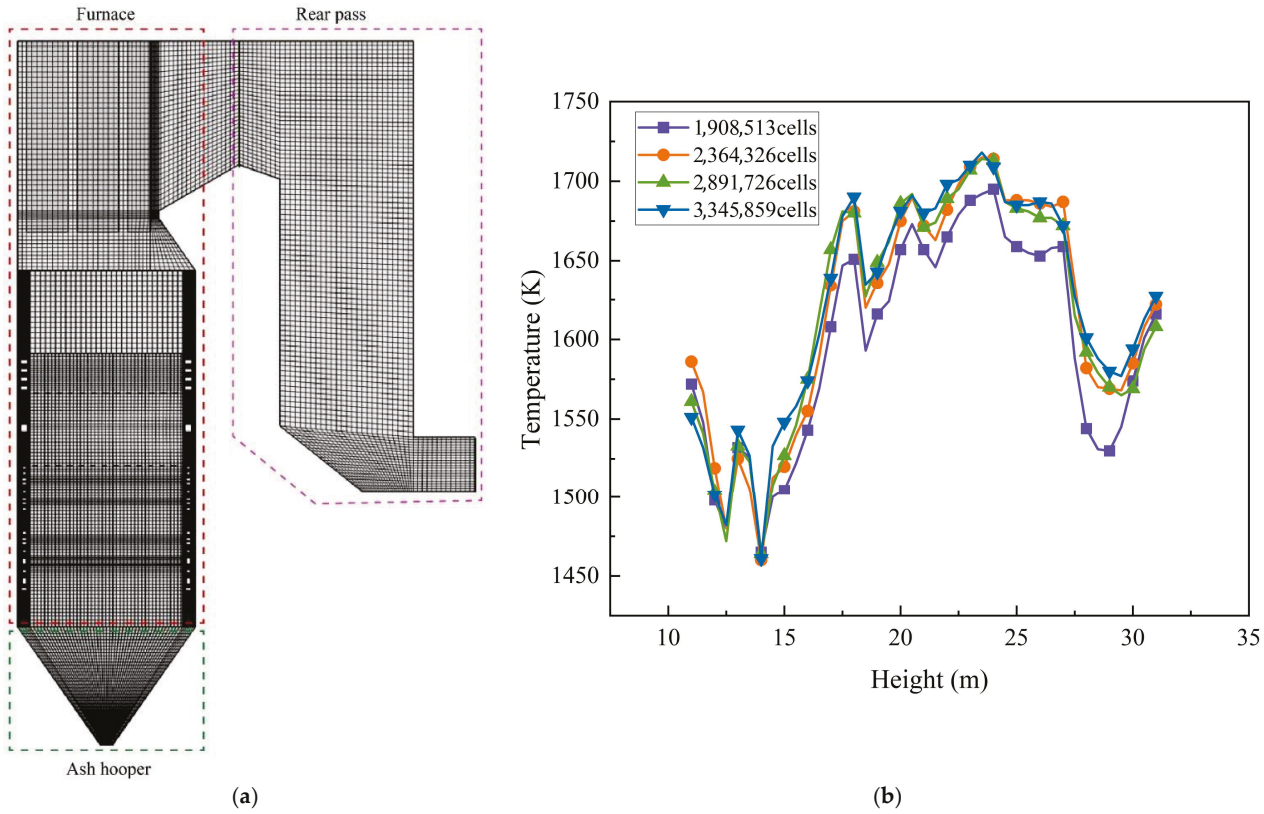


Figure 3. Detailed reaction pathways of the fuel-N.

2.4. Mesh System and Numerical Model Validation

Based on a 1:1 three-dimensional boiler model, the ICEM software is used to create a hexahedral-dominated grid. The computational domain extends to the rear pass to avoid uncertainties caused by outlet backflow in the in-furnace combustion process [36]. As shown in Figure 4a, the boiler's domain mainly includes the ash hopper, the furnace chamber, and the rear pass. Grid refinement is performed to accurately simulate flow,

heat transfer, and combustion in high-gradient regions. To eliminate the effect of grid size on computational accuracy, four sets of progressively refined grids are created for grid independence validation, with grid numbers ranging from 1.9 million to 3.3 million. Figure 4b compares cross-sectional average temperatures along the furnace height with different grid numbers. The results indicate that, aside from the 1.9-million-cell grid, the other three grids show negligible deviations. Considering the simulation accuracy and computational cost, the 2.36-million-cell grid is chosen for numerical simulation.



(**a**) (**b**)

Figure 4. Boiler mesh and mesh independence test. (**a**) Right view of boiler mesh. (**b**) Average temperature for mesh independence test.

The reliability of the numerical models is confirmed by comparing the calculated values with the actual measured data of the boiler. Field measurements were conducted at the SCR inlet to measure the O_2 and NO_x concentrations in the flue gas. Table 5 compares calculated and test values of the original and retrofitted boiler at full load. The calculated results agree well with the experimental data, with a maximum relative error of 6.1%. This confirms that the selected models are dependable for numerical simulations.

Table 5. Comparison between the experimental data and simulated data.

Item	330 MW (Original)			330 MW (Retrofitted)		
	Measured	**Simulated**	**Error**	**Measured**	**Simulated**	**Error**
O_2 (%)	2.98	3.16	6.0%	2.12	2.04	3.8%
NO_x (mg/m^3, at 6% O_2)	185.7	194.5	4.7%	126.7	121.1	4.4%
Gas temperature at the furnace outlet (K)	1279 (design value)	1200.1	6.1%	/	1254.9	/

3. Results and Discussion

3.1. Effect of Preheating Coal Input on Combustion Characteristics

3.1.1. Average Temperature Distribution

Figures 5 and 6 show the average temperature distribution with the preheating coal feeding rate from 0 t/h to 30 t/h. In the original boiler, all coal burns directly in the burner zone. After the retrofit, only part of the coal burns in the burner zone, while the preheated products are then combusted in the reduction zone. As a result, case 1 has the highest average furnace temperature before the burnout zone. As the preheating fuel input increases, the average temperature in the burner zone decreases gradually. More preheating fuel reduces coal feed rate and heat release in the burner zone. Since some fuel and air burn in the preheating combustion device at a SR of 0.42, the SR in the burner zone rises with the increase in preheating coal feed rate. Therefore, case 4 has the lowest coal feed rate and the highest SR in the burner zone, leading to the lowest average temperature and unstable combustion. The preheated products include char and reducing gases such as H_2, CH_4, and CO. When the preheated products are introduced at a furnace height of 23.5 m, their temperature is lower than the surrounding flue gas, causing a significant temperature drop in the reduction zone. Case 4, with the most considerable preheating fuel input, results in the greatest heat release and the highest average temperature in the reduction zone. In the burnout zone, the retrofitted boiler shows a notable temperature increase due to the preheated products, indicating that the reactive preheated products achieve complete combustion in this region.

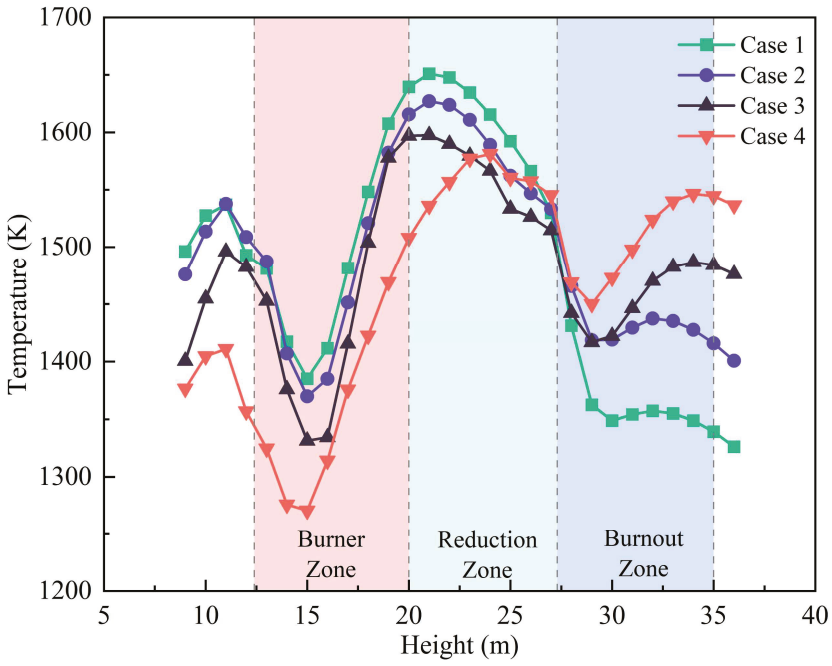


Figure 5. Cross-sectional average temperature in the furnace under different preheating coal input.

According to the temperature contours in Figure 6, as the preheating coal input increases, the high-temperature zone inside the furnace shifts noticeably upward, and the temperature distribution becomes more uniform. In case 4, which has the lowest coal feed rate and an SR value of 1.13 in the burner zone, the ignition heat of the pulverized coal stream increases. This leads to an ignition delay of pulverized coal in the burner zone, and the temperature is significantly lower than in other cases.

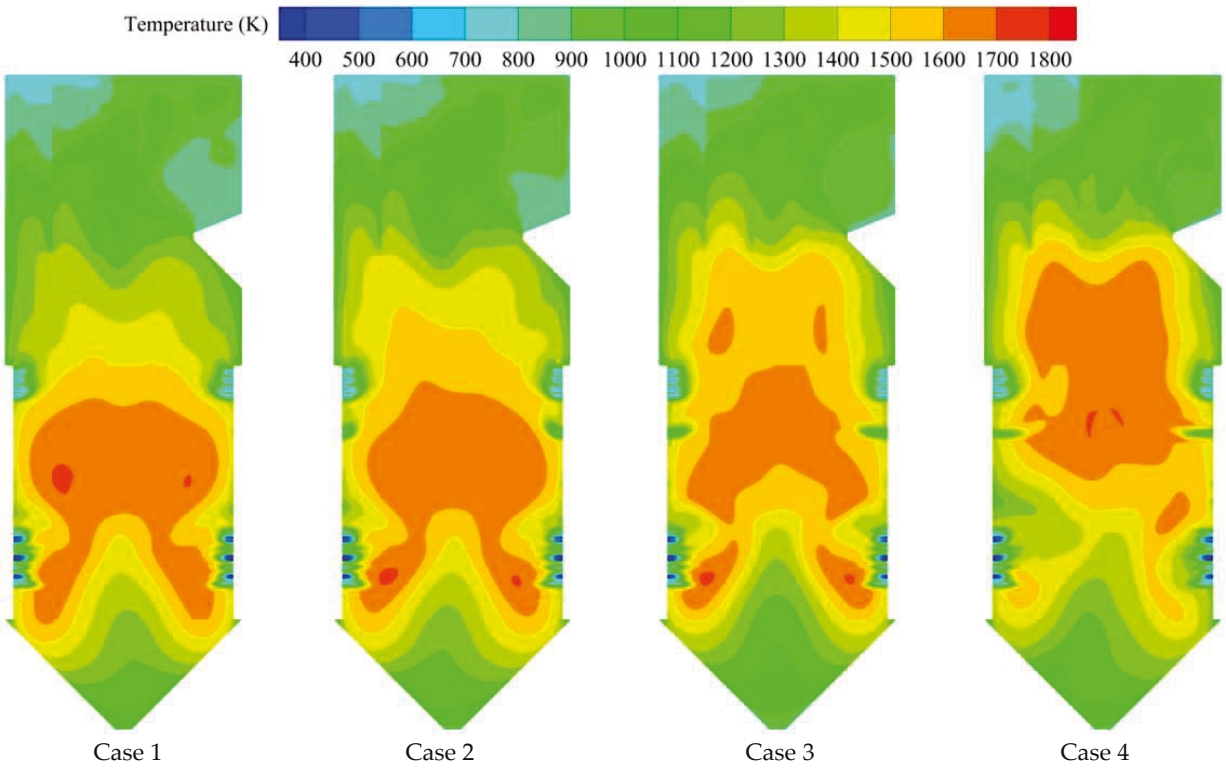


Figure 6. Temperature contours in the P1 plane under different preheating coal input.

3.1.2. Average O_2 and NO_x Concentration Distribution

Figure 7a illustrates the effects of different preheating coal inputs on O_2 distribution inside the furnace. As the preheating coal input increases, the oxygen concentration in the burner zone gradually rises. The use of preheating combustion devices influences the distribution of fuel and air in the boiler. The local mean stoichiometric ratio (LMSR) is introduced to analyze oxygen distribution in the retrofitted boiler. LMSR [3] is defined as the ratio of the actual air flow rate to the theoretical air flow rate in a given area. For cases 1–4, the LMSRs before the burnout zone are 0.9. As part of the fuel and air burn in the reduction zone, the LMSRs in the burner zone of the retrofitted boiler increase. Specifically, the LMSRs for cases 1–4 are 0.9, 0.95, 1.03, and 1.13, respectively. With higher preheating coal input, the SR in the burner zone increases significantly, while the coal feed rate decreases gradually. This indicates that lower combustion temperatures slow the combustion reaction rate, leading to higher oxygen concentrations. Due to reactions between preheated products and air in the burnout zone, the oxygen concentration in case 1 is much higher than in cases 2–4. For cases 2–4, increasing the preheated fuel flow rate speeds up the oxygen reaction rate in the burnout zone.

Figure 7b illustrates the effects of different preheating coal inputs on the NO_x concentration in the furnace. The formation of NO_x mainly depends on the combustion temperature and O_2 concentration. As shown in Figure 4, the NO_x levels in cases 2–4 are higher than in case 1 before the burnout zone. The average temperature in the burner zone of the retrofitted boiler is lower than that of the original boiler, which helps reduce thermal NO_x formation. However, increasing the flow rate of preheating coal causes a significant rise in the SR of the burner zone, leading to higher fuel NO_x formation. Fuel NO_x typically accounts for over 90% of the total NO_x produced in the furnace. Therefore, the NO_x levels in cases 2–4 before the burnout zone are much higher than in case 1. NO_x concentration drops sharply in the reduction zone for the original boiler, showing that air staging effectively limits NO_x formation. Due to the reduction effects of reducing gases

and char in the preheated products on NO_x, the NO_x concentration in the retrofitted boiler decreases rapidly in the reduction zone. As a result, the NO_x reduction rate increases with the increase in the feed rate of preheating fuel.

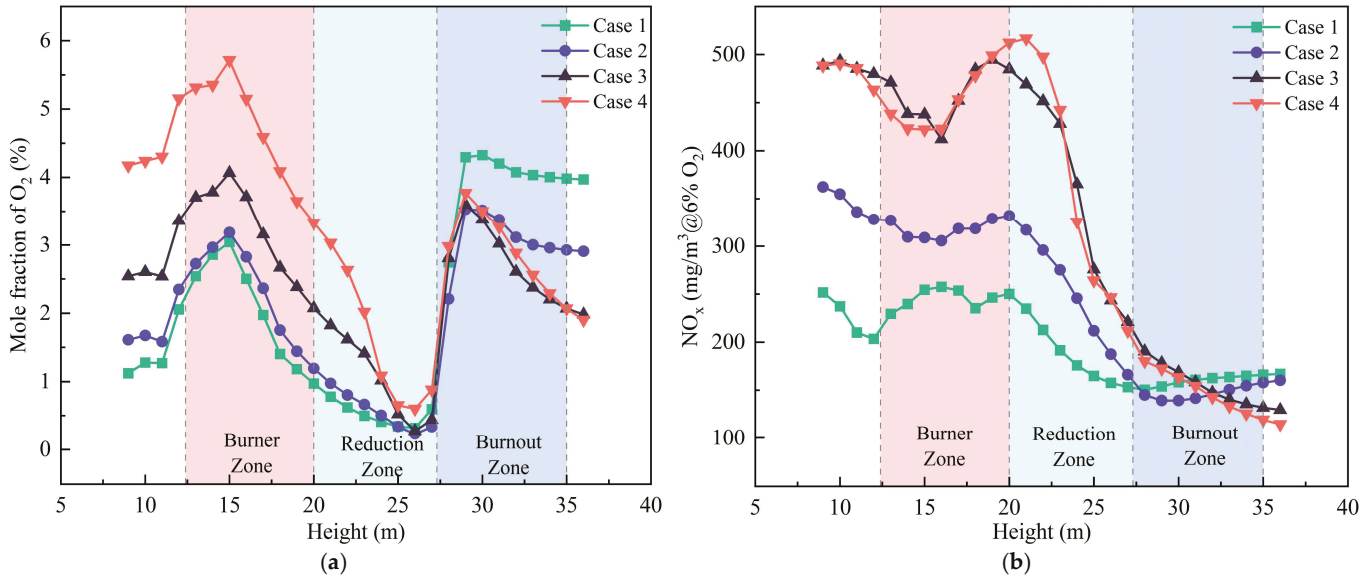


Figure 7. Cross-sectional average species concentration in the furnace under different preheating coal input (**a**) O_2 concentration; (**b**) NO_x concentration.

3.1.3. Combustion Efficiency and NO_x Emissions

Figure 8 compares combustion efficiency and NO_x concentration at the furnace outlet under different preheating fuel inputs. The following equation calculates the combustion efficiency [37]:

$$\eta_r = [100 - q_3 - q_4]\% \quad (15)$$

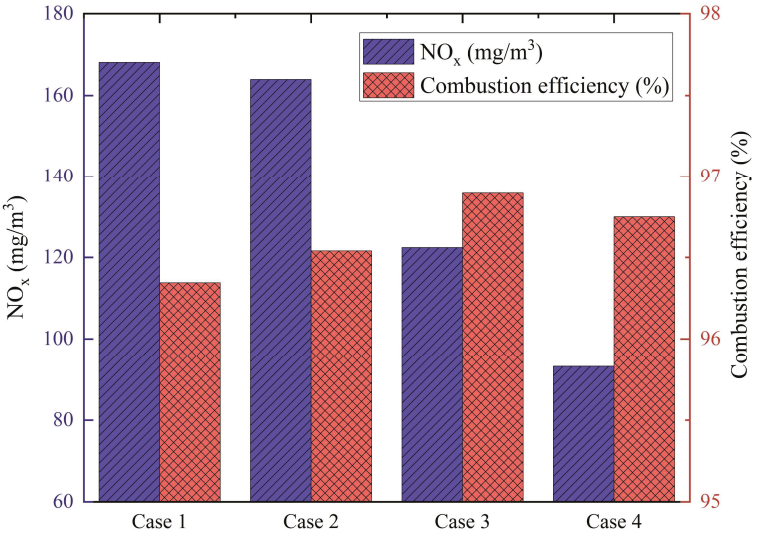


Figure 8. Combustion efficiency and NO_x concentration at the furnace outlet under different preheating coal input.

The heat losses from unburned gas and carbon q_3 and q_4 are expressed:

$$q_3 = \frac{V_{gy} \times 123.36CO}{Q_{ar,net}} \times 100\% \quad (16)$$

$$q_4 = \frac{C_f}{1 - C_f} \times \frac{33727 A_{ar}}{Q_{\text{net,ar}}} \times 100\% \quad (17)$$

where V_{gy} is the volume of outlet flue gas, Nm^3/kg, $Q_{\text{net,ar}}$ is the low heating value, kJ/kg, CO means volumetric fraction of carbon monoxide in flue gas, and C_f is the combustible percentage of fly ash, %.

Increasing the preheating coal input intensifies the reaction between the reducing gas from preheated products and NO_x, promoting NO_x reduction in the reduction zone. The experimental data in Table 3 also indicate that increasing the preheating fuel input significantly raises the product temperature, which enhances the NO_x reduction reaction rate. As a result, the NO_x concentration at the furnace outlet decreases as the preheated fuel input increases.

Compared to the original boiler, the combustion efficiency of the retrofitted boiler is improved. According to the analysis in Section 3.1, preheating combustion increases coal burnout rate by raising the SR in the burner zone. Additionally, the preheated products include char and reducing gases (CO, H_2, and CH_4). After devolatilization and gasification, the char's smaller particle size and larger specific surface area improve its reactivity. Furthermore, the reducing gases react with oxygen to ensure complete combustion. Therefore, increasing the preheating coal input in the preheating combustion device effectively improves combustion efficiency. However, in case 4, the highest preheating coal input causes the SR of the burner zone to reach 1.13, leading to unstable combustion. Consequently, the ignition delay causes the high-temperature zone to shift upward excessively and reduces the residence time of flue gas inside the furnace, ultimately decreasing boiler combustion efficiency. Based on the analysis above, case 3, with a preheating coal input of 20 t/h, is recommended due to its optimal combustion performance and low NO_x concentration.

3.2. Effect of Burner Arrangement on Combustion Characteristics

3.2.1. Average Temperature Distribution

Figures 9 and 10 illustrate the impact of the burner arrangement on the average temperature variation inside the furnace and the temperature contours of the P-1 plane, respectively. The burner arrangement significantly influences the temperature distribution within the furnace. As the height of the operating burners increases, the high-temperature zone shifts noticeably upward. According to Figure 10, case 3 demonstrates a symmetrical and uniform temperature distribution near the burner, suggesting stable ignition of pulverized coal under this scenario. Cases 3 and 5 use A and B layer burners, but case 5 exhibits a significantly lower average temperature at the bottom of the burner zone than case 3. Furthermore, the temperature contour indicates that case 5 has an uneven temperature distribution in the bottom burner zone, indicating delayed ignition and incomplete combustion during the initial combustion stage. From the comparison of average temperatures, it is evident that cases 6 and 7 display similar temperature variation trends in the furnace. Due to differences in burner height, case 7 shows higher temperatures in the upper furnace compared to case 6, while case 6 demonstrates a more uniform temperature distribution throughout the furnace chamber. As burner height rises, the residence time in the burner zone decreases, causing unburned carbon to react exothermically with residual oxygen in the reduction zone. Consequently, except for case 3, the flue gas temperature with preheated products significantly increases in the reduction zone under the other burner arrangements. In the burnout zone, the flue gas temperature drops rapidly after mixing with burnout air. The combustibles in the flue gas then react with excess oxygen to ensure complete combustion. Case 7 uses the top burner arrangement CDE, which results in the shortest residence time and a poor burnout rate in the burner zone. Case 7 shows the highest concentration of unburned combustibles and the greatest heat release in the

burnout zone. As a result, its temperature in this zone is considerably higher than that of the other cases.

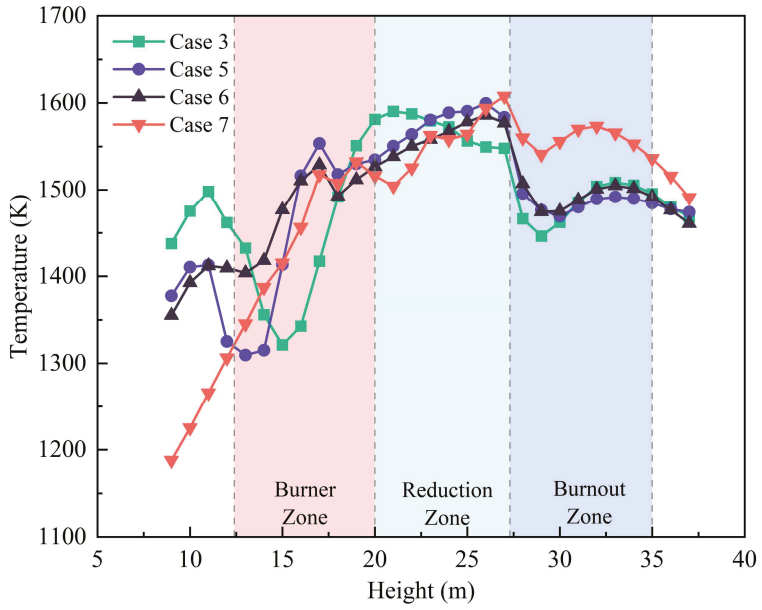


Figure 9. Cross-sectional average temperature in the furnace under different burner arrangements.

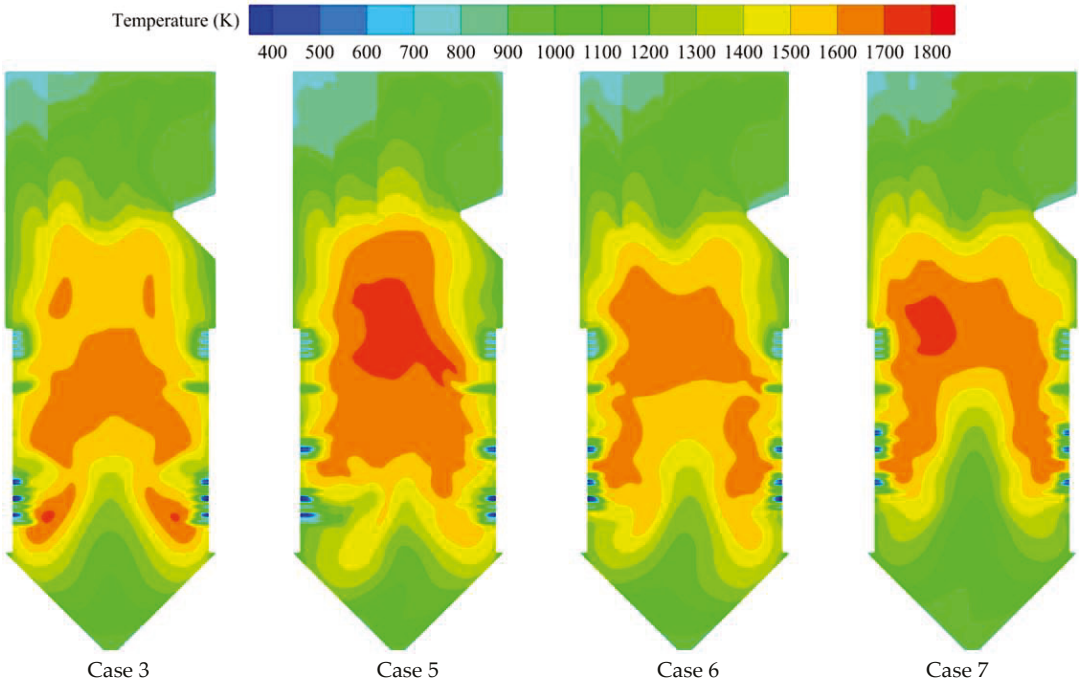


Figure 10. Temperature contours in the P1 plane under different burner arrangements.

3.2.2. Average O_2 and NO_x Concentration Distribution

Figure 11a shows the cross-sectional average O_2 variation under different burner arrangements. The oxygen distribution reflects the combustion behavior inside the furnace. According to Figure 10, ignition delay occurs at the outlet of the AB layer burners in case 5, leading to a low oxygen consumption rate. As a result, the oxygen concentration is highest at the bottom of the burner zone. The large spacing between the B and D layer burners causes the vertically adjacent burners to operate more independently, hindering the pulverized coal stream's mixing and heat exchange. Therefore, case 5 maintains a high

O_2 concentration throughout the furnace, indicating a poor burnout rate. Although the flame center in case 7 is located above that of case 5, its more compact burner arrangement results in more stable combustion and a more uniform temperature distribution in the furnace. In the reduction zone, after the preheated products are injected at a furnace height of 23.5 m, the oxygen reaction rate increases in all cases due to reactions between highly reactive reducing gases and coke with excess oxygen. In the burnout zone, a lower content of combustibles in the flue gas leads to a much higher air mixing rate than the reaction rate, causing a rapid rise in oxygen concentration. Subsequently, continuous combustion of the combustibles causes a quick decrease in oxygen concentration.

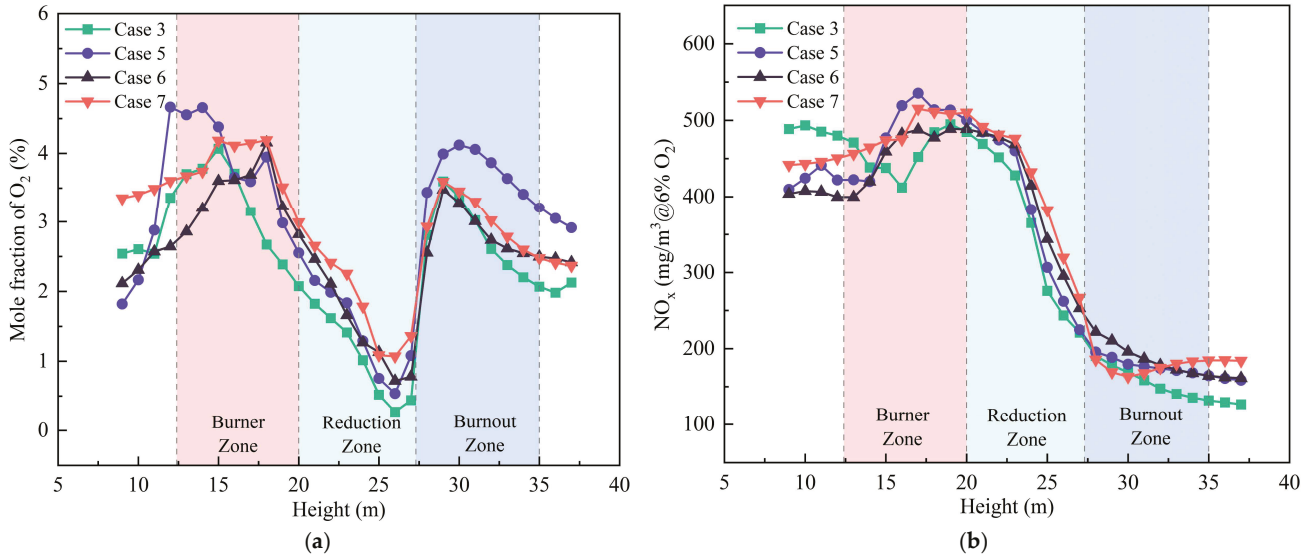


Figure 11. Cross-sectional average species concentration in the furnace under burner arrangements (**a**) O_2 concentration; (**b**) NO_x concentration.

Figure 11b illustrates the impact of burner arrangement on the average NO_x concentrations in the furnace. Using a three-layer burner arrangement in all cases results in similar NO_x variation trends. NO_x formation depends on the air staging degree, temperature, and species distribution during combustion. The top three-layer burner in case 7 reduces the distance to the burnout zone and decreases the air staging degree, which increases NO_x formation. Additionally, the high oxygen level in the reduction zone of case 7 prevents the reduction of NO_x by preheated products. As a result, case 7 shows a higher average NO_x level than the other cases. Conversely, the lower burner arrangements in cases 3 and 6, which promote a more uniform temperature distribution, lead to lower average NO_x concentration in the furnace. In the reduction zone, oxygen is largely consumed across all cases, significantly weakening the oxidizing atmosphere. Moreover, H_2 and CH_4 in the preheated products improve the reducing atmosphere, enhancing NO_x reduction. Consequently, NO_x concentrations drop rapidly in the reduction zone for all cases. Case 7 exhibits the highest unburned combustible content in the burnout zone, causing sustained combustion and higher NO_x levels. Based on this analysis, implementing the ABC or BCD burner arrangements can help reduce NO_x formation inside the furnace at 50% rated load.

3.2.3. Combustion Efficiency and NO_x Emissions

Figure 12 compares boiler combustion efficiency and NO_x concentration at the furnace outlet under different burner arrangements. At 50% rated load, all cases maintain combustion efficiency above 96%. Since case 7 uses the top burner arrangement CDE, it has the shortest in-furnace residence time, leading to the lowest combustion efficiency. However, combustion efficiency is not solely determined by the burner height and position.

Although the ABD configuration adopts the bottom two layers of burners A and B, the excessive spacing between burners B and D weakens their interaction. This causes ignition delays at burners A and B, resulting in lower combustion efficiency in case 5. Compared to case 3, case 6 has a shorter residence time for pulverized coal in the furnace; however, it decreases heat loss at the bottom of the burners, which improves ignition of pulverized coal during the initial combustion stage. Additionally, the appropriate spacing between C and D layer burners helps improve combustion stability [38]. Therefore, case 5 shows better combustion stability and maintains a consistent high-temperature zone, achieving optimal combustion efficiency.

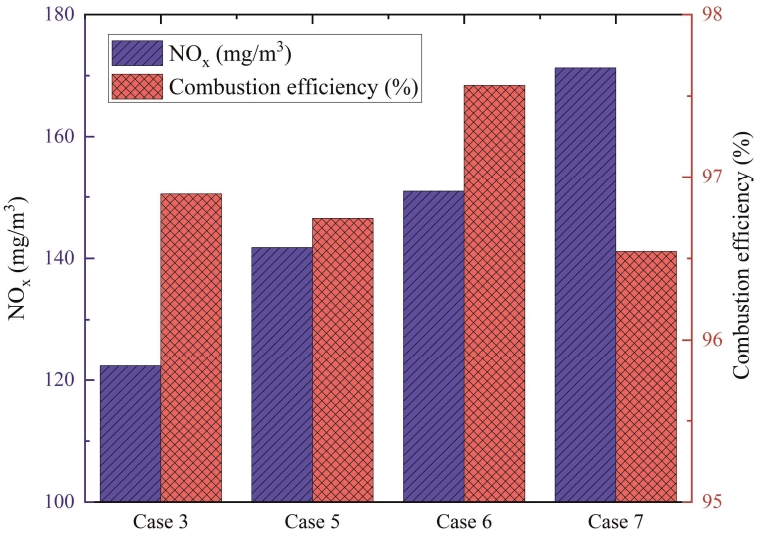


Figure 12. Combustion efficiency and NO_x concentration at the furnace outlet under different burner arrangements.

The NO_x concentration at the furnace outlet increases as the burner height rises. Increasing the burner height reduces the residence time in the burner zone, which raises the oxygen concentration in the flue gas within the reduction zone. This weakens the reducing atmosphere in that zone and inhibits the reduction of NO_x by preheated products. Additionally, using top-layer burners diminishes the effect of air staging in reducing NO_x formation, leading to the highest NO_x concentration in case 7. However, NO_x formation is also affected by the vertical spacing between burners. Although case 5 utilizes bottom AB-layer burners, the excessive vertical spacing between adjacent B and D layer burners causes unstable combustion, resulting in locally elevated oxygen levels and increased NO_x. Based on the above analysis, the top E-layer burners should be avoided, and appropriate vertical spacing between burners should be maintained to ensure efficient and clean boiler combustion at 50% rated load. Therefore, the burner arrangements in the bottom three layers (ABC) and the middle three layers (BCD) are considered reasonable.

4. Conclusions

(1) At 50% rated load, implementing preheating combustion devices in a 330 MW coal-fired boiler improves combustion efficiency and reduces NO_x emissions. Compared to the original boiler, the combustion efficiency of the retrofitted boiler increases from 96.3% to a maximum of 97.6%, while the NO_x concentration at the furnace outlet decreases from 168.1 to 93.2 mg/Nm^3 (at 6% O_2).

(2) As preheating coal input increases from 0 to 30 t/h, NO_x emissions decrease by 44.6% due to suppression of NO_x formation by preheated products. When the preheating

coal input is 20 t/h, the boiler's combustion efficiency reaches 96.89%. A preheating coal input of 30 t/h can cause unstable combustion in the burner zone.

(3) As the height of the burner arrangement increases, NO_x emissions gradually rise from 122.4 to 171.3 mg/Nm^3. The BCD-layer burner arrangement exhibits uniform temperature distribution in the furnace, with the highest combustion efficiency of 97.6%. Bottom and middle three-layer burner arrangements are recommended to ensure efficient and clean combustion.

Author Contributions: Methodology, S.W. and Z.X.; Software, S.W.; Validation, Z.L. and H.T.; Funding acquisition, Z.L. and L.S.; Writing—original draft preparation, S.W.; Writing—review and editing, S.W. and Z.X. All authors have read and agreed to the published version of the manuscript.

Funding: This research was funded by the National Natural Science Foundation of China (grant number 52376096) and the Program of the Education Department of Jilin Province (grant number JJKH20240138KJ).

Data Availability Statement: The authors will make the raw data supporting this article's conclusions available upon reasonable request.

Conflicts of Interest: The authors declare no conflicts of interest.

Nomenclature

A_1	Pre-exponential factors of devolatilization at low temperature (s^{-1})
A_2	Pre-exponential factors of devolatilization at high temperature (s^{-1})
E_1	Activation energy of devolatilization at low temperature (J/kmol)
E_2	Activation energy of devolatilization at high temperature (J/kmol)
d_p	Diameter of particle (m)
D_0	Diffusion rate coefficient (m^2/s)
$f_{\mathrm{w},0}$	Initial mass fraction of moisture in the coal particle
h	Gas enthalpy (J/kg)
h_j	Enthalpy of species j (J/kg)
g	Vector of gravitational acceleration (m^2/s)
G_b	Turbulence kinetic energy generated by buoyancy (kg/(m·s^3))
G_k	Turbulence kinetic energy generated by the mean velocity gradients (kg/(m·s^3))
J_j	Diffusion flux of species j (kg/(m^2·s))
$k_{\mathrm{f,i}}$	Rate constants for forward reactions of thermal NO formation (i = 1, 2, 3) (m^3/(gmol·s))
$k_{\mathrm{r,i}}$	Rate constants for reverse reactions of thermal NO formation (i = 1, 2, 3) (m^3/(gmol·s))
m_a	Ash content in the coal particle (kg)
m_p	Coal particle mass (kg)
$m_{\mathrm{p},0}$	Initial mass of particle (kg)
$m_\mathrm{v}(t)$	Volatile yield over time (kg)
p_ox	Partial pressure of oxidant around char (Pa)
q	Heat flux vector (W/m^2)
R	Universal gas constant (J/(kmol·K))
R_j	Net production rate of species j by chemical reactions (kg/(m^3·s))
R_p	Kinetic rate at particle surface (s^{-1})
S_h	Source term for energy (W/m^3)
S_j	Source term for mass of species j (kg/(m^3·s))
S_{ma}	Source term for mass (kg/(m^3·s))
S_{mo}	Source term for momentum (kg/(m^2·s^2))
u	Velocity vector of gas phase (m/s)
Y_j	Mass fraction of species j

Abbreviations

CCOFA	Close-coupled overfire air
SOFA	Separated overfire air
PA	Primary air
SA	Secondary air
SR	Stoichiometric ratio
Greek Symbols	
ρ	Gas density (kg/m^3)
α_1, α_2	Yield factors
τ	Stress tensor (kg/m^2 s^2)
η_r	Combustion efficiency (%)

References

1. Zhang, X.; Chen, Z.; Zhang, M.; Zeng, L.; Li, Z. Combustion stability, burnout and NO emissions of the 300-MW down-fired boiler with bituminous coal: Load variation and low-load comparison with anthracite. *Fuel* **2021**, *295*, 120641. [CrossRef]
2. Zeng, G.; Zhou, A.; Fu, J.; Ji, Y. Experimental and numerical investigations on NOx formation and reduction mechanisms of pulverized-coal stereo-staged combustion. *Energy* **2022**, *261*, 125358. [CrossRef]
3. Ma, D.; Zhang, S.; He, X.; Zhang, J.; Ding, X. Combustion stability and NOx emission characteristics of a 300 MWe tangentially fired boiler under ultra-low loads with deep-air staging. *Energy* **2023**, *269*, 126795. [CrossRef]
4. Gu, W.; Zheng, Z.; Zhao, N.; Wang, X.; Cheng, Z. Combustion characteristics of a 660 MW tangentially fired pulverized coal boiler considering different loads, burner combinations and horizontal deflection angles. *Case Stud. Therm. Eng.* **2024**, *64*, 105520. [CrossRef]
5. Li, D.; Cheng, Z.; Liu, C.; Wei, S.; Feng, Y.; Feng, H.; Zhao, G.; Nie, H.; Xiao, H.; Liu, Z.; et al. Investigation of combustion and NOx emission characteristics in 300 MW subcritical CFB boilers under low-load conditions. *Chem. Eng. Sci.* **2025**, *318*, 122175. [CrossRef]
6. Chen, G.; Li, Z.; Zhang, H.; Huang, L.; Liu, Z.; Fan, W. Influences of ultra-low load operation strategies on performance of a 300 MW subcritical bituminous coal boiler. *Appl. Therm. Eng.* **2024**, *256*, 124037. [CrossRef]
7. Liu, T.; Wang, Y.; Zou, L.; Bai, Y.; Shen, T.; Wei, Y.; Li, F.; Zhao, Q. Numerical investigation of stable combustion at ultra-low load for a 350 MW wall tangentially fired pulverized-coal boiler: Effect of burner adjustments and methane co-firing. *Appl. Therm. Eng.* **2024**, *246*, 122980. [CrossRef]
8. Jiang, Y.; Lee, B.-H.; Oh, D.-H.; Jeon, C.-H. Optimization of operating conditions to achieve combustion stability and reduce NOx emission at half-load for a 550-MW tangentially fired pulverized coal boiler. *Fuel* **2021**, *306*, 121727. [CrossRef]
9. Wang, H.; Jin, H.; Yang, Z.; Deng, S.; Wu, X.; An, J.; Sheng, R.; Ti, S. CFD modeling of flow, combustion and NOx emission in a wall-fired boiler at different low-load operating conditions. *Appl. Therm. Eng.* **2024**, *236*, 121824. [CrossRef]
10. Ma, D.; Zhang, S.; He, X.; Ding, X.; Li, W.; Liu, P. Combustion stability and NO emission characteristics of three combustion modes of pulverized coal boilers under low or ultra-low loads. *Appl. Energy* **2024**, *353*, 121998. [CrossRef]
11. Zhu, S.; Zhou, H.; Li, Z.; Zeng, X.; Ouyang, Z.; Hui, J.; Lin, J.; Su, K.; Wang, H.; Ding, H.; et al. Wide-load combustion characteristics of lean coal tangential preheating combustion. *Energy* **2025**, *323*, 135845. [CrossRef]
12. Yu, Y.; Xu, L.; Niu, Y. Synergistic reduction of PM and NOx in different preheating co-firing modes of coal and biomass. *J. Energy Inst.* **2025**, *121*, 102151. [CrossRef]
13. Tang, H.; Liu, Z.; Han, X.; Shen, X.; Liu, Y.; Wang, S.; Xu, Z. Experimental study on combustion characteristics of a 40 MW pulverized coal boiler based on a new low NOx burner with preheating function. *Energy* **2024**, *305*, 132319. [CrossRef]
14. Lv, Z.; Xiong, X.; Ruan, R.; Wang, Y.; Tan, H. NO emission and burnout characteristics in co-combustion of coal and sewage sludge following high-temperature preheating. *Fuel* **2023**, *331*, 125887. [CrossRef]
15. Wang, C.; Yu, Y.; Hu, R.; Niu, Y. NO and PM formation characteristics during preheating-combustion of semi-coke produced by coal pyrolysis at different temperatures. *J. Energy Inst.* **2025**, *121*, 102168. [CrossRef]
16. Yao, G.; Han, X.; Tang, H.; Sun, L.; Liu, G. Investigation of the gas-solid and Fuel-N conversion characteristics during pulverized coal preheating with an improved char model. *Case Stud. Therm. Eng.* **2025**, *65*, 105686. [CrossRef]
17. Yao, G.; Han, X.; Liu, Z.; Tang, H.; Zhou, Y.; Wang, Z. Low-NOx study of a 600 MW tangentially fired boiler based on pulverized coal preheating method. *Case Stud. Therm. Eng.* **2023**, *48*, 103156. [CrossRef]
18. Tang, H.; Yao, G.; Wang, Z.; Yang, J.; Han, X.; Sun, L.; Xu, Z. Study on low-load combustion characteristics of a 600 MW power plant boiler with self-sustaining internal combustion burners. *Appl. Therm. Eng.* **2025**, *267*, 125859. [CrossRef]

19. Zhang, H.; Lin, H.; Zhou, X.; Wang, X.; Zheng, H.; Liu, Y.; Tan, H. CFD modeling and industry application of a self-preheating pulverized coal burner of high coal concentration and enhanced combustion stability under ultra-low load. *Appl. Therm. Eng.* **2024**, *253*, 123831. [CrossRef]
20. Wang, S.; Tang, H.; Liu, Z.; Han, X.; Shen, X.; Xu, Z. Combustion performance and NOx emissions in a 330 MW tangentially fired boil-er retrofitted with preheating combustion devices. *Energy* **2025**, *318*, 134803. [CrossRef]
21. Jin, W.; Si, F.; Kheirkhah, S.; Yu, C.; Li, H.; Wang, Y. Numerical study on the effects of primary air ratio on ultra-low-load combustion characteristics of a 1050 MW coal-fired boiler considering high-temperature corrosion. *Appl. Therm. Eng.* **2023**, *221*, 119811. [CrossRef]
22. Li, S.; Chen, Z.; He, E.; Jiang, B.; Li, Z.; Wang, Q. Combustion characteristics and NO formation of a retrofitted low-volatile coal-fired 330 MW utility boiler under various loads with deep-air-staging. *Appl. Therm. Eng.* **2017**, *110*, 223–233. [CrossRef]
23. Laubscher, R.; Rousseau, P. Numerical investigation into the effect of burner swirl direction on furnace and superheater heat absorption for a 620 MWe opposing wall-fired pulverized coal boiler. *Int. J. Heat Mass Transf.* **2019**, *137*, 506–522. [CrossRef]
24. Kang, W.; Jo, H.; Lee, J.; Jang, K.; Ryu, C. Numerical investigations on overfire air design for improved boiler operation and lower NOx emission in commercial wall-firing coal power plants. *Appl. Therm. Eng.* **2023**, *219*, 119604. [CrossRef]
25. Xie, Y.; Liu, X.; Zhang, C.; Wang, H. Numerical investigations on the aerodynamics and flue gas recirculation of cyclone-fired coal boiler. *Fuel* **2022**, *316*, 123355. [CrossRef]
26. Smith, T.F.; Shen, Z.F.; Friedman, J.N. Evaluation of Coefficients for the Weighted Sum of Gray Gases Model. *J. Heat Transf.* **1982**, *104*, 602–608. [CrossRef]
27. Du, Y.; Wang, C.; Lv, Q.; Li, D.; Liu, H.; Che, D. CFD investigation on combustion and NO emission characteristics in a 600 MW wall-fired boiler under high temperature and strong reducing atmosphere. *Appl. Therm. Eng.* **2017**, *126*, 407–418. [CrossRef]
28. Liu, X.; Zhang, J.; Tan, H.; Mo, Q.; Wang, X.; Wang, Y. Numerical and experimental study on co-firing of low volatile coal in a 330 MW tangentially fired boiler. *J. Energy Inst.* **2021**, *96*, 242–250. [CrossRef]
29. Backreedy, R.; Habib, R.; Jones, J.; Pourkashanian, M.; Williams, A. An extended coal combustion model. *Fuel* **1999**, *78*, 1745–1754. [CrossRef]
30. Kobayashi, H.; Howard, J.; Sarofim, A. Coal devolatilization at high temperatures. *Symp. (Int.) Combust.* **1977**, *16*, 411–425. [CrossRef]
31. Bian, C.; Huang, J.; Sun, R. Numerical optimization of combustion and NOx emission in a retrofitted 600MWe tangentially-fired boiler using lignite. *Appl. Therm. Eng.* **2023**, *226*, 120228. [CrossRef]
32. Baum, M.M.; Street, P.J. Predicting the combustion behaviour of coal particles. *Combust. Sci. Technol.* **1971**, *3*, 231–243. [CrossRef]
33. Zeldvich, Y.B. The Oxidation of Nitrogen in Combustion and Explosions. *J. Acta Physicochim.* **1946**, *21*, 577.
34. De Soete, G.G. Overall reaction rates of NO and N_2 formation from fuel nitrogen. *Symp. (Int.) Combust.* **1975**, *15*, 1093–1102. [CrossRef]
35. Wang, Y.; Zhou, Y. Numerical optimization of the influence of multiple deep air-staged combustion on the NOx emission in an opposed firing utility boiler using lean coal. *Fuel* **2020**, *269*, 116996. [CrossRef]
36. Li, Z.; Miao, Z. Effects of moisture and its input form on coal combustion process and NOx transformation characteristics in lignite boiler. *Fuel* **2020**, *266*, 116970. [CrossRef]
37. Ding, H.; Ouyang, Z.; Su, K.; Wang, W.; Zhang, J.; Wang, H.; Zhu, S. Experimental research on effects of multi-layer injection of the high-temperature preheated pulverized coal on combustion characteristics and NOx emission. *Fuel* **2023**, *347*, 128424. [CrossRef]
38. You, M.; Chen, L.; Shang, Y.; Gao, A.; Su, S.; Xiang, J. Low load combustion characteristics of supercritical wall type tangentially fired boiler. *Clean Coal Technol.* **2023**, *29*, 145–152.

Disclaimer/Publisher's Note: The statements, opinions and data contained in all publications are solely those of the individual author(s) and contributor(s) and not of MDPI and/or the editor(s). MDPI and/or the editor(s) disclaim responsibility for any injury to people or property resulting from any ideas, methods, instructions or products referred to in the content.

energies

MDPI

Article

Hybrid Artificial Neural Network and Perturb & Observe Strategy for Adaptive Maximum Power Point Tracking in Partially Shaded Photovoltaic Systems

Braulio Cruz [1], Luis Ricalde [1,*], Roberto Quintal-Palomo [1], Ali Bassam [2] and Roberto I. Rico-Camacho [3]

[1] Facultad de Ingenieria, Universidad Autonoma de Yucatan, Merida 97302, Mexico; braulio.cruz@correo.uady.mx (B.C.); roberto.quintal@correo.uady.mx (R.Q.-P.)
[2] Laboratorio de Modelado y Optimizacion de Procesos Energeticos y Ambientales, Facultad de Ingenieria, Universidad Autonoma de Yucatan, Merida 97302, Mexico; baali@correo.uady.mx
[3] CRS Industrial Power Equipment, Plant 1, Calle 23 311, Itzincab 97390, Mexico; robertor@crspower.com
* Correspondence: lricalde@correo.uady.mx

Abstract

Partial shading in photovoltaic (PV) systems causes multiple local maximum power points (LMPPs), complicating tracking and reducing energy efficiency. Conventional maximum power point tracking (MPPT) methods, such as Perturb and Observe (P&O), often fail because of oscillations and entrapment at local maxima. To address these shortcomings, this study proposes a hybrid MPPT strategy combining artificial neural networks (ANNs) and the P&O algorithm to enhance tracking accuracy under partial shading while maintaining implementation simplicity. The research employs a detailed PV cell model in MATLAB/Simulink (2019b) that incorporates dynamic shading to simulate non-uniform irradiance. Within this framework, an ANN trained with the Levenberg–Marquardt algorithm predicts global maximum power points (GMPPs) from voltage and irradiance data, guiding and accelerating subsequent P&O operation. In the hybrid system, the ANN predicts the maximum power points (MPPs) to provide initial estimates, after which the P&O fine-tunes the duty cycle optimization in a DC-DC converter. The proposed hybrid ANN–P&O MPPT method achieved relative improvements of 15.6–49% in tracking efficiency, 16–20% in stability, and 14–54% in convergence speed compared with standalone P&O, depending on the irradiance scenario. This research highlights the potential of ANN-enhanced MPPT systems to maximize energy harvest in PV systems facing shading variability.

Keywords: photovoltaic systems; partial shading; maximum power point tracking; artificial neural networks; dynamic shading adaptation

1. Introduction

PV solar energy is a consolidating strategy for meeting the growing global energy demand and mitigating greenhouse gas emissions due to technology maturation, scalability of installations, economic viability, and abundance of the solar resource. Despite the installation and maintenance costs, PV systems often lead to significant savings on electricity bills over time. However, specific technical challenges must be addressed to maximize performance and efficiency. Partial shading is one of the most critical issues affecting PV conversion efficiency, causing hot spots which increase the risk of damage, and reducing the installation lifecycle [1].

Because solar panels have low conversion efficiency, the PV system must run at peak performance. Every temperature or irradiance change alters the current–voltage (I-V) and power–voltage (P-V) cell characteristics, requiring a new operating point. MPPT techniques address this need in most PV systems [2]. Under uniform irradiance, the P-V curve of a PV array shows a clear maximum power point. For situations with non-uniform irradiance, such as partial shading, the P-V curve has multiple local peaks where only one is the GMPP. MPPT designs require capturing all available power under any condition [3].

Partial shading in PV systems generates multiple LMPPs in the system's characteristic curve, making it challenging to locate the GMPP and reducing overall efficiency [4]. Partial shading produces cells with low energy output that affect the rest of the PV cells in the array, limiting total energy production. Shading can be classified as static or dynamic, depending on the nature and behavior of objects causing obstruction and environmental conditions. Static shading occurs when permanent objects, such as buildings, walls, chimneys, or other fixed structures, block sunlight at certain times of the day based on the sun's position. This type of shading is typically predictable. It can often be mitigated at the design stage by optimizing the orientation and placement of PV panels. Dynamic shading is caused by moving or temporary objects such as clouds, tree foliage, birds, or nearby vehicles. These intermittently block sunlight and introduce unpredictable fluctuations in solar irradiance. Dynamic shading is more complex to anticipate and manage, often resulting in rapidly changing operating conditions for the PV system. Both shading types should be considered in system design and in developing MPPT algorithms to ensure optimal PV power output and performance under varying conditions [5].

A recent study [6] analyzes the role of bypass diodes in PV modules under partial shading. When part of a PV module is shaded, the bypass diode conducts to keep the shaded cell from becoming reverse-biased and prevent hotspots and damage. This changes the current–voltage (I-V) and power–voltage (P-V) behavior, introducing multiple LMPPs and a GMPP. This causes a step-like current shape in the I–V curve and several peaks in the P-V curve, as shown in Figures 1 and 2. These peaks complicate MPPT and may reduce energy harvesting. Removing the bypass diode could eliminate these peaks and simplify the P-V curve, but the study shows this would cause significant power losses and a higher risk of damage from hotspots. Bypass diodes are therefore essential for protecting PV modules and maintaining efficiency under shading.

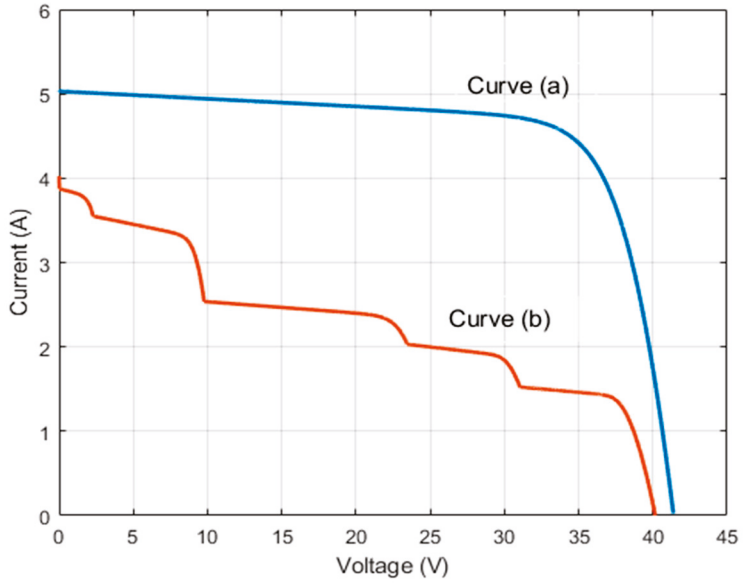


Figure 1. Characteristic of the I-V curve for: (**a**) uniform irradiance and (**b**) partial shading.

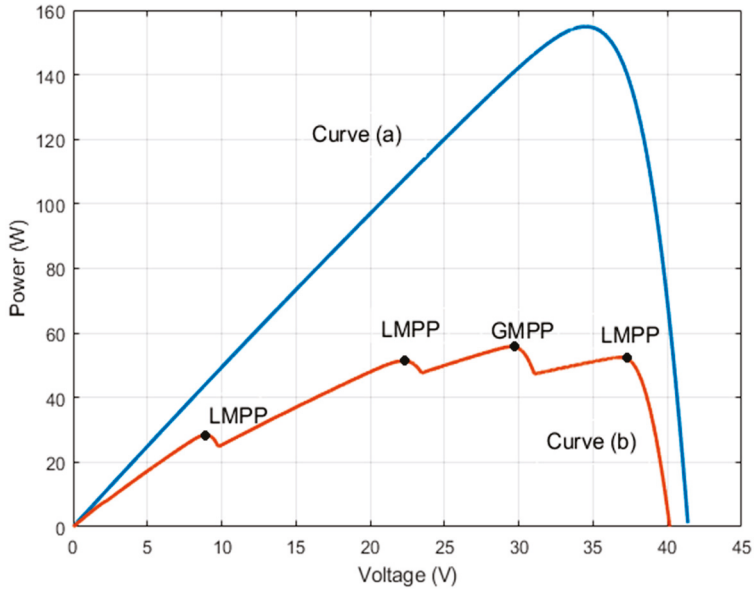


Figure 2. Characteristic of the P-V curve for: (**a**) uniform irradiance and (**b**) partial shading.

The most significant effect of partial shading is the mismatch between the array's maximum power point (MPP) and the MPPs of each module, which reduces system performance due to power losses. Bypass diodes further cause losses due to their forward conduction resistance. Partial shading causes reverse currents, converting the shaded cells into loads, which reduces power generation and increases thermal losses. It could also drive the MPP tracker to operate at local maximum values, increasing power losses [7,8]. These current mismatches cause localized cell heating and increase damage risk, raising maintenance costs.

MPPT techniques are fundamental to maintaining the effective operation of PV systems, as they allow panels to consistently operate at their peak power under diverse environmental conditions, ensuring system competitiveness and reliability [9]. Within this context, ref. [9] provides a comprehensive review of classical, intelligent, optimal, and hybrid MPPT methods, highlighting their strengths and limitations with respect to efficiency, tracking speed, and implementation complexity. Complementing this, a comparative study presented in [10] analyzes the two most widely used classical methods, Perturb and Observe (P&O) and Incremental Conductance (IC). While these algorithms are valued for their simplicity and low implementation cost, their effectiveness diminishes under partial shading or rapidly changing irradiance, where they often misidentify local operating points, leading to reduced stability and efficiency. Together, these contributions underscore the need for advanced and hybrid approaches, such as the ANN–P&O method proposed in this work, which aim to overcome the shortcomings of classical techniques in dynamic environments.

Optimization techniques for MPPT implement advanced algorithms such as swarm intelligence (e.g., Particle Swarm Optimization and Grey Wolf Optimization), bio-inspired methods (e.g., Ant Colony Optimization, Artificial Bee Colony, Cuckoo Search, and Firefly Algorithm), and hybrid approaches (e.g., GWO-P&O and PSO-P&O) to accurately track the GMPP under partial shading and rapidly varying environmental conditions. These methods outperform conventional techniques like P&O or Incremental Conductance (IC) by effectively avoiding local maxima, reducing steady-state oscillations, and improving both tracking speed and efficiency. However, they often require greater computational resources and involve more complex implementation due to their sophisticated nature [11].

Computational intelligence techniques provide effective solutions for MPPT in PV systems under partial shading, where traditional methods often face limitations. Approaches based on artificial intelligence and machine learning—such as neural networks, fuzzy logic, genetic algorithms (GAs), and adaptive neuro-fuzzy inference systems—can adapt to complex shading patterns and rapidly changing irradiance and temperature, offering high efficiency and reduced variability even without requiring detailed mathematical models [12,13]. A comprehensive review in [14] highlights the wide range of AI applications in PV systems, including GMPP tracking, energy forecasting, parameter identification, and fault detection. Nonetheless, these intelligent methods also introduce challenges, as their implementation can be complex, computationally demanding, and costly, which motivates the exploration of hybrid strategies that balance performance with practical feasibility.

Hybrid MPPT techniques combine multiple methods to use their strengths and minimize weaknesses. For example, conventional and intelligent methods can be integrated to improve accuracy and response speed in different operating conditions. Hybrid systems are especially useful in PV installations affected by partial shading. They adapt in real time to locate and maintain the GMPP more effectively [15].

Artificial intelligence (AI) has become a central focus in PV systems, especially for addressing partial shading conditions. Conventional MPPT methods often struggle to identify the GMPP. To address this challenge, recent works have investigated AI-based strategies such as PSO [16] and general AI techniques for dynamic tracking [17]. Notably, these studies reflect the growing interest in intelligent and hybrid approaches. Reviews highlight the effectiveness of ANN and fuzzy logic in handling complex scenarios [18], and adaptive fuzzy logic controllers have also been validated experimentally [19]. Building on this foundation, hybrid schemes that integrate ANN with metaheuristics or fuzzy logic further improve tracking robustness [20]. Additionally, practical implementations in microcontrollers confirm real-time feasibility [21]. Other contributions involve combining ANN with Hill-Climbing [22] or adaptive P&O, which achieves 100% efficiency under shading [23]. Broader reviews further emphasize the advantages of ANN–metaheuristic hybrids [24].

Building on these advances, recent studies extend the field to predictive and adaptive frameworks. For instance, hybrid AI models combining physics-informed neural networks and reinforcement learning optimize real-time panel orientation and forecasting [25]. Dual-mode algorithms using radial basis ANNs with LSTM prediction enable automatic switching between normal and shaded conditions, improving accuracy and robustness [26]. In addition, Genetic Algorithm (GA)-based MPPT methods effectively explore large solution spaces under shading and irradiance changes, although they remain computationally intensive and parameter-dependent [27]. Collectively, these works demonstrate the relevance of intelligent and hybrid MPPT strategies, providing context for positioning new contributions, such as the hybrid ANN–P&O approach developed in this study.

2. Materials and Methods

The simulation of the mathematical model of a PV cell in MATLAB/Simulink (2019b) allows for the representation of cell behavior under different environmental conditions, facilitating maximum power point analysis and real-time optimization of the PV system.

2.1. Mathematical Model Construction of a PV Cell Considering Different Shading Patterns

Accurate modeling of PV systems is essential for evaluating the performance of MPPT algorithms, especially under partial shading conditions where nonlinearities are more pronounced. This work focuses on establishing a validated and consistent simulation environment, rather than proposing a novel PV model or converter topology. The aim is to

construct a reliable PV cell model based on the single-diode equivalent circuit, providing a scientifically sound platform for assessing the proposed ANN–P&O algorithm under controlled and repeatable conditions. To achieve this, parameter extraction, model validation, and integration with a boost converter are systematically developed and described in the following subsections.

1. Parameter detection for the PV model.
    - The PV array was modeled using the single-diode equivalent circuit.
    - The parameters (I_{pv}, I_o, R_s, R_{sh}, A) were extracted from the manufacturer's datasheet of the selected PV module by solving the nonlinear system defined by the open-circuit voltage V_{oc}, short-circuit current I_{sc}, maximum power point (V_{MPP}, I_{MPP}), and temperature coefficients.
    - A Levenberg–Marquardt fitting procedure was applied to minimize the error between the PV model's simulated and datasheet I-V curves, ensuring accurate parameter detection. Subsequently, validation of the PV model was performed.
2. Validation of the PV model.
    - The obtained parameters were validated in simulation by comparing the simulated I-V and P-V curves with the datasheet curves at standard test conditions (STCs) and under partial irradiance.
    - The fitting error remained below 1% at STC and 3% under non-uniform irradiance, confirming the model's fidelity.
3. Following the validation of the PV model, the next key component is the boost converter model.
    - A conventional boost topology was used, representing the standard interface for MPPT algorithms.
    - The passive components (inductor and capacitor) and switching frequency were sized according to design guidelines to ensure continuous conduction mode (CCM).
    - The converter was validated by comparing its simulated step response and steady-state conversion ratio with analytical values, ensuring an agreement within a 2% deviation.
4. After establishing the PV and boost converter models, the overall purpose of the simulation model is clarified.
    - The role of the simulation model is not to propose a new converter or PV model, but to provide a robust, validated simulation platform for testing and benchmarking the proposed ANN–P&O algorithm under controlled and repeatable conditions, including dynamic partial shading scenarios.

Figure 3 presents the equivalent electrical circuit of a PV cell. This circuit consists of a current source, $I_{pv,}$ representing the current generated by solar radiation, a diode, and two resistances, i.e., R_s in series and R_{sh} in parallel. R_s represents the losses caused by contacts and connections. In contrast, R_{sh} represents the leakage current of the diode and V_{pv} is the output voltage of the cell [15].

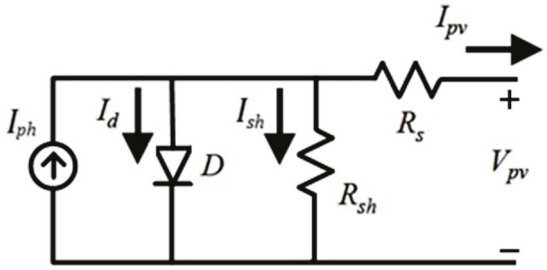


Figure 3. Single diode model of a PV cell.

By applying Kirchhoff's voltage and current law to the circuit in Figure 3, the current generated (I_{pv}) by the cell can be determined [15], as

$$I_{pv} = I_{ph} - I_d - I_{sh} \tag{1}$$

where I_{sh} represents the current losses in the parallel resistance, I_d is the diode current, and I_{ph} is the photogenerated current.

PV panels have an MPP on the power versus voltage curve depending on irradiance value. This variability requires an algorithm that adjusts V_{pv} to maximize the captured power. The efficiency of the MPPT system is fundamental in the control design for the optimal operation of PV generation systems despite variations in irradiance and temperature [28].

The current generated by the PV cell (I_{pv}) is described as

$$I_{pv} = N_p I_{ph} - N_p I_o \left(e^{\left(\frac{q\left(\frac{V_{pv}}{N_s} + \frac{R_s I_{pv}}{N_p}\right)}{KT_c A}\right)} - 1 \right) \tag{2}$$

where I_{ph} is the photocurrent, I_o is the reverse saturation current of the diode, q is the electron charge (1.6×10^{-19} C), K is the Boltzmann constant (1.38×10^{-23} J/K), T_c is the operating temperature of the cell, and A is the ideality factor of the diode. This last factor differentiates the behavior between silicon and germanium cells, depending on the manufacturing technology of the cell, and reflects how closely the photodiode behaves to an ideal diode. The resistance R_s reflects the losses due to contacts and connections, and the coefficients N_p, representing the number of modules in parallel, and N_s, representing the number of cells in series [29].

Shading of an individual cell within a series-connected string can substantially decrease the performance of a PV panel. Because current remains constant throughout the string, a single shaded cell limits the total current, thereby reducing the energy output of the entire panel. The classification of irradiance in a PV array under partial shading conditions is determined by how shadows impact specific cells or modules. Irradiance levels may vary considerably due to shadows cast by objects, clouds or adjacent structures.

Using block diagrams based on (1)–(2), a Simulink model is used to simulate voltage, current, and power data required for neural network training and to represent the configuration of solar cells within the panel. The simulation utilizes the Upsolar UP-M155M solar panel, which consists of 72 cells and has a 150 W output. The model allows us to adjust parameters such as temperature, cell count, and irradiation levels to replicate partial shading by altering irradiation on designated panel sections. Control switches are included to activate bypass diodes when shading decreases the efficiency of specific panel areas.

Different shading scenarios were tested, simulating dynamic irradiance input (G) at set intervals to simulate shadows on panel sections cast by passing clouds over the PV array. The scenarios included variations in irradiance levels, from fully illuminated modules (1000

W/m^2) to partially shaded modules (330 W/m^2, 470 W/m^2 and 665 W/m^2) and fully shaded modules (160 W/m^2) [30]. For this, a PV panel with six series-connected arrays of 12 cells each, totaling 72 cells, is considered, and different irradiance values are applied to each section of the panels.

Figure 4 shows the simulation model structure, presenting a PV system diagram in Simulink with the following components:

- Temperature (T) and irradiance (G) inputs modify the operating conditions of the PV cell.
- The PV cell outputs current (I) and voltage (V) to plot the system's characteristic curves.
- The I-V and P-V curves monitor cell behavior in response to irradiance and temperature.

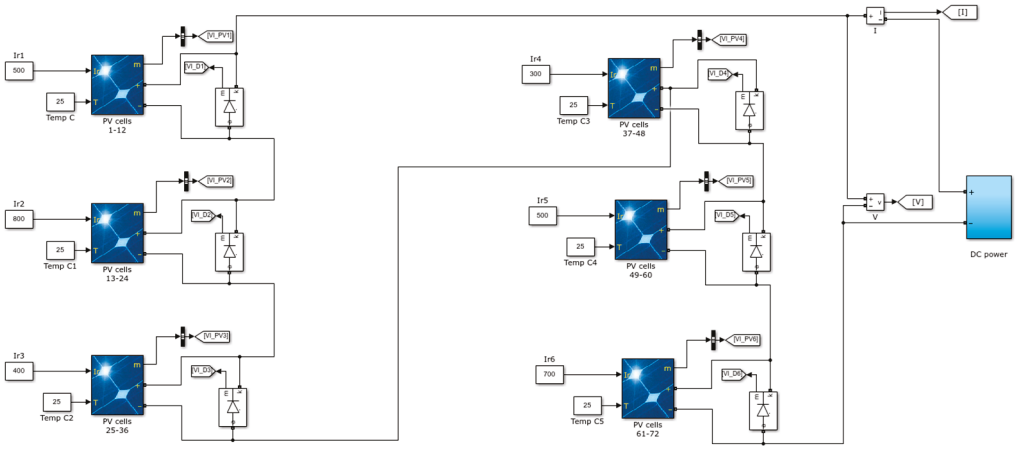


Figure 4. Block diagram of the PV system model in Simulink.

This model helps design partial shading scenarios, such as grouping cells into sections of 12 within a total of 72 cells. P-V curves are generated in real time in these scenarios as irradiance conditions change as shown in Figure 5. P-V curves are crucial for identifying the MPP, particularly under partial shading conditions where multiple peaks may occur.

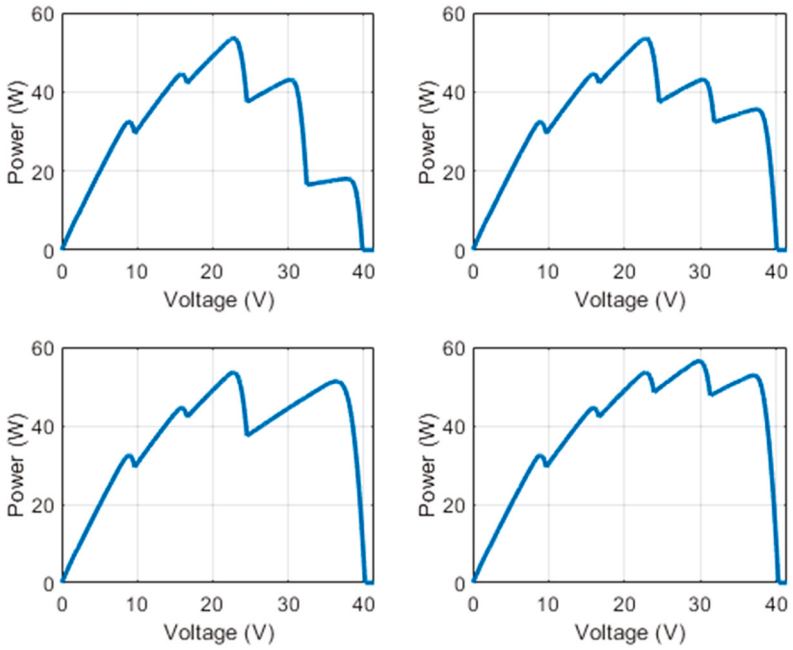


Figure 5. P-V curves generated by the PV model.

2.2. Desing of the Neural Network to Predict the MPP in the System

The predictive model for PV power using a neural network includes three steps: data collection and preprocessing, building and training the neural network, and model evaluation. This process enables the prediction of power generation under various conditions, facilitating the management and optimization of PV systems [31].

Feedforward networks become particularly relevant after constructing a predictive model for PV power. These neural networks organize neurons into interconnected layers, enabling them to solve complex problems and model nonlinear relationships. During training, forward propagation (to generate outputs) and backward propagation (to adjust weights via error backpropagation) are repeated multiple times, optimizing the weights to minimize errors in the training data. Once trained, the MLP is evaluated with new, unseen data to test its generalization ability, ensuring it can process inputs different from those encountered during training.

The predictive model used a multilayer perceptron (MLP) trained with the Levenberg–Marquardt algorithm (LMA) structure is:

- The model inputs are normalized voltage and irradiance values from PV array simulations under partial shading.
- Target output for the model is the normalized output power.
- Regarding the network structure, the input layer includes voltage and irradiance profile.
    - Following the input layer are two hidden layers, each consisting of 10 fully connected neurons.
    - The output layer then comprises one neuron, which predicts power.
- As for activation functions, the hidden layers utilize a sigmoid activation function.
    - Meanwhile, the output layer uses a linear function.

The neural network was trained on simulated data generated under varying shading conditions, allowing it to predict and regulate the system's output at the GMPP. Training was performed using the Levenberg–Marquardt Algorithm (LMA), which combines Newton's method with gradient descent to ensure fast and stable convergence. Through iterative weight adjustment, the network minimizes the error between predicted and actual power, effectively capturing the nonlinear characteristics of P-V curves. The training inputs consisted of voltage and irradiance from different module sections, while the desired output as the corresponding power at the GMPP, enabling the model to learn representative shading patterns and improve its accuracy in real-time MPPT applications. Figure 6 illustrates the structure of the artificial neural network used in the simulation.

To ensure the accuracy of the estimator, a training and validation process is carried out:

- First, simulation data is generated for multiple irradiance scenarios, representing different levels of partial shading. Specific training settings included a maximum of 1000 epochs. Performance was evaluated using the Mean Squared Error (MSE), with the best validation performance achieved at epoch 1000 ($MSE = 3.91 \times 10^{-3}$). To encourage generalization, early stopping with validation checks (patience = 6) was implemented.
- Data is divided into training and validation subsets to prevent overfitting and ensure the neural network generalizes well under different shading conditions.
- Finally, the error between the estimated MPP and the actual MPP (obtained by simulation) is calculated for each condition. A low error indicates good accuracy in the estimation. Figure 7 shows the correlation between the training, validation, and testing error data.

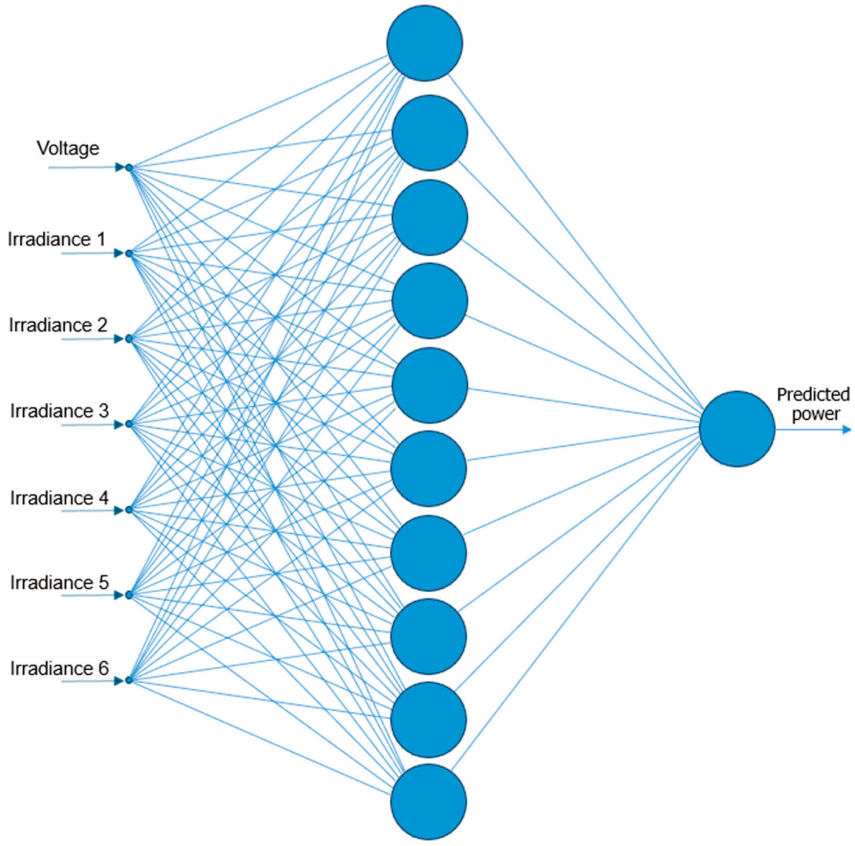


Figure 6. Neural network structure.

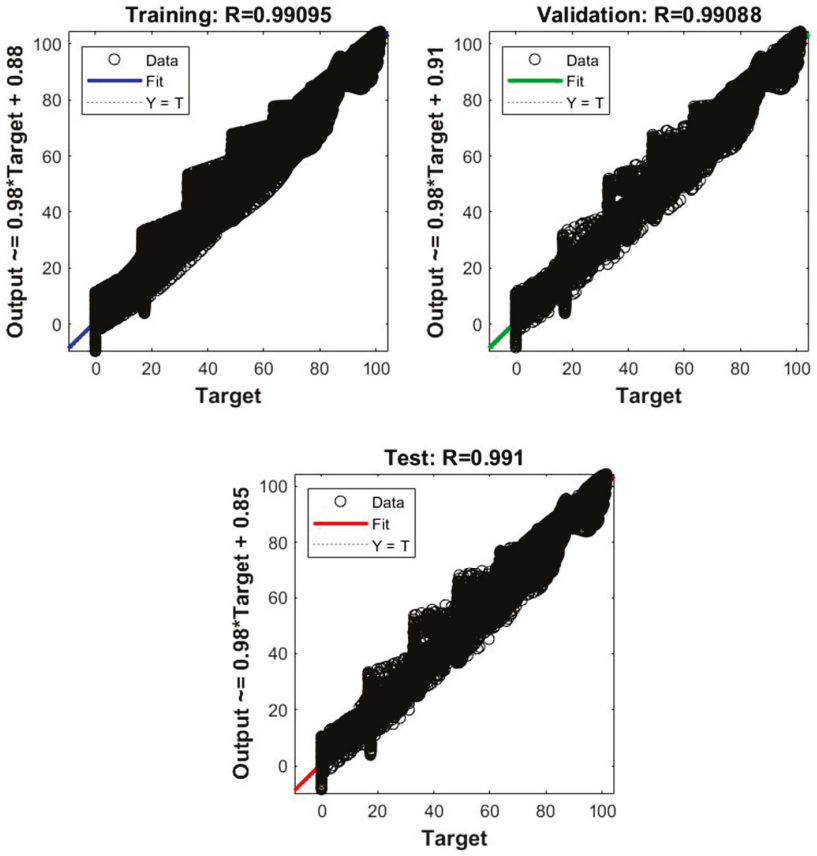


Figure 7. Scatter plots of neural network fit with $R^2 \approx 0.99$ across training, validation, and testing phases.

A slope near 1 and clustered points around the regression line show a highly accurate model and strong agreement between actual and predicted values. The high correlation coefficient (R = 0.99051) confirms that the neural network performed exceptionally well on the training, validation, and testing datasets, effectively learning the input-output relationship. Following training, the next step is to implement the model in the PV system for MPPT and the necessary code to embed it in the system controller.

2.3. Intelligent Control Algorithm for the MPPT

For the P&O algorithm, when the PV system's operating voltage shifts in a given direction and the generated power rises, the operating point nears MPP. In this case, the voltage should be adjusted in the same direction. If the power falls, the operating point shifts away from the MPP, and voltage must then be adjusted in the opposite direction to reapproach the MPP.

The proposed algorithm builds on the MPPT P&O method. It is enhanced by a neural network-derived search point which predicts maximum power (Pprev) and its associated voltage (Vprev). This streamlines efficiency by starting near the estimated MPP. After that, the P&O algorithm adjusts the voltage to pinpoint the MPP precisely. It makes incremental perturbations and monitors changes in generated power. The operation is adapted to align with the neural network's predicted maximum power point.

The proposed algorithm is based on a key premise: having a more precise knowledge of the solar panel's power-voltage (P-V) curve enables MPPT systems to operate more efficiently. Figure 8 illustrates the algorithm. It integrates the P&O method with neural network-generated values.

The algorithm simulation is performed in MATLAB, as shown in Figure 9, which includes an MPPT controller block. This block provides a control signal to adjust the PWM duty cycle, ensuring continuous MPPT operation. Within the controller, the P&O algorithm receives voltage and current data from the solar panel array and neural network, then generates a reference voltage to adjust the PWM duty cycle. A feedback control loop on the right side of the MPPT block produces a PWM signal for the DC-DC converter, regulating the panel's output power to maintain the system at its maximum power point. The control system consists of:

- PV array input: The intelligent control system uses an artificial neural network. This neural network was trained to predict the MPP under different environmental and operational conditions. This approach improves the system's efficiency and dynamic response compared to conventional control methods. The first block, 'NeuralNetwork-Function', receives the PV array's voltage and irradiance as inputs. It generates an output that predicts the maximum power. The output also determines the optimal operating point and the voltage at which maximum power is produced.
- Delay blocks (1/z): These blocks store previous values of variables. These include array voltage, array current, and array power. The stored values are required for computing differences in the P&O algorithm.
- P&O algorithm: This model operates in conjunction with a PWM generator to adjust the DC-DC converter's duty cycle. As a result, power regulation is effective. In the 'PO' block, the P&O algorithm uses previous voltage, power, and duty ratio values. It calculates the new duty cycle and adjusts the PV array's operating point.
- PWM generation: The resulting duty signal D is sent to a PWM generator that modulates the pulse width. It controls the power converter's switch in the power section of the system.

- DC-DC boost converter: In this power circuit, the PWM controls the voltage and current of the PV array and regulates the converter's switch to keep the system at its maximum power point.

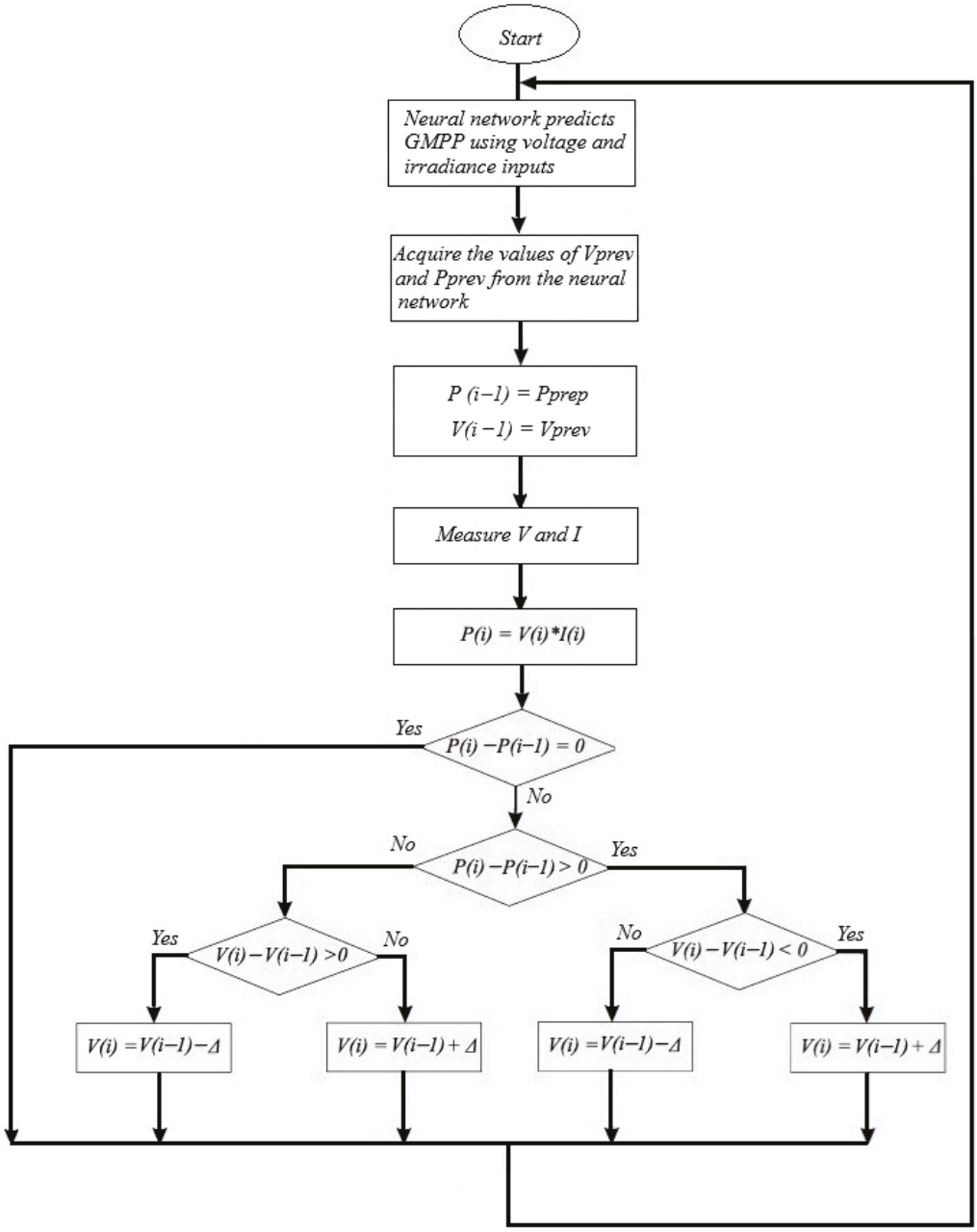


Figure 8. Flowchart of the proposed MPPT algorithm.

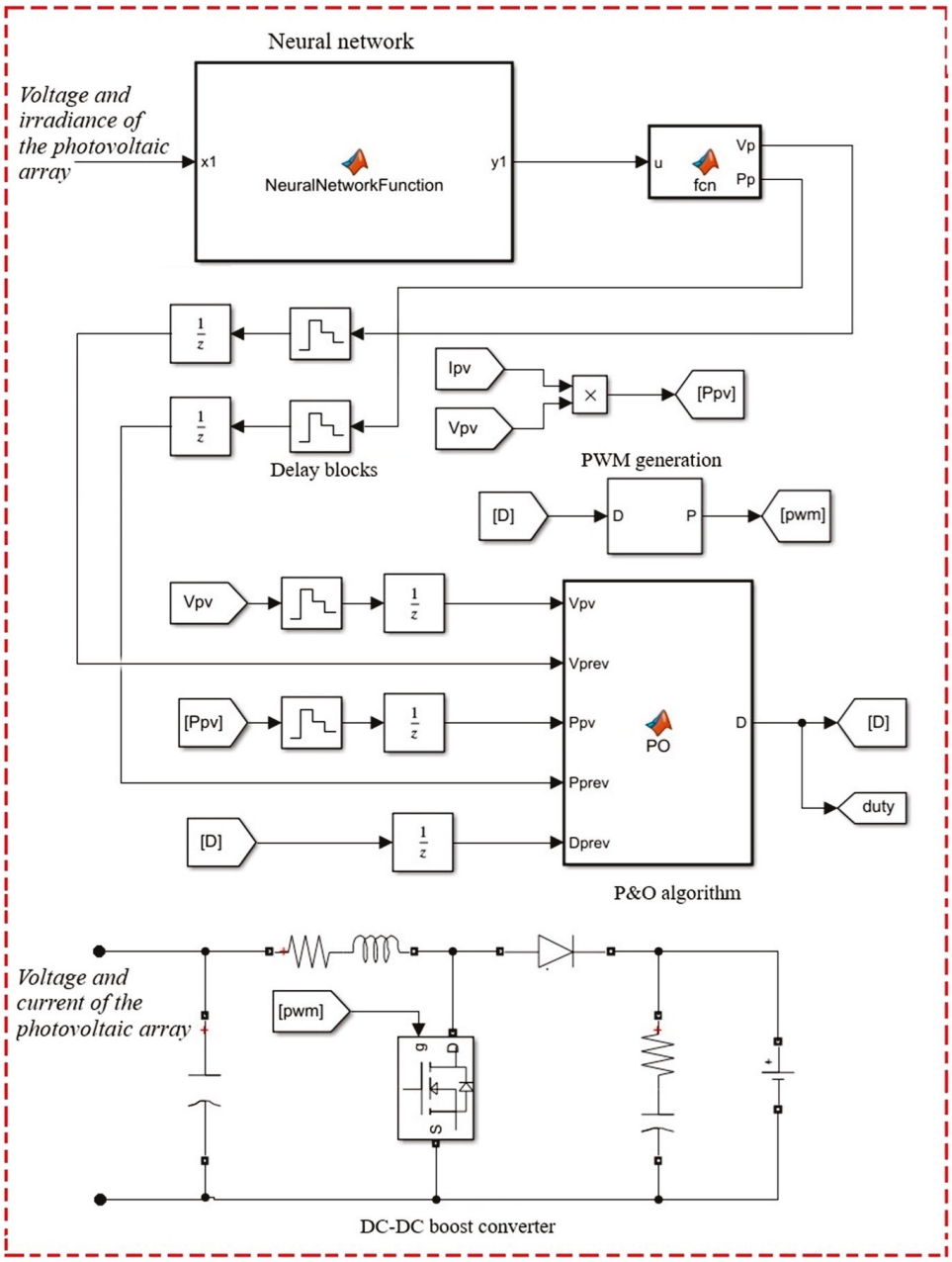


Figure 9. Simulation model of intelligent control.

2.4. Selection of Perturbation Period and Perturbation Magnitude in P&O

In the P&O algorithm, tracking efficiency and system stability strongly depend on two critical parameters:

1. the perturbation period (T_{pert}), and
2. the perturbation magnitude (ΔV).

An inappropriate choice of these parameters may lead to excessive oscillations around the MPP, considerable power losses, or even instability. Therefore, a scientifically sound and quantitative selection criterion is required.

2.4.1. Perturbation Period Selection

The perturbation period must be larger than the dominant time constant τ of the DC–DC converter and its control loop, so the PV power settles before each measurement.

The adopted rule is

$$T_{pert} = \beta\tau,\ \beta \in [3,5] \tag{3}$$

which ensures that the measured power corresponds to at least 95% of the settled response. In practice, this can be expressed as:

$$f_{pert} = \frac{1}{T_{pert}} \leq \frac{f_c}{10} \tag{4}$$

where f_c is the crossover frequency of the converter control loop, this criterion prevents the algorithm from acting on unsettled signals and guarantees stable operation.

2.4.2. Perturbation Magnitude Selection

Oscillation around the MPP introduces an average power loss proportional to the local curvature of the P-V curve. Using a quadratic approximation around the optimal voltage V_{MPP}:

$$\Delta\overline{P} \approx \frac{1}{2}\left|\frac{\delta^2 P}{\delta V^2}\right|_{V_{MPP}} \Delta V^2 \tag{5}$$

To limit this loss to a fraction ε of the maximum power P_{MPP}, the following condition is imposed:

$$\Delta V \leq \sqrt{\frac{2\varepsilon P_{MPP}}{\left|\frac{\delta^2 P}{\delta V^2}\right|_{V_{MPP}}}} \tag{6}$$

This condition provides a physically grounded upper bound for the perturbation step size, ensuring a trade-off between convergence speed and energy efficiency.

2.4.3. Lower Bound Due to Noise and Irradiance Variations

To avoid misinterpretation of the power increment due to measurement noise (σp) or fast irradiance variations ($\dot{P}_{env}$), a lower bound must also be enforced:

$$|\Delta P| = \left|\frac{\delta P}{\delta V}\right|\Delta V \geq \kappa\sigma p + \left|\dot{P}_{env}\right|T_{pert} \tag{7}$$

It should be noted that κ = 3 (three-sigma criterion). Near the MPP, $|\partial P/\partial V| \to 0$ |, so keeping ΔV constant would make |ΔP| vanish; therefore, ΔV must be adaptive. This ensures that perturbation produces a detectable effect beyond noise and environmental fluctuations.

2.4.4. Adaptive Strategy

Considering both the upper and lower bounds, an adaptive perturbation law is defined as

$$\Delta V_k = clip\left(\alpha\left|\frac{\delta P}{\delta V}\right|, \Delta V_{min}, \Delta V_{max}\right) \tag{8}$$

where α is a gain tuned so that far from MPP (large slope) steps are larger, while near MPP (small slope) steps shrink automatically, while ΔV_{min} and ΔV_{max} are derived from the above constraints.

Far from the MPP, the steep power slope leads to larger ΔV and faster convergence. Near the MPP, the slope decreases, and ΔV is automatically reduced, minimizing oscillations. This framework ensures that the perturbation period is directly related to the converter dynamics, preventing premature decisions and perturbation magnitude is bounded by the P-V curvature, limiting power losses. Algorithm robustness against noise and fast irradiance changes is guaranteed through a lower bound.

The parameter ε represents the relative loss tolerance defined as

$$\Delta\overline{P} \leq \varepsilon P_{MPP} \tag{9}$$

where $\Delta\overline{P}$ is the average power loss induced by steady oscillations around the MPP.

In practice, ε is a design choice that specifies how efficient degradation is acceptable in exchange for a feasible perturbation magnitude ΔV. Typical values range between 0.1% and 1% of P_{MPP}.

Figure 10 illustrates the impact of the perturbation magnitude (ΔV) in the P&O algorithm on the power–voltage (P-V) curve of the PV system. A very small ΔV (green point) achieves high accuracy near the MPP but results in slow convergence. In contrast, a large ΔV (blue point) yields faster convergence but introduces significant oscillations around the MPP. The adaptive ΔV strategy (yellow point) ensures an optimal trade-off since it dynamically adjusts the perturbation step according to the slope of the P-V curve, while keeping ΔV within ΔV_{min} and ΔV_{max} (using the clip operator). This approach combines the stability of small perturbations with the responsiveness of large ones.

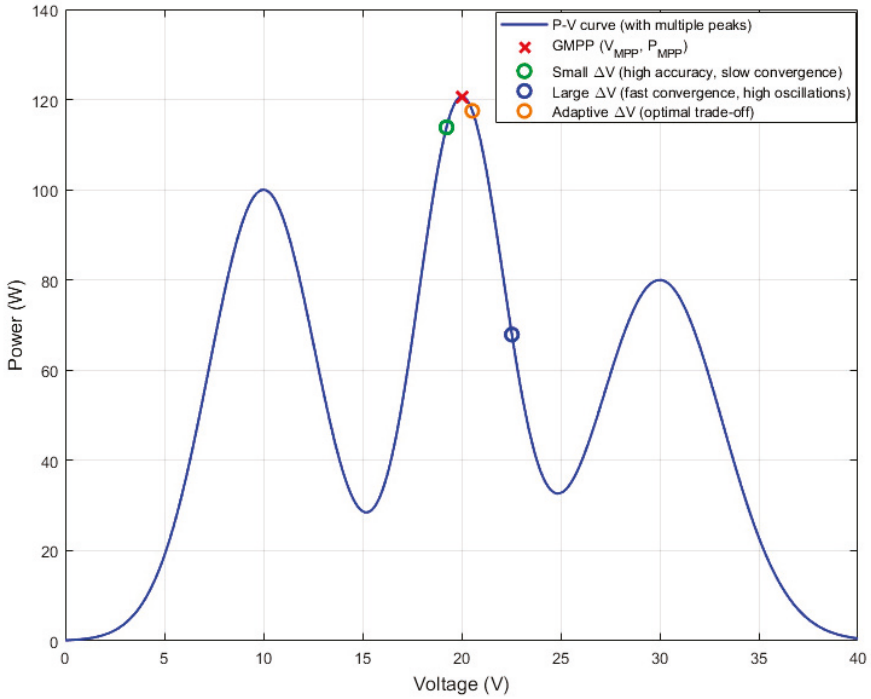


Figure 10. Effect of perturbation magnitude (ΔV).

Figure 11 shows how the perturbation period (T_{pert}) affects the P&O algorithm. A short T_{pert} (blue curve) causes the controller to take samples before converter dynamics settle, leading to oscillations and instability near the MPP. A long T_{pert} (green curve) brings stability, but tracking becomes slow and convergence to the MPP is delayed. The adaptive T_{pert} strategy (orange curve) adjusts the sampling interval based on converter bandwidth and settling time, achieving both fast convergence and stable operation near the MPP.

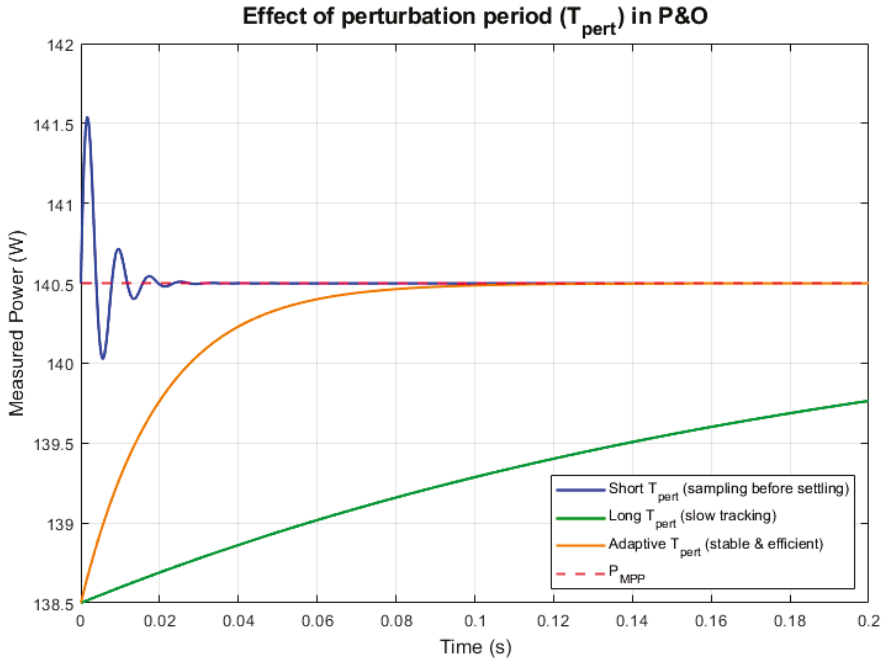


Figure 11. Effect of perturbation period (T_{pert}).

3. Results

Integrating subsystems into the Simulink model allows a more detailed and realistic simulation of how the PV system works. Figure 12 illustrates this setup: a PV array with a DC-DC boost converter is controlled by a system that utilizes both a neural network and an adaptive P&O algorithm. The PV array produces electricity from sunlight. The control system enhances performance by utilizing measurements such as PV current (I_{pv}), voltage (V_{pv}), and environmental data, including sunlight and temperature. The neural network estimates a starting reference voltage V*, defined as the predicted voltage at or near the GMPP, which the adaptive P&O algorithm fine-tunes with a variable adjustment method (T_{pert}) to find the GMPP. This setup enables the system to reach the maximum power point faster and remain stable when conditions change suddenly. The optimized output is used to create a duty cycle (D) in the PWM control block, which operates the boost converter. Ongoing voltage and current feedback keep the system steady and help maximize power output under changing conditions.

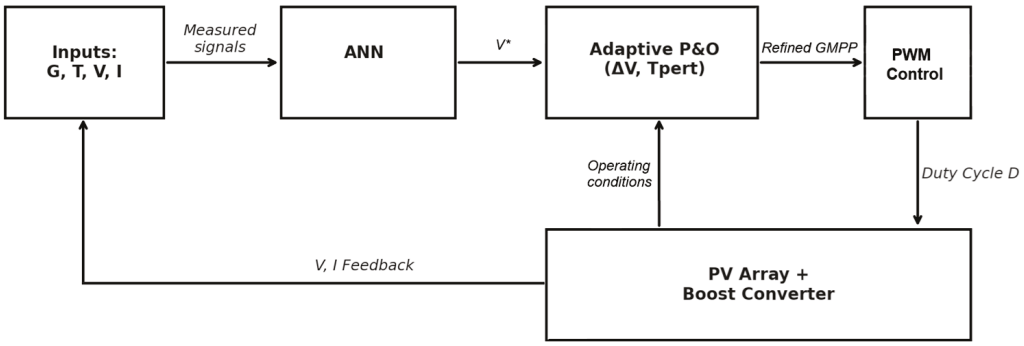


Figure 12. Components of the model.

Different scenarios were designed to evaluate the PV array's performance under dynamic partial shading, simulating real-world obstacles like fast-moving clouds or shifting shadows. These scenarios show how varying shading affects efficiency and help study how quickly and effectively the MPPT system adapts to changes in irradiance. This

analysis gives insight into stability and overall energy efficiency. For this, the 72 PV panel cells were divided into six groups of 12 cells each, as shown in Figure 13, allowing comparison to identify best practices for maximizing energy production when partial shading is unavoidable. The groups are:

- Group 1: includes cells 1 to 12.
- Group 2: includes cells 13 to 24.
- Group 3: includes cells 25 to 36.
- Group 4: includes cells 37 to 48.
- Group 5: includes cells 49 to 60.
- Group 6: includes cells 61 to 72.

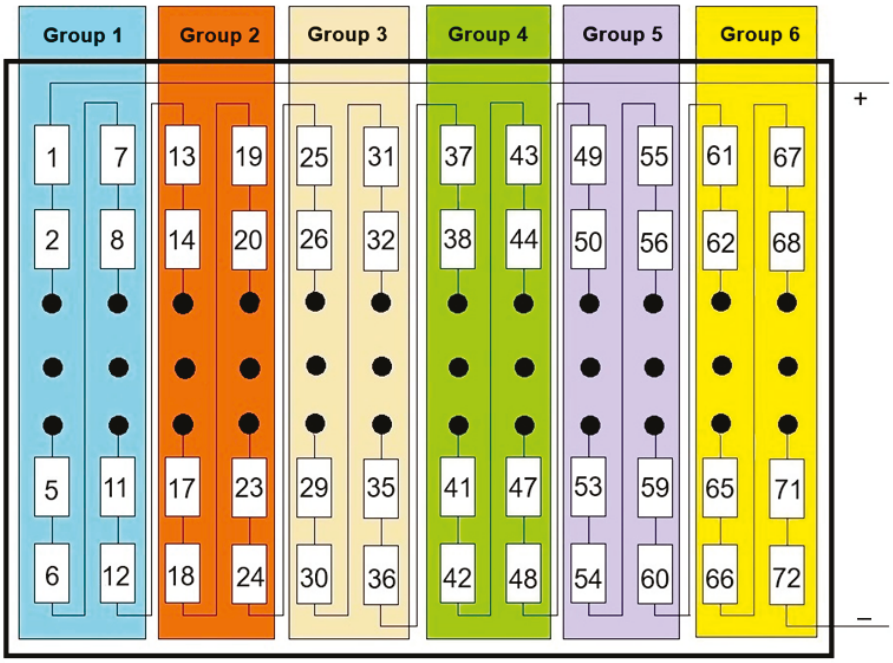


Figure 13. Cell groups integrated into the PV panel.

Each group connects two cells in series, thereby maximizing the PV panel's efficiency under partial shading. This arrangement also supports MPPT techniques, enabling more effective management of irradiance variations among groups. Below, several designed shading scenarios are detailed.

3.1. Scenario 1: Irregular and Uneven Shading

An irregular shadow covers cell groups unevenly and non-sequentially. For example, groups 3 and 5 (cells 25–36, 49–60) receive medium irradiance, while groups 1, 2 and 6 (cells 1–12, 13–24, 61–72) receive high irradiance. In contrast, group 4 (cells 37–48) receives low irradiance. Suddenly, all irradiance decreases by 100 W/m^2 and remains constant. This scenario could simulate the shadow from a tree, with dense leaves in some areas and lighter branches in others. Alternatively, it could represent an object suddenly blocking the panel, resulting in unpredictable and uneven shading. To illustrate these effects, Figure 14 shows the irradiance pattern applied to the PV system, both with and without the inclusion of a neural network. Furthermore, Figures 15 and 16 display system results for the P&O MPPT algorithm and the neural network implementation, respectively.

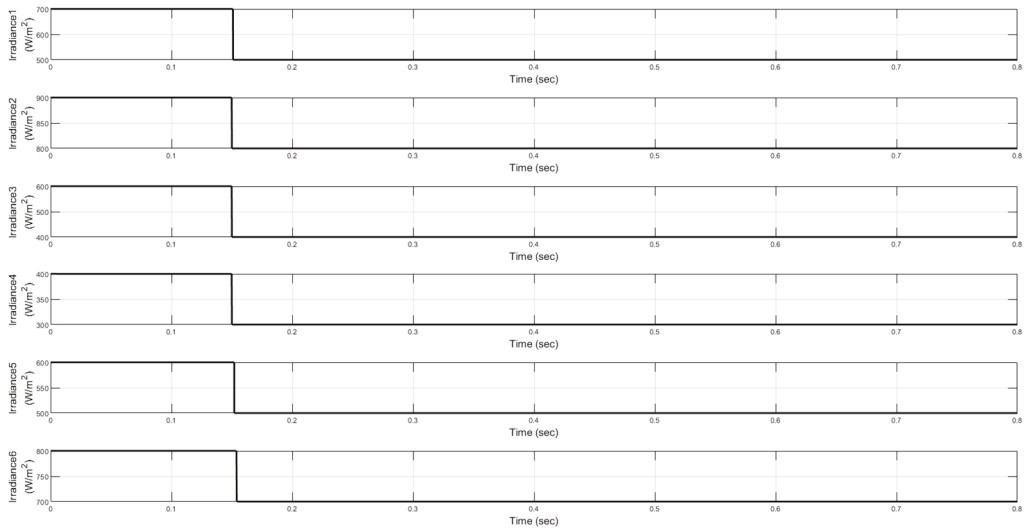


Figure 14. Irradiance patterns for scenario 1.

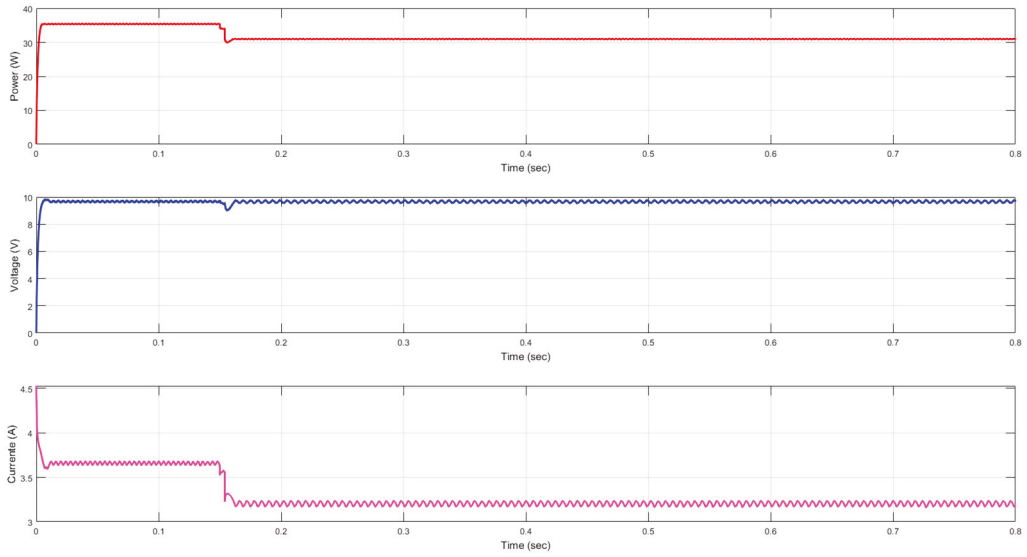


Figure 15. P&O MPPT curves for scenario 1.

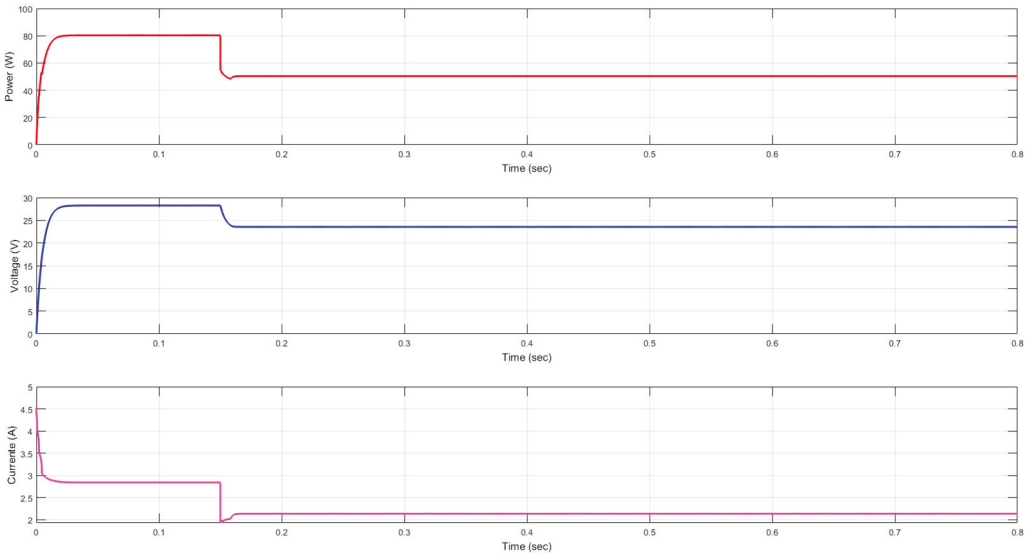


Figure 16. Curves with the MPPT algorithm and neural network for scenario 1.

Results of scenario 1:

- Adaptation to partial shading: The system in Figure 15 shows limited adaptation. Oscillations and power drops indicate that the MPPT algorithm struggles to adjust effectively to irradiance changes, resulting in energy losses. In contrast, Figure 16 shows improved adaptation, characterized by more stable power, voltage, and current. Power still fluctuates, but less severely and more predictably. This demonstrates that the neural network enables the system to respond more effectively to irradiance changes.
- Stability: Figure 15 shows that power fluctuates significantly over time, indicating the P&O algorithm struggles to remain stable during irradiance changes. This instability likely stems from a limited ability to adapt to rapid variations. Figure 16, however, shows steadier power with fewer fluctuations. These results suggest that the neural network improves system stability and helps the MPPT algorithm stay near the maximum power point for a longer period.
- Efficiency: In Figure 15, the system is less efficient due to ongoing power fluctuations, which means it operates away from the best point and captures less energy. Figure 16, in contrast, shows significantly higher efficiency and a steadier power output. With the neural network, the system captures more energy by staying closer to the maximum power point.
- Response time: Figure 15 illustrates a slow response to changing conditions, as evidenced by a prolonged power drop without recovery. This slow change hurts efficiency. In Figure 16, power still drops, but the neural network helps the system recover more quickly and stabilize more effectively. This demonstrates that the neural network enhances adaptation to shading and accelerates the response to irradiance changes.

Graphical analysis confirms that the PV system utilizing the P&O algorithm, enhanced with a neural network, performs significantly better under partial shading conditions, achieving a 49% greater efficiency and an average 16% improvement in stability. This hybrid system rapidly reached the initial maximum power point in just 0.012 s and the final point at 0.16 s, whereas the system using only the P&O algorithm failed to reach the maximum power point entirely within the observation period. By reducing power fluctuations and enabling faster, more precise tracking, the neural network allows the system to operate more stably and efficiently, maximizing energy capture despite dynamic shading conditions.

To validate the generality of the proposed ANN-based MPPT approach, experiments were conducted using a different PV module, the Future Solar Energy FSM572165. Figure 17 shows the power, voltage, and current response under the partial shading scenario 1. The ANN detects and tracks the GMPP under these conditions, ensuring stable convergence and effective operation. Performance with FSM572165 matches baseline dynamics and accuracy, confirming adaptability, robustness, and scalability of the hybrid ANN–P&O method for diverse PV systems.

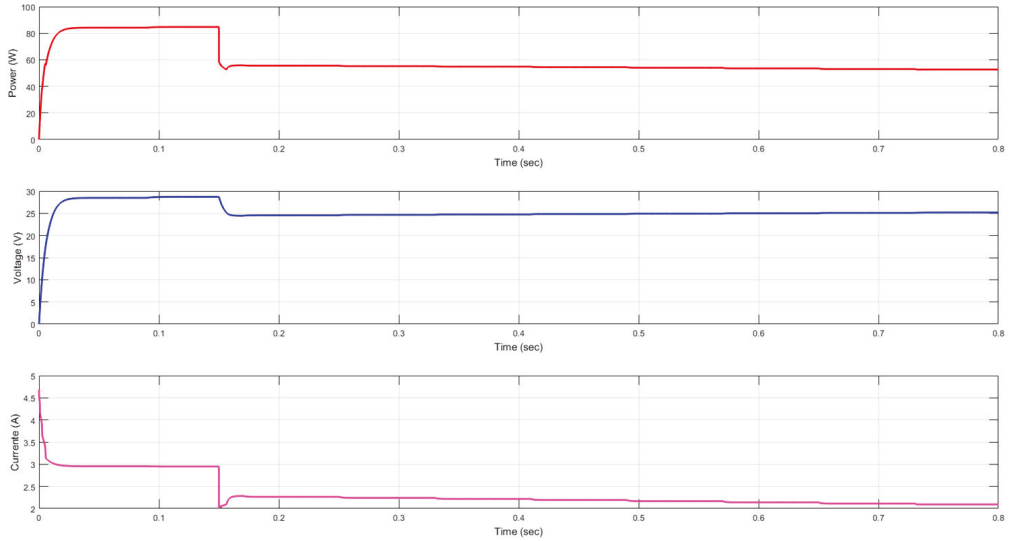


Figure 17. Performance curves of the MPPT algorithm and neural network applied to an alternative solar panel in scenario 1.

3.2. Scenario 2: Oscillating Shadow

In this scenario, a long, oscillating shadow dynamically affects all cell groups at different times. It initially covers groups 1 and 2, then moves toward groups 3 and 4. While doing so, it partially shades groups 5 and 6. This simulates variable shadows cast by elements such as tree branches or cables moving in the wind. Figure 18 illustrates the irradiance pattern applied to the PV system under these conditions. The results compare the performance of the conventional P&O MPPT algorithm with that of the neural network-enhanced system, as detailed in Figures 19 and 20.

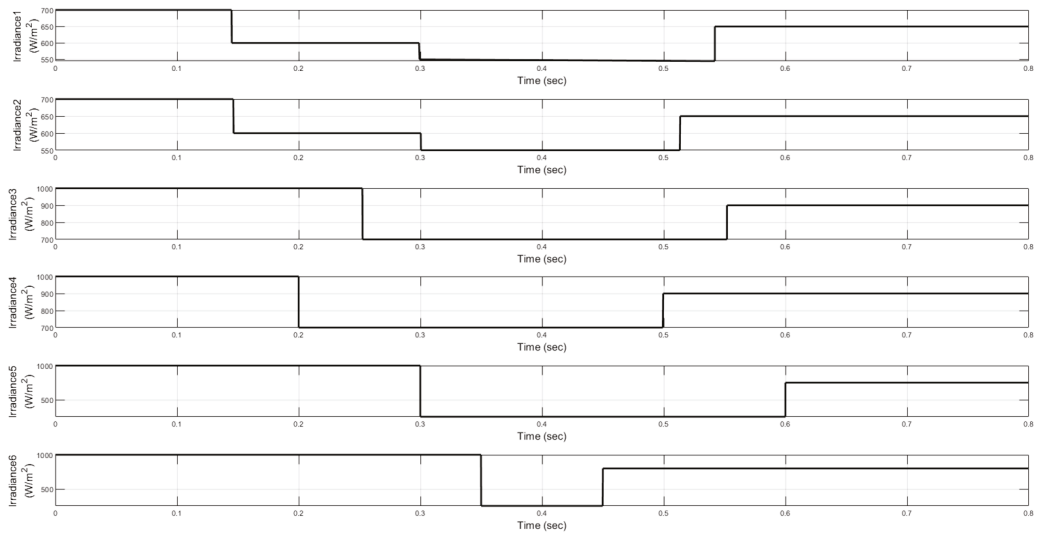


Figure 18. Irradiance patterns for scenario 2.

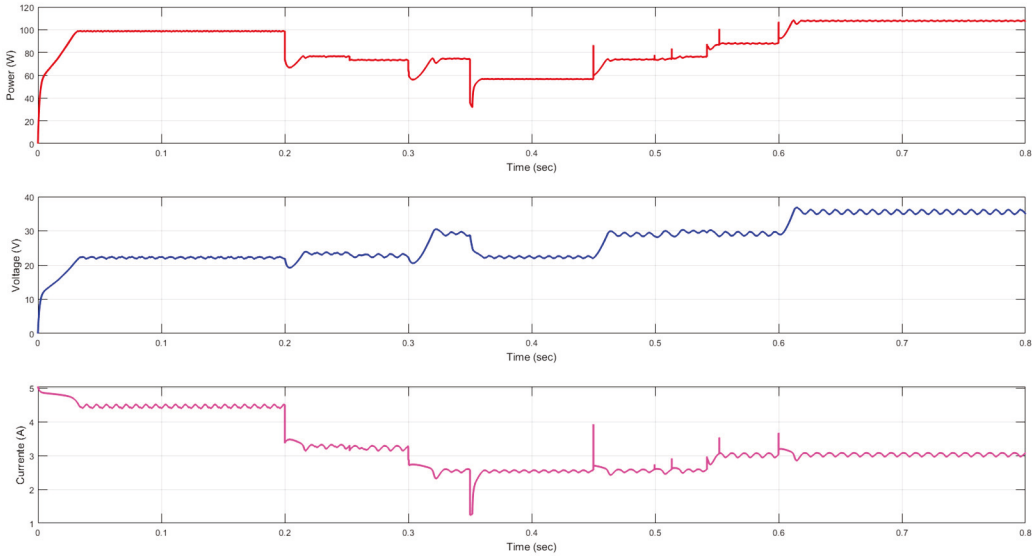


Figure 19. Curves with the P&O MPPT for scenario 2.

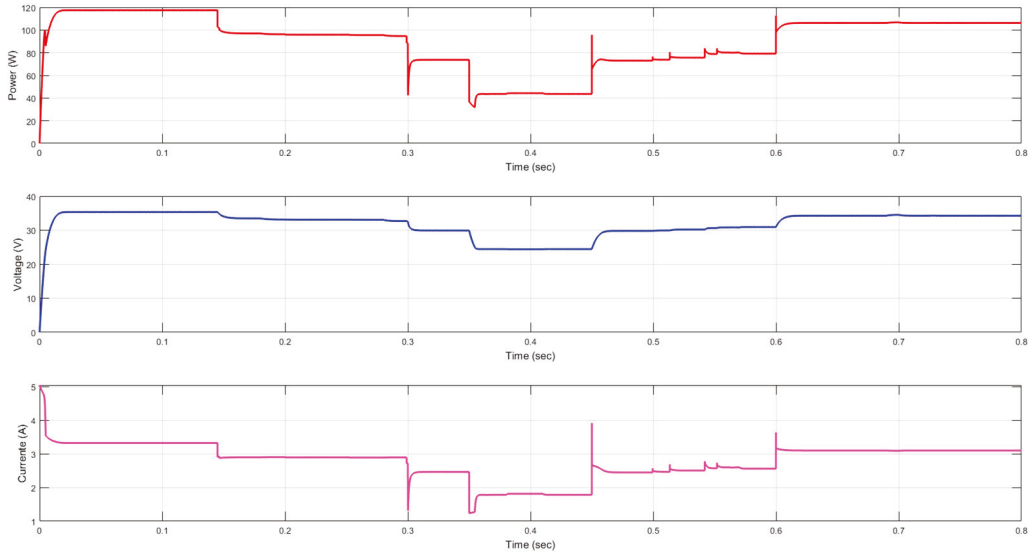


Figure 20. Curves with the MPPT algorithm and neural network for scenario 2.

Results of Scenario 2

- Adaptation to partial shading: The MPPT with only the P&O algorithm (Figure 19) struggles to quickly adapt, as seen in power fluctuations and lower efficiency. The MPPT supported by the neural network (Figure 20) adapts more effectively, although some power drops occur; the system recovers and stabilizes faster, indicating improved adaptation.
- Stability: As shown in Figure 19, power exhibits significant fluctuations under varying irradiance, indicating instability with the P&O algorithm. In Figure 20, fluctuations are less pronounced and more controlled. The neural network smooths transitions and mitigates oscillations, improving stability.
- Efficiency: Figure 19 illustrates lower efficiency, with significant power fluctuations leading to energy losses and reduced capture. In direct comparison, Figure 20 demonstrates higher and steadier power, indicating that the neural network-supported system is more efficient and operationally effective than the standard system.
- Response time: Figure 19 shows a slower response, with significant fluctuations and oscillations in power when irradiance changes, causing energy loss during adjustment.

In contrast, Figure 20 illustrates a faster and more efficient response. Although challenges persist, the neural network anticipates changes and adjusts the MPPT more quickly, allowing for rapid recovery and reduced energy loss.

A quantitative analysis of the power graphs reveals that the MPPT system with neural network support (Figure 20) demonstrates significant advantages over the P&O-only algorithm (Figure 18), showing 20% greater stability and 15.6% higher efficiency on average. Furthermore, the neural network-enhanced system reaches the initial maximum power point 54% faster and the final maximum power point 14% faster than the conventional system. While both systems face challenges under irradiance variations, neural network implementation better maintains optimal power levels and adapts more effectively to changing partial shading conditions. As a result, it offers improved overall performance in terms of stability, efficiency, and response time.

To strengthen the benchmarking of the proposed hybrid ANN–P&O method, an alternative optimization-based MPPT technique was also considered. In this case, the Differential Evolution (DE) algorithm was selected due to its simplicity, robustness, and proven effectiveness in nonlinear optimization problems. DE is a population-based metaheuristic inspired by natural evolution. The algorithm starts with a population of candidate solutions representing possible operating points of the PV system. Each candidate is updated iteratively through three main steps: mutation, crossover, and selection [32].

In the mutation stage, a new candidate (mutant vector) is generated by combining the weighted difference of two individuals with a third one. The crossover mechanism then recombines the mutant with the original candidate, controlled by a crossover probability. Finally, in the selection stage, the trial candidate replaces the original if it yields higher fitness, defined here as extracted PV power.

This iterative process allows DE to efficiently explore the solution space, avoiding local maxima that typically affects classical methods under partial shading. When applied to MPPT, DE dynamically adjusts the duty cycle of the DC–DC converter.

Figures 21 and 22, for scenarios 1 and 2, illustrate the effectiveness of the DE algorithm in MPPT under partial shading conditions. In scenario 1, DE achieves fast convergence to the GMPP, and after the initial transient, voltage and current remain stable. In contrast, scenario 2 features more complex shading, revealing the algorithm's robustness: although oscillations appear in current and power due to rapid irradiance variations, the algorithm successfully stabilizes around the GMPP. This behavior aligns with the applied training strategy, where DE was configured with a population size of NP = 150, a scaling factor of F = 0.8, and a crossover rate of CR = 0.7, iterating for up to 3000 generations. The algorithm optimized a 15-dimensional feature space, including linear, quadratic, and cubic terms of voltage and irradiance, minimizing the mean squared error (MSE) to a value of approximately 0.001, with a correlation coefficient of approximately 0.99 between the predicted and actual data. These results confirm that DE provides accurate prediction and tracking of the GMPP even under dynamic conditions, serving as a reliable reference for validating the proposed hybrid ANN–P&O approach.

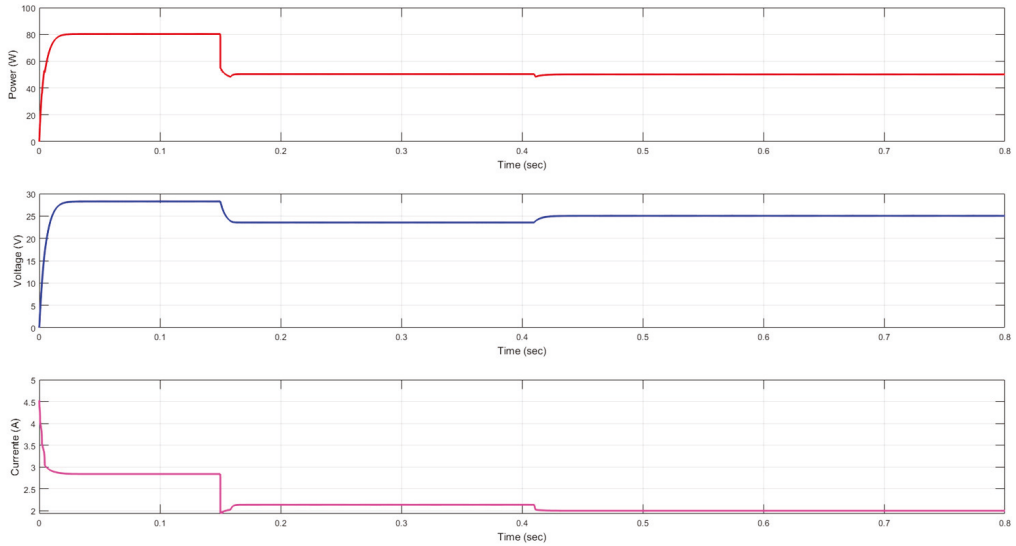


Figure 21. Curves with evolutionary differential (DE) algorithm for scenario 1.

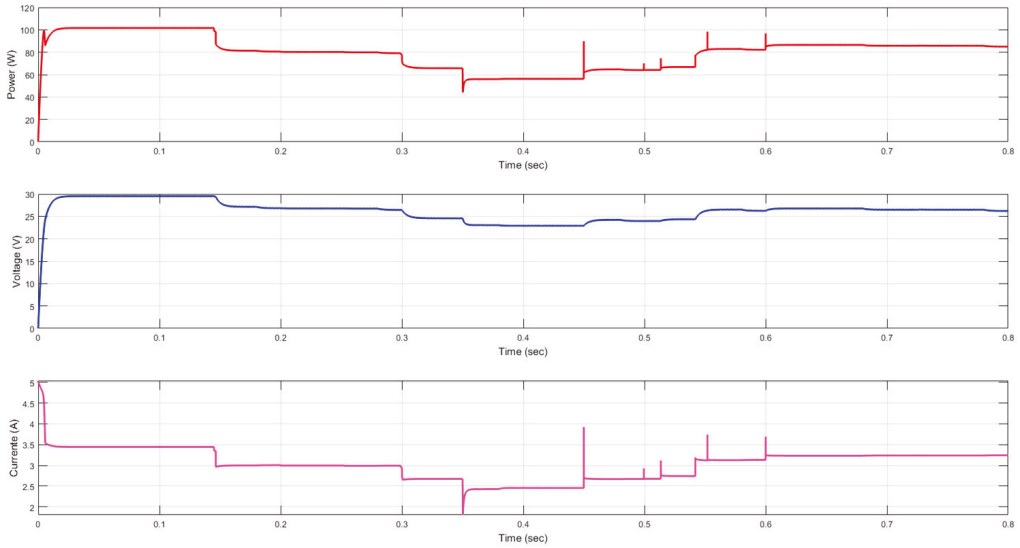


Figure 22. Curves with evolutionary differential (DE) algorithm for scenario 2.

To enable a direct comparison among the tested MPPT strategies, Table 1 presents the main quantitative metrics obtained under both uniform sunlight (irradiance) and partial shading scenarios. These metrics—tracking efficiency (how well the method follows the maximum power point), settling time (how quickly it stabilizes), stability index (the standard deviation to mean ratio, σ/μ, indicating consistency), and relative improvement in energy harvested—highlight distinct differences between methods.

In Scenario 1, which involves irregular and uneven shading, the classical P&O algorithm converges slowly and shows larger oscillations around the MPP, reducing energy harvesting efficiency. The ANN-based method, in comparison, improves tracking speed and stability, reaching the GMPP with minimal oscillations. The DE algorithm also accurately tracks the GMPP and achieves a similar final efficiency to the ANN but requires more computational time to converge.

Table 1. Quantitative performance comparison of MPPT methods under uniform irradiance and partial shading scenarios.

Scenario	MPPT Method	Efficiency (%)	Stability Index (σ/μ Power)	Response Time (ms)	Remarks
1. Irregular and uneven shading	P&O	82.5	0.145	420	Slow convergence, oscillations
	ANN	96.3	0.052	180	Fast tracking, stable
	DE	94.8	0.071	250	Accurate but higher computational load
2. Oscillating shadow	P&O	78.9	0.163	480	Frequent mis-tracking
	ANN	95.7	0.059	190	Robust, stable under fast irradiance changes
	DE	93.2	0.082	260	Good accuracy, slower adaptation

Moving to Scenario 2, which features an oscillating shadow, the classical P&O algorithm is less stable and frequently mis-tracks under rapidly changing irradiance. The ANN-based approach, as in Scenario 1, maintains a fast response and high stability, adapting well to dynamic conditions. DE continues to outperform P&O but adapts more slowly than ANN, underscoring the robustness of the hybrid ANN–P&O scheme.

The classical P&O method delivers reliable performance under uniform irradiance. However, its efficiency and stability decrease significantly in partial shading. This happens because it cannot distinguish between local and global maxima. To address this, the proposed hybrid ANN–P&O approach, as shown in Table 1, overcomes this limitation. It consistently maintains 98–99% tracking efficiency, ensures a fast response, and minimizes oscillations. As a result, harvested energy increases by 15–49% in all tested shading scenarios compared to conventional P&O. The hybrid method also matches the accuracy of intelligent algorithms, such as DE, while operating with lower computational demand. This demonstrates its practical suitability for real-time embedded implementation.

4. Discussion

Computational intelligence techniques, particularly ANNs, demonstrated significant improvements in MPPT under partial shading conditions. A detailed PV system model was developed in MATLAB to simulate P–V curves with multiple local peaks, allowing validation under four distinct shading scenarios. As a result, the ANN-based estimator showed strong predictive and adaptive capabilities, accurately identifying the global MPP across different irradiance patterns. When compared to the traditional P&O method, the hybrid ANN–P&O approach achieved faster convergence, reduced oscillations, and higher stability, especially under irregular or moving shadows, highlighting its potential for real-world applications. However, despite these advantages, some limitations were observed: neural networks demand greater computational resources and longer training times compared to conventional algorithms, and their accuracy is highly dependent on the quality and diversity of the training data. Taken together, these findings confirm the promise of ANNs in enhancing MPPT performance while emphasizing the need to balance accuracy with computational feasibility for practical deployment.

In the context of MPPT, many intelligent methods go beyond classical P&O and IC. Methods such as fuzzy logic, GAs, and PSO enhance tracking efficiency in partial shading by avoiding local maxima; however, each also presents practical issues. Fuzzy logic is fast and robust, but its set rules limit adaptability when conditions change quickly. GAs and PSO offer global optimization, but their repeated, population-based process increases

computation and slows them down, making them less ideal for real-time embedded use. Similarly, sliding mode and model predictive control offer high efficiency but require precise models and substantial processing power. In contrast, the hybrid ANN–P&O method proposed here strikes a balance between accuracy, computational efficiency, and ease of implementation, making it a suitable choice for real-time applications under changing partial shading conditions.

Against this backdrop, the proposed hybrid ANN+P&O method balances accuracy, speed, and complexity. The ANN offers global awareness of the powerand oltage landscape and directs the search to the true GMPP, while the lightweight P&O ensures local refinement with minimal computational overhead. This synergy results in:

1. Higher tracking efficiency than FLC and comparable to GAs/PSO,
2. Faster convergence due to ANN initialization, and
3. Lower runtime complexity, since ANN inference is lighter than metaheuristics.

The proposed ANN+P&O hybrid algorithm is suitable for deployment. Its computationally intensive Levenberg-Marquardt training occurs offline. After training, the ANN operates in forward mode, requiring only basic operations, such as multiplication and addition, per inference. With two hidden layers of 10 neurons each, the online computational cost is low and remains within the capabilities of low-cost embedded devices, such as ARM Cortex-M microcontrollers or DSP-based power inverters. The trained weights occupy only a few kilobytes negligible for current platforms. No additional sensors are needed beyond standard voltage and current measurements.

For larger or high-performance systems, the algorithm can be parallelized or implemented on FPGAs. This enables real-time ANN inference and P&O routine execution with a deterministic response, ensuring seamless integration into grid-tied converters without compromising power quality. The approach scales by matching implementation to system size, supporting lightweight, online microcontroller-based MPPT modules for small systems and industrial FPGA solutions for utility-scale PV plants.

Author Contributions: Conceptualization, A.B. and R.I.R.-C.; Methodology, B.C.; Software, B.C.; Validation, R.I.R.-C.; Investigation, B.C., L.R., R.Q.-P. and A.B.; Data curation, R.I.R.-C.; Writing—review and editing, B.C., L.R., R.Q.-P. and A.B.; Supervision, L.R.; Project administration, L.R. All authors have read and agreed to the published version of the manuscript.

Funding: This research received no external funding.

Data Availability Statement: The original contributions presented in this study are included in the article. Further inquiries can be directed to the corresponding author.

Conflicts of Interest: Author Roberto I. Rico-Camacho was employed by the company CRS Industrial Power Equipment. The remaining authors declare that the research was conducted in the absence of any commercial or financial relationships that could be construed as a potential conflict of interest.

References

1. Azad, M.A.; Sarwar, A.; Tariq, M.; Bakhsh, F.I.; Ahmad, S.; Noor Mohamed, A.S.; Islam, M.R. Global Maximum Power Point Tracking for Photovoltaic Systems under Partial and Complex Shading Conditions Using a PID-Based Search Algorithm (PSA). *IET Renew. Power Gener.* **2025**, *19*, e70005. [CrossRef]
2. Yang, B.; Xie, R.; Guo, Z. Maximum Power Point Tracking Technology for PV Systems: Current Status and Perspectives. *Energy Eng.* **2024**, *121*, 2009–2022. [CrossRef]
3. Sakthivel, S.S.; Arunachalam, V. Artificial Neural Network Assisted P&O-Based MPPT Controller for a Partially Shaded Grid-Connected Solar PV Panel. *Arab. J. Sci. Eng.* **2023**, *48*, 14333–14344. [CrossRef]
4. Mhanni, Y.; Lagmich, Y. Maximizing Solar Panel Efficiency in Partial Shade: The Improved POA Solution for MPPT. *Int. J. Adv. Comput. Sci. Appl.* **2024**, *15*, 975–984. [CrossRef]

5. Krarti, M.; Karrech, A. Evaluation of Static and Dynamic PV-Integrated Shading Systems for Office Spaces in Australia. *Sol. Energy* **2024**, *277*, 112736. [CrossRef]
6. Sezgin-Ugranli, H.G. Photovoltaic System Performance Under Partial Shading Conditions: Insight into the Roles of Bypass Diode Numbers and Inverter Efficiency Curve. *Sustainability* **2025**, *17*, 4626. [CrossRef]
7. Padmavathi, N.; Chilambuchelvan, A.; Shanker, N.R. Maximum Power Point Tracking during Partial Shading Effect in PV System Using Machine Learning Regression Controller. *J. Electr. Eng. Technol.* **2021**, *16*, 737–748. [CrossRef]
8. Mathew, D.; Ram, J.P.; Kim, Y.-J. Unveiling the Distorted Irradiation Effect (Shade) in Photovoltaic (PV) Power Conversion: A Critical Review on Causes, Types, and Minimization Methods. *Sol. Energy* **2023**, *266*, 112141. [CrossRef]
9. Bollipo, R.B.; Mikkili, S.; Bonthagorla, P.K. Hybrid, Optimal, Intelligent, and Classical PV MPPT Techniques: A Review. *CSEE J. Power Energy Syst.* **2021**, *7*, 9–33. [CrossRef]
10. Routray, D.; Rout, P.K.; Sahu, B.K. A Brief Review and Comparative Analysis of Two Classical MPPT Techniques. In *2021 International Conference on Advances in Power, Signal, and Information Technology (APSIT)*; IEEE: Piscataway, NJ, USA, 2021; pp. 1–6. [CrossRef]
11. Worku, M.Y.; Hassan, M.A.; Maraaba, L.S.; Shafiullah, M.; Elkadeem, M.R.; Hossain, M.I.; Abido, M.A. A Comprehensive Review of Recent Maximum Power Point Tracking Techniques for Photovoltaic Systems under Partial Shading. *Sustainability* **2023**, *15*, 11132. [CrossRef]
12. Sarvi, M.; Azadian, A. A Comprehensive Review and Classified Comparison of MPPT Algorithms in PV Systems. *Energy Syst.* **2022**, *13*, 281–320. [CrossRef]
13. Mateo Romero, H.F.; González Rebollo, M.Á.; Cardeñoso-Payo, V.; Alonso Gómez, V.; Redondo Plaza, A.; Moyo, R.T.; Hernández-Callejo, L. Applications of Artificial Intelligence to Photovoltaic Systems: A Review. *Appl. Sci.* **2022**, *12*, 10056. [CrossRef]
14. Boubaker, O. MPPT Techniques for Photovoltaic Systems: A Systematic Review in Current Trends and Recent Advances in Artificial Intelligence. *Discov. Energy* **2023**, *3*, 9. [CrossRef]
15. Bastidas-Rodriguez, J.D.; Ramos-Paja, C.A.; Saavedra-Montes, A.J. Implicit Mathematical Model of Photovoltaic Arrays with Improved Calculation Speed Based on Inflection Points of the Current–Voltage Curves. *Energies* **2023**, *16*, 4875. [CrossRef]
16. Abbas, A.; Farhan, M.; Shahzad, M.; Liaqat, R.; Ijaz, U. Power Tracking and Performance Analysis of Hybrid Perturb–Observe, Particle Swarm Optimization, and Fuzzy Logic-Based Improved MPPT Control for Standalone PV System. *Technologies* **2025**, *13*, 112. [CrossRef]
17. Rukhsar; Ajmal, A.M.; Yang, Y. Global Maximum Power Point Tracking of Photovoltaic Systems Using Artificial Intelligence. *Energies* **2025**, *18*, 3036. [CrossRef]
18. Huang, L.; Pan, B.; Wang, S.; Dong, Y.; Mou, Z. Review on Maximum Power Point Tracking Control Strategy Algorithms for Offshore Floating Photovoltaic Systems. *J. Mar. Sci. Eng.* **2024**, *12*, 2121. [CrossRef]
19. Endiz, M.S.; Gökkuş, G.; Coşgun, A.E.; Demir, H. A Review of Traditional and Advanced MPPT Approaches for PV Systems under Uniform Insolation and Partial Shading Conditions. *Appl. Sci.* **2025**, *15*, 1031. [CrossRef]
20. Ali, M.N.; Mahmoud, K.; Lehtonen, M.; Darwish, M.M.F. Promising MPPT Methods Combining Metaheuristic, Fuzzy-Logic and ANN Techniques for Grid-Connected Photovoltaic. *Sensors* **2021**, *21*, 1244. [CrossRef]
21. Mendez-Flores, E.; Ortiz, A.; Macias, I.; Molina, A. Experimental Validation of an Enhanced MPPT Algorithm and an Optimal DC–DC Converter Design Powered by Metaheuristic Optimization for PV Systems. *Energies* **2022**, *15*, 8043. [CrossRef]
22. Dawahdeh, A.; Sharadga, H.; Kumar, S. Novel MPPT Controller Augmented with Neural Network for Use with Photovoltaic Systems Experiencing Rapid Solar Radiation Changes. *Sustainability* **2024**, *16*, 1021. [CrossRef]
23. Liu, T.; Liu, S.; Yu, H.; Wu, Z.; Tong, J.; Yuan, Q. Research on Hybrid Approach for Maximum Power Point Tracking of Photovoltaic Systems under Various Operating Conditions. *Electronics* **2024**, *13*, 3880. [CrossRef]
24. Timur, O.; Uzundağ, B.K. Design and Analysis of a Hybrid MPPT Method for PV Systems under Partial Shading Conditions. *Appl. Sci.* **2025**, *15*, 7386. [CrossRef]
25. Mamodiya, U.; Kishor, I.; Almaiah, M.A.; Hamdi, M.; Shehab, R.; Alkhdour, T. Numerical Modeling and Neural Network Optimization for Advanced Solar Panel Efficiency. *Sci. Rep.* **2025**, *15*, 23492. [CrossRef] [PubMed]
26. Mwine, I.N.; Han, H.; Liu, H.; Wang, H.; Zheng, X.; Fei, L. A Novel Neural Network Based MPPT Method under Partial Shading Conditions. In *2023 Panda Forum on Power and Energy (PandaFPE)*; IEEE: Piscataway, NJ, USA, 2023; pp. 1057–1062. [CrossRef]
27. Fan, Z.-K.; Setianingrum, A.; Lian, K.-L.; Suwarno, S. A Hybrid Approach for Photovoltaic Maximum Power Tracking under Partial Shading Using Honey Badger and Genetic Algorithms. *Energies* **2024**, *17*, 3935. [CrossRef]
28. Bavarinos, K.; Dounis, A.; Kofinas, P. Maximum Power Point Tracking Based on Reinforcement Learning Using Evolutionary Optimization Algorithms. *Energies* **2021**, *14*, 335. [CrossRef]
29. Rachid, A.; Goren, A.; Becerra, V.; Radulovic, J.; Khanna, S. Photovoltaic Cells and Systems. In *Solar Energy Engineering and Applications*; Power Systems; Springer: Cham, Switzerland, 2023. [CrossRef]
30. Ishak, M.S.B.; Salimin, R.H.; Musirin, I.; Abdul Hamid, Z. Development of PV Array Configuration under Different Partial Shading Conditions. *Int. J. Power Electron. Drive Syst.* **2019**, *10*, 1263–1269. [CrossRef]

31. Lee, Y.; Lee, J. Solar Power Prediction Modeling Based on Artificial Neural Networks under Partial Shading. *Appl. Sci.* **2023**, *13*, 10013. [CrossRef]
32. Zhang, P.; Sui, H. Maximum Power Point Tracking Technology of Photovoltaic Array under Partial Shading Based on Adaptive Improved Differential Evolution Algorithm. *Energies* **2020**, *13*, 1254. [CrossRef]

Disclaimer/Publisher's Note: The statements, opinions and data contained in all publications are solely those of the individual author(s) and contributor(s) and not of MDPI and/or the editor(s). MDPI and/or the editor(s) disclaim responsibility for any injury to people or property resulting from any ideas, methods, instructions or products referred to in the content.

energies

MDPI

Article

Implementing Overfire Air Technology in Coal-Fired Power Plants to Promote Environmentally Friendly Energy Generation

Saltanat Bolegenova, Aliya Askarova, Aizhan Nugymanova *, Valeriy Maximov, Symbat Bolegenova, Nariman Askarov, Shynar Ospanova and Zhanar Shortanbayeva

Department of Thermal Physics and Technical Physics, Al-Farabi Kazakh National University, Al-Farabi Av., 71, Almaty 050040, Kazakhstan; saltanat.bolegenova@kaznu.edu.kz (S.B.); aliya.askarova@kaznu.edu.kz (A.A.); valeriy.maximov@kaznu.edu.kz (V.M.); bolegenova.symbat@kaznu.edu.kz (S.B.); aijoka01@gmail.com (N.A.); shynarospanova1987@gmail.com (S.O.); zhanar.shortanbaeva@kaznu.edu.kz (Z.S.)
* Correspondence: nugymanova.aizhana@gmail.com; Tel.: +7-707-899-98-41

Abstract

This paper presents a numerical study on the deployment of Overfire Air (OFA) technology in coal-fired thermal power plants in Kazakhstan to reduce harmful emissions. The simulation utilized a digital model of the combustion chamber of the BKZ-75 boiler at Shakhtinsk thermal power plant, which utilizes high-ash Karaganda coal containing 35.10% ash. During the development of two-stage combustion technology, different methods of supplying extra air via OFA injectors were examined. Various positions within the combustion chamber were evaluated for their placement: at heights of h = 0.165 m; 0.75 m; 1.375 m; 2.25 m; 2.5 m; 8 m; 9.4 m; 10 m; 11 m; and 12 m. The baseline combustion mode (OFA = 0%) and several additional air injector settings were analyzed, including OFA levels of 5%, 10%, 15%, 18%, 20%, 25%, and 30% of the total air volume. Numerical simulations generated temperature distributions along with carbon monoxide (CO) and nitrogen (NO) concentration fields, both inside and outside the combustion chamber outlet. Research indicates that the most effective reduction in pollutant emissions happens when OFA injectors are positioned at 9.4 m and supply supplementary air at an OFA rate of 18%. Under these settings, the carbon monoxide concentration at the combustion chamber outlet decreases by approximately 36%, while nitrogen oxide levels drop by 25%, compared to the baseline condition (OFA = 0%). These insights can be utilized to upgrade boiler units, promoting cleaner fuel combustion in coal-fired thermal power plants.

Keywords: low-carbon energy; reduction of CO and NO emissions; staged combustion; digital models in the energy sector

1. Introduction

Following the resolutions from the 2021 and 2023 COP conferences, developed nations commit to phasing out coal power plants without carbon capture and storage by 2030–2034. Developing nations are given a longer transition timeframe, until 2040–2050, reflecting the principle of common but differentiated responsibilities [1].

Coal-fired power generation presents a clear duality: it is the most carbon-intensive fossil fuel and a central target for global emissions reduction, yet it remains a dependable and cost-effective means of satisfying rising electricity needs. In developed nations, coal consumption is slowly decreasing, whereas in many Asian countries and other developing regions, it continues to expand. Consequently, despite the common perception that the coal

era is nearing its end, this energy source continues to make a significant contribution to the global electricity supply and helps maintain affordable energy for billions of people.

Since the early 1980s, a relatively moderate growth in coal production was observed: output volumes increased gradually and by the late 1990s reached approximately 20,000 TWh. However, since the 2000s the situation has changed dramatically, with coal production growing rapidly. This led to peak levels of global coal production in the early 2010s, exceeding 40,000 TWh. After reaching a maximum in 2012–2013, total production began to decline gradually, but remained at a high level and stabilized by 2020 [2,3].

Minor fluctuations were observed thereafter, while consumption levels remained consistently high and by 2025 had nearly returned to peak values. The largest contribution to coal consumption has traditionally come from China, whose share increased significantly during the first half of the period under consideration. India has also demonstrated steady growth in consumption, gradually becoming one of the key players in the global coal market. Other Asian countries have likewise increased demand, although at a more moderate pace. Other regions show only slight growth, and their share in total consumption remains relatively small.

Global coal consumption will continue to be driven primarily by Asian countries, while developed economies are reducing their dependence on coal. The highest CO_2 emissions from coal use are observed in Asia, reaching about 8400 million tonnes, which significantly exceeds the levels of other regions. North America stands out with emissions of around 1100 million tonnes, whereas Europe shows lower values, on the order of 430–600 million tonnes [4].

Thus, current trends in the global coal industry include a significant increase in coal production and consumption in Asia, a gradual decline in its role in developed regions, and a corresponding shift in the distribution of carbon emissions [5]. This highlights the continued importance of coal in the global energy balance, while simultaneously emphasizing the challenges associated with environmental impacts and the need for a transition to more sustainable energy sources [6].

Modern global energy systems continue to rely heavily on coal, making a complete phase-out of its use in the foreseeable future virtually impossible. Coal retains its status as one of the leading primary energy sources, providing a substantial share of global electricity and heat generation, while also remaining the largest anthropogenic source of greenhouse gas emissions [7].

It is precisely this dual role of coal—serving simultaneously as a fundamental component of the energy balance and as a major driver of climate risks—that creates a key contradiction and, at the same time, identifies the most promising pathway for accelerating the transition to a low-carbon energy system. Decarbonization measures in the coal sector are therefore capable of delivering the greatest volume of emission reductions in the short- and medium-term perspective.

For Kazakhstan, coal remains a key element of the national energy balance, serving as a reliable, affordable, and stable source of energy. Even with the growing share of renewable energy sources—such as solar, wind, and biomass—these technologies are not yet capable of fully replacing coal. Coal ensures the stability and energy security of Kazakhstan, especially during periods of peak demand. Today, Kazakhstan ranks among the world's top ten countries and holds third place among CIS countries in terms of proven coal reserves and production volumes (around 50 deposits with total resources of approximately 150 billion tonnes). The country produces the full range of coal types, from lignite to hard coal, and the coal industry remains a leading sector of the economy and the backbone of the national energy system [8].

https://doi.org/10.3390/en19020347

The coal produced fully satisfies domestic demand, while a significant portion is exported. Kazakhstan consistently accounts for about 1.7% of global coal exports. Owing to its vast resource base, favorable geographical location, well-developed transport and logistics systems, and strong demand in both domestic and international markets, the coal sector is expected to continue developing. The coal industry also benefits from recurring crises affecting the global oil sector. At the same time, proven coal reserves far exceed oil reserves, which means that, under the current technological paradigm, coal will become an increasingly important strategic resource in the near future [9].

Open-pit mining is still widely used in the development of large coal basins in Kazakhstan. This method allows relatively low-cost extraction and indicates the substantial potential of existing deposits. High-ash coal is produced, which is used at domestic power plants and actively supplied to foreign markets. The ash content of these coals ranges from 39% to 53%. Therefore, the competitiveness of Kazakhstan's coal industry depends largely on the timely modernization of production technologies.

To reduce nitrogen oxide (NO_x) emissions during fuel combustion at thermal power plants and industrial boilers, various methods are employed, including flue gas recirculation, steam or water injection, reduction in excess air ratio, non-stoichiometric combustion, and low-emission combustion technologies. Among these approaches, staged air supply technology, commonly known as overfire air (OFA), is particularly effective [10–13].

In [10], to address the problem of high NO_x emissions from 600 MW boilers at power plants, the authors developed an experimental test rig to model a cold gas–liquid flow at a 1:5 scale for a two-channel overfire air (OFA) system. In particular, the study investigated the effect of OFA injection velocity on the divergence angle of the outlet jet, jet penetration depth, and NO_x concentration in the flue gases.

In [11], a novel combustion system was applied to a 600 MW down-fired boiler to reduce NO_x emissions without a noticeable increase in unburned carbon in fly ash. The system involved relocating the burners designed for lean fuel combustion from the arches to the front and rear walls, redistributing staged air supply, and introducing separated overfire air (SOFA). Using numerical modeling, the authors evaluated the influence of SOFA location (at the arches, in the throat, and in the upper furnace region) on combustion characteristics and NO_x emissions.

In [12] investigated the retrofit of an aging 500 MW tangentially fired coal boiler with high pollutant emissions to achieve low NO_x emissions while maintaining high combustion efficiency. The study assessed and analyzed the combustion and emission characteristics of five different layout configurations aimed at optimizing the position and injection direction of separated overfire air (SOFA) using computational fluid dynamics (CFD) modeling.

In [13], optimization of air distribution was carried out for a proposed SOFA system in a 500 MW tangentially fired boiler consisting of 20 identical modules. The authors evaluated various ratios of burner secondary air, closely coupled overfire air (CCOFA), and SOFA. The results showed that increasing the overall overfire air ratio effectively suppressed NO formation in the burner zone but had a negative impact on boiler performance. Under moderate air staging conditions, NO reduction began between the CCOFA and SOFA levels; therefore, the overfire air distribution could be optimized to improve overall boiler performance.

Thus, studies conducted by various researchers worldwide have demonstrated that the use of OFA technology, in its various configurations, has become a standard approach for reducing NO_x emissions in coal-fired boilers and can also be applied to existing units through retrofit measures.

In the present study, for the first time for the BKZ-75 boiler at the Shakhtinsk TPP plant (Kazakhstan), operating on high-ash coal from the Karaganda basin, a comprehen-

https://doi.org/10.3390/en19020347

sive numerical investigation of staged combustion with overfire air (OFA) supply was performed. A detailed parametric analysis was carried out by varying both the fraction of additional air (OFA = 5%, 10%, 15%, 18%, 20%, 25%, and 30%) and the vertical location of the OFA injectors (h = 0.165 m; 0.75 m; 1.3375 m; 2.25 m; 2.5 m; 8 m; 9.4 m; 10 m; 11 m; and 12 m). Qualitative and quantitative relationships were established between the OFA injector position, the degree of air staging, and their effects on the temperature field as well as on the formation of carbon monoxide and nitrogen oxides. These findings provide deeper insight into the mechanisms governing harmful emission formation during the combustion of high-ash pulverized coal.

The essence of the OFA concept lies in dividing the combustion air into two streams. The primary air is supplied to the main combustion zone, while overfire air is injected at a higher level through dedicated injectors. As a result, two distinct zones are formed in the furnace: a fuel-rich (reducing) zone with limited oxygen availability, where NO_x formation is suppressed, and a burnout zone with excess air, where fuel combustion is completed.

At an optimal OFA fraction (15–30% of the total air supply) and with proper injector placement, NO_x emissions can be reduced by 30–50% without an increase in unburned carbon losses [14,15]. The NO_x suppression mechanism involves several factors: reduction in peak flame temperatures, creation of a reducing atmosphere that promotes the conversion of NO_x to N_2, and a decrease in oxygen concentration in the zone where fuel-bound nitrogen is released.

Various OFA injection schemes and injector designs (Figure 1) allow engineers to tailor air supply strategies, maximizing NO_x reduction while maintaining high combustion efficiency. OFA effectively represents a two-stage combustion process: the first stage limits NO_x formation, and the second stage ensures complete and clean fuel burnout, making this technology one of the most efficient approaches for low-emission coal combustion.

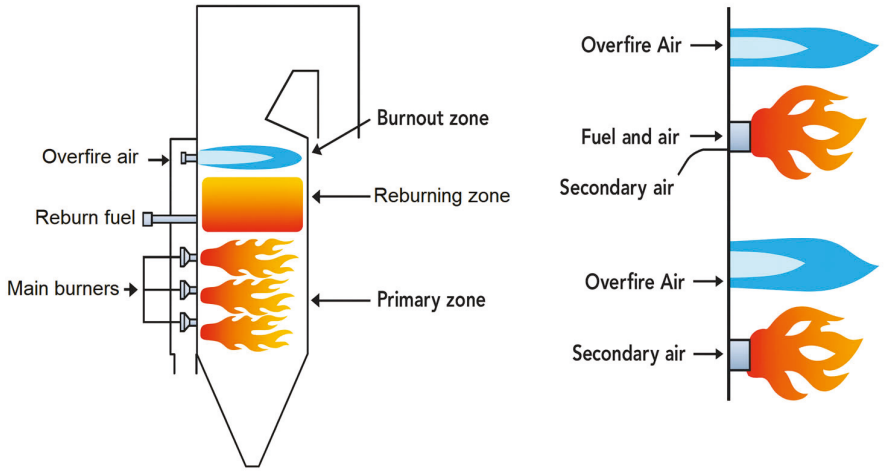


Figure 1. Different OFA injector layout options.

In accordance with the above, the aim of this study is to numerically investigate the effectiveness of applying OFA technology in the BKZ-75 pulverized coal boiler at the Shakhtinsk TPP plant in order to reduce harmful emissions during the combustion of high-ash Kazakh coal. To achieve this goal, the following scientific objectives are addressed: (1) determination of rational parameters for the placement of OFA injectors and the optimal OFA fraction that ensure maximum reduction of carbon monoxide and nitrogen oxide emissions without deterioration of combustion conditions; and (2) development of scientifically substantiated recommendations for the retrofit of existing pulverized coal boilers at thermal power plants in Kazakhstan to improve their environmental performance.

https://doi.org/10.3390/en19020347

This paper examines the application of modern information technologies, digital models (digital twins), and 3D computational modeling methods to implement staged combustion technology using the Overfire Air method in the furnace chamber of the BKZ-75 boiler at the Shakhtinsk TPP plant. The obtained results make it possible to optimize the combustion processes of high-ash thermal coal, reduce particulate and gaseous emissions into the atmosphere, and establish a scientific and technical basis for the subsequent implementation of "clean energy" technologies at other coal-fired combined heat and power plants.

2. Materials and Methods

2.1. Mathematical Model

This study uses coupled models that include equations for mass, momentum, energy, and gas component concentrations to simulate heat and mass transfer, along with physico-chemical processes in high-temperature combustion. It accounts for turbulence, multiphase combustion, chemical reactions, and radiant heat transfer. Overall, the system of equations is organized as follows [16–21]:

$$\frac{\partial \rho \phi}{\partial t} = -\frac{\partial \rho u_i \phi}{\partial x_i} + \frac{\partial}{\partial x_i}\left(\Gamma_\phi \frac{\partial \phi}{\partial x_i}\right) + S_\phi \quad (1)$$

where ϕ—transport variable (u, v, w, T, C, k, ε), Γ_ϕ—exchange rate, S_ϕ—source term that takes into account chemical reactions, radiation, and interfacial interactions.

The numerical solution employs the finite volume method, which the authors have previously used successfully to study high-ash coal combustion at Kazakh thermal power plants [22–24]. Turbulence is modeled through the standard k-ε model, where 'k' denotes turbulence kinetic energy and 'ε' signifies its dissipation rate.

$$\frac{\partial(\overline{\rho}\, k)}{\partial t} = -\frac{\partial\left(\overline{\rho}\ \overline{u_j}\, k\right)}{\partial x_j} + \frac{\partial}{\partial x_j}\left[\frac{\mu_{eff}}{\sigma_k}\frac{\partial k}{\partial x_j}\right] + P - \overline{\rho}\cdot\varepsilon \quad (2)$$

$$\frac{\partial(\overline{\rho}\, \varepsilon)}{\partial t} = -\frac{\partial\left(\overline{\rho}\ \overline{u_j}\, \varepsilon\right)}{\partial x_j} + \frac{\partial}{\partial x_j}\left[\frac{\mu_{eff}}{\sigma_\varepsilon}\frac{\partial \varepsilon}{\partial x_j}\right] + C_{\varepsilon,1}\cdot\frac{\varepsilon}{k}\cdot P - C_{\varepsilon,2}\cdot\frac{\varepsilon^2}{k}\cdot\overline{\rho} \quad (3)$$

$$\mu_t = \rho C_\mu \frac{k^2}{\varepsilon}, \text{ and } \mu_{\,eff} = \mu_{\,lam} + \mu_{\,t} \quad (4)$$

The k-ε constants of the turbulence model have the following values: $C_{\varepsilon 1}$ = 1.44; $C_{\varepsilon 2}$ = 1.92; C_μ = 0.09; σ_k = 1.0; σ_ε = 1.3.

A simplified kinetic scheme with integral reactions ending in final products is employed to simulate combustion. This approach reduces computational costs while still providing acceptable accuracy.

In modeling the processes occurring in the furnace of the studied boiler, the combustion process was considered in the following stages: pyrolysis with volatile release and formation of char residue, combustion of volatile matter, and combustion of carbon monoxide and char. When selecting pyrolysis and combustion models, the authors avoided the use of complex multi-component systems. In this study, a single-step pyrolysis model, as described in [25], was employed.

During the pyrolysis process, volatile matter was treated as fictitious hydrocarbons, and the combustion rate of the pyrolysis products was determined using the Eddy Dissipation Model (EDM) concept proposed by Magnussen and discussed in detail in Ref. [26]. These models have proven to be reliable and represent an excellent compromise for reducing computational costs [27].

https://doi.org/10.3390/en19020347

Initial conditions (t = 0): all velocities u = v = w = 0, excess pressure P = 0, other variables are taken as zero or taken from the convergent solution of previous calculations.

Boundary conditions:

At the entrance: u_i—velocity values, c_β—initial concentration of each component, enthalpy h = $c_p \cdot T$ determined by the flow temperature at the inlet, $k_{inlet} = \frac{3}{2}(\overline{u}_{i,inlet} T_u)^2$, where $T_u = \frac{(u'^2)^{1/2}}{\overline{u}}$—degree of turbulence. $\varepsilon_{inlet} = c_\mu^{0.75} \frac{k^{3/2}}{Lm}$, where L_m = 0.03 (4S/P), P—perimeter of the control volume at the entrance, S—its area.

At the exit: $\left.\frac{\partial u_i}{\partial x_i}\right|_{no} = 0$, $\left.\frac{\partial h}{\partial x_i}\right|_{no} = 0$, $\left.\frac{\partial c_\beta}{\partial x_i}\right|_{no} = 0$, $\left.\frac{\partial k}{\partial x_i}\right|_{no} = 0$; $\left.\frac{\partial \varepsilon}{\partial x_i}\right|_{no} = 0$.

In the plane of symmetry there is:

$$u_i|_{no} = 0;\ \left.\frac{\partial u_i}{\partial x_i}\right|_{no} = 0;\ \left.\frac{\partial h}{\partial x_i}\right|_{no} = 0;\ \left.\frac{\partial h}{\partial x_i}\right|_{ta} = 0;\ \left.\frac{\partial k}{\partial x_i}\right|_{no} = 0;\ \left.\frac{\partial \varepsilon}{\partial x_i}\right|_{no} = 0;\ \left.\frac{\partial c_\beta}{\partial x_i}\right|_{no} = 0$$

On a hard surface (the walls of the combustion chamber):

$$u_i|_{no} = 0,\ \left.\frac{\partial u_i}{\partial x_i}\right|_{no} = 0,\ u_i|_{ta} = 0,\ \left.\frac{\partial c_\beta}{\partial x_i}\right|_{no} = 0\ \varepsilon|_w = 0;\ k|_w = 0.$$

Boundary conditions for wall temperature are usually defined either by the wall temperature Tw or by the heat flux $q_w = \alpha(T_{WP} - T_W)$.

These models and methods provide a dependable representation of furnace processes with moderate computational effort.

2.2. Chemical Kinetics Model in Coal Combustion

In modeling the processes occurring in the furnace of the studied boiler, combustion was considered in the following stages: pyrolysis, with the release of volatile matter and formation of char; combustion of volatile products and carbon monoxide; and combustion of the char residue. The chemical model of pulverized coal combustion accounts for the overall oxidation reactions of fuel components to stable final products [16,20,21].

Char combustion occurs more slowly than the combustion of volatiles and determines the overall burnout time of the fuel, which for pulverized coal is on the order of several seconds. The reaction mechanism is complex and multi-stage, with heterogeneous reactions on the particle surface playing a significant role and homogeneous reactions occurring in the gas phase (Equations (5)–(12)).

$$C + \frac{1}{2}O_2 \rightarrow CO \quad (5)$$

$$C + O_2 \rightarrow CO_2 \quad (6)$$

$$CO_2 + C \rightarrow 2CO \quad (7)$$

$$H_2O + C \rightarrow CO + H_2 \quad (8)$$

$$H_2 + \frac{1}{2}O_2 \rightarrow H_2O \quad (9)$$

In heterogeneous reactions, oxides are formed on the surface of the char particles. At 926 °C, CO and CO_2 are produced in approximately equal amounts, while an increase in temperature accelerates the oxidation rate of CO. The formation of harmful substances is accounted for in the reaction-kinetic models, including intermediate products and the direct reaction of CO with O_2.

https://doi.org/10.3390/en19020347

$$CO + O_2 \rightarrow CO_2 + O \tag{10}$$

Atomic oxygen (O) does not initiate rapid chain reactions, but even a small amount of H_2 generates OH radicals. CO_2 formation occurs in two stages: first, the fuel decomposes into CO and H_2O, and then CO is oxidized to CO_2. At high temperatures and with abundant oxygen, the process is accelerated and can proceed as a single-step reaction, directly forming CO_2.

$$C_xH_y + \left(x + \frac{y}{4}\right)O_2 \rightarrow xCO_2 + \frac{y}{2}H_2O \tag{11}$$

In furnace chambers, calculating CO_2 emissions is a complex task. Sulfur in coal occurs in the form of pyrite, organically bound sulfur, and sulfates. At the initial stage of combustion, sulfur-containing compounds form sulfur monoxide (SO), which is subsequently oxidized to sulfur dioxide (SO_2). Upon contact with atmospheric moisture, SO_2 converts into sulfurous acid (H_2SO_3).

$$S + O_2 \rightarrow SO_2 \tag{12}$$

$$SO_2 + H_2O \rightarrow H_2SO_3 \tag{13}$$

A portion of the sulfur dioxide in the air is further oxidized to sulfur trioxide (SO_3) (Equation (14)). It then reacts with water vapor to form sulfuric acid (H_2SO_4), which, like SO_2, dissolves in atmospheric moisture (Equation (15)).

$$2SO_2 + O_2 \rightarrow 2SO_3 \tag{14}$$

$$SO_3 + H_2O \rightarrow H_2SO_4 \tag{15}$$

During coal combustion, the majority of nitrogen oxides are produced from fuel nitrogen (fuel NO_x), while a smaller portion originates from atmospheric nitrogen (thermal NO_x). The model accounts for volatile release, combustion of hydrocarbons and char, as well as NO_x formation. During the decomposition of coal particles, approximately 80% of the nitrogen is released into the gas phase as cyanides, which are then converted into amines and subsequently either form NO or are reduced to N_2.

$$HCN + H_2O + \frac{1}{2}O_2 \rightarrow NH_3 + CO_2 \tag{16}$$

$$NH_3 + O_2 \rightarrow NO + H_2O + \frac{1}{2}H_2 \tag{17}$$

$$NH_3 + NO \rightarrow N_2 + H_2O + \frac{1}{2}H_2 \tag{18}$$

Additionally, the following reactions occur: formation of HCN as a result of the interaction between hydrocarbons and NO:

$$NO + C_xH_y \rightarrow HCN + H_2O, \tag{19}$$

and the heterogeneous reaction between NO and the char particle:

$$C + 2NO \rightarrow CO_2 + N_2 \tag{20}$$

https://doi.org/10.3390/en19020347

The remaining 20% of nitrogen is oxidized directly to NO at a rate proportional to the char burnout rate.

$$N + \frac{1}{2}O_2 \rightarrow NO \quad (21)$$

For the NO_x formation model, it is necessary to determine the reaction rates affecting the concentrations of NH_3, HCN, NO, O_2, char, and volatile matter. Nitrogen oxides are among the most toxic emissions, so reducing their concentration at the furnace outlet is a critical task in coal combustion at thermal power plants.

2.3. Physical and Digital Models of Processes in the Combustion Chamber

The study examined the combustion chamber of the BKZ-75 boiler at Shakhtinsk TPP in Kazakhstan, which has a steam capacity of 75 tons per hour. The boiler is designed in a U-shape [22–24]. Inside the combustion chamber, there are four pulverized coal burners positioned on the front and rear walls, arranged in a single tier with two burners on each wall. Each burner can produce 3.2 tons per hour when burning Karaganda coal of the KR-200 type, characterized by an ash content of 35.1%, a fineness R_{90} of 20%, a coal density of 1350 kg/m^3, and a calorific value of coal is 1.8548×10^7 J/kg. The Tables 1–3 present the main technical specifications of the boiler along with details about the fuel composition.

Table 1. Calculated performance indicators of the BKZ-75 boiler unit.

№	Parameter	Symbol	Unit	Value
1	Nominal steam output	D	t/h	75
2	Boiler efficiency	η	%	80.88
3	Number of burners in the boiler	N_r	pcs	4
4	Fuel output per burner	B_r	t/h	3.2
5	Primary air flow to the boiler	V_{pa}	Nm^3/h	31.797
6	Secondary air flow to the boiler	V_{sa}	Nm^3/h	46.459
7	Superheated steam pressure	P_{sh}	kPa	3788
8	Superheated steam temperature	t_{sh}	°C	438.1
9	Feedwater pressure	P_{fw}	kPa	5880
10	Feedwater temperature	t_{fw}	°C	105.3
11	Flue gas temperature	t_{fg}	°C	128.9
12	Air excess factor in the furnace	α	-	1.2
13	Hot air temperature	t_{ha}	°C	290
14	Calculated fuel consumption	B_f	t/h	12.49
15	Cold air temperature	t_{ca}	°C	30
16	Aerosol temperature	t_a	°C	140
17	Wall temperature	t_w	°C	430.2
18	The calorific value	Q	J/kg	1.8548×10^7

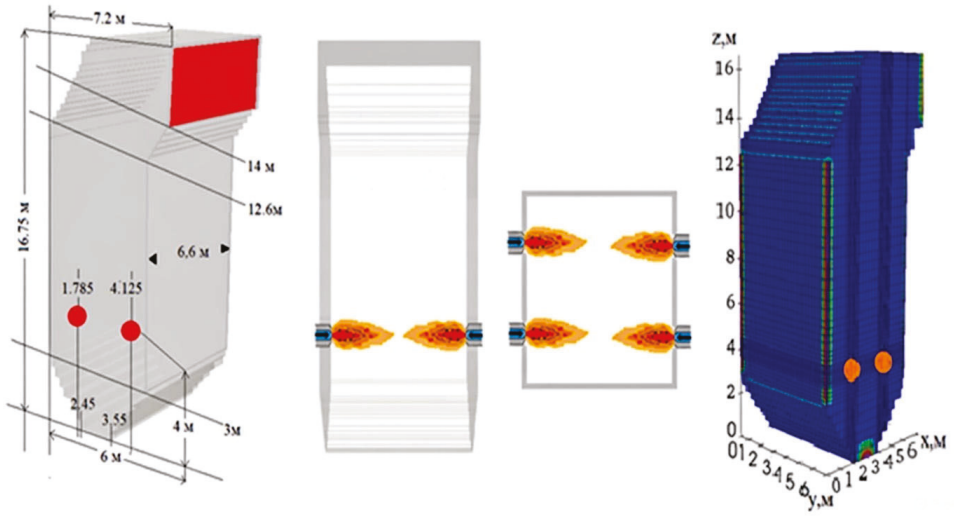
Table 2. Initial data regarding Karaganda coal.

Composition of the Original Coal Dust, Mass %							
C	**H_2**	**O_2**	**S_2**	**N_2**	**W**	***V***	**A**
43.21	3.6	5.24	1.04	1.21	10.60	22.00	35.10

A 3D digital model of the BKZ-75 boiler's combustion chamber was created, precisely representing its real dimensions and the placement of burner devices during operation at the Shakhtinsk TPP: four direct-flow pulverized coal burners arranged in a single tier, with two on opposite walls. All process parameters, including dust-air mixture and air supply, are considered (Figure 2).

Table 3. Dispersion composition of fuel.

Factions	Particle Size, m	Fraction Content, %
1	1.0×10^{-5}	10
2	3.0×10^{-5}	20
3	6.0×10^{-5}	40
4	1.0×10^{-4}	30



(**a**) (**b**) (**c**)

Figure 2. Overview and geometry (**a**), burner placements (**b**), and division into control volumes (**c**) of the BKZ-75 boiler's combustion chamber at Shakhtinsk TPP.

Figure 3 illustrates a general view of the BKZ-75 boiler's combustion chamber (Figure 3a), the arrangement of burner devices with injectors implementing two-stage combustion technology (Figure 3b), and the division of the chamber into control volumes for numerical analysis (Figure 3c).

The finite-difference grid has dimensions of $90 \times 32 \times 158$ along the X, Y, and Z axes, resulting in 455040 control volumes. Condensation takes place in the fuel and air inlet zones as well as near the walls, providing high modeling accuracy with moderate computational effort costs.

For the computational experiments aimed at investigating heat and mass transfer processes in the furnace of a thermal power plant boiler, the FLOREAN 5.0 computer system, developed in Germany, was used as the primary software tool [20,21,28–30]. This software is designed for comprehensive numerical modeling of reacting multiphase flows in domains with realistic geometries and is widely applied in the analysis of heat and mass transfer processes in the combustion chambers of various thermal power units.

Within the scope of this study, a methodology was developed to adapt the FLOREAN software system to the operating conditions in the Republic of Kazakhstan. The need for such adaptation is due to significant differences between Kazakh and German coals, primarily the high ash content of Kazakh fuel, reaching up to 50%, compared to approximately 8% for German coal, as well as differences in the design parameters of furnace chambers, types of burners, and methods of fuel and oxidizer supply. As a result, the original version of the FLOREAN software package was modified, expanded, and tested, enabling numerical experiments on the combustion of high-ash coal at Kazakh thermal power plants.

https://doi.org/10.3390/en19020347

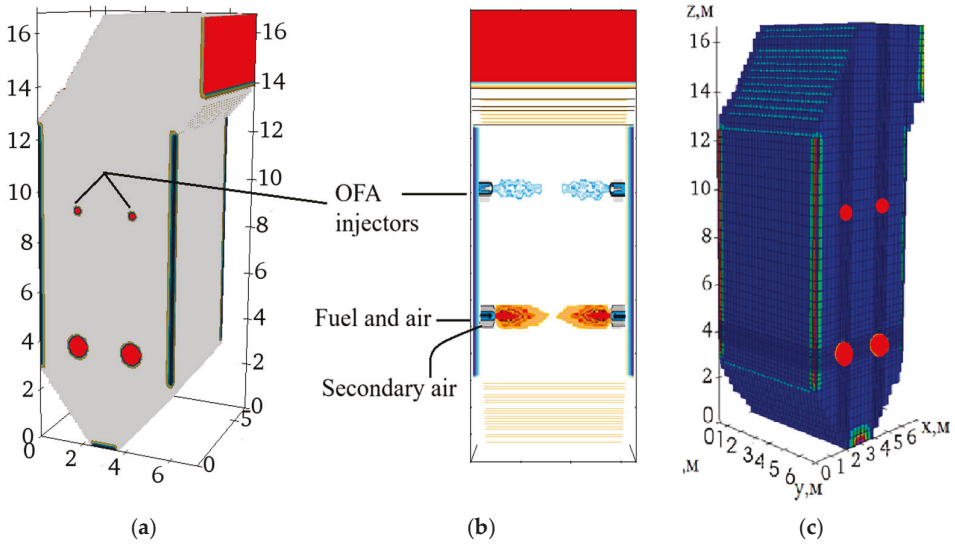


Figure 3. General view (**a**), layout of burner devices and OFA injectors (**b**), and breakdown into control volumes (**c**) of the combustion chamber of the BKZ-75 boiler at Shakhtinsk TPP.

When implementing staged combustion, the primary parameters are the height of the OFA injectors and the flow rate of the Overfire Air (OFA). These influence the reduction in harmful emissions such as carbon and nitrogen oxides while maintaining boiler stability. The optimal placement of the OFA nozzles and airflow depends on the specific geometry and aerodynamics of the chamber. The OFA must adequately mix with incomplete combustion products and complete afterburning, located high enough above the burners to establish a reducing atmosphere in the primary zone and ensure thorough fuel burnout. This study utilized digital models of the combustion chamber and CFD techniques to perform a parametric analysis to determine the ideal height, h, of the OFA nozzles. The proposed injector placement options in the BKZ-75 boiler furnace included: h = 0.165 m; 0.75 m; 1.3375 m; 2.25 m; 2.5 m; 8 m; 9.4 m; 10 m; 11 m; 12 m.

This study investigated various air ratios supplied through OFA injectors to enable two-stage combustion. The control was conventional combustion without OFA (0%), while other options included OFA at 5%, 10%, 15%, 18%, 20%, 25%, and 30% of the total air supply. Table 4 presents the calculated secondary air mass flow rates through the OFA nozzles for all the studied case modes.

Table 4. Aerodynamic properties for managing two-stage combustion.

% OFA	0	5	10	15	18	20	25	30
Mass airflow rate injectors, kg/s	0	0.186	0.461	0.692	0.830	0.922	1.152	1.383

3. Results

The research included a detailed analysis of how the height of the OFA injectors and the volume of additional air supplied through them impact the thermal regime of the BZK-75 boiler furnace, as well as the completeness of fuel combustion and dust-gas emissions of nitrogen oxides (NO) and carbon monoxide (CO). Model calculations and results demonstrated that altering OFA input parameters has a significant influence on temperature zone formation, mixture formation characteristics, reduction process development, and burnout efficiency. The findings reveal optimal air supply modes that reduce CO and NO emissions while maintaining stable combustion product temperatures, thereby enhancing both ecological and energy efficiency.

https://doi.org/10.3390/en19020347

3.1. The Effect of the Installation Height of OFA Injectors on the Temperature and the Concentrations of NO and CO at the Furnace Outlet

Figure 4 shows the dependence of the working medium temperature (curve 1), the concentrations of nitrogen oxide NO (curve 2), and carbon monoxide CO (curve 3) at the outlet of the BZK-75 boiler furnace on the height h at which the OFA injectors are located. Changing the height of the additional air supply significantly affects the temperature T in the burnout zone, the processes of NO_x formation, and the completeness of fuel combustion.

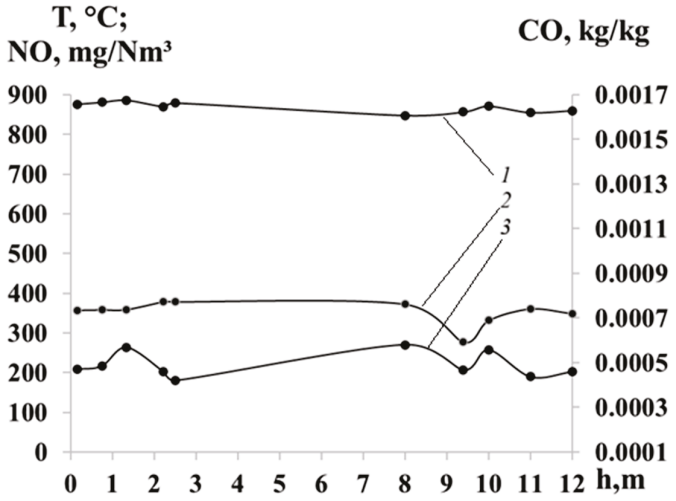


Figure 4. Dependence of temperature T and concentrations of carbon oxides CO and NO on the outlet from the furnace chamber on the height h of the OFA-injectors: curve 1—T; curve 2—NO; curve 3—CO.

As shown in the figure, the average temperature values (Figure 4, curve 1) at the furnace outlet remain relatively stable, around 820–870 °C, regardless of the injector height. Small fluctuations of 30–40 °C may be due to shifts in air and fuel flow distributions, changes in mixing in the upper furnace zone, or local variations in heat release. The lack of sudden temperature shifts suggests that repositioning the OFA injectors within a reasonable range does not significantly disturb the furnace's thermal performance regime.

The concentration of nitrogen oxide NO (Figure 4, curve 2) at the outlet from the furnace space demonstrates an average level of about 350–400 mg/Nm^3, with a tendency to decrease in the height range of 8–9.4 m. This can be explained by the formation of a more pronounced reduction zone beneath the injectors, an increase in the interaction time of combustion products with volatile reducers (CO, hydrocarbons), as well as effective partial cooling of the thermal NO formation zone.

After surpassing a height of approximately 10 m, the NO concentration begins to rise slightly. This suggests a decrease in regenerative reactions, improved after-burning efficiency, and a potential increase in temperature in the over-jet air zone.

The concentration of CO (Figure 4, curve 3) is an indicator of the completeness of fuel combustion. The distribution analysis reveals characteristic features:

- At low injector placement (h = 1–3 m), the CO concentration increases—incomplete combustion occurs due to early interference of air flows into the flame;
- In the interval h = 8–9.4 m, the concentration of CO is minimal, indicating the most efficient combustion and optimal turbulent mixing;
- With further increase in height (h $\geq$ 10 m), the concentration of CO rises again: the over-fuel air is supplied too high, the afterburning zone shifts upwards, and some CO does not have time to oxidize.

https://doi.org/10.3390/en19020347

The behavior of CO aligns with that of NO, confirming the presence of an optimal height h for installing OFA injectors. Figure 5 compares CO concentration distributions in the BKZ-75 boiler's outlet section for three different OFA-injector heights. A consistent color scale (from 1×10^{-4} to 7×10^{-4} [kg/kg]) was applied across all cases, enabling an accurate comparison of results.

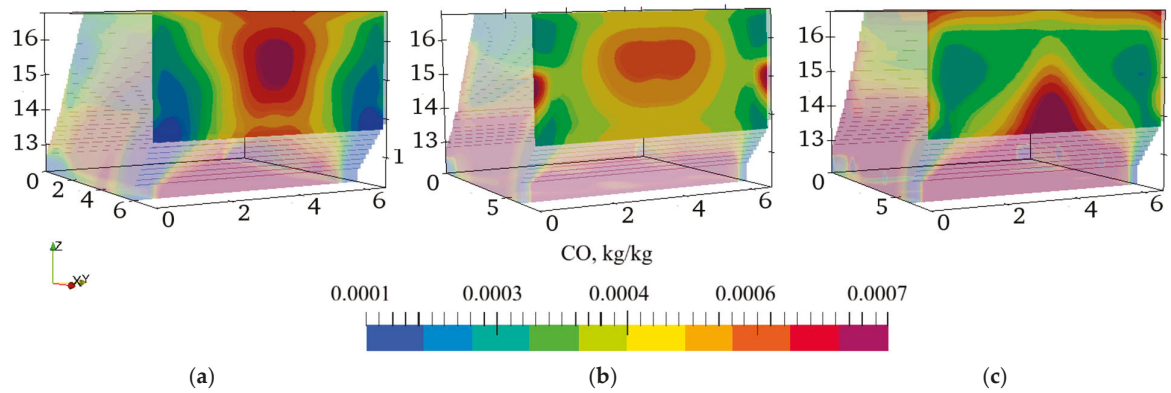


Figure 5. Distribution of carbon monoxide CO concentration at the outlet of the firing chamber at various heights of the OFA injectors: (**a**) h = 2.25 m; (**b**) h = 9.4 m; (**c**) h = 12 m.

Analysis of Figure 5a reveals that installing OFA injectors at a height of 2.25 m results in the most noticeable heterogeneity in concentration flow. In this scenario, a zone with elevated CO levels develops in the central part of the combustion chamber, reaching nearly the upper limit of acceptable levels at 0.00079 kg/kg. This zone has a well-defined local maximum and spans a significant portion of the cross-sectional height. Such a distribution suggests inadequate mixing of fuel and secondary air when the OFA injectors are placed too low, leading to zones of incomplete combustion and increased local CO accumulation.

From Figure 5c, it is evident that the region of increased CO concentration shifts downward and partially moves towards the center of the furnace. The peak values again approach the upper scale limit—0.00095 kg/kg—but their distribution differs from the first case. It appears more vertically stretched and less sharply defined, yet still indicates areas of local under-combustion. This pattern is characteristic of overly high OFA injector settings, where secondary air is introduced too late, creating an elongated zone of incomplete CO oxidation that is transported by the gas flow towards the upper part of the furnace.

When OFA injectors are installed at a height of h = 9.4 m (see Figure 5b), the CO concentration distribution throughout the entire area studied is the most uniform. The figure shows that this distribution is notably smoother, with no distinct high-concentration zones, and the peak CO levels are considerably lower than in the other two scenarios. Most concentration values cluster around 0.00073 kg/kg on the scale. This configuration offers an optimal balance of aerodynamics and mixture formation: placing OFA at this height ensures efficient air distribution, better burnout of volatile components, and lower overall CO concentrations.

The second option, with the OFA injectors placed at a height of h = 9.4 m, offers the best mixture formation quality and the most complete CO oxidation. In contrast, the first and third options show drawbacks when the OFA is introduced too early or too late, respectively: they cause local zones with higher carbon monoxide concentrations, reduce the uniformity of the gas flow, and increase the amount of incomplete combustion. Figure 6 illustrates the nitrogen oxide (NO) concentration distributions at the furnace outlet of the BKZ-75 boiler for different heights (h) of the OFA injector installation.

https://doi.org/10.3390/en19020347

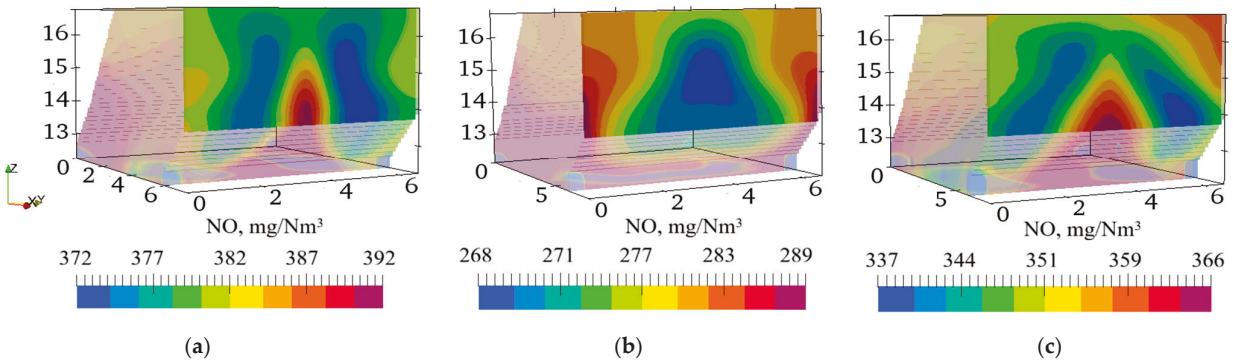


Figure 6. Distribution of nitrogen oxide NO concentration at the combustion chamber outlet at different heights of the OFA injectors: (**a**) h = 2.25 m; (**b**) h = 9.4 m; (**c**) h = 12 m.

The distributions of nitrogen oxide (NO) concentration shown in Figure 6 demonstrate a significant influence of the additional air supply (OFA) mode on the intensity of NO_x formation. Thus, in the first case (Figure 6a), corresponding to a low height of the OFA system placement (h = 2.25 m), a pronounced zone of increased NO concentrations is formed, with maximum values of approximately 378.89 mg/Nm^3. This distribution is characterized by considerable heterogeneity and the presence of local maxima. It indicates a persistent area of elevated temperatures and insufficient efficiency of staged combustion, resulting in increased thermal NO formation.

In the second variant, corresponding to the middle position of the OFA (h = 9.4 m), areas of minimal NO levels emerge—277.12 mg/Nm^3. Nitrogen oxide concentrations are more uniformly spread, lacking distinct peaks. This pattern results from the ideal mixing of combustion gases with overfire air, a decrease in temperature within the reaction zone, and the progression of reduction processes, all of which contribute to the most efficient suppression of nitrogen oxide formation.

In the third variant, where OFA injectors are placed at a high position (h = 12 m), NO concentrations reach intermediate levels, ranging from 337 to 366 mg/Nm^3, with an average of 348.85 mg/Nm^3. The distribution remains moderately heterogeneous, and areas of higher nitrogen oxide levels tend to shift towards the outer edges of the cross-section. Adding extra air at this height does not significantly improve the stable suppression of NO formation, as the reduction processes are confined within a limited zone volume.

The comparison of three options for supplying additional air reveals that the lowest NO concentrations occur at an average height of h = 9.4 m when placing OFA injectors. Both low and high placements of secondary air lead to increased NO formation, resulting from the premature or delayed development of low-temperature zones and inadequate reduction processes. Table 5 presents quantitative data on temperature, carbon oxide, and nitrogen oxide concentrations across different modes, with heights h ranging from 0.165 m to 12 m.

Table 5. Average values of the main heat and mass transfer characteristics (T, CO, NO) at the furnace outlet for different heights h of the injectors for introducing additional air.

h, m	0.165 m	0.75 m	1.3375 m	2.25 m	2.5 m	8 m	9.4 m	10 m	11 m	12 m
CO, kg/kg	0.00083	0.00084	0.00099	0.00079	0.00073	0.00083	0.00073	0.00077	0.00071	0.00095
T, °C	876.06	880.83	886.20	870.14	879.21	847.23	856.27	870.84	854.60	859.72
NO, mg/Nm^3	357.59	358.66	359.19	378.89	379.00	372.66	277.12	331.86	360.93	348.85

https://doi.org/10.3390/en19020347

3.2. The Dependence of the Temperature T of Combustion Products, as Well as the Concentrations of Carbon Oxides CO and Nitrogen NO on the Volume of Air Supplied Through OFA Injectors

Figure 7 shows the dependence of the temperature T of the combustion products (Figure 7, curve 1), as well as the concentrations of carbon monoxide CO (Figure 7, curve 2) and nitrogen oxide NO (Figure 7, curve 3) at the outlet of the combustion chamber on the volume of air supplied through the OFA injectors. The volume of additional air OFA is indicated as a percentage of the total amount of air supplied to the combustion chamber. Therefore, the following values were selected: OFA = 5%; 10%; 15%; 18%; 20%; 25% and 30%. Analysis of this figure shows that increasing the proportion of additional air has a complex effect on combustion processes and the formation of harmful dust and gas emissions into the atmosphere.

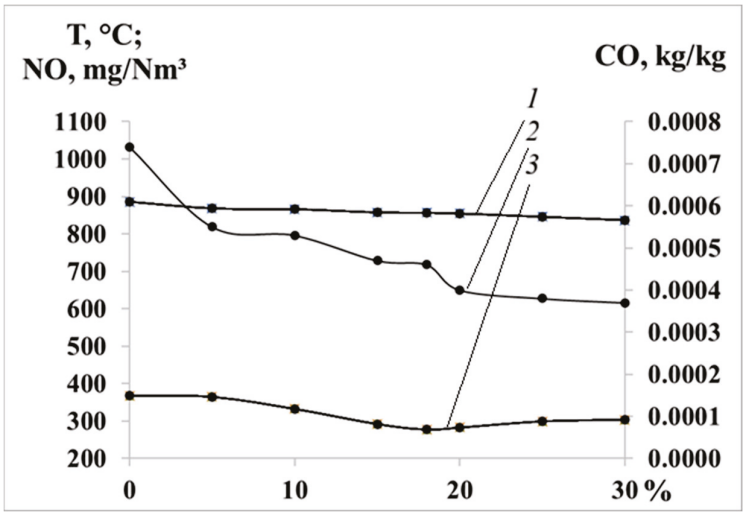


Figure 7. Dependence of temperature T and concentrations of carbon oxides CO and nitrogen NO at the outlet of the combustion chamber on OFA: curve 1—T; curve 2—CO; curve 3—NO.

As the OFA supply increases, the furnace outlet temperature drops sharply within the 0–5% range due to the cooling effect of incoming air, then stabilizes around 820–860 °C, confirming stable thermal conditions at moderate OFA levels. The CO concentration gradually declines: at low OFA levels, incomplete combustion results in higher CO levels. As more air is added above the flame, the flame improves after burning, and turbulent mixing reduces the CO concentration by nearly half. The NO concentration also decreases to its lowest point at OFA levels between 10 and 18%, due to a more developed reduction zone and less thermal NO formation. Beyond this, an increased air supply slightly raises NO levels due to higher oxygen and temperature in the afterburning zone. Figure 8 displays the 3D distribution of CO at the BKZ-75 boiler's outlet for various over-flame air volumes, providing insights into combustion completeness and how staggered air supply influences reducing zones in the upper combustion chamber.

When examining the baseline mode (OFA = 0%, conventional combustion), distinct areas of elevated carbon oxide CO concentrations are observed, primarily localized in the central and upper parts of the outlet cross-section (Figure 8a). This distribution is due to insufficient oxidizer supply to the afterburning zones of volatile fuel components. The formation of a reducing environment leads to CO accumulation, indicating an insufficient efficiency of oxidation processes.

At OFA = 18% and 30%, the carbon monoxide concentration CO decreases significantly, and the distribution becomes more uniform (Figure 8b,c). Additional air introduced above the main combustion zone intensifies turbulent mixing and promotes more complete oxidation of CO to CO_2. A decrease in the intensity of local CO concentration maxima indicates

https://doi.org/10.3390/en19020347

an increase in the degree of combustion completion in the region under consideration. In addition, the absence of pronounced zones of elevated CO concentrations indicates that the fuel has undergone the most complete afterburning and that the aerodynamic regime in the combustion chamber has been optimized. Uniform distribution of the oxidizer ensures effective suppression of reducing zones, significantly reducing the likelihood of CO formation.

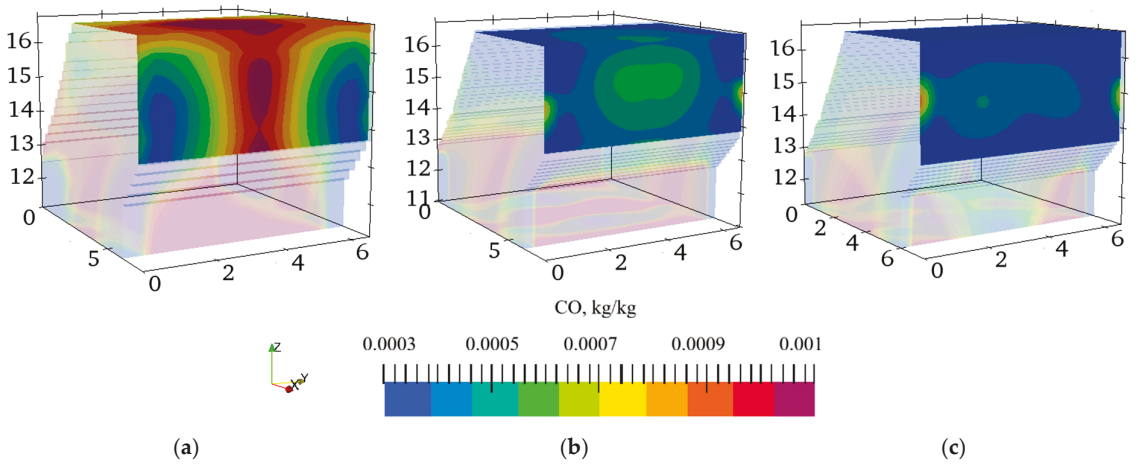


Figure 8. Distribution of carbon monoxide CO concentration at the combustion chamber outlet for different volumes of air supplied through the injectors: OFA = 0% (**a**); OFA = 18% (**b**); OFA = 30% (**c**).

Below, Figure 9 shows the calculated concentration fields of nitrogen oxide (NO) at the BKZ-75 boiler combustion chamber outlet for three air supply options through OFA injectors. The resulting spatial distributions allow us to evaluate the impact of staggered air supply on the formation and reduction of nitrogen oxides (NO_x) in the upper zones of the combustion chamber.

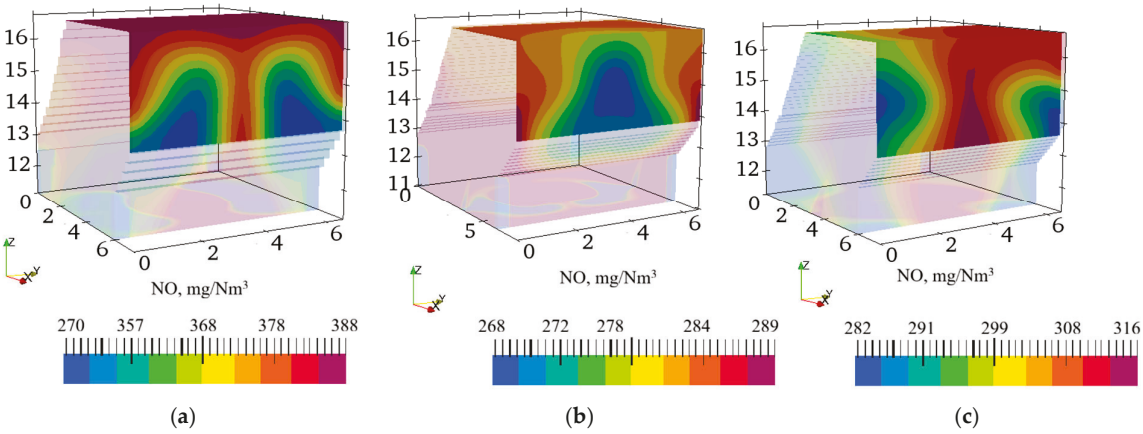


Figure 9. Distribution of nitrogen oxide (NO) concentration at the combustion chamber outlet for different volumes of air supplied through the injectors: OFA = 0% (**a**); OFA = 18% (**b**); OFA = 30% (**c**).

The analysis of the figure indicates that without additional air (Figure 9a), NO oxide concentrations reach their peak, approximately 380–388 mg/Nm^3, with an average of 368.08 mg/Nm^3. The distribution pattern features prominent zones of high NO levels in the upper part of the cross-section, a symmetrical structure with two local maxima, and stable hot spots where the thermal mechanism of NO formation is most active.

The absence of a cold air supply causes the temperature in the afterburning zone to stay high, with almost no reduction processes taking place. This leads to a typical scenario of "hard" single-stage combustion—characterized by maximum thermal NO formation.

https://doi.org/10.3390/en19020347

In Figure 9b, supplying 18% of the above-flare air results in a 22–25% reduction in NO concentration relative to the baseline, yielding a range of 272–282 mg/Nm^3 and an average of 277.12 mg/Nm^3. The figure shows that the highest NO values move toward the edges, while the intensity of the central "hot spots" decreases, resulting in a more symmetrical concentration distribution across the outlet cross-section.

The introduction of OFA causes partial cooling of the upper combustion chamber zone and enhances reduction reactions (NO $\rightarrow$ N_2) due to a localized oxygen deficiency in the main combustion zone. Simultaneously, the contribution of the Zeldovich thermal mechanism decreases. As the supplied air volume increases to OFA = 30% (Figure 9c), a secondary rise in nitrogen oxide (NO) concentration occurs. With this setup, the NO concentration reaches 298–316 mg/Nm^3, with an average of 303.25 mg/Nm^3.

This behavior results from excess oxygen in the OFA zone, a temperature increases due to the active afterburning of CO and volatiles, and an increased formation of thermal NO in the upper part of the furnace. The distribution pattern clearly reveals large areas of higher concentration in the upper cross-section, indicating excessive secondary air supply when the reduction zone collapses, and nitrogen oxidation processes restart, dominating.

Overall, the results indicate that the ideal range for additional air supply via OFA injectors, which reduces CO and NO emissions while maintaining a stable thermal regime, is approximately 18–20%, with 18% being the optimal value. Table 6 shows the numerical data for temperature, carbon oxides, and nitrogen concentrations across different modes when OFA varies from 0 to 30%.

Table 6. Average cross-sectional values of the main heat and mass transfer characteristics at the furnace outlet for different amounts of additional air supplied through the OFA injectors.

OFA, %	Ofa-0	Ofa-5	Ofa-10	Ofa-15	Ofa-18	Ofa-20	Ofa-25	Ofa-30
CO, kg/kg	0.001172	0.000929	0.000929	0.000824	0.000733	0.000655	0.000645	0.000760
T, °C	885.80	868.10	865.91	857.40	856.27	854.37	845.72	836.66
NO, mg/Nm^3	368.08	364.30	332.27	291.78	277.12	282.39	299.05	303.25

3.3. Distribution of Aerodynamic and Heat-Mass Transfer Characteristics Under the Optimal OFA Mode

Figure 10 illustrates the total velocity vector field in two key sections of the combustion chamber: the longitudinal section at x = 3 m and the central section at y = 3.3 m, with air supplied through nozzles at OFA of 0% and 18%. In both scenarios (see Figure 10), the flame core is situated in the center of the chamber, marked by a zone where counter-current jets from opposite burners collide intensely. As the distance from the burners increases, the velocity field becomes more uniform, and the gas flow velocity noticeably decreases toward the furnace outlet window.

When extra air is supplied through the OFA nozzles (18%), the highest overall velocity stays concentrated in the flame core. Still, in the zone around the OFA injectors (h = 9.4 m), there is a localized drop in flow velocity. Once the main burner jets merge with the OFA jets, two symmetrical vertical vortex structures form above the burner, moving toward the center of the furnace. These vortices enhance turbulent mixing, improve oxidizer delivery to the coal dust particles, and facilitate a more complete and uniform fuel combustion burnout.

Figure 11 presents two-dimensional graphs illustrating the temperature T (a) and nitrogen oxide (NO) concentration (b) along the height of the combustion chamber, h, for the different operating modes. In Figure 11a, it is shown that with an OFA level of 18%, the peak temperature within the flame core increases relative to the baseline, and the high-temperature zone expands considerably, resulting in a longer high-temperature core.

https://doi.org/10.3390/en19020347

Near the OFA injectors, curve 2 indicates a localized temperature drop due to the cold jet introduced by the additional air injection.

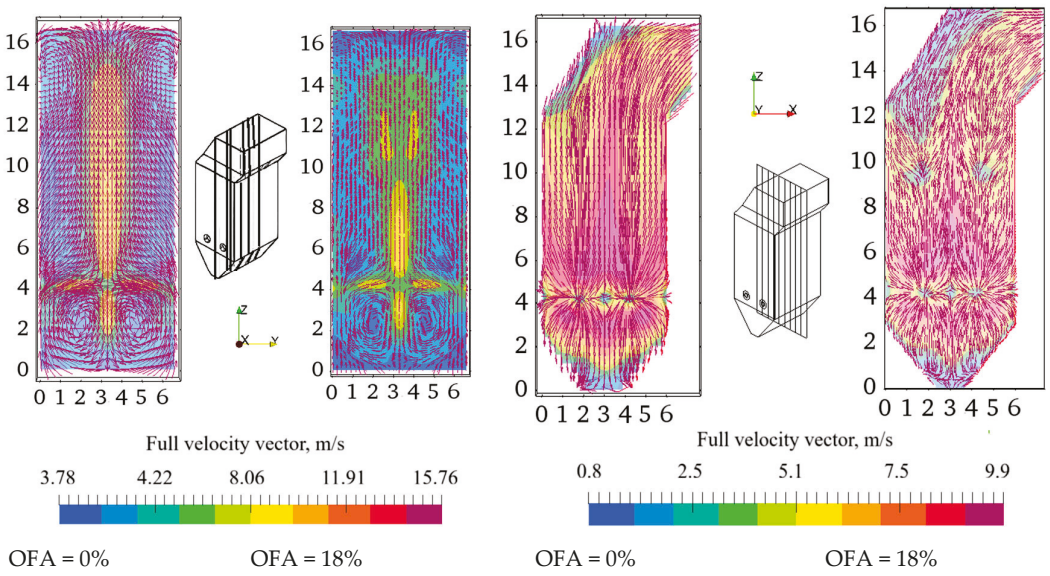


Figure 10. The 3D distribution of the total velocity vector is displayed in the longitudinal (x = 3 m) and central (y = 3.3 m) cross-sections of the combustion chamber for different supplied air volumes injectors: OFA = 0% and OFA = 18%.

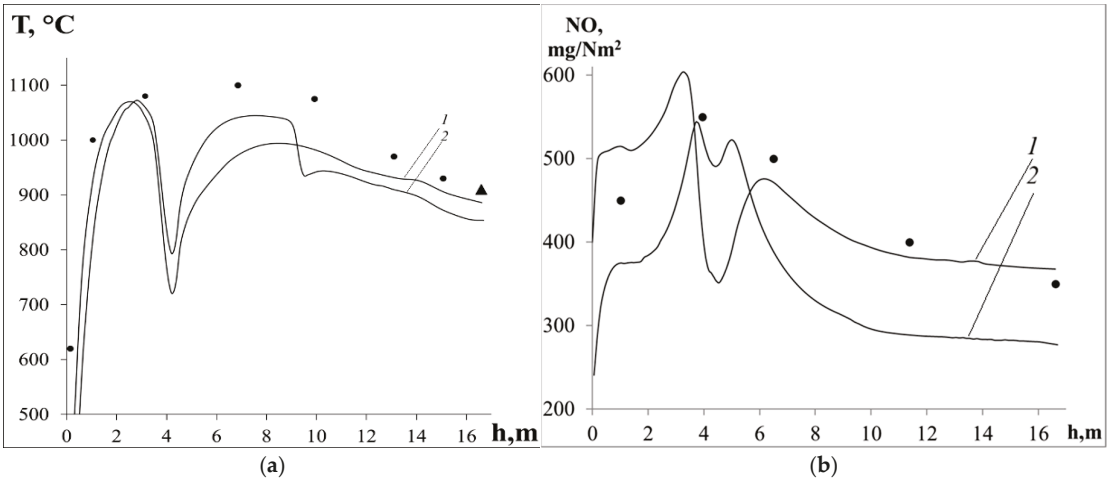


Figure 11. Two-dimensional distribution of temperature (**a**) and nitrogen oxide (NO) concentration (**b**) along the height h of the combustion chamber for different air volumes supplied through the injectors: curve 1—OFA = 0%; curve 2—OFA = 18%; ●—experiment at a thermal power plant [31]; ▲—theoretical value obtained by the CBTI method [32].

Above the OFA injectors, the temperature on curve 2 stays higher than on curve 1 almost until the outlet. However, at the combustion chamber outlet, the average temperature when OFA = 18% is lower, at 856.26 °C, compared to 885.79 °C when OFA = 0%. The graph also shows experimental data from full-scale tests at the Shakhtinsk TPP [31] for the base mode (OFA = 0%) and the calculated outlet temperature from thermal calculations by the Central Boiler and Turbine Institute (CBTI) [32], which matches well with the numerical results data.

Using direct blast technology with an OFA setting of 18% causes the flame to lengthen noticeably, improves heat distribution along the furnace's height, and lowers exhaust gas temperature by about 30 °C. This indicates more effective heat transfer to the upper zone

https://doi.org/10.3390/en19020347

and better combustion efficiency within the chamber. Raising the temperature at the flame core while reducing it at the outlet speeds up oxidation reactions, improves mixing, and decreases losses from incomplete combustion. Nonetheless, these adjustments alone do not reduce CO and NO_x emissions because higher temperatures can enhance thermal NO_x formation, and CO levels may increase in reduction zones due to insufficient combustion after burning.

Reducing NO_x and CO levels at OFA = 18% involves a two-stage combustion process: initially, a reducing zone is formed in the lower furnace, followed by intense oxidative afterburning in the OFA feed area. Analysis of nitrogen oxide distribution (Figure 11b) reveals that increasing the air supplied through the OFA injectors (OFA = 18%) results in a slight increase in NO_x concentration in the burner zone compared to baseline conditions (OFA = 0%). This rise is due to higher temperatures and more vigorous oxidation of nitrogen-containing fuel components.

At the peak of the OFA injectors, there is a noticeable and steady decrease in NO_x levels, caused by cold air supplied through the injectors and the dilution of combustion gases with excess air. Along the entire furnace height, the highest NO_x concentrations are found in the lower region, known as the active combustion zone, which is typical for all direct-flow furnaces. Additionally, in the base mode, elevated NO_x levels continue until the combustion chamber's exit. However, two-stage combustion significantly reduces nitrogen oxides near the exit [33,34].

The emission reduction mechanism is as follows:

- A reducing (oxygen-depleted) environment forms in the lower zone, inhibiting the formation of fuel NO_x;
- In the OFA injector zone, a moderate-temperature oxidizing region develops, which decreases the thermal production of NO_x based on the Zeldovich mechanism.

The two-stage combustion method, with 18% air supplied via OFA injectors, effectively reduces the formation of fuel and thermal nitrogen oxides. This results in notably lower levels of these emissions in the combustion chamber outlet environment.

Figure 12 illustrates the three-dimensional distribution of nitrogen oxide (NO) concentrations at the combustion chamber outlet of the BKZ-75 boiler, with different injected air volumes: OFA = 0% (baseline, standard combustion) and OFA = 18%. Analyzing the NO_2 concentrations in the outlet section (refer to Figure 12) indicates that Overfire Air technology (acute blast) markedly affects this component's distribution. At OFA = 18%, there is a significant decrease in both the average and maximum NO concentrations compared to the baseline (OFA = 0%).

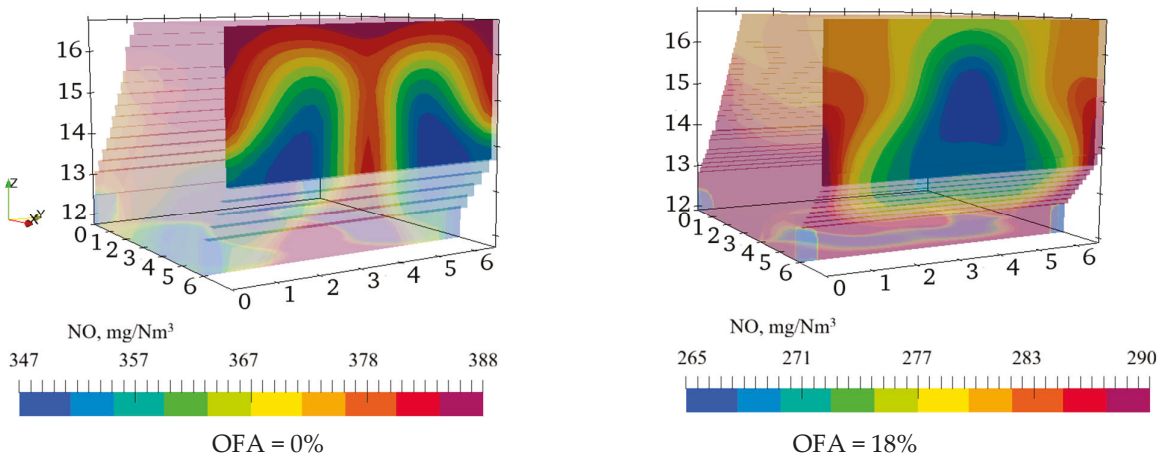


Figure 12. Three-dimensional distribution of nitrogen oxide (NO) at the combustion chamber outlet for various air volumes supplied through the injectors: OFA = 0% and OFA = 18%.

https://doi.org/10.3390/en19020347

Despite the significant results obtained, this study has a limitation that should be taken into account when interpreting the findings and their practical application: the optimal parameters for the placement of OFA injectors and the amount of secondary air obtained are specific to the BKZ-75 boiler and the high-ash coal of the Karaganda Basin and cannot be directly extrapolated to other boiler types or fuels without further analysis.

Overall, the identified optimal parameters for implementing OFA technology in the BKZ-75 boiler at the Shakhtinsk TPP can be used in the modernization of existing coal-fired power plants, contributing to improvements in their environmental and energy efficiency. Thus, this work makes a significant contribution to the development of "clean" coal combustion technologies and demonstrates the potential of digital approaches for transitioning the energy sector toward more sustainable and environmentally safe solutions.

4. Conclusions

The following findings were established based on the completed research:

- Digital and mathematical models of the combustion chamber and combustion processes were developed that adequately describe heat and mass transfer during the combustion of low-grade coal and can be used when implementing two-stage combustion technology (Overfire Air).
- Computational experiments yielded aerodynamic characteristics, temperature fields, and carbon oxide (CO) and nitrogen oxide (NO) concentrations throughout the entire combustion chamber volume and at the BKZ-75 combustion chamber outlet.
- Various OFA injector placement options were studied. The optimal height (h) was found to be 9.4 m. This height ensures the maximum reduction in carbon oxide (CO) and nitrogen oxide (NO) concentrations at the combustion chamber outlet.
- Fuel combustion modes were simulated with OFA values varying from 0% (baseline, conventional combustion) to 30%. It was demonstrated that increasing the additional air volume through the OFA nozzles results in an increase in temperature in the central zone of the furnace, accompanied by a local decrease in the injector area, followed by equalization of the temperature field toward the outlet. The optimal supply of additional air is achieved at an OFA of 18%.
- Temperature distribution across the furnace height was confirmed by field experiments at the Shakhtinsk TPP, and the exhaust gas temperature in the baseline mode was confirmed by thermal calculations using the CBTI methodology.
- The use of two-stage combustion with an OFA of 18% and the placement of OFA injectors at a height of 9.4 m reduces the concentration of CO at the furnace outlet by approximately 36% and NO by 25% compared to traditional combustion (OFA = 0%).
- The obtained results provide a basis for optimizing the combustion process for low-grade coal, increasing burnout efficiency, and significantly reducing harmful emissions. This enables us to recommend the implementation of OFA technology in similar coal-fired boilers at other TPP plants and, more broadly, at any energy facility in the fuel industry—both in Kazakhstan and in countries where traditional coal-fired power generation is still prevalent.

Author Contributions: Conceptualization, A.A., S.B. (Saltanat Bolegenova), and A.N.; methodology, A.A., V.M., A.N., and S.B. (Saltanat Bolegenova); validation, A.A., N.A., A.N., and S.B. (Symbat Bolegenova); formal analysis, A.A., S.B. (Saltanat Bolegenova), A.N., S.O.; investigation, A.A., A.N., and S.B. (Saltanat Bolegenova); writing—original draft preparation, A.A., S.B. (Saltanat Bolegenova), V.M., A.N., S.B. (Symbat Bolegenova), N.A.; writing—review and editing, A.A., S.B. (Saltanat Bolegenova), V.M., A.N., S.B. (Symbat Bolegenova), A.N., N.A., Z.S.; supervision, A.A. All authors have read and agreed to the published version of the manuscript.

Funding: This work was supported by the Ministry of Education and Science of the Republic of Kazakhstan (No. AP23490571).

Data Availability Statement: The original contributions presented in this study are included in the article. Further inquiries can be directed to the corresponding author.

Conflicts of Interest: The authors declare no conflicts of interest.

Abbreviations

TPP	Thermal power plant
COP	Conference of the Parties
OFA	Overfire Air
CBTI	Central Boiler and Turbine Institute

References

1. International Energy Agency (IEA). Coal Market Report. 2022. Available online: https://www.iea.org/reports/coal-2022?referrer= (accessed on 15 December 2025).
2. International Energy Agency (IEA). Global Energy Review. 2025. Available online: https://www.iea.org/reports/global-energy-review-2025?referrer= (accessed on 15 December 2025).
3. World Coal Association. Coal Industry Overview. 2025. Available online: https://www.iea.org/reports/coal-2025/executive-summary (accessed on 15 December 2025).
4. U.S. Energy Information Administration (EIA). International Energy Statistics. Available online: https://www.eia.gov/international/data/world (accessed on 15 December 2025).
5. Saletnik, A.; Saletnik, B.; Puchalski, C. Coal as the world's dominant energy source and its role in the energy transformation and regulations of European Green Deal. *J. Environ. Manag.* **2025**, *392*, 126815. [CrossRef] [PubMed]
6. Srivastava, R.K.; Hall, R.E.; Khan, S.; Culligan, K.; Lani, B.W. Nitrogen oxides emission control options for coal-fired electric utility boilers. *J. Air Waste Manag. Assoc.* **2005**, *55*, 1243–1267. [CrossRef] [PubMed]
7. Milićević, A.; Marković, Z.; Belošević, S.V.; Erić, M.; Žarković, M.; Marinković, A. Influence of fuel and operation mode on air pollutants emission from pulverized coal-fired power plant: Field experiments and ML predictions. *Therm. Sci. Eng. Prog.* **2025**, *57*, 103151. [CrossRef]
8. Coal sector of Kazakhstan: Challenges and opportunities for Decarbonizing the Economy. Available online: https://unctad.org/system/files/information-document/unda2030d26-kazakhstan-coal_en.pdf (accessed on 3 December 2025).
9. Bizhanova, G. The Coal Sector—A Strategic Basis for Kazakhstan's Energy Security. Available online: https://factories.kz/news/ugolnaya-promyshlennost-kazakhstana (accessed on 15 December 2025).
10. Wang, H.; Ti, S.; Jin, H.; Wang, H.; Gao, K.; Liu, Y.; Li, J. Influence of the overfire air rate of the two-channel overfire air on flow and combustion characteristics in a 600-MWe boiler. *Asia-Pac. J. Chem. Eng.* **2022**, *17*, e2726. [CrossRef]
11. Ma, L.; Fang, Q.; Tan, P.; Zhang, C.; Chen, G.; Lv, D.; Duan, X.; Chen, Y. Effect of the separated overfire air location on the combustion optimization and NO_x reduction of a 600 MWe FW down-fired utility boiler with a novel combustion system. *Appl. Energy* **2016**, *180*, 104–115. [CrossRef]
12. Jiang, Y.; Ahn, S.; Oh, D.H.; Lee, B.H.; Jeon, C.H. Optimization of separated overfire air to reduce NO_x emissions under combustion stability for the retrofit of a 500 MW tangentially pulverized coal boiler. *Fuel* **2021**, *289*, 119764. [CrossRef]
13. U.S. Department of Energy. *The Advanced Tangentially Fired Combustion Techniques for the Reduction of Nitrogen Oxides (NO_x) Emissions from Coal-Fired Boilers Demonstration Project*; OSTI.GOV Report: Washington, DC, USA, 2000.
14. Askarova, A.; Bolegenova, S.; Mazhrenova, N.; Manatbayev, R.; Ospanova, S.; Berezovskaya, I.; Maximov, V.; Nugymanova, A.; Shortanbayeva, Z. 3D modelling of heat and mass transfer processes during the combustion of liquid fuel. *Bulg. Chem. Commun.* **2016**, *48*, 229–235. Available online: http://www.bcc.bas.bg (accessed on 15 December 2025).
15. Messerle, V.; Ustimenko, A.; Karpenko, E.I.; Loktionova, I.V. Optimization of the combustion of power station coals using plasma technologies. *Therm. Eng.* **2004**, *51*, 488–493.
16. Georgiev, A.; Askarova, A.S.; Bolegenova, S.; Maximov, V.; Toktarov, D.; Nugymanova, A. Highly efficient plasma technology for ignition and thermochemical preparation of high-ash fuel in various power boilers in Kazakhstan. *Energy* **2025**, *322*, 135677. [CrossRef]
17. Askarova, A.S.; Bolegenova, S.A.; Maximov, V.Y.; Beketayeva, M.T. Modeling of heat mass transfer in high-temperature reacting flows with combustion. *High Temp.* **2018**, *56*, 738–743. [CrossRef]

18. Askarova, A.S.; Bolegenova, S.A.; Georgiev, A.; Maximov, V.Y.; Manatbayev, R.K.; Yergaliyeva, A.B.; Nugymanova, A.O.; Baizhuma, Z.T. The use of a new "clean" technology for burning low-grade coal in boilers of Kazakhstan TPPs. *Bulg. Chem. Commun.* **2018**, *50*, 53–60.
19. Messerle, V.E.; Bolegenova, S.A.; Maximov, V.Y.; Nugymanova, A.O. 3D-modelling of Kazakhstan low-grade coal burning in power boilers with application of plasma gasification and stabilization technologies. *J. Phys. Conf. Ser.* **2019**, *1261*, 012022. [CrossRef]
20. Muller, H. *Numerische Berechnung Dreidimensionaler Turbulenter Strömungen in Dampferzeugern Mit Wärmeübergang und Chemischen Reaktionen am Beispiel des SNCR-Verfahrens und der Kohleverbrennung*; VDI-Verlag: Düsseldorf, Germany, 1992; Volume 6, p. 268.
21. Leithner, R. *Simulation von Kraftwerken und Wärmetechnischen Anlagen*; Springer: Vienna, Austria, 2009.
22. Safarik, P. 3-D modeling of heat and mass transfer process during the combustion of solid fuel in a swirl furnace. *Acta Polytech.* **2019**, *59*, 543–553. [CrossRef]
23. Safarik, P.; Nugymanova, A.; Maximov, V. Simulation of low-grade coal combustion in real chambers of energy objects. *Acta Polytech.* **2019**, *59*, 98–108. [CrossRef]
24. Georgiev, A.; Bolegenova, S.; Askarova, A.; Beketayeva, M.; Maximov, V. Computational modeling of pollutants in furnaces of pulverized coal boilers of the Republic of Kazakhstan. *Energy* **2022**, *258*, 124826. [CrossRef]
25. Harmor, R.J. Kinetics of combustion of pulverized brown coal char. *Combust. Flame* **1973**, *21*, 153. [CrossRef]
26. Magnussen, B.F. On the mathematical modeling of turbulent combustion with special emphasis on soot formation and combustion. In *Proceedings of the Symposium (International) on Combustion*; Elsevier: Amsterdam, The Netherlands, 1977.
27. Belošević, S.V.; Tomanović, I.D.; Crnomarković, N.Đ.; Milićević, A.R.; Tucaković, D.R. Modeling and optimization of processes for clean and efficient pulverized coal combustion in utility boilers. *Therm. Sci.* **2016**, *20*, 183–196. [CrossRef]
28. Leithner, R.; Müller, H. CFD studies for boilers. In *Computational Fluid and Solid Mechanics*; Elsevier: Amsterdam, The Netherlands, 2003; pp. 988–991. [CrossRef]
29. Leithner, R.; Müller, H.; Fischer, K.; Schiller, A. Optimierung der Simulation von Feuerungen. *VDI Berichte* **1999**, *1492*, 63–68. Available online: https://www.scopus.com/pages/publications/31244432870?origin=resultslist (accessed on 1 December 1999).
30. Leithner, R.; Loehr, T.; Dobrowolski, R. Simulation und Optimierung von Kraftwerksprozessen. *VDI Berichte* **1998**, *1390*, 109–126. Available online: https://www.scopus.com/pages/publications/2542568225?origin=resultslist (accessed on 1 December 1998).
31. Aliyarov, B.; Aliyarova, M. *Combustion of Kazakhstan Coals at TPPs and Large Boiler Houses: Experience and Problems*; Gylym Ordasy: Almaty, Kazakhstan, 2012.
32. NPO CBTI. *Thermal Calculation of Boilers (Normative Method)*; NPO CBTI: St. Petersburg, Russia, 1998.
33. Ti, S.; Chen, Z.; Kuang, M.; Li, Z.; Zhu, Q.; Zhang, H.; Wang, Z.; Xu, G. Numerical simulation of the combustion characteristics and NO_x emission of a swirl burner: Influence of the structure of the burner outlet. *Appl. Therm. Eng.* **2016**, *104*, 565–576. [CrossRef]
34. Glarborg, P.; Miller, J.A.; Ruscic, B.; Klippenstein, S.J. Modeling Nitrogen Chemistry in Combustion. *Prog. Energy Combust. Sci.* **2018**, *67*, 31–68. [CrossRef]

Disclaimer/Publisher's Note: The statements, opinions and data contained in all publications are solely those of the individual author(s) and contributor(s) and not of MDPI and/or the editor(s). MDPI and/or the editor(s) disclaim responsibility for any injury to people or property resulting from any ideas, methods, instructions or products referred to in the content.

energies

MDPI

Article

Design Requirements for a Common-Shaft Switch-Mode Power Transformer for Ocean Wave-Powered Reverse Osmosis

Sayak Pradhan [1], Jeremy W. Simmons [1,2] and James D. Van de Ven [1,*]

[1] Department of Mechanical Engineering, University of Minnesota, Minneapolis, MN 55455, USA; pradh101@umn.edu (S.P.); jeremy@integralpower.systems (J.W.S.)
[2] Integral Power Systems, Minneapolis, MN 55413, USA
* Correspondence: vandeven@umn.edu

Abstract

Wave-powered reverse osmosis (RO) desalination with cogeneration of electricity is promising for freshwater production. The design performance of the default architecture seen in literature and commercialization suffers on metrics of power density, cost, and productivity. The design choices constraining this performance is the choice to drive a seawater pump with the WEC that operates at the same pressure as the reverse osmosis process. There have been studies comparing this default, baseline architecture with architectures operating at higher pressure, either by introducing a series of processes or by including a power transformer. This work contributes three studies that expand on the work on one such architectural choice, the inclusion of a switch-mode power transformer (SMPT). This study expands on the SMPT architecture and introduces a common-shaft power distribution approach, in which the rotary machines are mechanically coupled on a shared shaft. Three studies are performed: a static power-flow study comparing the baseline architecture with two SMPT-based architectures, a shaft-dynamics study quantifying the trade-off between switching frequency, flywheel inertia, and shaft-speed variation, and a pressure-dynamics study evaluating the effects of switch valve area, transition ratio, switching volume, and switching frequency on throttling losses. The baseline architecture delivers 34.97% of the input power to permeate production, whereas the SMPT and SMPT with common-shaft architectures deliver 32.47% and 34.02%, respectively. The shaft dynamics study found that switching frequencies above 15 Hz kept the shaft speed variations below 5%, while lower frequencies require added shaft inertia. A pressure dynamics study shows that switching losses are dominated by valve-opening transients, favoring a large effective flow area and short transition time. The overall findings are that (i) the SMPT enables significant pump downsizing at a small cost in efficiency, (ii) most of the efficiency loss is recovered with the common shaft approach, and (iii) the shaft inertia and valve requirements for the SMPT are reasonable.

Keywords: wave-powered desalination; reverse osmosis; wave energy converter; hydraulic power take-off system; switch-mode power transformer; switching valve; common-shaft architecture

1. Introduction

Oceans and seas cover over 70% of the Earth's surface, making it one of the most abundant sources of renewable energy in the form of wave and tidal energy. Waves are a promising source of energy because of the low environmental impact, high power

density, and better predictability [1] compared to other renewable energy resources [2]. However, a large portion of the wave energy remains untapped due to the lack of mature and cost-effective technologies [3,4].

Over the years, different combinations of wave energy converters (WECs) and power take-off (PTO) systems have been used to convert wave energy into electrical energy [5–7]. Various types of PTOs that have been explored including (i) turbines driven by compressed air or water [8], (ii) direct-mechanical drive PTO that uses mechanical interfaces like cables, sprockets or gearboxes [9], (iii) direct-electrical drive PTO [10] that converts the wave energy absorbed by the WEC into electrical energy using rotary or linear generators and (iv) hydraulic PTOs [11]. Among all these, hydraulic PTOs offer high power density and are well-suited for wave energy applications characterized by the low-frequency and high forces exerted by WECs.

While the majority of prior studies focused on the conversion of the wave energy to electrical energy [12], direct wave-powered desalination is a promising alternative application [13]. Using wave energy to power desalination plants has emerged as an alternative, as both the energy source and seawater are located in the same place. Among the available desalination technologies, reverse osmosis (RO) is promising as it requires less energy compared to other desalination methods [14].

There are three primary approaches for wave-powered desalination. The first approach converts wave energy into electrical energy and uses it to power a desalination plant, but suffers from low overall efficiency due to multiple energy conversion losses [15]. The second approach uses the wave energy to directly pressurize feed water, thereby avoiding some of the energy conversion losses. Numerous numerical investigations [16–18], techno-economic [19], and experimental studies [20] conducted for different combinations of WECs and PTOs have demonstrated the feasibility of direct wave-powered desalination systems. However, further experimental studies are required to assess their long-term operational performance under real-sea conditions [21]. A challenge experienced by these systems is the large pressure fluctuations at the RO membrane as it is directly coupled with the WEC, which reduces the lifetime of the system [21]. Large hydraulic accumulators are used to mitigate the pressure fluctuations [17,18]. The third approach uses wave energy for desalination along with cogeneration of electricity. This helps to meet the electrical requirements of the water treatment system, allowing it to operate independently of the local grid. Additionally, in this approach, the system pressure can be regulated through control of the generator.

A baseline hydraulic PTO used for desalination with co-generation of electricity is illustrated in Figure 1. This system consists of a WEC-driven pump, a RO membrane for desalination, an energy recovery unit (ERU) to recover residual energy from the pressurized brine discharge, a charge pump to prevent cavitation at the WEC pump inlet, and an electric generator coupled with a hydraulic motor for generating electrical energy. The WEC-driven pump can have different configurations, such as a hydraulic cylinder coupled with a check valve rectifier [11,22].

There are some drawbacks to the baseline system shown in Figure 1. The RO module and the WEC-driven pump are connected by a common high-pressure rail, resulting in both components operating at the same pressure. The operating pressure of the RO membrane is typically in the range of 7–8.3 MPa [11], which is significantly lower than conventional hydraulic pumps that are designed for 20–35 MPa. The low pressure demands a higher flow rate for a given power, which in turn requires larger components than a higher-pressure system. This is of particular concern for the WEC-driven pump, as it is the most costly component in this system.

https://doi.org/10.3390/en19112692

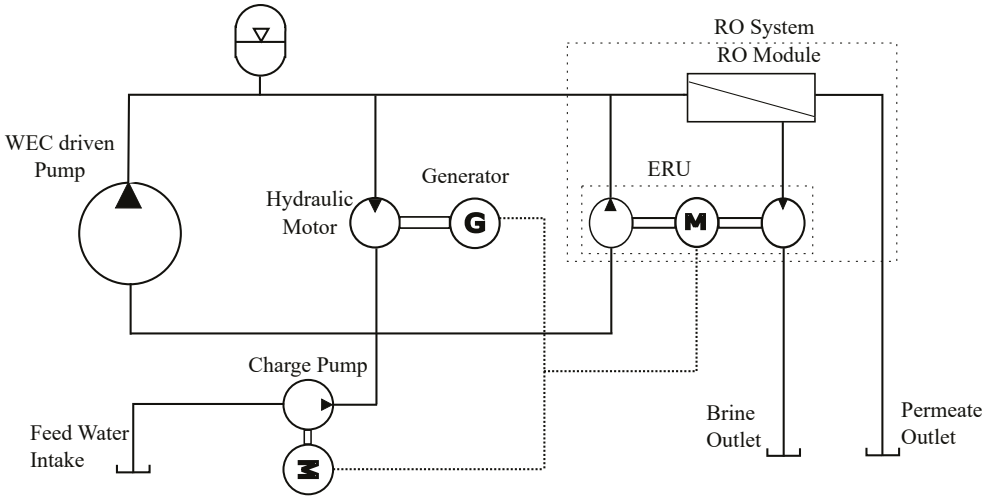


Figure 1. Schematic of the baseline PTO architecture used for desalination with cogeneration of electricity.

This work explores decoupling the pressure at the pump and the RO module in order to operate the pump at a higher pressure and lower flow rate, allowing it to be downsized, saving cost. The pressure can be decoupled by using a hydraulic transformer. The conventional hydraulic transformer, a hydraulic motor and pump shaft coupled together, is bulky, expensive, and inefficient [23]. The approach used in this work is a buck converter [24] switch-mode power transformer (SMPT) [25,26] to reduce the outlet pressure relative to the inlet pressure. The schematic of the PTO architecture using an SMPT is shown in Figure 2 [27]. The SMPT operates in two discrete states, one with the switch valve open and the other with the switch valve closed, where flow is drawn through the check valve. Through controlling the duty cycle of the rapidly switching valve, the pressure transformation ratio is controlled. Fluctuations in the inlet pressure are minimized through an accumulator, and fluctuations in the outlet flow rate are minimized through the inertia of the hydraulic motor and generator.

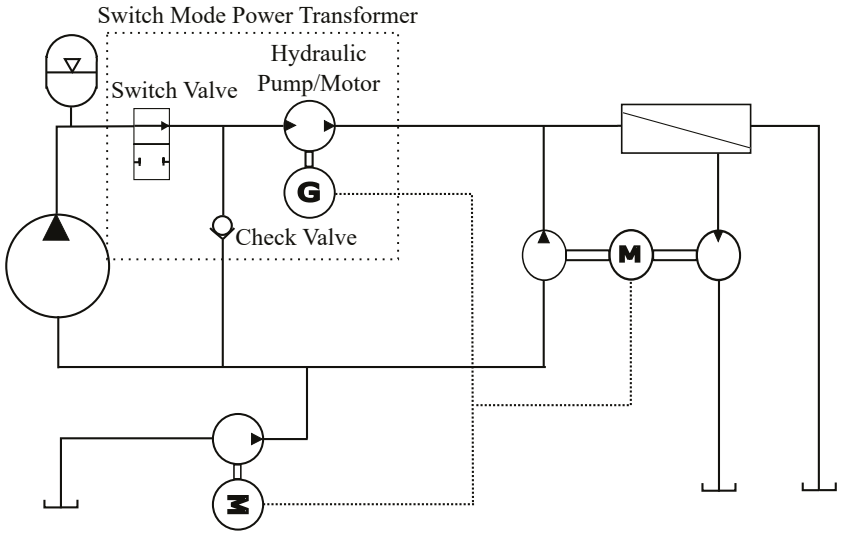


Figure 2. Schematic of a hydraulic PTO architecture using a Switch mode power transformer (SMPT).

Studies suggest that the performance of the switch valve is the most important factor to determine the efficiency of an SMPT [25]. Several valve configurations have been explored, including rotary four-port valves [28], rotary phase-shift valves [29], and linear poppet valves actuated by various mechanisms [30–32]. The rotary valves can achieve high

https://doi.org/10.3390/en19112692

switching frequencies but suffer from friction and throttling losses. In contrast, poppet valves can achieve high switching frequencies with low leakage, but large actuation forces are required to obtain large flow areas. This study will evaluate the influence of valve parameters on the circuit efficiency, allowing the selection of an appropriate valve.

In the SMPT architecture shown in Figure 2, multiple electric motors are used to drive auxiliary components, including a charge pump and ERU, which increases system cost and energy conversion losses. This motivates the exploration of an architecture using a common shaft connecting all the rotary components except the WEC-driven pump, thereby reducing the number of components and the energy loss associated with it. In this circuit shown in Figure 3, two electric motors and one hydraulic pump are eliminated while achieving the same functionality. The high-pressure outlet of the WEC-driven pump is connected to the switch valve through a high-pressure accumulator to attenuate pressure fluctuations. A charge pump maintains pressure in the low-pressure rail to prevent cavitation. The SMPT consists of a switch valve, check valve, and a hydraulic motor/pump, and it regulates system pressure. The common-shaft inertia alternatively stores and releases energy during switching. The pressurised brine discharge from the RO module passes through ERU, which recovers some of the residual energy. The generator supplies electrical power and regulates the RO inlet pressure. This results in an underactuated system that requires careful component sizing.

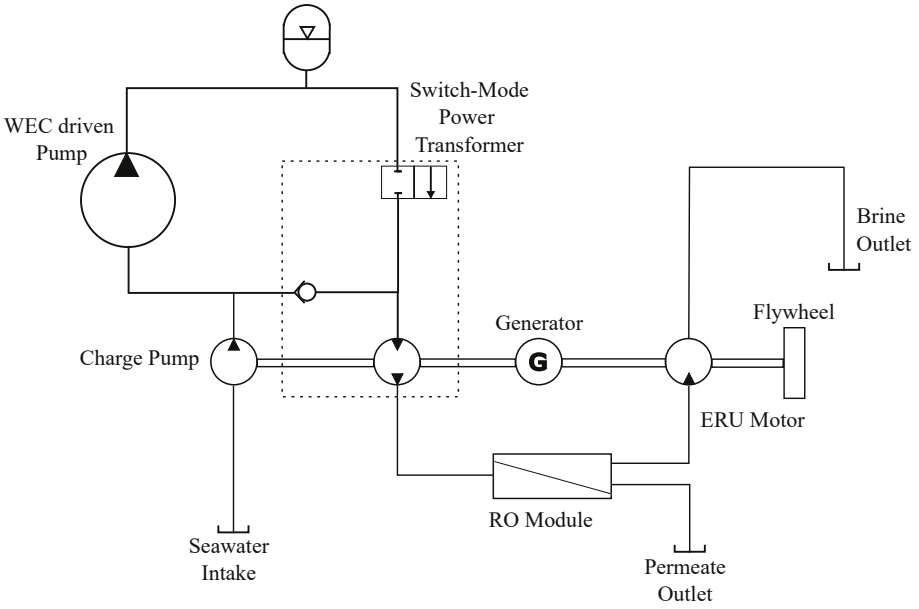


Figure 3. Hydraulic schematic of the PTO architecture with a switch-mode power transformer (SMPT) and common-shaft coupling of the rotary machines.

This paper seeks to quantify the advantages and challenges of the three architectures presented. This study specifically focuses on two questions: (i) what improvement in overall productivity can be expected using the SMPT with a common shaft architecture, and (ii) what performance and design requirements must the switching valve satisfy to enable such operation. The following section presents the methods used to address these questions. A mathematical model of the system components and their coupling is described, followed by a description of the analysis. The results are provided and discussed in Section 3. Conclusions drawn from these analyses are given in Section 4, and they are accompanied by suggestions for future work.

https://doi.org/10.3390/en19112692

2. Materials and Methods

To understand and evaluate the feasibility, performance, and design requirements of the SMPT with common-shaft architecture, three complementary studies were conducted. The analysis begins with a static, time-averaged power flow study to quantify the productivity of each architecture, given several loss mechanisms. This model provides system-level insight into efficiency and permeate productivity without considering dynamic effects. The second study investigates the impact of the inertia of the common-shaft assembly on the rotational speed fluctuations caused by the switching action of the switch valve, exploring the trade-offs between the switching frequency, the added mass for flywheel inertia, and generator speed variation. Finally, a pressure dynamic model of the SMPT is developed to determine the performance requirements and sizing of the switching valve.

2.1. Static Power Flow Modeling

In this section, models are developed of the static power flows for (i) the baseline PTO architecture shown in Figure 1, (ii) the PTO architecture with the SMPT shown in Figure 2, and (iii) the PTO architecture incorporating the SMPT with the common-shaft assembly shown in Figure 3. The three system architectures are modeled on a time-averaged, steady-state basis to quantify the power flow throughout each system and ultimately determine the equivalent power delivered to permeate production. The power input from the wave energy converter (WEC) is set arbitrarily to 100 kW, resulting in constant flow rates and pressures throughout the system. For the switch-mode architectures, the time-varying operation of the switch-mode power transformer (SMPT) is characterized by a duty cycle, and the power flow and losses are averaged over a switching period based on this duty. A surplus electrical power output is assumed (5kW) to cover auxiliary electrical power demands of the system. Compressibility and valve throttling losses are not considered in the static power-flow analysis.

The modeling methodology follows a loop and node analysis approach, similar to electrical circuit analysis. Flow conservation is enforced at nodes, pressure relationships are defined around loops, and power balances are established for key subsystems.

2.1.1. Common Component Models

In this subsection, mathematical models are developed for the common components: (i) WEC driven pump, (ii) RO module, (iii) energy recovery unit, (iv) generator, and (v) charge pump.

The WEC-driven pump receives mechanical power from the wave energy converter and pressurizes flow from a low-pressure charge rail at pressure p_c to a high-pressure outlet. For the parallel architecture, the outlet pressure is the RO feed pressure, p_f. For the SMPT-based architectures, the outlet pressure is elevated to $p_w > p_f$, enabled by the switch-mode power transformation.

The volumetric flow rate delivered by the WEC-driven pump is

$$q_w = \frac{\eta_w P_w}{p_{out} - p_c} \tag{1}$$

where P_w is the mechanical power input from the WEC, η_w is the pump efficiency, and p_{out} is the outlet pressure (p_f or p_w depending on the architecture).

For the RO module, the permeate flow rate is treated as a recovered fraction of the feed flow rate, such that $q_p = Yq_f$, where Y is the recovery ratio. The concentrate discharge from the RO module is therefore $q_b = (1 - Y)q_f$. The power input to the RO module is $P_{ro} = q_f p_f$, with the power delivered to permeate being $P_p = YP_{ro}$ and the power remaining in the brine discharge being $P_b = (1 - Y)P_{ro}$.

https://doi.org/10.3390/en19112692

The energy recovery unit consists of a hydraulic motor (recovery motor) driven by the brine discharge and a hydraulic pump (recovery pump) that pressurizes a portion of the feed flow. The shafts of the recovery motor and pump are mechanically coupled through an electric motor that provides torque balancing and controls the speed.

The volumetric flow rate through the recovery motor is $q_{rm} = q_b = (1 - Y)q_f$. Because the shafts are coupled, the shaft speed and the recovery motor flow rate are related by

$$\omega_{rm} = \frac{\eta_{rm,v} q_{rm}}{D_{rm}} \tag{2}$$

where D_{rm} is the volumetric displacement of the recovery motor and $\eta_{rm,v}$ is its volumetric efficiency.

The volumetric flow rate delivered by the recovery pump is therefore

$$q_{rp} = \eta_{rp,v} D_{rp} \omega_{rm} = \lambda q_{rm} = \lambda(1 - Y)q_f \tag{3}$$

where

$$\lambda = \eta_{rp,v} \eta_{rm,v} \frac{D_{rp}}{D_{rm}} \tag{4}$$

and D_{rp} and $\eta_{rp,v}$ are the volumetric displacement and volumetric efficiency of the recovery pump, respectively.

The shaft power delivered by the recovery motor is

$$P_{rm} = \eta_{rm,m} \eta_{rm,v} q_{rm} p_f \tag{5}$$

where $\eta_{rm,m}$ is the mechanical efficiency of the recovery motor. The total efficiency of the recovery motor is $\eta_{rm} = \eta_{rm,m} \eta_{rm,v}$.

The shaft power consumed by the recovery pump is

$$P_{rp} = \frac{q_{rp}(p_f - p_c)}{\eta_{rp,m} \eta_{rp,v}} \tag{6}$$

where $\eta_{rp,m}$ is the mechanical efficiency of the recovery pump. The total efficiency of the recovery pump is $\eta_{rp} = \eta_{rp,m} \eta_{rp,v}$.

For the parallel and SMPT architectures (without a common shaft), an electric motor balances the power on the energy recovery unit shaft. The electric power required is

$$P_{re} = \frac{P_{rp} - P_{rm}}{\eta_{re}^{\sigma}} \tag{7}$$

where $\sigma = \mathrm{sgn}(P_{rp} - P_{rm})$ determines whether the electric motor consumes or generates electricity. The sign can be determined without knowledge of the feed flow rate:

$$\sigma = \mathrm{sgn}\left(\frac{\lambda(p_f - p_c)}{\eta_{rp}} - \eta_{rm} p_f \right) \tag{8}$$

For SMPT with a common shaft, the recovery motor is directly coupled to the common shaft. The generator provides torque balancing and shaft speed control, and there is no recovery pump.

The generator converts mechanical shaft power to electrical power with efficiency η_{gen}. For the parallel and SMPT architectures, a dedicated hydraulic motor (house power motor) drives the generator. For the SMPT architectures, the generator is integrated with the switch-mode pump/motor or connected to the common shaft.

https://doi.org/10.3390/en19112692

The charge pump pressurizes flow from atmospheric pressure to the low-pressure rail at pressure p_c. The volumetric flow rate through the charge pump is equal to the average RO feed flow rate, $q_c = q_f$. The shaft power consumed by the charge pump is

$$P_c = \frac{1}{\eta_c} q_f p_c \tag{9}$$

where η_c is the charge pump efficiency.

When the charge pump is driven by an electric motor (parallel and SMPT architectures), the electric power demand is

$$P_{ce} = \frac{1}{\eta_c \eta_{ce}} q_f p_c \tag{10}$$

where η_{ce} is the electric motor efficiency. When driven directly from a common shaft (SMPT with common shaft), only the shaft power P_c is required.

2.1.2. Parallel Architecture (Baseline)

In the parallel architecture, the WEC-driven pump delivers pressurized flow at p_f directly to a high-pressure rail. This flow is split between the RO module and a house power hydraulic motor. The house power motor drives a generator to produce electrical power for the charge pump, the energy recovery unit electric motor, and to meet the prescribed surplus electrical power demand, P_e.

The flow split is characterized by the parameter α, defined as the fraction of the WEC-driven pump flow that feeds the RO module:

$$q_f = \frac{\alpha q_w}{1 - \lambda(1 - Y)} \tag{11}$$

where the denominator accounts for the flow from the energy recovery pump.

The flow through the house power motor is therefore

$$q_m = (1 - \alpha) q_w \tag{12}$$

The house power motor draws from the high-pressure rail at p_f and discharges to the low-pressure rail at p_c, delivering shaft power to the generator:

$$P_{mg} = \eta_{pm} q_m (p_f - p_c) \tag{13}$$

where $\eta_{pm} = \eta_{pm,v} \eta_{pm,m}$ is the total efficiency of the pump/motor unit.

The electrical power generated is

$$P_{gen} = \eta_{gen} P_{mg} \tag{14}$$

The generator is designed to produce sufficient electrical power to supply the auxiliary components, while simultaneously providing a prescribed surplus power. Accordingly, the flow split α is determined by the power balance on the electrical bus, which must satisfy the prescribed surplus power P_e along with the demands of the charge pump and energy recovery unit:

$$P_{gen} = P_e + P_{re} + P_{ce} \tag{15}$$

Solving this power balance using Equations (5)–(14) yields

$$\alpha = \frac{\eta_{gen}\eta_{pm}(p_f - p_c) - \frac{P_e}{q_w}}{\eta_{gen}\eta_{pm}(p_f - p_c) + \frac{1}{1-\lambda(1-Y)}\left(\frac{p_c}{\eta_{ce}\eta_c} + \frac{1-Y}{\eta_{re}^{\sigma}}\left(\frac{\lambda}{\eta_{rp}}(p_f - p_c) - \eta_{rm} p_f\right)\right)} \tag{16}$$

https://doi.org/10.3390/en19112692

With α known, all flow rates, pressures, and power flows throughout the system can be determined, including the power to permeate, $P_p = Yq_f p_f$.

2.1.3. SMPT Architecture

The switch-mode power transformer enables hydraulic power transformation through the time-varying operation of a switching valve. The average flow rate through the WEC-driven pump is equal to the average flow rate through the pump/motor during the valve-open phases:

$$q_w = Dq_{pm} \tag{17}$$

where D is the duty cycle of the switching valve and q_{pm} is the **volumetric** flow rate through the pump/motor.

The average shaft power generated by the switch-mode pump/motor over a single switching period, T_{sw}, is

$$\bar{P}_{pm} = \frac{1}{T_{sw}} \int_0^{T_{sw}} P_{pm}(\tau)\, d\tau \tag{18}$$

where the instantaneous power delivered by the pump/motor is piece-wise

$$P_{pm}(\tau) = \begin{cases} \eta_{pm} q_{pm} \Big(p_w - p_f \Big) & 0 \le \tau \le DT_{sw} \\ \frac{1}{\eta_{pm}} q_{pm} \Big(p_c - p_f \Big) & DT_{sw} < \tau \le T_{sw} \end{cases} \tag{19}$$

assuming $p_c \le p_f \le p_w$. During the valve-open phase ($0 \le \tau \le DT_{sw}$), the pump/motor operates as a motor, drawing from the high-pressure WEC outlet at p_w and discharging to the RO feed rail at p_f. During the valve-closed phase ($DT_{sw} < \tau \le T_{sw}$), the pump/motor operates as a pump, drawing from the low-pressure charge rail at p_c and pressurizing flow to p_f. Integrating over the switching period yields

$$\bar{P}_{pm} = D\eta_{pm} q_{pm} \Big(p_w - p_f \Big) - \frac{1-D}{\eta_{pm}} q_{pm} \Big(p_f - p_c \Big) \tag{20}$$

The RO feed flow rate is the sum of the **volumetric** flow from the switch-mode pump/motor and the energy recovery pump:

$$q_f = \frac{q_{pm}}{1 - \lambda(1-Y)} \tag{21}$$

The electrical power generated is

$$P_{gen} = \eta_{gen} \bar{P}_{pm} \tag{22}$$

Similar to the parallel architecture, the duty cycle D is determined by the power balance on the electrical bus:

$$P_{gen} = P_e + P_{re} + P_{ce} \tag{23}$$

By solving the power balance, using Equations (5)–(7), (10) and (20)–(22), the following expression is obtained:

$$D = \frac{\frac{\eta_{gen}}{\eta_{pm}}(p_f - p_c) + \frac{1}{1-\lambda(1-Y)} \left(\frac{p_c}{\eta_{ce}\eta_c} + \frac{1-Y}{\eta_{re}^{\sigma}} \left(\frac{\lambda}{\eta_{rp}}(p_f - p_c) - \eta_{rm} p_f \right) \right)}{\eta_{gen}\eta_{pm}(p_w - p_f) + \frac{\eta_{gen}}{\eta_{pm}}(p_f - p_c) - \frac{P_e}{q_w}} \tag{24}$$

With D known, all flow rates and power flows can be determined. It must be noted that the time-averaged SMPT model neglects compressibility effects which is considered later in the pressure dynamic study.

https://doi.org/10.3390/en19112692

2.1.4. SMPT with Common Shaft Architecture

The SMPT with common shaft architecture integrates the switch-mode pump/motor, generator, charge pump, and recovery motor on a common mechanical shaft. This eliminates the electric motors that would otherwise be required to drive the charge pump and balance power on the energy recovery unit, thereby reducing conversion losses associated with electrical power flow.

The switch-mode pump/motor operates as the SMPT architecture described above:

$$\bar{P}_{pm} = D\eta_{pm}q_{pm}\left(p_w - p_f\right) - \frac{1-D}{\eta_{pm}}q_{pm}\left(p_f - p_c\right) \tag{25}$$

However, in this configuration, the shaft power is mechanically coupled directly to the generator, charge pump, and recovery motor.

The power balance on the common shaft is

$$\bar{P}_{pm} + P_{rm} = P_c + \frac{P_{gen}}{\eta_{gen}} \tag{26}$$

where P_{rm} is the shaft power delivered by the recovery motor, P_c is the shaft power consumed by the charge pump, and P_{gen}/η_{gen} is the mechanical power input to the generator.

As the rotary components are mechanically coupled through the common shaft, electrical power from the generator is not required to operate them. Therefore, the generator only needs to produce sufficient electrical power to meet the prescribed surplus:

$$P_{gen} = P_e \tag{27}$$

The RO feed flow rate is

$$q_f = q_{pm} \tag{28}$$

In this configuration, the recovery pump is eliminated, and the charge pump and recovery motor are driven directly from the shaft, eliminating electrical power demand for these components. The power recovered from the brine discharge by the recovery motor contributes directly to the common shaft to power the charge pump and generator.

By solving the shaft power balance for the duty cycle D, using Equations (5) and (25)–(28), yields

$$D = \frac{\eta_{rm}(1-Y)p_f - \frac{p_f - p_c}{\eta_{pm}} - \frac{p_c}{\eta_c}}{\frac{P_e}{\eta_{gen}q_w} - \eta_{pm}(p_w - p_f) - \frac{p_f - p_c}{\eta_{pm}}} \tag{29}$$

With D known, all flow rates and power flows throughout the system can be determined.

2.1.5. Study Parameters

The three architectures are evaluated using consistent operating conditions and component efficiencies to enable direct comparison. Table 1 summarizes the baseline study parameters.

The 100 kW input power provides a convenient basis for interpreting results as percentages or fractions of the WEC power input. The surplus electrical power of 5 kW represents auxiliary loads and control power requirements. Component efficiencies are selected to represent achievable performance with current technology. The WEC-driven pump efficiency and charge-pump efficiency are based on representative component-efficiency values reported in a previous study [11]. The hydraulic machine efficiency values are based on documented performance of the Danfoss (Nordborg, Denmark) Nessie APP 26/1500 axial piston pump/motor [33]. All hydraulic machines (pump/motor units,

https://doi.org/10.3390/en19112692

recovery motor, recovery pump) share the same volumetric and mechanical efficiency values, and all electric machines (generator, charge pump motor, recovery unit motor) share the same efficiency value.

Table 1. Baseline study parameters for system comparison.

Parameter	Symbol	Value
WEC input power	P_w	100 kW
Surplus electrical power	P_e	5 kW
Charge pressure	p_c	1 MPa
RO feed pressure	p_f	8 MPa
WEC pump outlet pressure (SMPT with c.s.)	p_w	30 MPa
RO recovery ratio	Y	0.3
Displacement ratio	D_{rp}/D_{rm}	1.0
WEC-driven pump efficiency	η_w	0.90
Hydraulic machine volumetric efficiency	η_v	0.96
Hydraulic machine mechanical efficiency	η_m	0.85
Electric machine efficiency	η_e	0.95
Charge pump efficiency	η_c	0.70

2.2. Transformer Shaft Dynamic Model

Due to the switching action, the SMPT relies on storing and releasing energy in the shaft inertia, which results in shaft speed variations. The purpose of this section is to quantify the influence of the shaft inertia on the speed variation.

The allowable speed fluctuation is expressed in terms of percentage speed deviation ϵ. The maximum and minimum speeds are defined as deviations about the nominal speed ω_n as

$$\omega_{max,min} = \omega_{\mathrm{n}}\left(1 \pm \frac{\epsilon}{100}\right) \tag{30}$$

The energy exchanged with the rotating assembly depends on the torque provided by the pump/motor, which is obtained by

$$T_{hyd} = \frac{(p_f - p_s)D_{pm}}{2\pi}, \tag{31}$$

where p_s is the pressure at the switching volume, which fluctuates between the high-pressure (WEC operating pressure) and low-pressure (inlet pressure of the WEC pump) as the switch valve opens and closes, and D_{pm} is the displacement of the pump/motor. The total energy exchanged can be obtained as

$$E_{cs} = \int_0^{DT_{sw}} T_{hyd}\omega_n dt = \int_0^{DT_{sw}} \frac{(p_f - p_s)D_{pm}}{2\pi}\omega_n dt \tag{32}$$

where D is the duty cycle and T_{sw} is the switching period. Thus, the required mass moment of inertia needed to restrict the speed fluctuation within the desired limit can be obtained by conserving energy:

$$J = \frac{2E_{cs}}{\omega_{max,min}^2 - \omega_{\mathrm{n}}^2} \tag{33}$$

where J is the equivalent mass moment of inertia of the entire rotating assembly, which consists of the shaft, flywheel, hydraulic motor/pump, charge pump, and the generator.

Study Parameters

The study parameters considered for the transformer shaft dynamic study are listed in Table 2. The inertia of the common shaft is composed of the inertia of the rotating

https://doi.org/10.3390/en19112692

machines and the flywheel. The flywheel is considered to be a solid cylinder made of steel. The diameter of the flywheel is considered to be 300 mm, slightly larger than the diameter of the casing of the generator. Following the preliminary sizing of the components based on the static power flow model, the inertia of the rotating machines is obtained from manufacturer catalogs. Based on those values, the inertia of the common-shaft assembly without the flywheel is obtained to be approximately 1.02 kg·m^2. The required inertia of the shaft assembly is evaluated for 5% and 10% allowable speed deviations under different switching frequencies. The mass of the flywheel needed to achieve the required inertia is used as a trade-off parameter to select the nominal switching frequency.

Table 2. Flywheel and shaft inertia parameters.

Parameter	Symbol	Value
Percentage speed deviation	ϵ	5, 10 (%)
Nominal Speed	ω_n	3600 RPM
Switching frequency		1 to 20 (Hz)
Transition ratio		0 to 0.2
Switch valve area	A_s	10 to 50 cm^2
Switching volume	V	0.4 to 2 L
Shaft outer diameter		0.14 m
Shaft length		2 m
Shaft assembly inertia (without flywheel)		1.02 kg·m^2
Flywheel material density		7850 kg/m^3
Flywheel outer diameter		0.3 m

2.3. SMPT Pressure Dynamic Model

The third study focuses on the pressure dynamics of the switch-mode power transformer, with the primary objective of determining the switch valve parameters. In this analysis, the shaft dynamics considered in the second study are neglected to isolate the effects of the valve dynamics. The switch-mode transformer subsystem consists of the active switch valve, the passive check valve, the hydraulic motor/pump, and the hydraulic accumulator, as shown in Figure 4. The flow rate supplied by the WEC-driven pump is considered the input to the system, and the pressure and flow rate delivered to the RO membrane are considered the output.

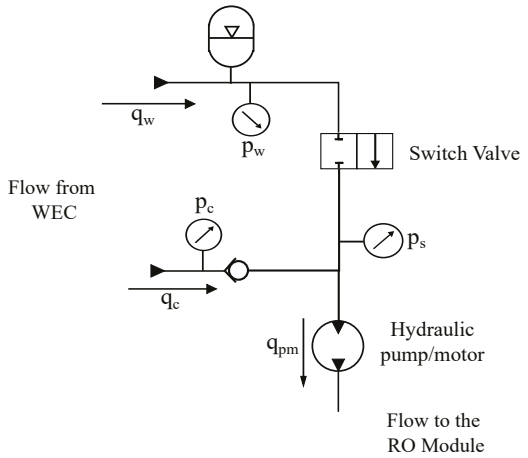


Figure 4. Schematic of SMPT subsystem for dynamic modeling.

To facilitate the dynamic analysis, the flow rate delivered by the WEC-driven pump is assumed to vary sinusoidally, which captures the oscillatory behavior of the waves without

modeling WEC hydrodynamics: The volumetric flow rate from the double-acting cylinder with a check valve rectifier can therefore be expressed as

$$q_w = A|\sin[2\pi f_c t]| \tag{34}$$

where A is the amplitude, f_c is the frequency of WEC. The amplitude of the volumetric flow rate is determined from the prescribed pump power, P_w, and the desired operating pressure, p_{des}.

$$q_{avg} = \frac{P_w}{p_{des}} \tag{35}$$

$$q_{avg} = \frac{\int A|\sin[2\pi(f_c)t]|\,dt}{\int dt} \tag{36}$$

The gas-charged accumulator is used to increase the capacitance of the system, thereby reducing pressure fluctuations. The compression of the charged gas inside the accumulator is considered to be an isothermal, ideal gas process. Under this assumption, the pressure of the high-pressure rail can be expressed as

$$p_w = \frac{p_{charge} V_{acc}}{V_{gas}} \tag{37}$$

where p_{charge} is the pre-charge pressure of the accumulator and V_{acc} is the total volume of the accumulator. The volume of gas present inside the accumulator V_{gas}, can be obtained from

$$V_{gas} = V_{acc} - \int (q_w - q_s)dt \tag{38}$$

where q_w is the flow rate delivered by the WEC and q_s is the flow rate supplied to the switch valve. The inertia of the diaphragm and resistance to the fluid flow at the accumulator outlet are not considered.

The switch valve operates between a fully open and a fully closed state, which is governed by the switching frequency and the duty cycle. The valve area is modeled as a trapezoidal profile to account for the finite transition time required for switch valve actuation. The instantaneous switch valve area can be obtained from the equation

$$A_{sv}(t') = \begin{cases} \frac{A_s}{t_r}\,t', & \text{during opening transition} \\ A_s, & \text{during fully open} \\ \frac{A_s}{t_r}(DT_{sw} - t'), & \text{during closing transition} \\ 0, & \text{during fully closed} \end{cases} \tag{39}$$

where A_s represents the maximum valve opening area, the variable t' defines the time within a single switching time period. The parameter t_r is the transition time required for the valve to fully open or fully close. The flow through the switch valve is modeled using the orifice equation:

$$q_s = C_d A_{sv}(t')\sqrt{\frac{2}{\rho}(p_w - p_s)} \tag{40}$$

The check valve is considered to behave ideally. The volumetric flow rate through the check valve is modeled using the orifice equation

https://doi.org/10.3390/en19112692

$$q_c = \begin{cases} C_d A_c \sqrt{\frac{2}{\rho}(p_c - p_s)} & \text{if} \quad p_s < p_c \\ 0 & \text{if} \quad p_s \geq p_c \end{cases} \tag{41}$$

where A_c is the check valve area, C_d is the discharge coefficient, p_c is the charge pump outlet pressure and p_s is the switching volume pressure.

Considering the fluid in the switched volume to be compressible, the dynamic pressure of the switch volume depends on the continuity equation

$$\frac{dp_s}{dt} = \frac{\beta_{\text{eff}}}{V}(q_s + q_c - q_{pm}) \tag{42}$$

where V is the switch volume, q_s and q_c are the inflow of fluid from the high-pressure rail and the low-pressure rail respectively, q_{pm} is the outflow which is delivered to the RO module, and β_{eff} is the effective bulk modulus of the seawater.

The bulk modulus as a function of pressure is modeled considering isentropic compression of the entrained air and the liquid using the method of Cho et al. [34]:

$$\beta_{eff}(p) = \beta \left(\frac{\left(\frac{p}{p_{atm}}\right)^{\frac{1}{\gamma}} e^{\frac{(p_{atm}-p)}{\beta}} + R}{\frac{R}{\gamma}\frac{\beta}{p} + \left(\frac{p}{p_{atm}}\right)^{\frac{1}{\gamma}} e^{\frac{(p_{atm}-p)}{\beta}}} \right) \tag{43}$$

where β is the bulk modulus of pure liquid, γ is the air heat ratio, and R is the entrained air volume fraction at atmospheric pressure, p_{atm}.

2.3.1. Control

A proportional-integral (PI) controller with a feedforward term and a low-pass filter is designed to control the operating pressure of the WEC-driven pump. The control input used to control the pressure is the duty of the switching valve. The PI control system is based on a linearized model obtained about a nominal operating condition. The nominal pre-charge pressure, volume of water in the accumulator and the desired WEC operating pressure are provided in Table 3.

A first-order low-pass filter is used to suppress the excessive variations in the duty cycle ratio. The low-pass filter is expressed as

$$\frac{dp_{w,fil}}{dt} = \frac{1}{\tau}\left(p_w - p_{w,fil}\right) \tag{44}$$

where τ is the time constant of the low-pass filter. The cut-off frequency is selected to be lower than the frequency of the ocean waves. This is done to attenuate the large and slow pressure fluctuations, resulting in a smoothing effect of the duty-cycle response at the expense of a moderate phase lag.

The maximum and minimum limits of the duty cycle ratio were set to 1 and 0, respectively. The control law for the PI control system is expressed as

$$D = min\left(1, max\left(0, D_{ff} + k_p\varepsilon + k_i \int \varepsilon, dt\right)\right) \tag{45}$$

where D_{ff} is the feedforward term, and ε is the error between the desired pressure p_{des} and the filtered pressure $p_{w,fil}$. The error can be expressed as

$$\varepsilon = p_{des} - p_{w,fil} \tag{46}$$

https://doi.org/10.3390/en19112692

The gains k_p and k_i were selected from the root locus of the linearized system such that the system is deliberately slow and smooth. The oscillating closed-loop poles were placed at $-0.0985 \pm 0.39\,j$, corresponding to a natural frequency of 0.41 rad/s and a settling time of approximately 70 s. The small integral gain k_i ensures zero steady-state error while having very little impact on the system's oscillatory behavior. Together, these gains place the slow pole at -0.0531, which dominates the long-term response and produces a slow, stable, and smooth system. The values of the gains and time constant of the control system are summarized in Table 3.

Table 3. Control system parameters used in PI controller.

Control Parameter	Symbol	Value
Desired WEC operating pressure	p_{des}	21 MPa
Nominal volume of water in HPA		0.04 m^3
Pre-charged pressure	p_{charge}	12 MPa
Proportional gain	k_p	-7×10^{-8}
Integral gain	k_i	-3.5×10^{-9}
Filter time constant	τ	4 s
Feedforward duty cycle	D_{ff}	0.5

2.3.2. Objective Functions

The main losses considered for the switch-mode circuit are the throttling losses across both the check valve and the switch valve. The energy losses for a duration of four wave cycles are obtained by integrating the instantaneous power losses, given by

$$E_{loss,SV} = \int (p_w - p_s) q_s \, dt \tag{47}$$

$$E_{loss,CV} = \int (p_c - p_s) q_c \, dt \tag{48}$$

where $E_{loss,SV}$ is the energy loss experienced by the switch valve and $E_{loss,CV}$ is the energy loss experienced by the check valve. Since the present study focuses mainly on the SMPT, the desired output is taken as the flow delivered to the RO module. Although in the physical system, the flow passes through the hydraulic pump/motor coupled to the common shaft, any energy exchange with the shaft is neglected in this study, so that the objective function reflects only the hydraulic performance of the SMPT. The electric power generated by the generator and the potable water obtained through the RO membrane are not considered for the design study of the SMPT. Furthermore, the objective functions focus only on the losses incurred by the switch valve and the check valve. Based on this definition, the energy loss fraction for the SMPT is calculated as the ratio of the energy losses to the sum of the energy losses and the energy delivered to the RO module.

$$E_{frac} = 1 - \frac{\int (p_s - p_{atm}) q_{pm} \, dt}{\int (p_s - p_{atm}) q_{pm} dt + \int ((p_w - p_s) q_s + (p_c - p_s) q_c) dt} \tag{49}$$

The energy loss fraction serves as the principal evaluation metric for comparing the performance of the SMPT across different operating conditions.

3. Results and Discussion

Similar to the previous section, the Results and Discussion section is organized into three main subsections. In the first subsection, the results for the static power flow studies are presented and discussed for the three PTO architectures. The next subsection examines the results for the transformer shaft dynamics study with emphasis mainly on the impact

https://doi.org/10.3390/en19112692

of the shaft inertia on system behavior. Finally, the results for the pressure dynamic study of the SMPT are presented and discussed.

3.1. Static Power Flow Model

This subsection presents the system efficiency and the permeate production and provides a comparative study of their performance. The three architectures were compared using the time-averaged static power flow models with the baseline parameters defined in Table 1.

Figure 5 illustrates the power flow paths through each architecture with values derived from the model results. In these schematics, the green arrows denote power transfer between components, while the red arrows indicate power losses. The parallel baseline architecture delivers 34.97% of the WEC input power to permeate production, establishing the benchmark for comparison. The SMPT architecture without a common shaft delivers 32.47% of input power to permeate, representing a 2.5 percentage point reduction (7.1% relative reduction) compared to the baseline. The SMPT with common shaft architecture achieves 34.02% permeate power, a 1.5 percentage point improvement (4.8% relative improvement) over the standalone SMPT configuration and within 1.0 percentage point (2.7% relative) of the parallel baseline.

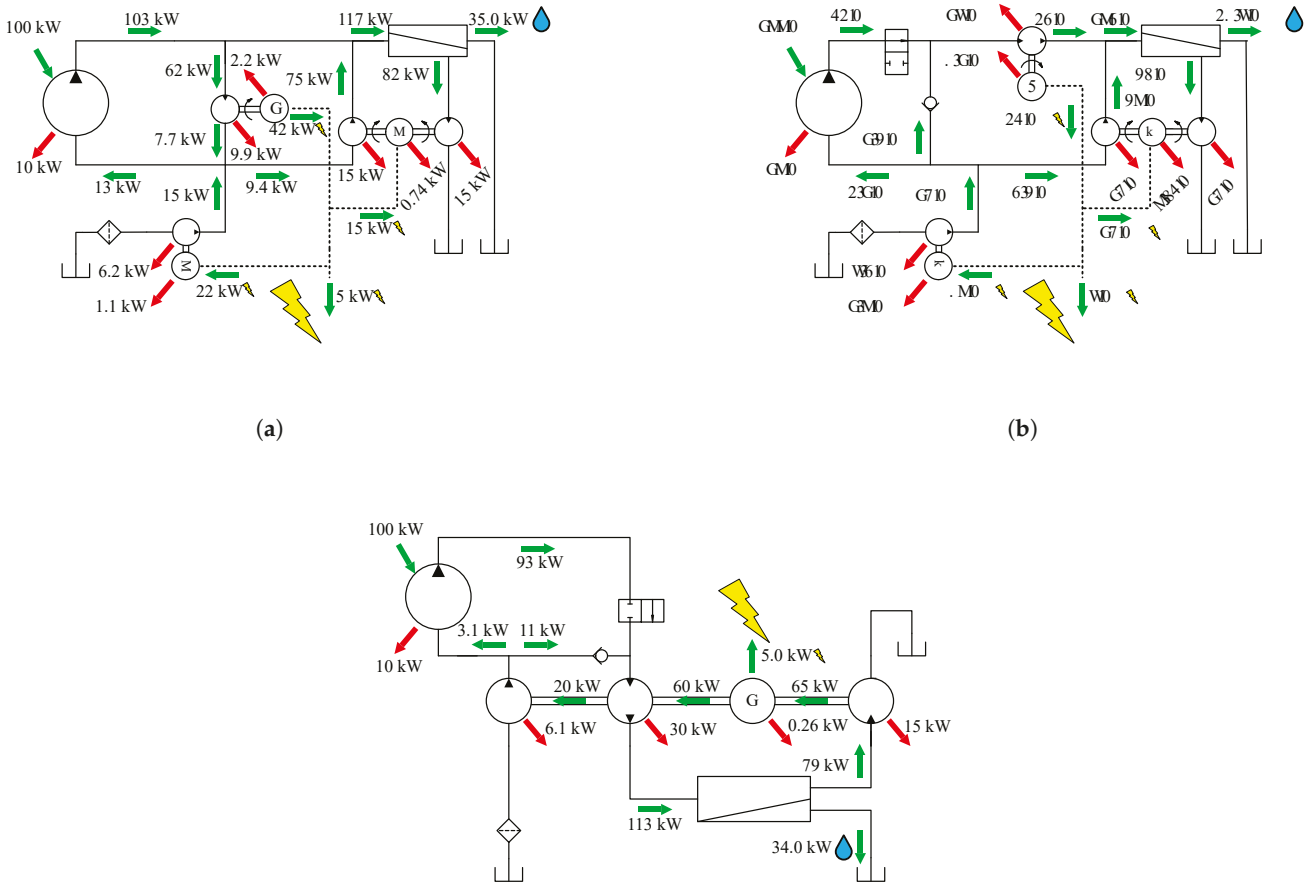


Figure 5. Power flow schematics of three PTO architectures: (**a**) Baseline, (**b**) SMPT, and (**c**) SMPT with common shaft. The green arrows indicate power transfer between components, while the red arrows indicate power losses.

https://doi.org/10.3390/en19112692

The SMPT architecture exhibits reduced efficiency compared to the parallel baseline due to recirculating energy within the switch-mode power transformer. During each switching cycle, kinetic energy is stored in the rotating inertia of the generator and pump/motor when the switching valve opens, then released when the valve closes to pump low-pressure fluid to the RO feed pressure. This bidirectional power flow between the mechanical inertia and hydraulic system introduces additional losses in the pump/motor compared to the unidirectional power flow in the parallel baseline. While the SMPT operates the WEC pump at elevated pressure ($p_w = 30$ MPa versus $p_f = 8$ MPa), reducing the required displacement for a given power level, the switching losses dominate under the baseline efficiency parameters.

The common shaft architecture mitigates the efficiency penalty of the SMPT by eliminating two electric motors present in both the baseline and standalone SMPT configurations: the charge pump motor and the energy recovery unit motor. By mechanically coupling the charge pump, energy recovery motor, generator, and switch-mode pump/motor to a single shaft, power flows between these components without intermediate electrical conversion. This eliminates the round-trip electrical conversion losses (η_e^2 for motor-generator pairs) that occur when power is transmitted through the electrical bus. The recovered efficiency nearly compensates for the switching losses, bringing the common shaft architecture to within 1% of the baseline parallel configuration.

3.2. Transformer Shaft Dynamic Model

This section presents results showing the influence of shaft inertia and switching frequency on speed variation in the common shaft. Figure 6 shows the common-shaft assembly inertia required to limit speed fluctuations to 5% and 10%. Increasing the switching frequency reduces the time available for acceleration and deceleration about the mean shaft speed during each cycle. Thereby reducing speed variation and lowering the inertia required to achieve a target fluctuation limit. The mass and the thickness of the flywheel to achieve the required inertia for different switching frequencies are given in the Table 4. Three different switching frequencies are considered for further parametric studies. (i) Switching frequency of 15 Hz, where no flywheel is added and the inertia of the common shaft assembly without the flywheel is enough to maintain the speed fluctuations to 5%, (ii) Switching frequency of 5 Hz, where a flywheel of 159 kg is required, (iii) and a switching frequency of 1 Hz, which requires flywheel of 1133 kg to maintain the shaft speed fluctuations within 5%. The required inertia for a switching frequency of 1 Hz, 5 Hz, and 15 Hz is specifically highlighted by the dashed horizontal lines in Figure 6.

Table 4. Influence of flywheel thickness on system inertia and switching frequency for 5% speed variation.

Switching Frequency (Hz)	System Inertia (kg·m^2)	Flywheel Inertia (kg·m^2)	Thickness (m)	Flywheel Mass (kg)
15	1.02	No Flywheel	–	–
7	2.26	1.24	0.2	111
5	2.81	1.79	0.29	159
4	3.51	2.49	0.4	222
3	4.76	3.74	0.6	333
1	13.8	12.7	2	1133

https://doi.org/10.3390/en19112692

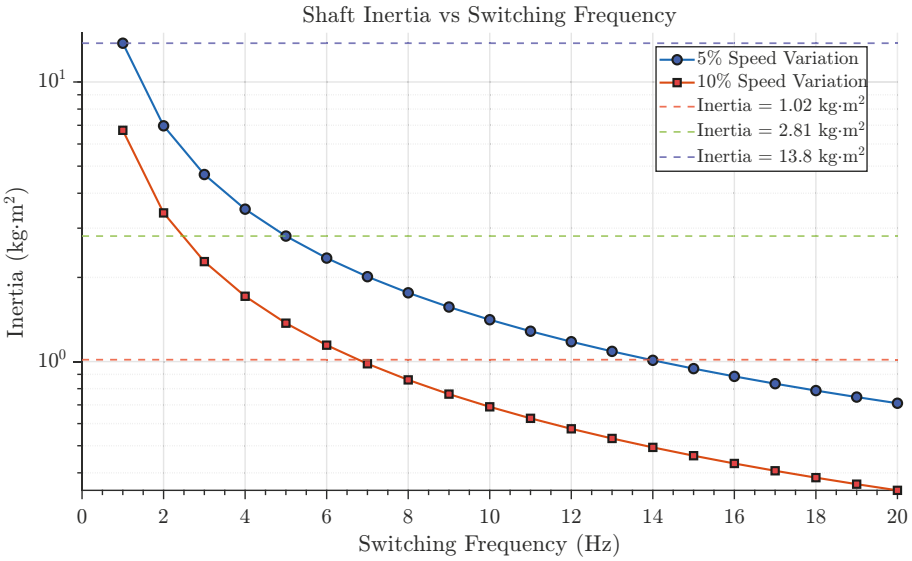


Figure 6. Plot showing the required common shaft inertia required to limit shaft-speed fluctuations to 5% and 10% for different switching frequencies.

3.3. SMPT Pressure Dynamic Model

The results for the pressure dynamic modeling of the SMPT are presented in this subsection, focusing on pressure and flow ripple, energy losses, and the sensitivity of the system performance based on switching frequency, transition ratio, switch valve area, and switching volume.

The switch-mode power transformer dynamics are presented in Figure 7. Two switching cycles at a switching frequency of 10 Hz and with a duty of 0.21 are shown. The pressure of the switched volume and switch valve area are presented in the top subplot, and the flow rate through the switch valve and check valve are shown in the bottom subplot. As the switch valve opens, there is a significant spike in the flow rate, because of the large pressure difference between the high-pressure rail and the pressure at the switched volume. These surges in flow are driven by the large pressure differential across the valve. The flow rate from the switch valve settles as the switched volume pressure increases and approaches the WEC operating pressure. During the closing transition of the switch valve, the switched volume pressure drops, and when it goes below the outlet pressure of the charge pump, the check valve opens and maintains the switching pressure at the outlet pressure of the charge pump, resulting in flow through the check valve.

The dynamics of the WEC-driven pump are presented in Figure 8. The top subplot shows the flow rate delivered by the WEC-driven pump over one wave cycle, exhibiting two distinct pulses corresponding to the reciprocating motion of the WEC. The duty of the switch valve is controlled to maintain the operating pressure of the pump at 21 MPa. The bottom subplot shows the pressure dynamics at the high-pressure rail along with the duty of the switch valve. As evident from the plot, there are two different oscillatory behaviors in the WEC pump pressure curve, reflecting two dominant time-scales in the system. The slow, large amplitude variations in the pressure arise from the WEC-driven pump operating at a frequency of 0.1 Hz. The fast, small-amplitude fluctuations that are superposed on the curve are due to the switch valve operating at a frequency of 10 Hz. Figure 8 shows that the duty is oscillating between 0.21 and 0.23, and there is a slight phase lag with respect to the pressure curve. The phase lag is due to the low-pass filter employed in the control loop, which has a cut-off frequency lower than the WEC frequency.

https://doi.org/10.3390/en19112692

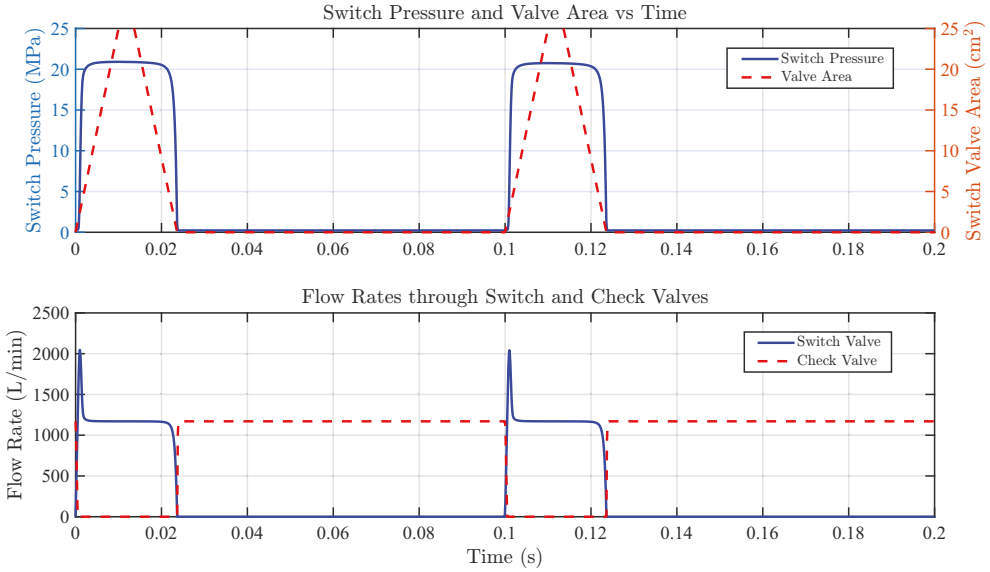


Figure 7. Switch-mode power transformer dynamics over two switching cycles at 10 Hz and duty cycle 0.21. **Top subplot**: switched-volume pressure and switch valve area. **Bottom subplot**: switch valve and check-valve flow rates.

Interpreting these results, the low duty cycle implies a lower effective pressure transformation ratio of the SMPT, resulting in a cycle-averaged switching pressure lower than the RO module pressure. Consequently, the hydraulic pump/motor operates predominantly in pumping mode, drawing fluid from the low-pressure switching volume and delivering it to the comparatively higher-pressure RO module. Under this condition, the shaft power is supplied to the fluid, part of which is supplied by the recovery motor.

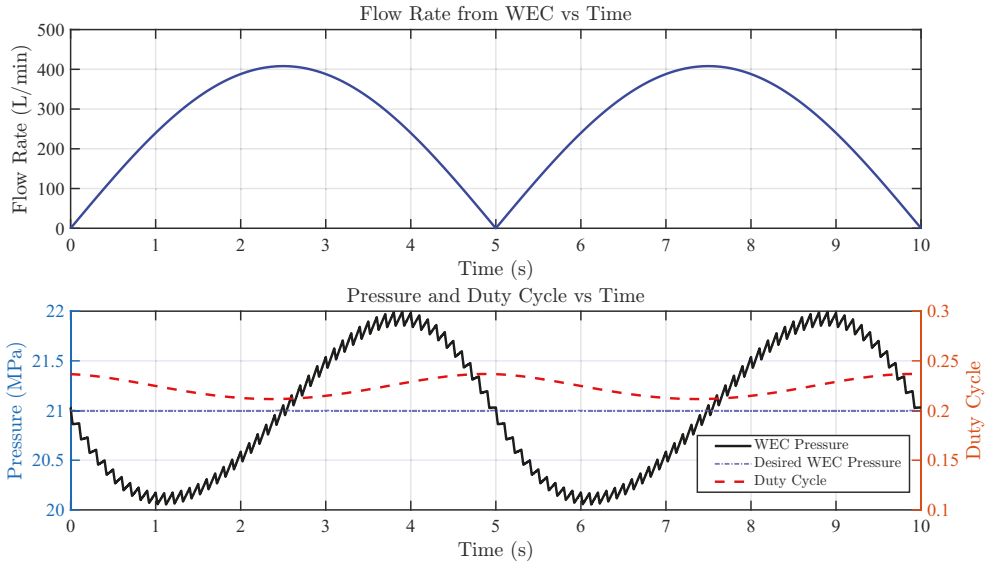


Figure 8. Plot showing the WEC-driven pump dynamics; **Top subplot**: flow rate delivered by the WEC-driven pump over one wave cycle. **Bottom subplot**: high-pressure rail pressure and switch valve duty.

3.3.1. Power Loss Study

The instantaneous throttling power loss through a switching cycle is presented in Figure 9. There is a significant power loss spike that reaches nearly six times the WEC input power when the switch valve is opening. This coincides with flow surges shown in Figure 7 and at the same time, the pressure in the switched volume rises rapidly from about 300 kPa to 20 MPa. As the pressure of the switched volume rises rapidly and approaches

pressure at the high-pressure rail, the throttling power loss across the valve becomes less significant. There is another power loss spike during the closing event of the switch valve due to the decreasing switch valve area.

When the switch valve is opening there is a large pressure differential between the WEC pressure and the switched volume pressure. This results in a large transient flow rate through the valve as the fluid in the switched volume is compressed to the WEC pressure. Due to the capacitance of the switched volume, its pressure cannot rise instantaneously. So the large pressure drop across the valve persists during the opening transition of the switch valve and results in a large spike in power loss as shown in Figure 9. Among the losses experienced by the valves the compressibility-related loss is the major source of power loss. In contrast, the compressibility effects are negligible during the switch valve closing, resulting in a smaller throttling valve power loss spike during this transition shown in Figure 9. The check valve throttling losses are insignificant compared to the losses across the switch valve.

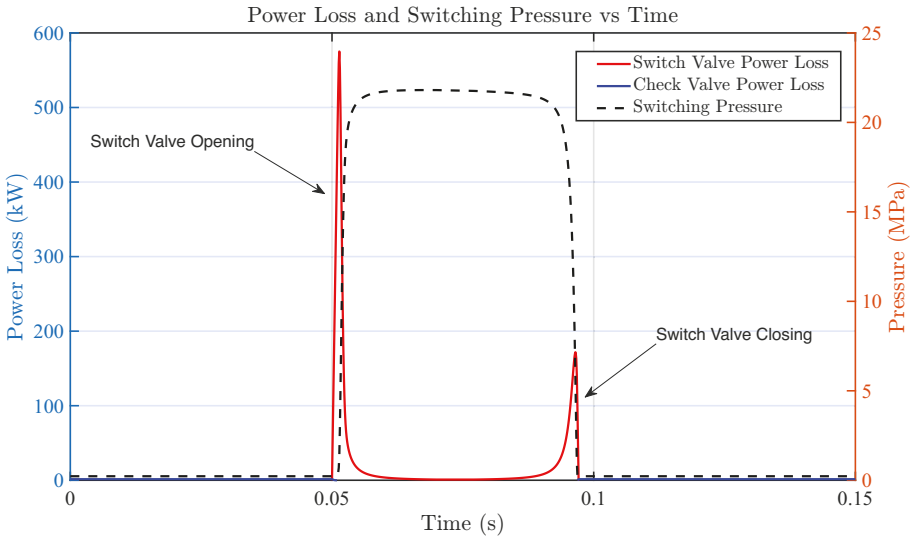


Figure 9. Plot showing the instantaneous power loss in the switch valve and the check valve and switching pressure vs. time over a switching cycle.

3.3.2. Parameter Studies

This section presents the influence of four parameters: (i) switching frequency, (ii) transition ratio, (iii) switch valve area, and (iv) switch volume on SMPT performance. The parametric results are not intended to characterize generic valve losses. Instead, these results quantify the relative energy loss fraction of the SMPT within the design space considered in this study. The main purpose of this subsection is to identify practical design trends for selecting valve parameters.

The influence of switching frequency on the energy loss fraction is presented in Figure 10. The trend of increasing energy loss with increasing frequency occurs because each switching event generates a transient power loss spike, as shown in Figure 9. Although a low switching frequency is desirable as it is more efficient, it increases speed variation in the common-shaft assembly as discussed in the previous subsection, highlighting the trade-off between flywheel size and the efficiency of the system.

The transition ratio represents the fraction of the switching period during which the valve is transitioning either from the closed state to the open state or vice versa. In this work, the opening and closing transition ratios are assumed to be identical. During the transition phase, the valve area is smaller, causing higher throttling losses. The increase in energy loss fraction with increasing transition ratio is shown in Figure 11. Smaller transition ratios reduce throttling losses and provide faster response, but result in sharp pressure

https://doi.org/10.3390/en19112692

spikes. Having a relatively larger transition time slightly smoothens out the switching pressure as shown in Figure 12.

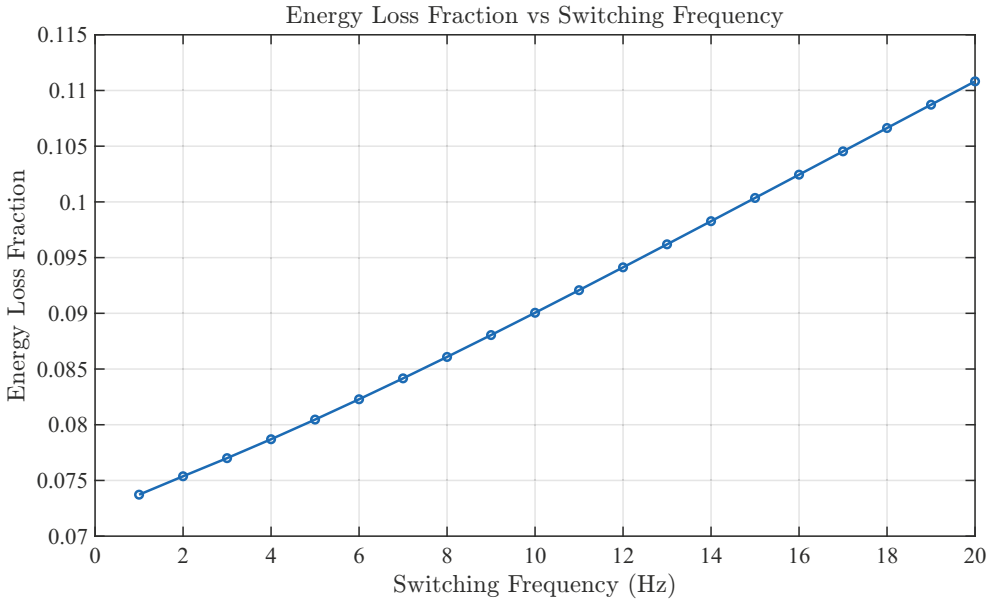


Figure 10. Plot showing relation between switching frequency and energy loss fraction.

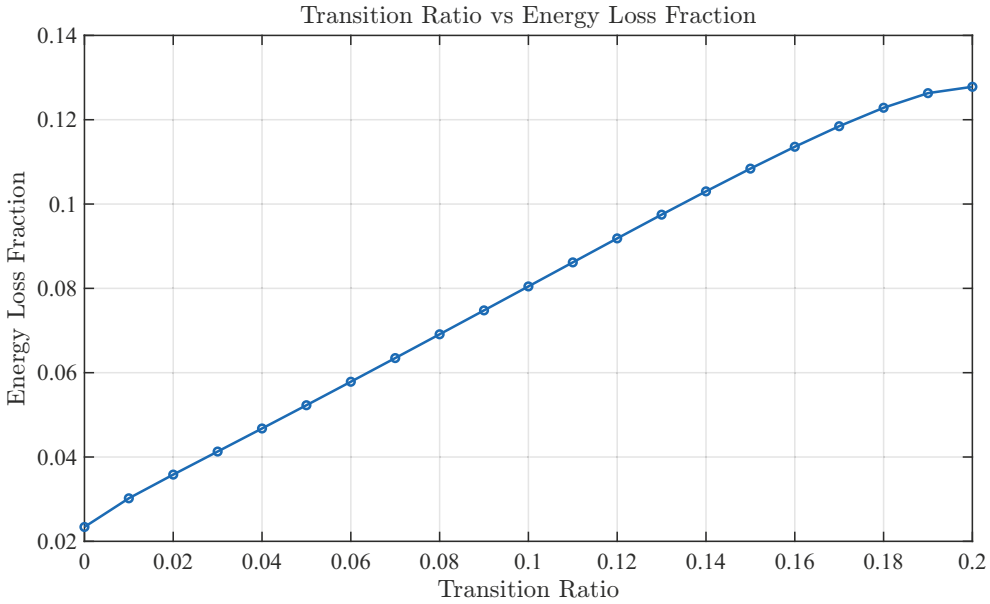


Figure 11. Plot showing relation between transition ratio and energy loss fraction.

To investigate the effect of the switch valve area, the maximum valve area is varied, and its influence on the energy loss fraction is analyzed. As shown in Figure 13, the energy loss fraction decreases with increasing switch valve area, with the steepest slope occurring at small valve areas. This trend occurs because a larger valve area reduces the pressure drop across the fully open valve, thereby decreasing the throttling losses. While larger valve area reduces throttling energy losses, it requires larger moving elements in the valve, increasing the actuation energy required for rapid switching. This trend needs to be considered in future work designing a specific valve architecture for this application to identify a practical design trade-off between reducing throttling energy losses and limiting valve actuation energy requirement.

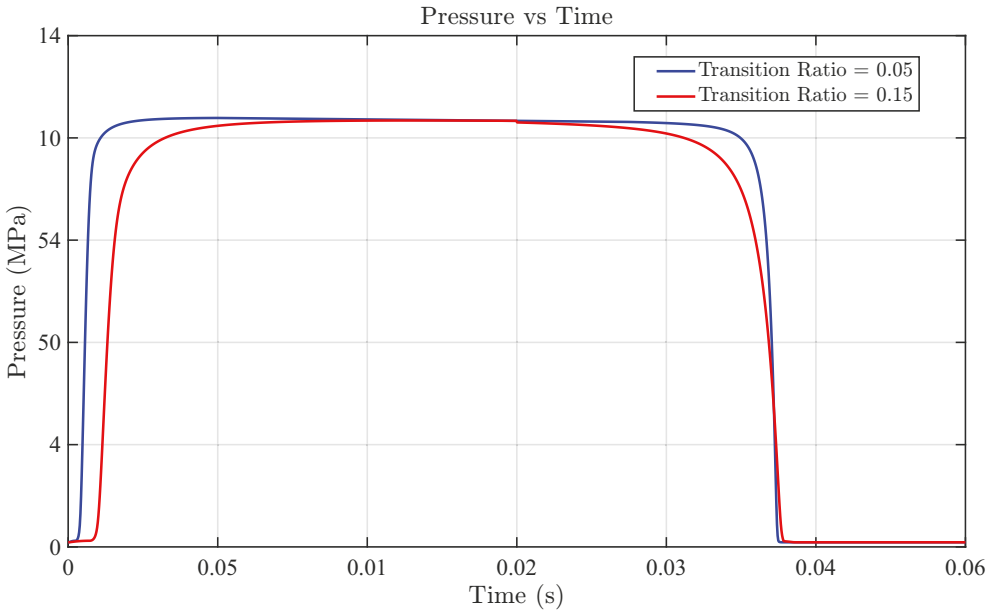


Figure 12. Plot showing the switched-volume pressure response for two transition ratios, illustrating the effect of transition time on the pressure transient during switch valve operation.

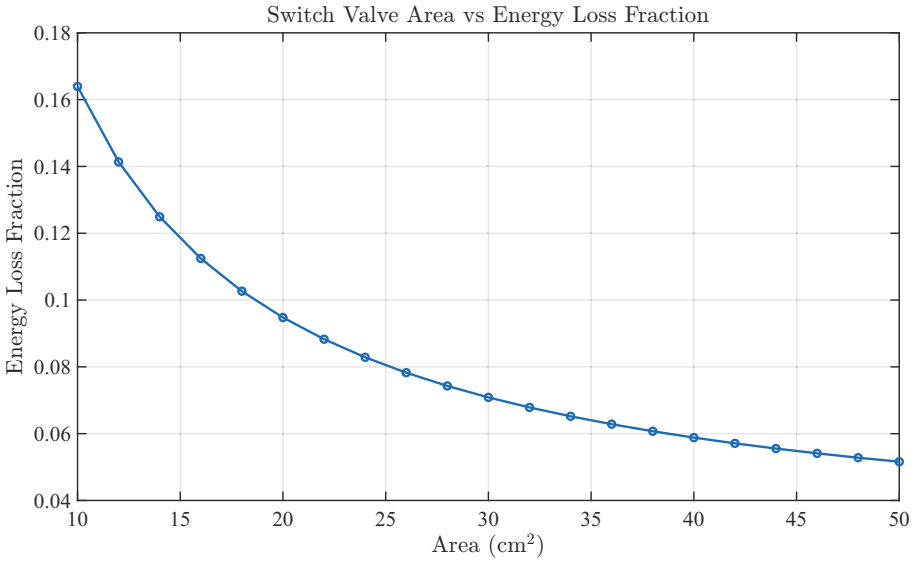


Figure 13. Plot showing relation between switch valve area and energy loss fraction.

The influence of switching volume is also studied. Figure 14 presents the variation in energy loss fraction with switching volume for switching frequencies of 1 Hz, 5 Hz, and 15 Hz. The energy loss fraction increases with switching volume because the fluid in the switched volume needs to be compressed and decompressed during each switching event. As a result, a larger switching volume requires more fluid to enter the switched volume through the transitioning valve to raise the pressure during each cycle. The energy loss due to this effect increases at higher switching frequencies, as the same compression-related loss occurs more frequently. Reducing the switching volume, within physical limitations, is critical to an efficient SMPT.

Figures 10–14 indicate a preferred design from an energy loss perspective, has a smaller switching volume, a larger switch valve area, lower switching frequency, and a shorter transition ratio. However, the grid studies do not account for the required actuation energy, which favors a longer transition ratio and smaller switch valve area. Moreover, the shaft speed variation is also not considered, which favors faster switching frequencies.

https://doi.org/10.3390/en19112692

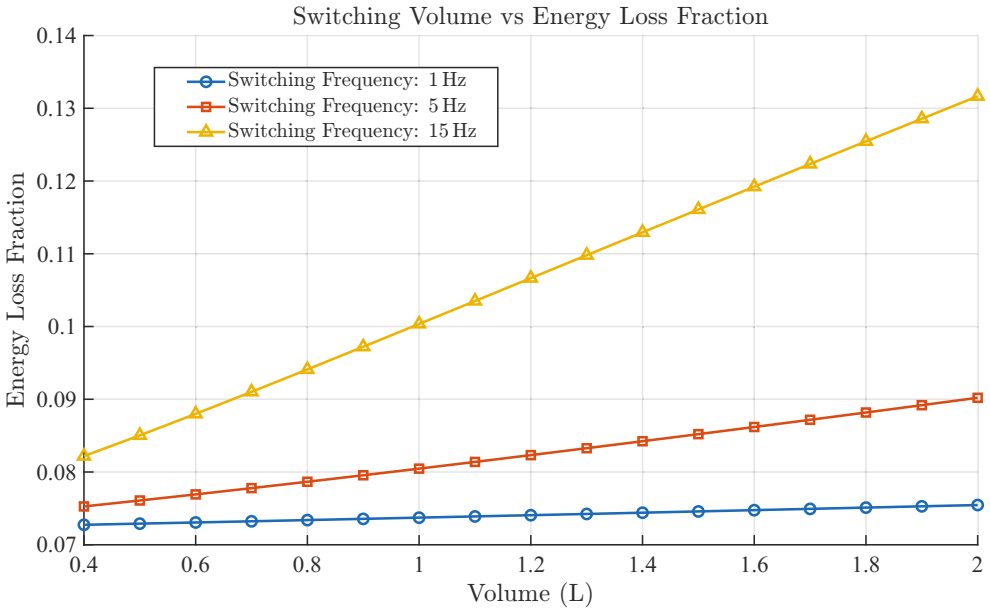


Figure 14. Energy loss fraction as a function of switching volume for switching frequencies of 1 Hz, 5 Hz, and 15 Hz.

4. Conclusions

This study proposes and models a new hydraulic PTO architecture for desalination of seawater with cogeneration of electricity. The architecture incorporates a SMPT with a common shaft. Its performance is evaluated relative to the baseline architecture and the SMPT architecture without a common shaft. The SMPT allows (1) the pressure at the WEC pump to be elevated above the RO module pressure, allowing for a smaller WEC-driven pump, the most expensive component in the PTO and (2) allows independent control of the pressure at the WEC pump to maximize power capture at the WEC through varying wave states. The analysis is based on a static power flow study, transformer shaft dynamics, and the SMPT pressure dynamics study.

The static power flow study provides an overall system-level comparison of the three architectures. Along with a prescribed surplus of 5 kW of electrical output from the generator, the baseline architecture delivers 34.97% of the WEC input power to permeate production, the SMPT architecture delivers 32.47%, and the SMPT with common-shaft delivers 34.02%. The efficiency of the SMPT architectures reduces slightly due to the bi-directional power flow through the motor/pump during each switching cycle. The common-shaft SMPT architecture reduces losses by eliminating some components.

The transformer shaft dynamics study uses switching frequency as a design variable to estimate the mass of the flywheel required to reduce the shaft speed fluctuations to 5% or 10%. Higher switching frequencies reduce the inertia required by the shaft and flywheel assembly to maintain the allowable speed variation. No flywheel is required to maintain a shaft speed fluctuation of 5% for a 15 Hz switching frequency. However, for a switching frequency of 5 Hz and 1 Hz, 159 kg and 1133 kg of flywheel are required, respectively.

The pressure dynamics study shows that switch valve losses dominate the SMPT performance. The dominant losses are the throttling losses during the transition phase of the switch valve, which are not considered in the time-averaged model. For a pressure dynamics case with a switch valve area of 25 cm^2, transition ratio of 0.1, switching volume of 1 L, and switching frequency of 5 Hz, incorporating the switch valve throttling losses in the time-averaged power flow model reduces the overall efficiency of the SMPT with common-shaft architecture from 34% to 32%. The maximum energy loss occurs during the opening phase of the switch valve, where a large pressure difference across a small transition valve

https://doi.org/10.3390/en19112692

area and the high transient flow required to pressurize the switching volume produce the peak throttling loss spike. The parametric studies show that the energy loss fraction increases with increasing switching frequency, transition ratio, and switching volume, and decreases with increasing switch valve area. These trends create a trade-off as a larger valve area and shorter valve transition require higher valve actuation power, lower switching frequency increases shaft speed variation, and reduces the response time of the system, and there is a limit on the minimum switching volume due to component packaging.

Overall, these results suggest that the proposed architecture offers system-level advantages, in terms of reducing system cost and allowing independent control of the torque at the WEC pump to increase average power capture across varying wave states at the expense of a slight reduction in efficiency. The dominant energy loss is throttling across the switch valve during valve transitions due to fluid compressibility in the switched volume. Reducing the throttling losses in the switch valve will be essential in improving its practical performance. Future work should therefore focus on soft-switching strategies that minimize the transitional throttling losses by equalizing pressure across the valve before transition.

Author Contributions: Conceptualization, J.W.S. and J.D.V.d.V.; Methodology, S.P. and J.W.S.; Software, S.P. and J.W.S.; Formal Analysis, S.P. and J.W.S.; Writing—Original Draft Preparation, S.P. and J.W.S.; Writing—Review and Editing, J.W.S. and J.D.V.d.V.; Visualization, S.P.; Supervision, J.D.V.d.V.; Project Administration, J.D.V.d.V.; Funding Acquisition, J.D.V.d.V. All authors have read and agreed to the published version of the manuscript.

Funding: This research was supported in part by the U.S. Department of Energy (DOE), Office of Critical Minerals and Energy Innovation, under Award No. EE0011961, and by the National Science Foundation (NSF). Any opinions, findings, and conclusions or recommendations expressed in this material are those of the authors and do not necessarily reflect the views of the DOE or NSF.

Data Availability Statement: The data presented in this study are available on request from the corresponding author.

Conflicts of Interest: Author Jeremy W. Simmons is the owner of the company Integral Power Systems, Minneapolis. The remaining authors declare that the research was conducted in the absence of any commercial or financial relationships that could be construed as a potential conflict of interest.

Abbreviations

The following abbreviations are used in this manuscript:

RO	Reverse Osmosis
HPA	High Pressure Accumulator
PTO	Power Take Off
WEC	Wave Energy Converter
ERU	Energy Recovery Unit
SMPT	Switch Mode Power Transformer

References

1. Reikard, G.; Robertson, B.; Bidlot, J.R. Combining wave energy with wind and solar: Short-term forecasting. *Renew. Energy* **2015**, *81*, 442–456. [CrossRef]
2. Bouhrim, H.; El Marjani, A.; Nechad, R.; Hajjout, I. Ocean wave energy conversion: A review. *J. Mar. Sci. Eng.* **2024**, *12*, 1922. [CrossRef]
3. Drew, B.; Plummer, A.R.; Sahinkaya, M.N. A review of wave energy converter technology. *Proc. Inst. Mech. Eng. Part A J. Power Energy* **2009**, *223*, 887–902. [CrossRef]
4. Maheen, M.H.; Yang, Y. Wave energy converters with rigid hull encapsulation: A review. *Sustain. Energy Technol. Assess.* **2023**, *57*, 103273. [CrossRef]

5. Falcão, A.d.O. The shoreline OWC wave power plant at the Azores. In Proceedings of the 4th European Wave Energy Conference, Aalborg, Denmark, 4–6 December 2000; pp. 42–47.
6. Igic, P.; Zhou, Z.; Knapp, W.; MacEnri, J.; Sørensen, H.; Friis-Madsen, E. Multi-megawatt offshore wave energy converters—Electrical system configuration and generator control strategy. *IET Renew. Power Gener.* **2011**, *5*, 10–17. [CrossRef]
7. Amundarain, M.; Alberdi, M.; Garrido, A.J.; Garrido, I. Modeling and simulation of wave energy generation plants: Output power control. *IEEE Trans. Ind. Electron.* **2010**, *58*, 105–117. [CrossRef]
8. Babarit, A. Working principles and technologies of wave energy conversion. *Wave Energy Convers.* **2017**, 99–151. [CrossRef]
9. Li, X.; Chen, C.; Li, Q.; Xu, L.; Liang, C.; Ngo, K.; Parker, R.G.; Zuo, L. A compact mechanical power take-off for wave energy converters: Design, analysis, and test verification. *Appl. Energy* **2020**, *278*, 115459. [CrossRef]
10. Blanco, M.; Torres, J.; Santos-Herrán, M.; García-Tabarés, L.; Navarro, G.; Nájera, J.; Ramírez, D.; Lafoz, M. Recent advances in direct-drive power take-off (DDPTO) systems for wave energy converters based on switched reluctance machines (SRM). *Ocean Wave Energy Syst. Hydrodyn. Power Takeoff Control Syst.* **2021**, 487–532. [CrossRef]
11. Simmons, J.W.; Van de Ven, J.D. A Comparison of Power Take-Off Architectures for Wave-Powered Reverse Osmosis Desalination of Seawater with Co-Production of Electricity. *Energies* **2023**, *16*, 7381. [CrossRef]
12. Davies, P.A. Wave-powered desalination: Resource assessment and review of technology. *Desalination* **2005**, *186*, 97–109. [CrossRef]
13. Folley, M.; Suarez, B.P.; Whittaker, T. An autonomous wave-powered desalination system. *Desalination* **2008**, *220*, 412–421. [CrossRef]
14. Yu, Y.H.; Jenne, D. Analysis of a wave-powered, reverse-osmosis system and its economic availability in the United States. In Proceedings of the International Conference on Offshore Mechanics and Arctic Engineering. American Society of Mechanical Engineers, Trondheim, Norway, 25–30 June 2017; Volume 57786, p. V010T09A032. [CrossRef]
15. Sharmila, N.; Jalihal, P.; Swamy, A.; Ravindran, M. Wave powered desalination system. *Energy* **2004**, *29*, 1659–1672. [CrossRef]
16. Cheddie, D.; Maharajh, A.; Ramkhalawan, A.; Persad, P. Transient modeling of wave powered reverse osmosis. *Desalination* **2010**, *260*, 153–160. [CrossRef]
17. Yu, Y.H.; Jenne, D. Numerical modeling and dynamic analysis of a wave-powered reverse-osmosis system. *J. Mar. Sci. Eng.* **2018**, *6*, 132. [CrossRef]
18. Brodersen, K.M.; Bywater, E.A.; Lanter, A.M.; Schennum, H.H.; Furia, K.N.; Sheth, M.K.; Kiefer, N.S.; Cafferty, B.K.; Rao, A.K.; Garcia, J.M.; et al. Direct-drive ocean wave-powered batch reverse osmosis. *Desalination* **2022**, *523*, 115393. [CrossRef]
19. Folley, M.; Whittaker, T. The cost of water from an autonomous wave-powered desalination plant. *Renew. Energy* **2009**, *34*, 75–81. [CrossRef]
20. Mi, J.; Wu, X.; Capper, J.; Li, X.; Shalaby, A.; Wang, R.; Lin, S.; Hajj, M.; Zuo, L. Experimental investigation of a reverse osmosis desalination system directly powered by wave energy. *Appl. Energy* **2023**, *343*, 121194. [CrossRef]
21. Leijon, J.; Salar, D.; Engström, J.; Leijon, M.; Boström, C. Variable renewable energy sources for powering reverse osmosis desalination, with a case study of wave powered desalination for Kilifi, Kenya. *Desalination* **2020**, *494*, 114669. [CrossRef]
22. Falcão, A.F.d.O. Modelling and control of oscillating-body wave energy converters with hydraulic power take-off and gas accumulator. *Ocean Eng.* **2007**, *34*, 2021–2032. [CrossRef]
23. Li, W.; Zhang, Z.; Liu, T.; Cao, H.; Ni, T.; Wang, Y. Analysis of and experimental research on a hydraulic traction system based on a digital hydraulic transformer. *Sensors* **2022**, *22*, 3624. [CrossRef]
24. Kogler, H. *The Hydraulic Buck Converter—Conceptual Study and Experiments*; Trauner: Linz, Austria, 2012.
25. Yuan, C.; Pan, M.; Plummer, A. A review of switched inertance hydraulic converter technology. *J. Dyn. Syst. Meas. Control* **2020**, *142*, 050801. [CrossRef]
26. Cao, J.; Gu, L.; Wang, F.; Qiu, M. Switchmode hydraulic power supply theory. In Proceedings of the ASME International Mechanical Engineering Congress and Exposition, Orlando, FL, USA, 5–11 November 2005; Volume 42207, pp. 85–91. [CrossRef]
27. Simmons, J.W.; Van de Ven, J.D. Switch-mode power transformer in a wave-powered, reverse osmosis desalination plant. In *Proceedings of the Fluid Power Systems Technology*; American Society of Mechanical Engineers: New York, NY, USA, 2019; Volume 59339, p. V001T01A020. [CrossRef]
28. Brown, F.; Tentarelli, S.; Ramachandran, S. A hydraulic rotary switched-inertance servo-transformer. *J. Dyn. Sys. Meas. Control* **1988**, *110*, 144–150. [CrossRef]
29. Katz, A.A.; Van de Ven, J.D. Design of a high-speed on-off valve. In Proceedings of the ASME International Mechanical Engineering Congress and Exposition, Lake Buena Vista, FL, USA, 13–19 November 2009; Volume 43833, pp. 237–246. [CrossRef]
30. Yokota, S.; Akutu, K. A fast-acting electro-hydraulic digital transducer: A poppet-type on-off valve using a multilayered piezoelectric device. *JSME Int. J. Ser. 2 Fluids Eng. Heat Transf. Power Combust. Thermophys. Prop.* **1991**, *34*, 489–495. [CrossRef]
31. Ouyang, X.; Yang, H.; Jiang, H.; Johnston, D.N. Simulation of Piezoelectric high-speed digital valves. In Proceedings of the Bath/ASME Symposium on Fluid Power and Motion Control, Bath, UK, 10–12 September 2008. [CrossRef]

32. Manhartsgruber, B. A hydraulic control valve for PWM actuation at 400 Hz. In *Power Transmission and Motion Control*; Centre for Power Transmission and Motion Control: Bath, UK, 2006; pp. 373–385.
33. Danfoss. APP Pumps, APP 26/1500. Product no. 180B3057. Available online: https://store.danfoss.com/fi/en/High-pressure-pumps/Desalination/Pumps/Pumps-for-sea-water/APP-0-6-46-pumps/APP-pumps%2C-APP-26-1500/p/180B3057 (accessed on 18 May 2026).
34. Cho, B.H.; Lee, H.W.; Oh, J.S. *Estimation Technique of Air Content in Automatic Transmission Fluid by Measuring Effective Bulk Modulus*; SAE Mobilus: Warrendale, PA, USA, 2000.

Disclaimer/Publisher's Note: The statements, opinions and data contained in all publications are solely those of the individual author(s) and contributor(s) and not of MDPI and/or the editor(s). MDPI and/or the editor(s) disclaim responsibility for any injury to people or property resulting from any ideas, methods, instructions or products referred to in the content.

https://doi.org/10.3390/en19112692

energies

MDPI

Article

Fluid-Driven Opposed-Piston Pumps for Dense-Phase CO_2 Injection: Direct Force Coupling and Energy Efficiency Analysis

Xiaoyu Wang [1,2], Hongtao Chen [2,3], Hongbao Liang [1,2,*], Yang Liu [1,2], Zhanheng Ma [2,4], Haibo Lin [2,4] and Wanchun Sun [2,5]

[1] Machinery Institute of Science and Engineering, Northeast Petroleum University, Daqing 163318, China
[2] Carbon Peak, Carbon Neutrality, and Environmental Protection Technology Research Center, Daqing 163318, China
[3] Startwell Intelligent Oil Recovery Technology Co., Ltd., Changchun 130102, China
[4] China National Petroleum Corporation Jilin Oilfield Branch Survey and Design Institute, Songyuan 138000, China
[5] Water Pump Factory of Boshan, Zibo 255202, China
* Correspondence: lhbao1966@163.com; Tel.: +86-13045056869

Abstract

Large-scale dense-phase carbon dioxide (CO_2) injection is an energy-intensive process in the carbon capture, utilization, and storage (CCUS) value chain. To address insufficient utilization of inlet pressure potential energy and sealing/friction losses of conventional reciprocating pumps under high-base-pressure dense-phase CO_2 transport conditions, this study develops a dense-phase CO_2-oriented structural optimization scheme for a hydraulically driven opposed-piston reciprocating pump based on force-coupling. A dynamic model was established to clarify the in situ recovery mechanism by which inlet pressure potential energy is converted into auxiliary thrust, enabling the drive load to shift from absolute pressure to net pressure difference. Simulation results show that under the rated 8 MPa inlet and 25 MPa discharge condition, the optimized opposed-piston configuration reduces peak driving oil pressure by 31.39% compared with the non-opposed reference configuration. Field reliability operation data show an average normalized specific energy consumption of 0.422 kWh/(MPa·m^3) during the selected 24 h continuous operating period. The optimized configuration improves inlet-pressure utilization and reduces hydraulic power demand under high-base-pressure dense-phase CO_2 injection conditions, providing theoretical support and engineering reference for low-energy CCUS injection systems.

Keywords: dense-phase CO_2 injection; opposed reciprocating pump; structural optimization; suction-pressure-assisted load compensation; CCUS

1. Introduction

As the commercialization of large-scale CCUS technology accelerates, high-pressure fluid compression equipment—serving as the core power unit of the entire CCUS chain [1–3]—naturally makes energy efficiency and operational reliability the most critical factors determining the system's economic viability over its entire lifecycle [4,5]. More importantly, dense-phase CO_2 exhibits several characteristic properties, including low viscosity, compressibility, and thermal sensitivity [6–8]. Consequently, traditional gas injection equipment faces significant challenges regarding flow assurance and operational stability when transporting dense-phase CO_2 over long distances [9–11]. Currently,

research in both academia and industry on this issue has clearly focused on three directions: performance optimization of traditional three-plunger reciprocating pumps, fundamental research on the mechanisms of high-pressure CO_2 fluid transport, and innovative design of new hydraulic drive topologies.

Thanks to their proven manufacturing processes and high-pressure output capabilities, traditional multi-plunger reciprocating pumps have long held a dominant position in the field of pressure-boosted injection [12,13]; however, the inherent kinematic characteristics of the crank-connecting rod mechanism make pressure pulsations the most direct and fundamental cause of pipeline vibration [14]. Aakre et al. [14,15] provided a clear and logical explanation of the mechanism by which multi-cylinder configurations suppress pressure pulsations: although multi-cylinder designs theoretically help offset some higher-order harmonics, the compressibility of the fluid when transporting supercritical CO_2 significantly amplifies the pulsation amplitude; therefore, passive buffering devices are generally required to mitigate this effect.

More importantly, traditional mechanical drive trains exhibit significant friction-related deficiencies when handling high-pressure fluids [16]. Li et al. [17] conducted an extremely thorough and rigorous analysis of the mechanisms of internal friction power loss in plunger pumps, clearly and accurately identifying the periodic lateral forces generated by the connecting rod's angular displacement as the root cause of seal wear and reduced mechanical efficiency. For low-viscosity CO_2 media, this lateral load disrupts the normal formation of the oil film, leading to a sharp increase in boundary friction, which severely compromises both pump lifespan and energy efficiency. Even more concerning is that the unique thermophysical behavior of CO_2 itself causes volumetric efficiency to deteriorate sharply with changes in operating conditions [18–20]. Unlike conventional fluids, the density and viscosity of dense-phase CO_2 are highly sensitive to thermodynamic parameters [21,22]. Ma et al. [23,24] provide a highly intuitive and convincing explanation for this: the high compressibility of CO_2 inevitably results in a pronounced "compression lag" effect, causing the effective displacement to decrease significantly.

Due to the limitations of mechanical drive chains in terms of dynamic characteristics and energy efficiency, opposed-piston and hydraulic-drive configurations have been widely investigated in recent years. Liu et al. [25,26] analyzed the pressure-bearing capacity and energy-efficiency characteristics of opposed-piston reciprocating pumps, showing that opposed layouts can improve load balance and operating stability under suitable conditions. Li et al. [27] designed a novel hydraulic oil-extraction pump unit suitable for oilfield conditions, systematically and thoroughly demonstrating that a symmetrical structural layout facilitates mutual balancing of hydraulic-end loads, thereby offering superior energy efficiency compared to traditional units. More notably, Qi et al. [28] proposed an active control scheme based on hydraulic oil supply regulation to address the issue of pressure mismatch during multistage compression, successfully achieving adaptive balancing of inter-stage pressure ratios and significantly enhancing the system's thermodynamic stability.

Current studies on hydraulic and double-acting reciprocating pumps mainly focus on general-purpose applications, such as flow/pressure pulsation suppression, dynamic response optimization, and load balancing [29]. However, the use of opposed-cylinder force coupling to utilize the 6–8 MPa suction pressure of dense-phase CO_2 as a load-compensation term during high-pressure injection has not been sufficiently clarified. In this scenario, the inlet pressure of pipeline CO_2 can reach 6–8 MPa, while conventional triplex plunger pumps and reciprocating pumps usually suffer from insufficient utilization of inlet pressure, high driving energy consumption, and limited pump efficiency. Therefore, low-energy CO_2 pressurization and injection remain key technical challenges.

https://doi.org/10.3390/en19122886

To address these issues, this study develops a dense-phase CO_2-oriented structural optimization of a conventional hydraulically driven opposed-piston reciprocating pump. The optimized configuration introduces force-transmission cylinders, vertical CO_2 cylinders, rodless pistons, and an ionic-liquid isolation layer to improve force transmission, sealing performance, and volumetric efficiency under high-base-pressure injection conditions.

In this configuration, the high suction pressure of pipeline CO_2 is introduced into the force balance of the opposed piston assembly and provides auxiliary thrust for the compression process of the opposite cylinder. Consequently, the hydraulic load is transformed from a discharge-pressure-dominated load to an inlet-outlet net-pressure-difference-dominated load, thereby reducing the required hydraulic driving pressure and energy input. The force-transmission cylinders further convert horizontal hydraulic actuation into vertical CO_2 compression, providing the structural basis for stable ionic-liquid coverage above the rodless piston under low-viscosity dense-phase CO_2 conditions.

In summary, this paper presents a structural optimization and performance evaluation of a hydraulically driven opposed-piston reciprocating pump for high-base-pressure dense-phase CO_2 injection. The work focuses on suction-pressure-assisted load compensation, vertical force transmission through force-transmission cylinders, and ionic-liquid-assisted sealing. By combining dynamic modeling, AMESim simulation, and field reliability operation data, this study supplements existing opposed-piston pump research and provides theoretical and engineering references for high-base-pressure fluid injection systems.

(1) A suction-pressure-assisted load-compensation mechanism is established for high-base-pressure dense-phase CO_2 injection. The high inlet pressure of 6–8 MPa inherent to dense-phase CO_2 in the pipeline is utilized to participate in the force balance of the opposite compression cylinder, thereby reducing the hydraulic load required for discharge.
(2) A structural optimization scheme is developed by integrating a horizontal hydraulic cylinder, intermediate force-transmission cylinders, vertical CO_2 cylinders, rodless pistons, and ionic-liquid isolation. This layout converts horizontal hydraulic actuation into vertical CO_2 compression, reduces lateral loading on the sealing interface, and provides the structural basis for improved sealing and volumetric efficiency.
(3) The energy-saving effect of the optimized opposed-piston configuration under high-base-pressure conditions is evaluated by dynamic modeling, AMESim simulation, and field reliability operation data. The results clarify how the suction pressure of dense-phase CO_2 participates in the force balance of the opposite compression cylinder and reduces the hydraulic power demand.

2. Structural Design

2.1. Structural Characteristics of the Opposed Reciprocating Pump

Figure 1 shows the overall structure of a hydraulically driven opposed-type dense-phase CO_2 reciprocating pump. The characteristics of this pump during the transmission and pressurization processes can be summarized as follows:

(1) During the pressurization process, the hydraulic direct-drive mechanism replaces the traditional crank–connecting rod mechanism. By adapting the inherent force-coupling characteristics of the opposed structure to high-base-pressure dense-phase CO_2 injection, the inlet pressure is introduced as an auxiliary thrust for the opposite compression chamber, thereby improving the utilization of suction-pressure potential energy. The hydraulic transmission also simplifies the mechanical structure and reduces lateral-force-related wear associated with crank–connecting rod mechanisms under high-pressure conditions.

https://doi.org/10.3390/en19122886

(2) The design combines a rodless piston with ionic fluid isolation, reliably physically separating the hydraulic oil from the dense-phase CO_2 medium and preventing medium contamination. Meanwhile, the relatively high viscosity of the ionic liquid provides auxiliary sealing and lubrication, helping to mitigate leakage and dry-friction problems caused by the low viscosity of dense-phase CO_2.

(3) Considering the control characteristics of the hydraulic system and the compressibility of dense-phase CO_2, the piston motion follows a constant-speed and smooth-reversal profile. Simulation results indicate that this hydraulic constant-speed profile is more stable than a conventional sinusoidal motion profile. Combined with the force-coupling mechanism, the hydraulic cylinder mainly compensates for the inlet–outlet net pressure load, which reduces the required driving pressure and supports efficient high-pressure injection.

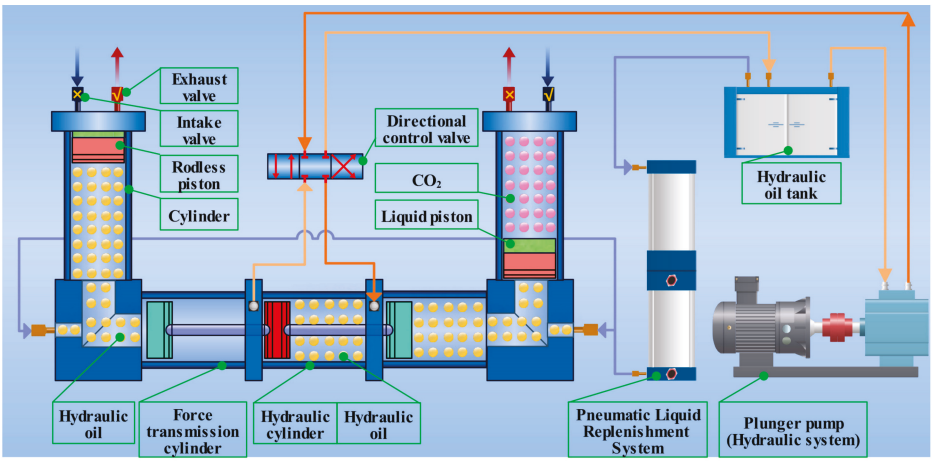


Figure 1. Schematic diagram of the opposed reciprocating pump.

2.2. Detailed Structural Design

Based on the conventional opposed-piston layout, a single-stage dense-phase CO_2 injection pump structure was optimized by introducing force-transmission cylinders, vertical CO_2 cylinders, rodless pistons, and an ionic-liquid isolation layer. Figure 1 shows the detailed structure of the core unit of the injection pump, which mainly consists of two parts: a hydraulic drive unit and an opposed pressurization structure. The entire pump body adopts a modular design to meet the delivery requirements of high-pressure dense-phase fluids. The pressurization section of the core unit includes a main hydraulic cylinder, a force transmission cylinder, a CO_2 cylinder, a rodless piston assembly, and corresponding sealing assemblies.

Taking a single reciprocating motion as an example, the pressurization process is driven by the double-acting hydraulic cylinder in the middle. When the piston rod of the hydraulic cylinder moves to one side, it pushes the hydraulic oil in the force transmission cylinder on that side into the bottom of the vertical CO_2 cylinder, thereby driving the rodless piston upward to compress the dense-phase CO_2. At the same time, the opposite CO_2 cylinder is in the suction stroke, and the high-pressure intake gas pushes the piston downward, assisting the retraction of the main hydraulic cylinder through hydraulic transmission, thus achieving direct force coupling.

As shown in Figure 1, the overall structure of the drive system is a hydraulically direct-driven opposed mechanism. The middle hydraulic cylinder is connected to the force-transfer pistons on both sides through a rigid piston rod, realizing bidirectional power transmission. This arrangement reduces lateral loading, improves force balance, and maintains a compact structural layout.

https://doi.org/10.3390/en19122886

The force-transmission cylinder is the key component that links the horizontal hydraulic cylinder and the vertical CO_2 cylinder. During operation, the central hydraulic cylinder drives the piston in the force-transmission cylinder, and the hydraulic oil in this cylinder transmits pressure to the bottom of the rodless piston in the vertical CO_2 cylinder. In this way, the horizontal hydraulic drive is converted into the vertical compression motion of CO_2 without using a crank-link mechanism. This arrangement allows the CO_2 cylinder to be installed vertically, providing the structural basis for maintaining a stable ionic-liquid layer above the rodless piston.

During normal operation, to address the problems of low viscosity and poor lubricity of dense-phase CO_2, a layer of ionic liquid is arranged above the rodless piston in the vertical cylinder. As a liquid seal and lubricant, the ionic liquid helps suppress gas leakage and improve the friction condition between the piston and the cylinder wall. Meanwhile, the chemical stability of the ionic liquid must be ensured to prevent reaction or emulsification with high-pressure CO_2.

Considering the possible dissolution of CO_2 in ionic liquids under high pressure [30], the ionic liquid layer should not be regarded as an independent energy-saving mechanism in this study. Its function is limited to sealing, lubrication, and medium isolation. During cyclic pressure variation, CO_2 desorption may disturb the gas–liquid interface and increase the risk of droplet entrainment. Therefore, the ionic liquid should be selected with low CO_2 solubility, high viscosity, low volatility, and good chemical compatibility with dense-phase CO_2. In addition, the vertical cylinder arrangement, sufficient liquid-layer height, and discharge-side gas–liquid separation are required to suppress liquid carryover through the discharge valve.

Figure 2 shows the schematic diagram of the hydraulic control system for the injection pump. To ensure smooth piston reversal at each stroke and improve the utilization of suction-pressure potential energy, the hydraulic system is designed with inlet–outlet pressure-difference sensing and commutation logic.

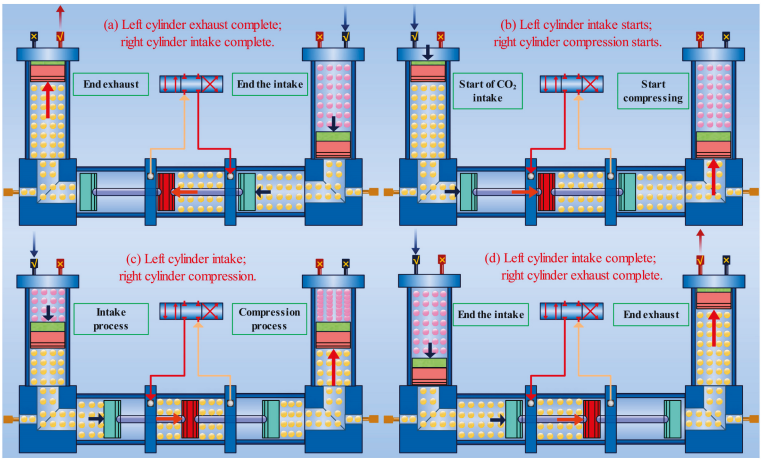


Figure 2. Schematic diagram of the injection pump operating process. (**a**) Left cylinder exhaust complete; right cylinder intake complete, (**b**) Left cylinder intake starts; right cylinder compression starts, (**c**) Left cylinder intake; right cylinder compression, (**d**) Left cylinder intake complete; right cylinder exhaust complete.

Figure 2a shows that the left cylinder has just completed the discharge process, and the pressurization of the right cylinder begins. As shown in Figure 2b, the hydraulic power unit starts, and high-pressure oil enters the left chamber of the middle hydraulic cylinder, pushing the piston rod of the hydraulic cylinder to move rightward. At the same time, the intake valve of the left cylinder opens to start the intake process.

https://doi.org/10.3390/en19122886

As shown in Figure 2c, the rodless piston in the left vertical cylinder moves downward under the intake pressure of 6–8 MPa. Through the hydraulic oil medium below the piston, the force is applied to the piston of the left force transmission cylinder, which couples with the thrust provided by the hydraulic oil of the hydraulic cylinder to jointly drive the hydraulic cylinder piston to move rightward. The oil in the right force transmission cylinder is squeezed into the right vertical cylinder, pushing the rodless piston upward to compress the CO_2 in the cylinder.

As shown in Figure 2d, the piston of the left cylinder reaches the bottom dead center to complete the intake process, while the piston of the right cylinder reaches the top dead center to complete the discharge process synchronously. The piston of the hydraulic cylinder and the pistons of both force transmission cylinders all reach the rightmost ends of the corresponding cylinders, triggering the position sensor at the right end of the hydraulic cylinder. At this moment, the directional control valve starts to operate, and the flow direction of the hydraulic oil is switched to "outlet left, inlet right", initiating the compression process of the left cylinder and the intake process of the right cylinder. The specific technical parameters are listed in Table 1.

Table 1. Main technical parameters of the hydraulically driven opposed reciprocating pump.

Parameter	Value	Unit
Cylinder stroke frequency	10.19	cpm
Rated Inlet Pressure	6.00~8.00	MPa
Rated Discharge Pressure	25.00	MPa
Design Flow Rate	15.00	m^3/h
Motor Frequency	50.00	Hz
Rated Motor Power	110.00	kW
Driving Medium	Hydraulic Oil	/
Working Fluid	Dense-phase CO_2	/

For high-base-pressure dense-phase CO_2 injection, the essential energy-saving feature of the optimized structure is that the suction stroke of one CO_2 cylinder is synchronized with the compression stroke of the opposite cylinder. The 6–8 MPa inlet pressure acts on the intake-side piston and is transmitted through the force-transmission cylinder and coupled piston assembly, thereby providing auxiliary thrust for the opposite compression process. As a result, the hydraulic actuator mainly compensates for the inlet–outlet net pressure load rather than the full discharge-pressure load, which reduces the required driving pressure and hydraulic power input.

To prevent the rodless piston from striking the cylinder head or cylinder bottom at high speed at the end of the stroke, a cushion circuit is integrated into the hydraulic system. An air-controlled oil replenishment system is installed on both sides of the force transmission cylinder (see Figure 1), which can monitor and supplement the hydraulic oil pressure in the force transmission cylinder in real time.

2.3. Structural Differences from the Non-Opposed Reference Pump

A conventional non-opposed reciprocating pump is shown in Figure 3. Compared with the non-opposed reference pump, the optimized opposed-piston configuration offers the following advantages under dense-phase CO_2 injection conditions:

(1) Conventional non-opposed hydraulic reciprocating pumps typically consist of a single hydraulic cylinder and a single CO_2 cylinder connected in series. Although this design is simpler than a mechanical crank mechanism, it has low space utilization, discharges gas only during half a working cycle, and exhibits significant output pulsation from the single cylinder. The optimized opposed-piston structure retains the alternating two-cylinder operation of conventional opposed pumps, while introducing force-

https://doi.org/10.3390/en19122886

transmission cylinders and vertical CO_2 cylinders to adapt the layout to dense-phase CO_2 injection. This configuration increases the effective displacement, improves space utilization, and enhances the continuity of high-pressure dense-phase CO_2 discharge.

(2) Although both designs employ hydraulic drive to eliminate the lateral friction found in traditional mechanical pumps, the non-opposed configuration faces significant load fluctuations during the compression and suction phases. The hydraulic transmission system must frequently withstand unidirectional high-pressure shocks, which can easily induce low-frequency vibrations and accelerate fatigue wear of the sealing components. The optimized structure uses the opposed layout to balance alternating cylinder loads, while the force-transmission cylinders convert the horizontal hydraulic drive into vertical CO_2 compression and reduce lateral loading on the sealing interface. This structure helps reduce inertial shocks and improve the smoothness of linear piston motion, which is beneficial for reducing wear of the sealing components.

(3) In a non-opposed single-cylinder design, the inlet pressure potential energy associated with the 6–8 MPa high-base-pressure CO_2 stream cannot be effectively converted into compression assistance. During the compression stroke, the hydraulic main pump overcomes absolute exhaust back pressure. The opposed reciprocating pump utilizes a force-coupling mechanism to synchronize the suction process on one side with the compression process on the other. The inlet pressure of the high-base-pressure CO_2 stream is introduced into the coupled force balance and acts as an auxiliary thrust for the opposite compression stroke. This reduces the energy input required by the main pump and lowers the system's energy consumption.

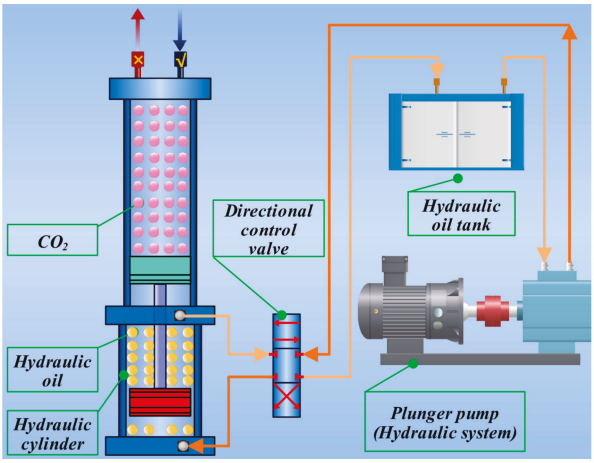


Figure 3. Schematic diagram of a non-opposed reciprocating pump.

3. Working Principle and Theoretical Analysis of the Injection Pump

3.1. Theoretical Mass Flow Rate Model

The discharge capacity of the injection pump is determined by the cylinder geometry and the piston reciprocation frequency. Dense-phase CO_2 in the pressure range of 6–25 MPa exhibits liquid-like high-density characteristics, while its compressibility remains sensitive to pressure and temperature variations. Therefore, to avoid numerical oscillations caused by nonlinear fluid properties and ensure good convergence of the model, this paper reasonably neglects the second-order nonlinear variation of density and treats the medium as a linearly compressible fluid based on the effective bulk modulus K_{eff}. Accordingly, the established theoretical mass flow rate model m_{th} still strictly complies with the basic principles of positive displacement pumps [31]:

$$m_{th} = \rho_{in} \cdot A_{gas} \cdot S \cdot f \cdot n \quad (1)$$

Considering the volumetric loss, the actual discharge flow rate m_{act} needs to be corrected by the volumetric efficiency η_v [31]:

$$\eta_v = 1 - \varepsilon(\frac{\rho_{out}}{\rho_{in}} - 1) \tag{2}$$

ρ_{in} and ρ_{out} denote the suction and discharge thermodynamic-state densities of CO_2, respectively, which are determined by the corresponding pressure-temperature conditions. They are not instantaneous densities at a specific moment during the discharge process. The influence of residual CO_2 expansion and compression hysteresis in the clearance volume is accounted for by the relative clearance volume coefficient (ε).

For the ionic-liquid isolation structure proposed in this study, CO_2 remains the working medium in the volumetric-efficiency model; therefore, the form of Equation (2) remains applicable. The ionic liquid mainly modifies the effective gas-side clearance volume and leakage boundary, and ε is therefore interpreted as the effective clearance volume coefficient after considering the ionic-liquid isolation layer.

3.2. Energy Efficiency Evolution Mechanism and Energy Flow Model

The core of the proposed optimization lies in adapting the force-coupling mechanism of the opposed configuration to utilize the suction pressure potential of high-base-pressure dense-phase CO_2. Due to the rigidly coupled opposed configuration, the intake-side pressure acts as a load-compensation term in the force balance of the opposite compression cylinder. The instantaneous power $P_{oil}(t)$ required by the hydraulic system is given by:

$$P_{oil}(t) = \frac{[p_{out}(t) - p_{in}] \cdot A_{gas} \cdot v(t)}{\eta_h} \tag{3}$$

In Equation (3), η_h denotes the overall hydraulic transmission efficiency from the hydraulic pump outlet to the actuator. It accounts for the combined influence of pump mechanical loss, volumetric loss, valve throttling loss, and pipeline pressure loss.

The normalized specific energy consumption (e_s) of the hydraulic system is defined as the ratio of the steady-state peak hydraulic output power to the product of the inlet–outlet net pressure difference and the volumetric flow rate:

$$e_s = \frac{P_{oil}(t)}{Q_v \cdot (p_{out} - p_{in})} \tag{4}$$

When electrical energy is converted into the output power of a reciprocating pump drive system, the energy transmission efficiency of the motor and the oil pump must be taken into account. The actual active power input to the drive motor is determined by the hydraulic power and the mechanical/volumetric transmission efficiencies at each stage:

$$P_{in}(t) = \frac{P_{oil}(t)}{\eta_m \times \eta_p} \tag{5}$$

Equations (4) and (5) can be used to derive the normalized specific energy consumption (e_n) of a reciprocating pump system. This parameter quantifies the actual electrical energy required to compress 1 m^3 of fluid and overcome a pressure difference of 1 MPa.

$$e_n = \frac{P_{in}(t)}{Q_v \cdot (p_{out} - p_{in})} \tag{6}$$

https://doi.org/10.3390/en19122886

3.3. Dynamic Characteristic Analysis of the Piston Assembly

In this design, the piston assembly consists of a central hydraulic piston, a force-transmitting piston rod, and rodless pistons located in the cylinders on either side. To quantify the energy-saving mechanism of the optimized opposed-piston configuration under a 6–8 MPa high-base-pressure suction condition, this section derives the dynamic equilibrium equations.

The optimized opposed-cylinder configuration retains the inherent force-coupling feature of opposed pumps and adapts it to high-base-pressure dense-phase CO_2 injection. Because the suction cylinder and compression cylinder are coupled through the piston assembly and the force-transmission cylinders, the 6–8 MPa pressure on the suction side is introduced into the force balance of the opposite compression cylinder. The suction-side pressure acts as a load-compensation term rather than an independent energy source.

Therefore, the hydraulic pressure (p_{oil}) required by the actuator is governed by both the inlet-outlet pressure difference and the area ratio between the CO_2 cylinder and the hydraulic cylinder.

For the opposed configuration, when the piston assembly moves rightward, the force balance can be written as:

$$M\ddot{x} = p_{oil}A_{hyd} + p_{in}A_{gas} - p_{out}A_{gas} - F_f \tag{7}$$

where F_f is treated as the lumped friction resistance of the moving assembly, including the sliding friction in the hydraulic cylinder, the force-transmission cylinder, and the CO_2 cylinder sealing interface.

Thus, the hydraulic oil pressure required by the opposed configuration is obtained as:

$$p_{oil,op} = \frac{(p_{out} - p_{in})A_{gas} + F_f + M\ddot{x}}{A_{hyd}} \tag{8}$$

For a non-opposed hydraulic reciprocating pump with the same CO_2 cylinder and hydraulic cylinder dimensions, the suction-side compensation term does not exist. The required hydraulic oil pressure can therefore be expressed as:

$$p_{oil,no} = \frac{p_{out}A_{gas} + F_f + M\ddot{x}}{A_{hyd}} \tag{9}$$

Equations (8) and (9) indicate that the maximum required hydraulic pressure is not determined by the discharge pressure alone, but by the gas-side pressure load transmitted through the effective area ratio (A_{gas}/A_{hyd}). For the same CO_2 cylinder and hydraulic cylinder dimensions, the opposed configuration introduces the suction-pressure term ($p_{in} \cdot A_{gas}$) into the coupled force balance, whereas this term is absent in the non-opposed reference pump. Therefore, the suction pressure acts as a load-compensation term under a specified cylinder-area ratio, rather than as an independent energy source. As a result, the hydraulic load is transformed from a discharge-pressure-dominated load to an inlet-outlet net-pressure-difference-dominated load.

4. Results and Discussions

4.1. Simulation Model Establishment and Parameter Setting

In this study, a full-system model of the injection pump was constructed using the hydraulic and mechanical libraries within the AMESim 2020.1 simulation environment. Given that this study focuses on the force transmission mechanism of the opposed-cylinder configuration, the model employs an equivalent fluid modeling approach. In the simulation,

https://doi.org/10.3390/en19122886

a hydraulic fluid with equivalent elastic modulus properties was used to replace the dense-phase CO_2 medium, with the bulk modulus set to match the average modulus of CO_2 within the operating temperature and pressure range. The core components of the model include a variable-displacement hydraulic pump, a three-position four-way electro-hydraulic directional control valve, a central double-acting hydraulic cylinder, a force-transmitting cylinder, and two opposing cylinders on either side. Each cylinder is equipped with an intake and exhaust check valve, and the opening and closing of these valves are controlled by pressure. The main simulation boundary conditions are set as shown in Table 2, and the simulation model is illustrated in Figure 4.

Table 2. Key parameters and boundary conditions for AMESim dynamic simulation.

Parameter	Value	Description
CO_2 cylinder bore	250.00 mm	
CO_2 cylinder stroke	500.00 mm	
Force cylinder bore	300.00 mm	
Force cylinder stroke	350.00 mm	
Hydraulic cylinder bore	300.00 mm	
Hydraulic cylinder stroke	350.00 mm	
Cylinder piston speed	0.102 m/s	Constant speed phase
Simulation step	10^{-2} s	Fixed time step
Oil bulk modulus	1700.00 MPa	
CO_2 bulk modulus	120.00~300.00 MPa	
Inlet pressure	6.00~8.00 MPa	
Outlet pressure	25.00 MPa	

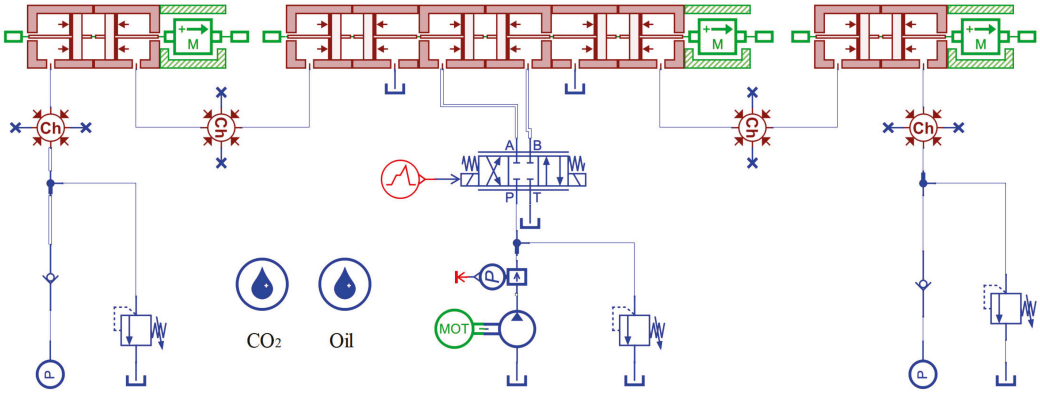


Figure 4. AMESim simulation model of the hydraulically driven opposed injection pump.

4.2. Dynamic Response and Pulsation Characteristics

4.2.1. Piston Motion and Operational Stability

In the reciprocating pump described in this paper, the constant-flow characteristics of the hydraulic system ensure that the cylinder piston moves steadily and at a uniform speed throughout the entire main compression stroke, resulting in a trapezoidal distribution of piston displacement. This long-stroke constant-speed characteristic effectively suppresses the violent fluid fluctuations caused by changes in the volume of the compressible medium.

Figure 5a,b illustrates the kinematic characteristics of a complete reciprocating cycle in an opposed-piston reciprocating pump. The piston's uniform motion provides stable kinematic conditions for pressure transfer and force coupling during the reciprocating cycle. The piston's uniform main power stroke lasts 4.8 s, and the directional control valve's response time is 0.2 s. A slight displacement lag effectively prevents high-pressure hydraulic shock.

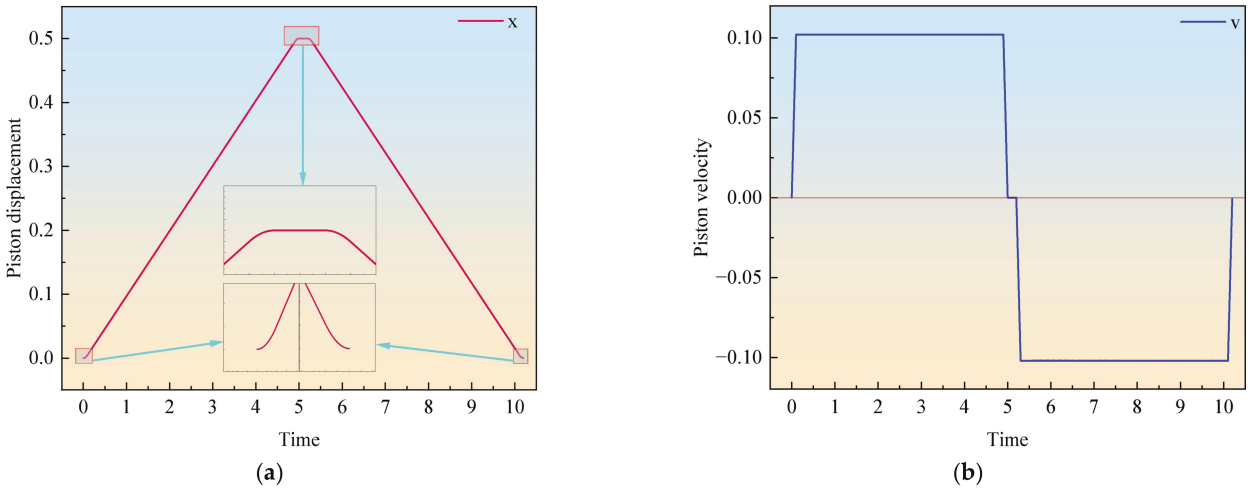


Figure 5. Cylinder piston motion curves: (**a**) Cylinder piston displacement curve. (**b**) Cylinder piston velocity curve.

4.2.2. Pressure and Discharge Flow Characteristics

To further characterize the complete-cycle dynamic response of the optimized opposed-piston pump, the time-domain pressure and discharge-flow responses under the rated 8 MPa inlet condition were compared with those of a non-opposed single-cylinder reference pump.

Figure 6 compares the cylinder pressure responses of the opposed-piston pump and the non-opposed single-cylinder reference pump under an inlet pressure of 8 MPa. In the opposed-piston pump, Cylinder B first undergoes compression and discharge. Its pressure rises from the suction-pressure level to approximately 25.11 MPa and remains at the discharge-pressure plateau from about 0.46 s to 5.20 s. During this period, Cylinder A is in the suction stroke, and its pressure is maintained near the inlet pressure of 8.03 MPa. After hydraulic reversal, Cylinder B completes the discharge stroke, enters the suction stroke, and maintains the inlet-pressure level of approximately 8 MPa. Meanwhile, Cylinder A is compressed to approximately 25.12 MPa and enters the subsequent discharge phase.

This alternating pressure phase reflects the force-coupling mechanism of the opposed-cylinder configuration. When Cylinder B performs compression and discharge, Cylinder A simultaneously executes the suction stroke. The high-base suction pressure acting on Cylinder A provides auxiliary thrust to the piston assembly, partially offsetting the discharge load of Cylinder B. After reversal, the working states of the two cylinders are exchanged, and the same force-coupling effect is produced in the opposite direction. Therefore, the gas load transmitted to the hydraulic actuator is mainly determined by the pressure difference between the discharge-side cylinder and the suction-side cylinder, rather than by the full discharge pressure. In contrast, the non-opposed single-cylinder reference pump exhibits an intermittent pressure response: the cylinder pressure rises to approximately 25.11 MPa during the compression/discharge stroke and then returns to the suction-pressure level during the return stroke. In this case, the 8 MPa inlet pressure acts only as the suction boundary and does not participate in load compensation.

Figure 7 shows the discharge flow-rate responses under the 8 MPa inlet condition. For the opposed pump, Cylinders A and B discharge alternately, with a stable instantaneous flow-rate plateau of approximately 286 L/min in each discharge stroke. Cylinder A discharges during the first half-cycle, while Cylinder B discharges after hydraulic reversal. Therefore, the total outlet flow of the opposed pump is obtained by superposing the discharge flow rates of the two cylinders at the same time instant.

https://doi.org/10.3390/en19122886

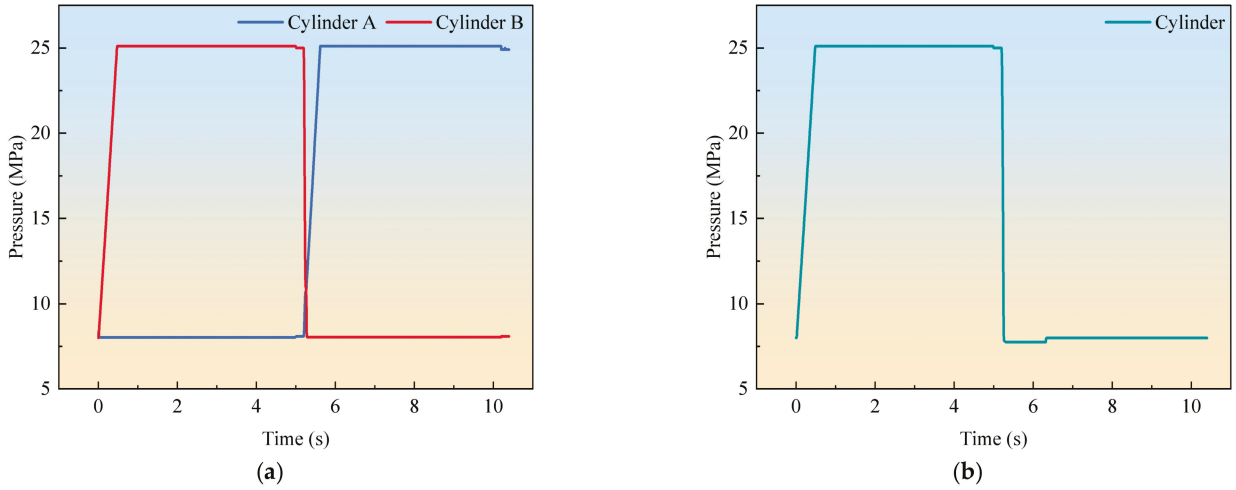


Figure 6. Comparison of CO_2 cylinder pressure responses under the 8 MPa inlet condition: (**a**) Opposed reciprocating pump. (**b**) Non-opposed reciprocating pump.

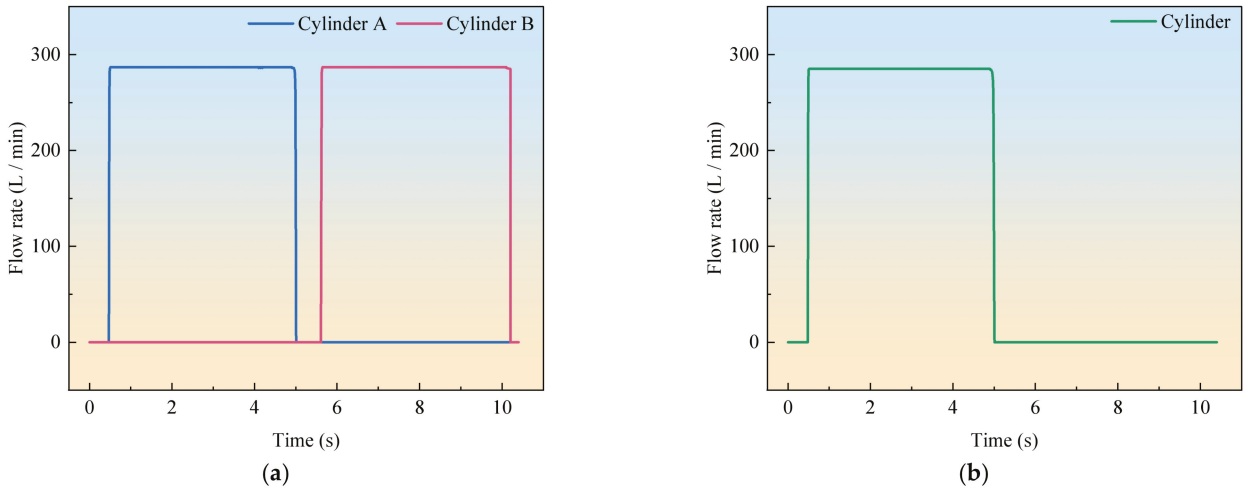


Figure 7. Comparison of discharge flow-rate responses under the 8 MPa inlet condition: (**a**) Opposed reciprocating pump; (**b**) Non-opposed reciprocating pump.

In contrast, the non-opposed single-cylinder reference pump only produces outlet flow during the discharge stroke. During the suction stroke, the discharge valve remains closed, and the outlet flow rate is zero because no discharge process occurs. Although the instantaneous discharge-flow plateaus of the two configurations are similar, the opposed pump provides two alternating discharge stages within one reciprocating cycle, thereby extending the effective discharge duration and shortening the zero-flow interval. Based on the complete-cycle superposition of the two cylinder discharge flows, the cycle-averaged outlet flow rate of the opposed pump is approximately 250 L/min, corresponding to 15 m^3/h, which agrees well with the designed flow rate of 15 m^3/h. This confirms that the phase-shifted discharge of the two cylinders weakens outlet-flow intermittency and improves discharge continuity.

4.3. Force-Coupling Mechanism and Hydraulic-Pressure Reduction

4.3.1. Pressure Response Under Different Inlet Pressures

To verify the force coupling characteristics of the opposed-cylinder configuration in this reciprocating pump, real-time response curves for the hydraulic drive pressure, intake and discharge pressures, and the intake-discharge pressure differential were extracted from the model over a single complete stroke.

Figure 8a–e illustrates the transient pressure evolution of a reciprocating pump operating under a constant discharge backpressure of 25 MPa as the inlet pressure increases from 6 MPa to 8 MPa. Within the steady-state discharge range, fluctuations in the actual hydraulic oil pressure on the drive side consistently track changes in the net pressure difference between the cylinder's intake and exhaust ports and remain below the discharge pressure at all times. This pressure inversion phenomenon confirms that the high potential energy of dense-phase CO_2 can be continuously converted into mechanical thrust and applied to the rear surface of the cylinder piston.

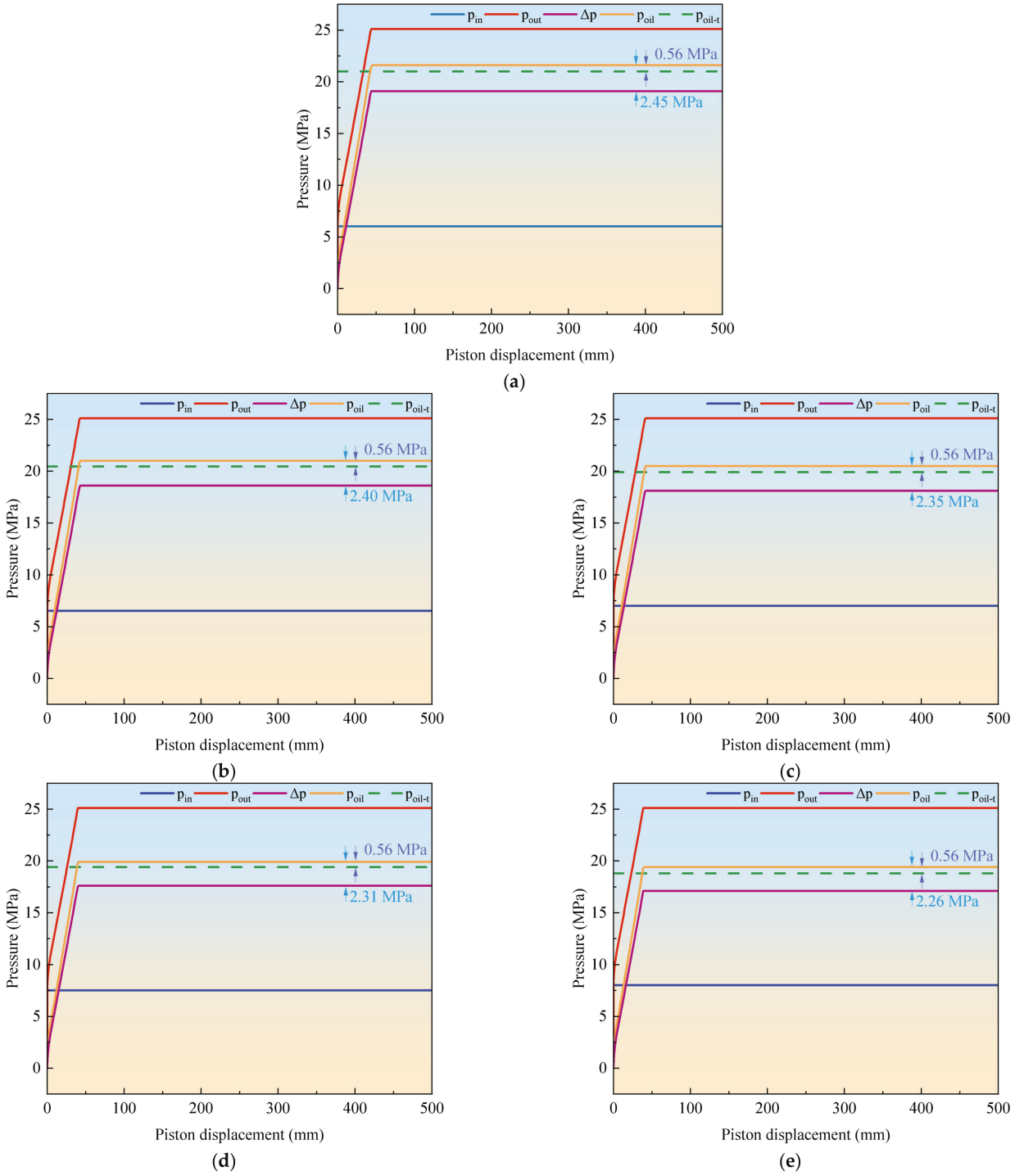


Figure 8. Comparison of cylinder pressures under different intake conditions: (**a**) 6.0 MPa inlet conditions; (**b**) 6.5 MPa inlet conditions; (**c**) 7.0 MPa inlet conditions; (**d**) 7.5 MPa inlet conditions; (**e**) 8.0 MPa inlet conditions.

https://doi.org/10.3390/en19122886

When the inlet pressure is 6 MPa, 6.5 MPa, 7 MPa, 7.5 MPa, and 8 MPa, respectively, the peak operating pressure of the hydraulic pump required to maintain system exhaust is 21.56 MPa, 21.01 MPa, 20.46 MPa, 19.91 MPa, and 19.37 MPa, respectively. The peak hydraulic pressure of the drive system gradually decreases as the inlet CO_2 pressure increases.

During the discharge strokes under these five operating conditions, the actual hydraulic oil pressure curve consistently maintains a pressure difference of approximately 0.56 MPa relative to the theoretical curve. This discrepancy is primarily attributed to the system overcoming high-pressure friction in the main sealing assembly, pressure drop due to throttling in the directional control valve, and fluid transient compression hysteresis.

4.3.2. Comparison of Driving Pressures Between Opposed and Non-Opposed Configurations

This section further compares the hydraulic oil pressure response characteristics of non-opposed and opposed configurations under different supply pressures. Figure 9a,b illustrate the pressure variation patterns of the hydraulic cylinders for both configurations under a constant exhaust load of 25 MPa.

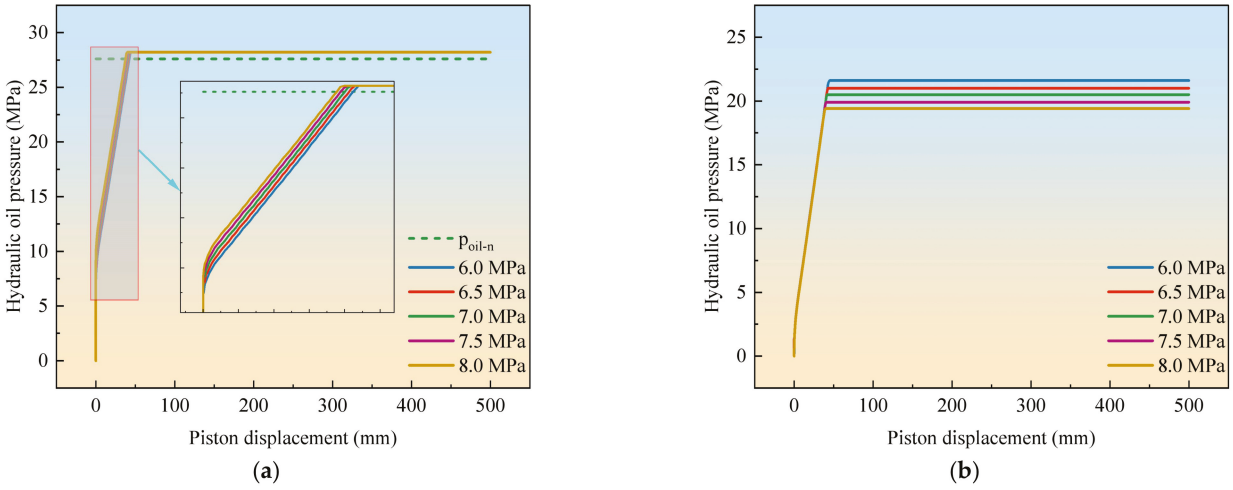


Figure 9. Comparison of hydraulic cylinder pressures under 6–8 MPa intake conditions: (**a**) Without an opposed structure. (**b**) With an opposed structure.

The simulation curve for the non-opposed structure shown in Figure 9a indicates that as the inlet CO_2 pressure increases from 6 MPa to 8 MPa, the peak pressure of the hydraulic system remains consistently around 28.23 MPa. However, as the inlet pressure rises, the initial displacement point at which the pressure begins to rise shifts, resulting in inconsistent growth curves during the compression phase, although the rate of increase remains the same.

In traditional non-opposed configurations, during the fluid displacement process, hydraulic oil from the rear of the piston flows to the low-pressure return line, and the main hydraulic pump must overcome an exhaust absolute pressure of 25 MPa as well as system friction. Therefore, regardless of how the inlet pressure changes, the load faced by the hydraulic pump remains constant at 25 MPa.

The trend of drive pressure in the opposed-cylinder configuration shown in Figure 9b differs from that of the non-opposed configuration. The pressure rise curves for the hydraulic oil remain consistent across different intake pressures, but the peak pressure achieved gradually decreases as the CO_2 source pressure increases. When the intake pressure is increased from 6 MPa to 8 MPa, the actual peak oil pressure decreases from 21.56 MPa to 19.37 MPa. This phenomenon reflects the inherent nature of direct force coupling in the opposed configuration. Through the hydraulic oil in the intermediate force-transmitting cylinder and the rigid connecting rods, the suction process of one cylinder is

synchronized with the compression process of the other, allowing the high-pressure fluid at the intake end to act directly on the back of the compression piston, converting it into forward auxiliary thrust.

This structural difference results in a shift in the driving load. While traditional designs are subjected to absolute loads, opposed-piston designs are subjected to net pressure differential loads. The opposed-piston design enables on-site recovery of potential energy; for every 0.5 MPa increase in intake pressure, the driving-end load decreases by approximately 0.55 MPa. Under the rated simulation condition of 8 MPa inlet pressure and 25 MPa discharge pressure, the opposed-piston configuration reduced the peak driving oil pressure by 31.39% compared with the non-opposed reference pump with the same CO_2 cylinder and hydraulic cylinder dimensions.

4.4. Comparative Analysis of Energy Efficiency Characteristics for Different Configurations

4.4.1. Output Power Characteristics of Non-Opposed Reciprocating Pump Drive Systems

Using AMEsim's sensor module, the output power of the hydraulic pump in a reciprocating pump drive system was monitored to investigate the evolution of the drive system's transient output power under different inlet CO_2 pressures ranging from 6 to 8 MPa.

As shown in Figure 10, under different intake pressures, the output power curves of traditional non-opposed reciprocating pumps exhibit consistent peaks during the discharge stroke, but show differences in power growth during the compression stroke. Simulation data show that under intake conditions ranging from 6 MPa to 8 MPa, the peak output power during the exhaust phase is approximately 120.62 kW. Since the hydraulic system cannot obtain force assistance from a high-pressure CO_2 stream, the main hydraulic pump must continuously bear a constant back pressure of 25 MPa during the liquid displacement and exhaust phases.

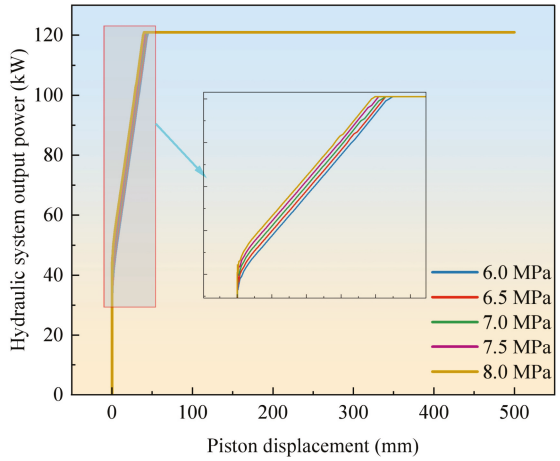


Figure 10. Output Power Curve of Hydraulic System for Non-opposed Reciprocating Pump (6~8 MPa).

During the compression stroke, as the intake base pressure increases from 6 MPa to 8 MPa, the system's pressure ratio decreases from 4.17 to 3.125. At higher initial intake pressures, the density of CO_2 inside the cylinder increases, causing the piston to encounter greater fluid resistance at the same displacement point. Differences in the compressibility characteristics of the fluids result in inconsistent power increase rates in the hydraulic system during the early compression phase; therefore, the higher the intake pressure, the more dramatic the increase in transient power.

The difference in hydraulic system output power between the 8 MPa and 6 MPa operating conditions reached a maximum of 10.62 kW at a piston displacement of approximately

https://doi.org/10.3390/en19122886

0.47 mm. Furthermore, the non-opposed configuration causes the power load to increase sharply during the early compression phase, exacerbating the hydraulic transient impact.

4.4.2. Output Power Characteristics of the Drive System for an Opposed-Piston Reciprocating Pump

Figure 11 reveals obvious differences in the output power characteristics between non-opposed reciprocating pumps and opposed reciprocating pumps. During the compression stroke, the growth trajectories and rates of the power curves under different intake conditions are nearly identical. However, during the steady-state discharge phase, the peak output power gradually decreases as the intake pressure increases. Data shows that under operating conditions ranging from 6 MPa to 8 MPa, the maximum difference in transient power during the early compression phase is only 0.93 kW.

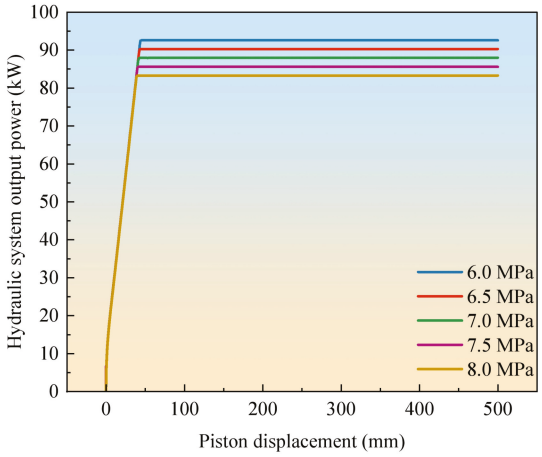


Figure 11. Output Power Curve of Hydraulic System for Opposed Reciprocating Pump (6–8 MPa).

However, when the system enters the 25 MPa steady-state discharge phase, as the inlet pressure increases from 6 MPa to 8 MPa, the peak output power of the hydraulic main pump decreases from 92.59 kW to 83.31 kW. For every 0.5 MPa increase in inlet pressure, the system's steady-state peak power decreases by approximately 2.32 kW.

This power output behavior is mainly caused by the suction-pressure-assisted load compensation of the opposed-piston configuration. At the beginning of each stroke, the same suction-pressure level exists on the intake side. Therefore, the initial hydrostatic load is largely balanced in the coupled opposed-piston assembly. As the discharge-side pressure increases during compression, the suction-side pressure continues to act as a load-compensation term. Consequently, the hydraulic power demand is mainly governed by the inlet–outlet net pressure difference rather than the full discharge pressure.

As the compression process progresses, the pressure inside the cylinder gradually rises, and the compensatory power required from the hydraulic side varies with the net pressure difference, ultimately resulting in a monotonically decreasing trend in steady-state peak power.

4.4.3. Relationship Between Net Pressure Difference and Hydraulic Output Power Under Different Inlet Pressures

Figure 12 compares the inlet–outlet net pressure difference and the steady-state peak hydraulic power of the opposed and non-opposed pumps under different inlet pressures. As the inlet pressure increases from 6 MPa to 8 MPa, the net pressure difference decreases from approximately 19.11 MPa to 17.11 MPa. Correspondingly, the peak hydraulic power of the opposed pump decreases from approximately 92.59 kW to 83.31 kW, indicating that the increase in suction pressure effectively reduces the hydraulic load required for CO_2 pressurization.

https://doi.org/10.3390/en19122886

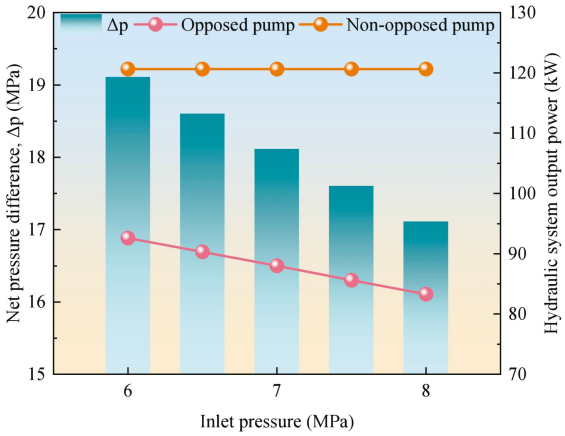


Figure 12. Variations in net pressure difference and hydraulic system output power under different inlet pressures.

In contrast, the non-opposed pump maintains an almost constant peak hydraulic power of approximately 120.62 kW over the same inlet-pressure range. This indicates that the inlet pressure in the non-opposed configuration acts only as a suction boundary and does not contribute to compression-load compensation. Compared with the non-opposed pump, the opposed pump reduces the peak hydraulic power by approximately 28.03 kW at 6 MPa and 37.31 kW at 8 MPa, corresponding to reductions of about 23.2% and 30.9%, respectively. Therefore, the energy-saving advantage of the opposed configuration becomes more pronounced as the inlet pressure increases.

5. Field Testing and Performance Comparison

5.1. Test System Setup

To verify the practical operating performance and model prediction accuracy of the optimized opposed-piston reciprocating pump, a field reliability operation test was carried out under actual dense-phase CO_2 injection conditions. Considering the need for a direct comparison with the simulation results, a continuous 24 h stable operating dataset was selected for detailed analysis. The selected dataset was used to evaluate the agreement between theoretical prediction, AMESim simulation, and field measurement, including hydraulic oil pressure, effective flow rate, and energy-consumption fluctuation.

The test was performed at an actual CCUS injection site, with the discharge pressure based on the on-site wellhead pressure. CO_2 from the pipeline entered the injection pump via a front-end throttling and separation skid, with an inlet pressure range of 6–8 MPa. The test system is shown in Figure 13, and the field test setup is shown in Figure 14.

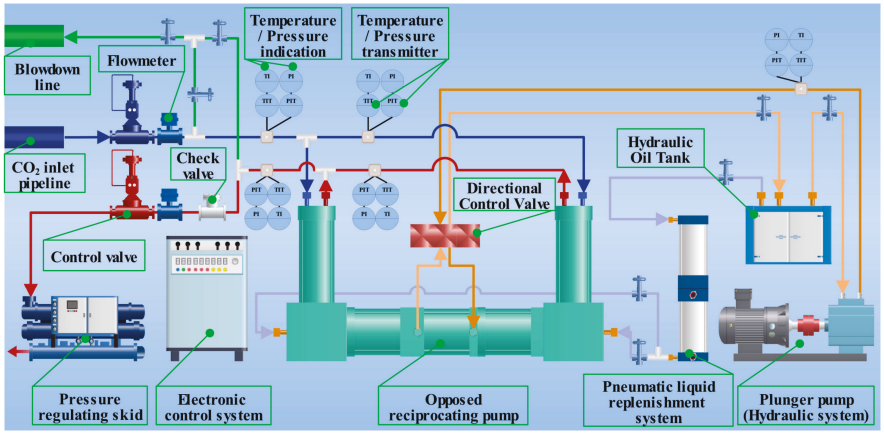


Figure 13. Schematic diagram of a field test of an opposed-piston reciprocating pump.

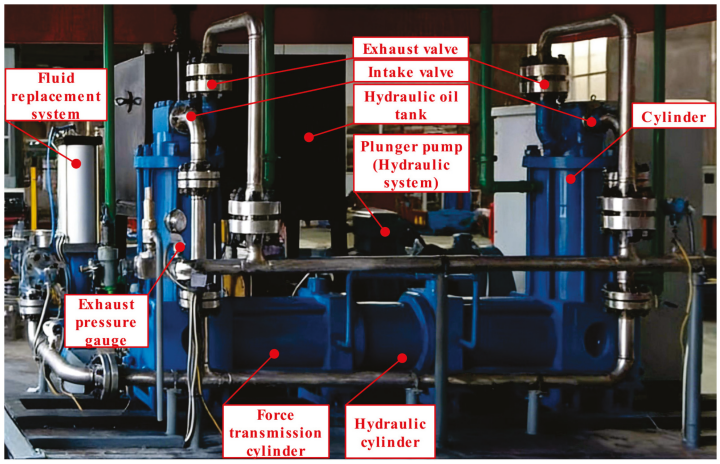


Figure 14. On-site test setup for an opposed-piston reciprocating pump.

To ensure the reliability of the field test data, the test system performed high-precision monitoring of key thermodynamic parameters. The main technical parameters of the field test are shown in Table 3.

Table 3. Table of key technical parameters for field tests.

Category	Parameter	Value	Description
Fluid & Thermodynamic	Rated inlet pressure	6.00~8.00 MPa	
	Rated discharge pressure	20.00~25.00 MPa	
	Ambient temperature	28.00 °C	
	Design Flow Rate	15.00 m^3/h	
	Working Fluid	Dense-phase CO_2	
Hydraulic & Control	Max hydraulic pressure	31.5 MPa	
	Directional valve response time	0.2 s	
	Motor Rated Power	110 kW	
Measurement & Sensors	High-frequency pressure transmitters	0~40 MPa	±0.1% FS
	RTD temperature transmitters	−20~80 °C	Class A accuracy
	Shock-proof pressure gauges	0~40 MPa	Class 1.6
	Bimetallic thermometers	−20~80 °C	Class 1.5
	Coriolis mass flowmeter	--	±0.2%

5.2. Field Reliability Operation and Simulation Validation

5.2.1. Comparison of Hydraulic Pressure Responses Between Simulation and Field Operation

To validate the dynamic model under practical operating conditions, the hydraulic pressure response obtained from the selected 24 h field reliability dataset was compared with the theoretical and AMESim simulation results. Due to limitations imposed by the on-site CO_2 feed conditions and the actual backpressure at the injection wellhead, the inlet pressure during the selected test period fluctuated mainly between 6.18 and 6.56 MPa, while the discharge pressure remained within 21.3–21.5 MPa.

Figure 15a,b show the simulated and measured pressure curves for the inlet, discharge, and hydraulic oil pressures of the optimized opposed-piston pump system, respectively. A comparison of the simulated data and field measurements for the actual drive pressure within the hydraulic cylinder reveals that both sets of data exhibit a pressure inversion phenomenon. During the full-load fluid displacement stroke, the actual hydraulic oil pressure remained below the absolute exhaust load of 21.4 MPa, fluctuating above the net pressure difference curve between intake and exhaust, which consistently maintained a value of approximately 15 MPa.

https://doi.org/10.3390/en19122886

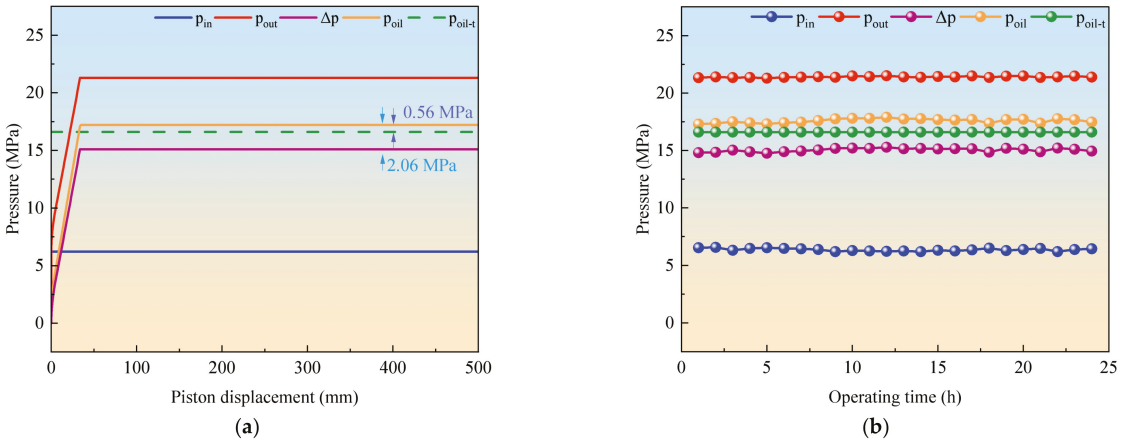


Figure 15. Pressure responses under field conditions: (**a**) Simulated pressure responses. (**b**) Measured pressure responses.

This phenomenon demonstrates that, during continuous and fluctuating actual engineering operations, the potential energy of the high-pressure gas source is transferred through the opposing mechanism, continuously providing forward thrust to the rear of the compression piston, thereby reducing the system's working load from the absolute discharge pressure to the net pressure difference.

Table 4 compares the theoretical, simulated, and experimental data for the oil pressure of this opposed-piston reciprocating pump. Based on Pascal's principle, the theoretical reference oil pressure (p_{oil-t}) required to maintain the system's static equilibrium under these operating conditions is 16.60 MPa. After incorporating friction damping for each piston in the AMESim simulation, the model output a steady-state peak oil pressure of 17.16 MPa; meanwhile, the actual operating peak oil pressure captured by the on-site high-pressure sensor fluctuated slightly between 17.29 MPa and 17.84 MPa. The data indicates that the relative error between the theoretical value, the simulated prediction, and the on-site measured value of the hydraulic oil pressure is within 4%.

Table 4. Relative errors in hydraulic oil pressure between theoretical, simulated, and experimental values.

Time (h)	Theoretical Value (MPa)	Simulation Value (MPa)	Relative Error (%)	Experimental Value (MPa)	Relative Error (%)
1	16.60	17.17	3.40	17.29	0.75
2	16.60	17.17	3.40	17.36	1.12
3	16.60	17.17	3.40	17.50	1.97
4	16.60	17.17	3.40	17.40	1.38
5	16.60	17.17	3.40	17.32	0.88
6	16.60	17.17	3.40	17.42	1.46
7	16.60	17.17	3.40	17.47	1.77
8	16.60	17.17	3.40	17.60	2.53
9	16.60	17.17	3.40	17.76	3.44
10	16.60	17.17	3.40	17.80	3.67
11	16.60	17.17	3.40	17.79	3.66
12	16.60	17.17	3.40	17.84	3.92
13	16.60	17.17	3.40	17.73	3.32
14	16.60	17.17	3.40	17.77	3.55
15	16.60	17.17	3.40	17.69	3.05
16	16.60	17.17	3.40	17.64	2.77
17	16.60	17.17	3.40	17.69	3.08
18	16.60	17.17	3.40	17.38	1.22
19	16.60	17.17	3.40	17.69	3.06
20	16.60	17.17	3.40	17.71	3.18
21	16.60	17.17	3.40	17.37	1.20
22	16.60	17.17	3.40	17.76	3.49
23	16.60	17.17	3.40	17.68	2.99
24	16.60	17.17	3.40	17.48	1.81

https://doi.org/10.3390/en19122886

The simulated values were approximately 0.56 MPa higher than the theoretical values, primarily due to volumetric hysteresis caused by fluid compressibility, frictional resistance along the pipeline, and high-pressure dry friction at the main seal. The on-site measured values were 1% to 3.96% higher than the simulated values. This is primarily due to unavoidable interference factors at the project site, such as localized friction spikes caused by assembly tolerances, microscopic cavitation distortions during high-frequency fluid direction changes, and the measurement tolerance of the load cell itself.

It should be noted that the 31.39% hydraulic-pressure reduction was obtained from the rated 8 MPa/25 MPa comparative simulation rather than directly from the field test. Due to the limitations of the on-site CO_2 supply pressure and injection-well backpressure, the field test was conducted under an inlet pressure of 6.18–6.56 MPa and a discharge pressure of 21.3–21.5 MPa. Therefore, the field test was used to validate the force-balance-based hydraulic pressure prediction under practical operating conditions. The agreement among the theoretical, simulated, and measured hydraulic pressures within 4% confirms the applicability of the force-balance model for actual dense-phase CO_2 injection.

5.2.2. Analysis of Normalized Specific Energy Consumption During Field Operation

Based on the selected 24 h continuous operating data, the rated flow rate of the opposed-piston reciprocating pump was 15 m^3/h, while the measured effective flow rate remained approximately 14.7 m^3/h. The corresponding volumetric efficiency was about 98%, indicating that the pump maintained stable displacement output during field reliability operation.

Figure 16 shows the variation in the normalized specific energy consumption of the field-test system during the selected 24 h continuous operation. The average normalized specific energy consumption was 0.422 kWh/(MPa·m^3). During most of the test period, the energy-consumption level remained relatively stable, indicating that the opposed-piston pump maintained steady energy-conversion performance under actual dense-phase CO_2 injection conditions.

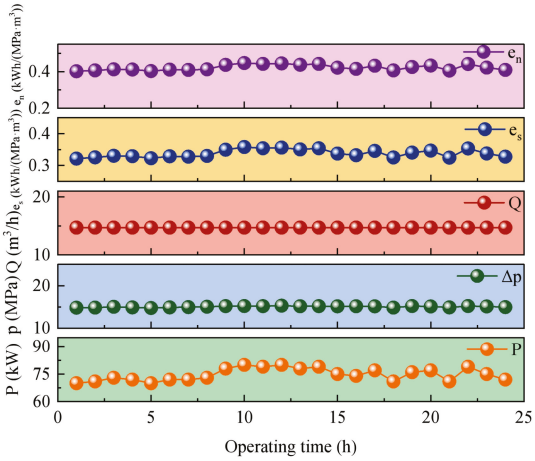


Figure 16. Normalized specific energy consumption of the field test system.

A moderate increase in normalized specific energy consumption was observed during approximately 10:00–14:00. This period corresponded to the strongest solar radiation and the highest environmental heat load at the test site. The increase in ambient temperature affected the thermophysical properties of the dense-phase CO_2 stream. As the feed-fluid temperature increased, the CO_2 density decreased and its compressibility increased, which increased the elastic compression work required for pressurization. In addition, the reciprocating pump is a positive-displacement machine, and the delivered volume per stroke

https://doi.org/10.3390/en19122886

is essentially fixed. Therefore, when the CO_2 density decreases, a higher reciprocating frequency is required to maintain the rated mass delivery. This increases the average hydraulic power of the drive system and consequently leads to a temporary rise in normalized specific energy consumption.

After this high-temperature period, the normalized specific energy consumption gradually returned to a lower level, demonstrating that the system retained good adaptability to field operating-condition fluctuations.

Although the selected field dataset covers 24 h rather than a full lifetime test, it provides a preliminary assessment of the short-term operational stability of the optimized opposed-piston pump under practical dense-phase CO_2 injection conditions. During the selected test period, no continuous upward drift in hydraulic oil pressure, no obvious decrease in effective flow rate, and no progressive increase in normalized specific energy consumption were observed. These results indicate that the hydraulic drive system maintained stable pressure regulation during continuous operation.

In addition, the rodless piston, vertical CO_2 cylinder, and ionic-liquid isolation layer reduce direct contact between dense-phase CO_2 and the mechanical sealing interface, which is beneficial for suppressing seal wear and leakage. The observed energy-consumption fluctuation was mainly related to external operating-condition variations, such as ambient heat load and CO_2 property variation, rather than progressive deterioration of the pump itself.

6. Conclusions

To reduce the high energy consumption of large-scale dense-phase CO_2 pressurized injection in CCUS applications, this study developed a structural optimization scheme based on a conventional hydraulically driven opposed-piston reciprocating pump under high-base-pressure operating conditions. By establishing a dynamic model, conducting AMESim simulations, and performing a field reliability operation test, this study clarified the suction-pressure-assisted load-compensation mechanism and evaluated the operating performance of the optimized pump under both rated simulation and practical field conditions. The main conclusions are as follows:

(1) A dense-phase CO_2-oriented structural optimization was developed on the basis of a conventional hydraulically driven opposed-piston reciprocating pump. By introducing the 6–8 MPa suction pressure into the force balance of the opposite compression cylinder, the hydraulic load was transformed from a discharge-pressure-dominated load to an inlet–outlet net-pressure-difference-dominated load.

(2) Under the rated simulation condition of 8 MPa inlet pressure and 25 MPa discharge pressure, the optimized opposed configuration reduced the peak driving oil pressure by 31.39% compared with the non-opposed reference configuration. The driving load decreased by approximately 0.55 MPa for every 0.5 MPa increase in inlet pressure, confirming the suction-pressure-assisted load-compensation effect.

(3) The introduced force-transmission cylinder enabled vertical CO_2-cylinder arrangement and converted horizontal hydraulic actuation into vertical CO_2 compression, reducing lateral loading on the sealing interface. The rodless piston and ionic-liquid isolation layer improved sealing and lubrication under low-viscosity dense-phase CO_2 conditions, contributing to an effective flow rate of approximately 14.7 m^3/h and a volumetric efficiency of about 98% in the selected 24 h field dataset.

(4) The selected 24 h field reliability dataset verified the applicability of the theoretical and AMESim models under practical operating conditions. The measured hydraulic oil pressure agreed with the predicted values within 4%, and the average normalized specific energy consumption was 0.422 kWh/(MPa·m^3). The optimized pump showed stable short-term field performance and adaptability to operating-condition fluctua-

https://doi.org/10.3390/en19122886

tions. The suction-pressure-assisted load-compensation principle may also provide a reference for other high-base-pressure fluid pressurization systems.

Author Contributions: Conceptualization, W.S.; methodology, Z.M.; validation, Y.L.; data curation, H.L. (Haibo Lin); writing—original draft preparation, X.W.; writing—review and editing, X.W., H.C. and H.L. (Hongbao Liang); visualization, Y.L.; supervision, H.L. (Haibo Lin); funding acquisition, H.L. (Hongbao Liang), Z.M. All authors have read and agreed to the published version of the manuscript.

Funding: This research was funded by the National Major Science and Technology Project of China National Petroleum Corporation (Research and Demonstration of Key Technologies for the Industrial Chain of CO_2 Capture, Oil Recovery, and Buried Storage) grant number 2021ZZ01-08 and the Fund for the Construction of Advantageous and Characteristic Disciplines in High-Level Universities of Heilongjiang Province grant number 15141230201. And The APC was funded by the Fund for the Construction of Advantageous and Characteristic Disciplines in High-Level Universities of Heilongjiang Province.

Data Availability Statement: Data will be made available on request.

Acknowledgments: The authors acknowledge the use of ChatGPT (GPT-5.5; OpenAI, San Francisco, CA, USA) during the preparation of this manuscript to improve English expression and text readability. All AI-assisted revisions were carefully reviewed and edited by the authors, who take full responsibility for the final content.

Conflicts of Interest: The funders had no role in the design of the study; in the collection, analyses, or interpretation of data; in the writing of the manuscript; or in the decision to publish the results. Hongtao Chen was employed by Startwell Intelligent Oil Recovery Technology Co., Ltd. Zhanheng Ma and Haibo Lin were employed by China National Petroleum Corporation Jilin Oilfield Branch Survey and Design Institute. Wanchun Sun was employed by Water Pump Factory of Boshan. The remaining authors declare that the research was conducted in the absence of any commercial or financial relationships that could be construed as a potential conflict of interest.

Nomenclature

ρ_{in}	CO_2 density at the suction thermodynamic state	ρ_{out}	CO_2 density at the discharge thermodynamic state
A_{gas}	Cylinder piston area	A_{hyd}	Annular area of the hydraulic cylinder piston
$v(t)$	Piston velocity	p_{in}	Inlet pressure
$p_{out}(t)$	Instantaneous discharge pressure	Δp	Inlet–outlet net pressure difference
m_{th}	Theoretical mass flow rate	m_{act}	Actual mass flow rate
M	Equivalent mass of the moving piston assembly	$\ddot{x}$	Acceleration of the piston assembly
x	Displacement of the piston assembly	F_f	Lumped friction resistance of the piston assembly and sealing interfaces
p_{oil-t}	Theoretical hydraulic oil pressure	p_{oil}	Hydraulic oil pressure
$P_{in}(t)$	Instantaneous power of the reciprocating pump system	$P_{oil}(t)$	Instantaneous power of the hydraulic system
ε	Relative clearance volume coefficient	Q_v	Volumetric flow rate
S	Cylinder piston effective stroke	f	Reciprocation frequency
η_v	Volumetric efficiency	n	Work times per cycle
e_s	The hydraulic system normalized specific energy consumption.	η_h	Overall hydraulic transmission efficiency from the hydraulic pump to the actuator
η_m	Motor efficiency	η_p	Hydraulic pump efficiency
K_{eff}	Effective bulk modulus of dense-phase CO_2	e_n	System normalized specific energy consumption.

References

1. Al-Breiki, M.; Bicer, Y. *Sustainable Energy Carriers for Energy Storage and Transport: Exploring Advanced Solutions for a Green Future*; Springer Nature: New York, NY, USA, 2025.
2. Wang, X.; Chen, H.; Liang, H.; Liu, Y.; Chen, B.; Ma, Z.; Lin, H. Comprehensive Evaluation of CO_2 Geological Storage: Mechanisms, Methods and Project Progress. *Sustain. Geosci. People Planet Prosper.* **2025**, *1*, 100010. [CrossRef]

3. Li, Q.; Li, Q.; Wang, F.; Xu, N.; Wang, Y.; Bai, B. Settling behavior and mechanism analysis of kaolinite as a fracture proppant of hydrocarbon reservoirs in CO_2 fracturing fluid. *Colloids Surf. A Physicochem. Eng. Asp.* **2025**, *724*, 137463. [CrossRef]
4. Cao, C.; Liu, H.; Hou, Z.; Mehmood, F.; Liao, J.; Feng, W. A review of CO_2 storage in view of safety and cost-effectiveness. *Energies* **2020**, *13*, 600. [CrossRef]
5. Allahyarzadeh-Bidgoli, A.; Yanagihara, J.I. Energy efficiency, sustainability, and operating cost optimization of an FPSO with CCUS: An innovation in CO_2 compression and injection systems. *Energy* **2023**, *267*, 126493. [CrossRef]
6. Raju, D.; Ramdin, M.; Vlugt, T.J. Thermophysical Properties and Phase Behavior of CO_2 with Impurities: Insight from Molecular Simulations. *J. Chem. Eng. Data* **2024**, *69*, 2735–2755. [CrossRef] [PubMed]
7. Li, Q.; You, D.; Li, Q.; Wang, F.; Wang, Y.; Yang, Y. Analysis of sedimentation behavior and influencing factors of solid particles in CO_2 fracturing fluid. *Processes* **2025**, *13*, 4049. [CrossRef]
8. Li, Q.; Li, Q.; Cao, H.; Wu, J.; Wang, F.; Wang, Y. The crack propagation behaviour of CO_2 fracturing fluid in unconventional low permeability reservoirs: Factor analysis and mechanism revelation. *Processes* **2025**, *13*, 159. [CrossRef]
9. Saxena, A.; Prakash Gupta, J.; Tiwary, J.K.; Kumar, A.; Sharma, S.; Pandey, G.; Biswas, S.; Raghav Chaturvedi, K. Innovative pathways in carbon capture: Advancements and strategic approaches for effective carbon capture, utilization, and storage. *Sustainability* **2024**, *16*, 10132. [CrossRef]
10. McMillan, C.; Buksh, N.; McSpadden, A.; Trevisan, R.; Howard, J. Development of a Fit-for-Purpose CO_2 Injection Model for Carbon Capture, Utilization, and Storage Casing and Tubing Design. *SPE J.* **2025**, *30*, 3364–3381. [CrossRef]
11. Shen, M.; Guo, W.; Tong, L.; Wang, L.; Chu, P.K.; Kawi, S.; Ding, Y. Behavior, mechanisms, and applications of low-concentration CO_2 in energy media. *Chem. Soc. Rev.* **2025**, *54*, 2762–2831. [CrossRef] [PubMed]
12. Yao, Z.; Cui, X.; Gebraeel, N.; Xia, T.; Xi, L. Metric learning-based two-stage imbalanced fault diagnosis model for water injection pump. *J. Reliab. Sci. Eng.* **2025**, *1*, 045402. [CrossRef]
13. Shen, K.; Xiong, W.; Ba, Q.; Liao, Y.; He, L. Research on Parallel Operation Characteristics of High-pressure Pumps Applied in Coal Mine Hydraulics permeability improvement. *J. Phys. Conf. Ser.* **2021**, *2029*, 012030. [CrossRef]
14. Wang, Y.; Liu, Y.; Dong, J. Analysis of flow pulsation in a crankshaft tri-piston pump. *Ships Offshore Struct.* **2025**, 1–10. [CrossRef]
15. Aakre, S.R.; Anderson, M.H.; Brooks, P.W. Volumetric efficiency and pressure pulsations of a triplex reciprocating supercritical CO_2 pump. *J. Supercrit. Fluids* **2021**, *168*, 105072. [CrossRef]
16. Zhao, S.; Liu, Y.; Wu, D.; Wang, C.; Wang, Z. Theoretical and experimental flow characteristics of a large-scale annular channel in terms of deformation gradient, eccentricity, and water compressibility. *Lubricants* **2023**, *11*, 134. [CrossRef]
17. Li, Y.; Wu, X.; Liu, X.; Cui, Y.; Wang, Z. Different structures for fatigue life analysis of plunger pair considering stress distribution. *Aust. J. Mech. Eng.* **2026**, 1–10. [CrossRef]
18. Rony, R.U.; Yang, H.; Krishnan, S.; Song, J. Recent advances in transcritical CO_2 (R744) heat pump system: A review. *Energies* **2019**, *12*, 457. [CrossRef]
19. Bruno, F.; Belusko, M.; Halawa, E. CO_2 refrigeration and heat pump systems—A comprehensive review. *Energies* **2019**, *12*, 2959. [CrossRef]
20. Mathie, R.; Markides, C.N.; White, A.J. A framework for the analysis of thermal losses in reciprocating compressors and expanders. *Heat Transf. Eng.* **2014**, *35*, 1435–1449. [CrossRef]
21. Xiao, C.; Lu, Z.; Yan, L.; Yao, S. Transient behaviour of liquid CO_2 decompression: CFD modelling and effects of initial state parameters. *Int. J. Greenh. Gas. Control* **2020**, *101*, 103154. [CrossRef]
22. Devraj, L.; Naik, M.G.; Modupalli, N.; Thangaraju, S.; Natarajan, V. Dense phase carbon dioxide. In *Handbook of Research on Food Processing and Preservation Technologies: 5-Volume Set*; John Wiley & Sons, Ltd.: Chichester, UK, 2022; Volume 169.
23. Ma, H.; Tong, Y.; Wang, X.; Wang, H. Advancements and assessment of compressed carbon dioxide energy storage technologies: A comprehensive review. *RSC Sustain.* **2024**, *2*, 2731–2750. [CrossRef]
24. Huang, J.; Zhou, Y.; Huang, Y.; Luo, Q.; Yuan, Y.; Yang, C.; Hu, W. Experimental study of pressure drop oscillation in a supercritical carbon dioxide natural circulation loop. *Int. J. Heat Mass Transf.* **2024**, *220*, 125005. [CrossRef]
25. Liu, C.; Wei, X.; Yi, Z.; Li, Z.; Zhu, C.; Ma, Z. Strength analysis and structure optimization of the crankshaft of an opposed-power reciprocating pump. *Machines* **2023**, *11*, 123. [CrossRef]
26. Zhao, K.; Lou, Y.; Peng, G.; Liu, C.; Chang, H. A review of the development and research status of symmetrical diaphragm pumps. *Symmetry* **2023**, *15*, 2091. [CrossRef]
27. Li, Z.; Song, J.; Huang, Y.; Li, Y.; Chen, J. Design and analysis for a new energy-saving hydraulic pumping unit. *Proc. Inst. Mech. Eng. Part C J. Mech. Eng. Sci.* **2018**, *232*, 2119–2131.
28. Qi, Q.; Ren, S.; Wang, C.; Chen, Z.; Jia, X.; Peng, X. Thermodynamic performance optimization of two-stage hydraulic-driven piston hydrogen compressors based on variable speed control method. *Int. J. Hydrogen Energy* **2025**, *145*, 205–214. [CrossRef]
29. Sun, Z.; Zeng, Q.; Wan, L.; Dai, H. Control and dynamic characteristics analysis for the double-compound axial piston pump based on working conditions. *Machines* **2022**, *10*, 411. [CrossRef]

30. Karadas, F.; Köz, B.; Jacquemin, J.; Deniz, E.; Rooney, D.; Thompson, J.; Yavuz, C.T.; Khraisheh, M.; Aparicio, S.; Atihan, M. High pressure CO_2 absorption studies on imidazolium-based ionic liquids: Experimental and simulation approaches. *Fluid Phase Equilibria* **2013**, *351*, 74–86. [CrossRef]
31. Gazarov, R. Principles of operation and calculation of parameters of single-acting three-cylinder pumps. *Chem. Pet. Eng.* **2008**, *44*, 275–281. [CrossRef]

Disclaimer/Publisher's Note: The statements, opinions and data contained in all publications are solely those of the individual author(s) and contributor(s) and not of MDPI and/or the editor(s). MDPI and/or the editor(s) disclaim responsibility for any injury to people or property resulting from any ideas, methods, instructions or products referred to in the content.

MDPI AG
Grosspeteranlage 5
4052 Basel
Switzerland
Tel.: +41 61 683 77 34

Energies Editorial Office
E-mail: energies@mdpi.com
www.mdpi.com/journal/energies



Disclaimer/Publisher's Note: The title and front matter of this reprint are at the discretion of the Guest Editors. The publisher is not responsible for their content or any associated concerns. The statements, opinions and data contained in all individual articles are solely those of the individual Editors and contributors and not of MDPI. MDPI disclaims responsibility for any injury to people or property resulting from any ideas, methods, instructions or products referred to in the content.





Academic Open
Access Publishing

mdpi.com

ISBN 978-3-7258-8654-8